To Mum and Dad

with love.

UNIVERSITY OF SOUTHAMPTON

Mesoporous Nickel- an Odyssey Through Synthesis, Characterisation and Application to Electrochemical Power Devices

by

Phillip A. Nelson

Doctor of Philosophy

Faculty of Science

Department of Chemistry

May 2003

UNIVERSITY OF SOUTHAMPTON

ABSTRACT

FACULTY OF SCIENCE

CHEMISTRY

Doctor of Philosophy

MESOPOROUS NICKEL- AN ODYSSEY THROUGH SYNTHESIS, CHARACTERISATION AND APPLICATION TO ELECTROCHEMICAL POWER DEVICES

by Phillip Andrew Nelson BSc. (Hons)

This thesis describes the synthesis, characterisation and application of mesoporous nickel to electrochemical technologies. Mesoporous nickel was synthesised by electroreduction of nickel salts within the aqueous domains of self-assembled liquid crystalline templates. These materials were characterised structurally and electrochemically.

Materials with both hexagonal and bicontinuous cubic pore geometry with pore sizes of the former between 3.5 and 7 nm were fabricated with appropriate selection of the surfactant template and deposition conditions. Pores were shown to be of uniform diameter and possessing long range continuity. Electrochemical characterisation revealed a very high capacity for charge storage in alkaline solution (up to 824 mC cm^{-2} for a 0.65 μm thick electrode), coupled with extremely rapid rates of charge transfer.

These properties were used to create a supercapacitor device utilising aqueous chemistry and consisting of all-mesoporous electrodes with exceptionally high power and energy densities. Cyclic voltammetry and potential step experiments demonstrated delivery of 222 mC cm^{-2} or 166 mA.h g^{-1} (of nickel electrode) in 50 ms at a mean discharge voltage of 1.18 V using an aqueous electrolyte. This translates into energy and power densities of 706 kJ kg^{-1} and 14.1 MW kg^{-1} respectively for the $Ni/Ni(OH)_2$ electrode. Cycling behaviour of this device was also unique in that charge storage capacity was observed to increase by 10 % over 15000 cycles.

The principal of the mesoporous supercapacitor was extended to non-aqueous lithium storage chemistries with the demonstration of mesoporous nickel as a lithium ion storage electrode.

Finally, the deposition process was examined in detail. This investigation examined the fundamental properties of ionic conductivity and diffusion in liquid crystalline template phases and from this established methods by which high quality mesoporous electrode films may be deposited using the inexpensive Brij® surfactants. In particular, the effects on mesostructure quality of thermally annealing the template were discussed. Issues concerning the fabrication of thicker and larger area mesoporous films were also discussed.

List of Contents

Chapter 2 The Preparation of Mesoporous Nickel

Chapter 3 The All-Mesoporous Supercapacitor

Chapter 4 Application of Mesoporous Nickel to Lithium Battery Electrodes

Chapter 5 Ionic Conductivity in Liquid Crystalline Phases and the Production of High Quality Mesostructures

Preface

The work described in this thesis was carried out under the supervision of Doctor John R. Owen at the University of Southampton between January 2000 and January 2003 while in registered postgraduate candidature. No part of this thesis has been submitted at this or any other University.

Acknowledgements

There are many people who helped me in the completion of this PhD and many more to whom I should give thanks for being in the position that I now am in. I will try to do them justice.

First I would like to thank Professor John Owen (who needs a Chair if everyone already thinks you have one?) who supervised not only my chemistry but all matters of my life. John's door was always open and his presentation as a friend rather than just a supervisor made students in the Owen group the envy of many in the department. Phil 'the pores are definitely standing up' Bartlett and George Attard I thank for their stimulating discussions. Derek Pletcher whose silent walks (except for the noisy shoes) down the 7th floor walkway always made me feel like I didn't know enough about electrochemistry and whose abundant red pen marks turned the first draft of this thesis into what I hope is a better version.

To the 1st generation of Owen group members I give thanks for your camaraderie and help when I joined the group. Joanne Elliott who gave me my first lessons in electrochemistry and mesoporous materials, Emmanual Eweka the wise old man of the group, Emmanuelle Raekelboom (she's only quiet so she can listen to your gossip) and Yaser Abu-Lebdeh who became a good friend and always took an active interest in enhancing my 'social' life. To the 2nd generation Owen group members I send equal thanks. Ailsa Leck for struggling to maintain the testosterone-oestrogen balance in the lab and for ordering a lab computer with a TV card in it, Alan Spong for those Red Alert 2 stress relieving sessions and for making me feel better by graciously losing every naval battle we ever had, to Girts Vitins for his endless electrochemical advice and funny impersonations of a Soviet block scientist, Thierry Le Gall for keeping the lab tidy and Kenno Helmut Reiman for his contribution in making the lab a fun place to work and for showing me what a wide-boy is.

Thank you to Dr. Geoff Edwards in my Honours Year at the University of Queensland who introduced me to research and encouraged me to spread my wings and do a PhD abroad.

To the countless tea ladies in the Chemistry tea room whose dish washing skills made sure I was thinking about surfactants even when I was on a tea break.

I would like to thank Mizio Matteucci for making 36 Sirdar Road more than just a student house and for his friendship.

Most of all I would like to thank those who have given me love. To my Mother and Father and Shane and Michelle who always asked when I was coming home and supported me from the other side of the world. To Rossella I send thanks for making my time in Southampton a special one.

Chapter 1

Introduction to Porous Materials and Their Applications

1.1 The Need for Porous Materials

In many electrochemical systems, particularly those of industrial importance, it is desirable for reaction processes to occur as rapidly as possible. High reaction rates in reactions such as the electrochemical oxidation of species O to R in Equation 1, are manifest by high currents since the degree of reactant conversion is proportional to the current (Equation 2).

$$O \rightarrow R + e^- \qquad (1)$$

$$-\frac{d[O]}{dt} \propto I \qquad (2)$$

High reaction rates may be achieved in a number of ways. One of the easiest ways of increasing current in a cell is to increase the overpotential at the electrode which causes an exponential increase in the current (where the reaction is not mass transport limited) as dictated by the general form of the Tafel equation (3):

$$\eta = a + b \log I \qquad (3)$$

where η is the overpotential and I is current. This method is generally acceptable in electrolytic cells however in energy producing galvanic cells an increase in the cell overpotential is manifest as a decrease in the cell output voltage. To avoid this problem, in certain systems such as fuel cells the equilibrium potential of a reaction may be shifted such that the same cell potential produces a higher current. This is achieved by selecting an electrode material of higher catalytic activity. This approach constitutes the first of the two methodologies used in optimisation of electrode performance, that is, optimisation of electrode composition. Very much an empirical art, optimisation of electrode performance by tuning electrode composition is now the focus of combinatorial investigations.

Another means of increasing cell current is to increase the area of an electrode. This is achieved by simply extending the geometric area of the electrode (as in a dielectric capacitor), or less crudely, by increasing the roughness of the electrode such that the current density per unit geometric area is increased. The latter approach is the basis of the second methodology used in enhancing electrode performance, that is, optimisation of electrode structure and is the topic of discussion in this thesis.

1.2 Existing Porous Materials

1.2.1 Nanoparticulates

Electrodes based on nanoparticle powders are the most commonly used high surface area electrodes. The premise of their operation is simple: in creating a finely divided material, the surface area to volume ratio and therefore their ability to deliver charge quickly is increased. Electrode fabrication is equally simple, involving aggregation of a nanoparticle powder into a continuous form, usually by sintering.

Powders are generally formed via the sol-gel process which can be expedited in 2 ways. The spontaneous solution sol-gel method[1,2] proceeds by formation of a precipitate from aqueous/alcoholic solution containing a precursor metal salt, most commonly a chloride. For example, fine platinum particles are precipitated by warming a solution of KOH and $PtCl_2$ in ethanol.[3] The second and more popular method of synthesising nanoparticles involves the use of network forming species and their hydrolysis in an appropriate solution.[4] In an example synthesis[5], the process begins with hydrolysis of a silicon alkoxide to produce silicic acids as portrayed in Reaction 1. The thus formed acids then undergo self-condensation polymerisation by Reaction 2 to form soluble high molecular mass polysilicates (a sol), and these polysilicates then polymerise to form a three-dimensional network, the pores of which are filled with solvent molecules (a gel). Hence the name 'sol-gel polymerisation'. Oxide particles are obtained after filtering the solvent from the suspended solid particles and sintering. The sintering step removes excess water from the sol and converts the usually amorphous hydrated mass into a crystalline oxide. The electrode itself is usually fabricated by tape casting or doctor blading a paste

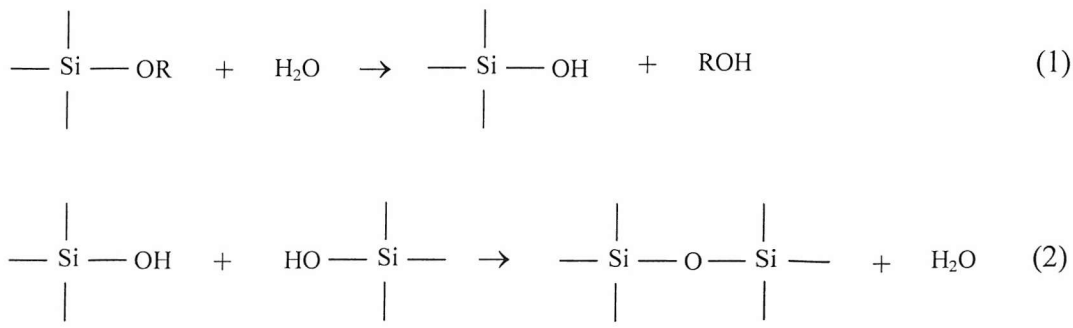

(1)

(2)

containing the oxide particles, an organic dispersing agent and solvent onto a substrate. After sintering the cast electrode, the final product has a structure consisting of a random network of interconnected spheres with porosity of varying diameter as illustrated in Figure 1.1[6].

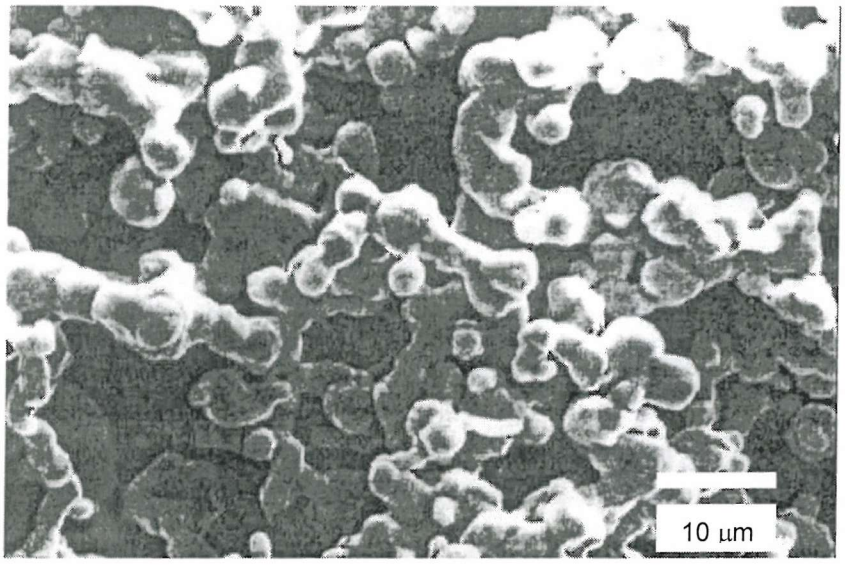

Figure 1.1.[6] The porosity of this sintered TiO_2 electrode used in photovoltaic applications is constituted by a random and non-uniform structure.

The porosity of nanoparticulate electrodes possess a considerable amount of tortuosity and bottle necking which often results in mass transport limitation in the movement of reacting species within the structure. Pore size and volume may be controlled to a limited extent by variation in precursor particle size and packing

density (the latter may in turn be controlled by variation in the casting process). However, the process of fabricating electrode structures from nanoparticle powders is still a relatively random one and does not allow the maker to design electrode structure.

1.2.2 Aerogels and Xerogels

Aerogels are high surface area nanoporous materials composed of a network of interconnected solid species. Aerogels differ from nanoparticulate materials in that the former have significantly lower densities and higher porosities as illustrated in Figure 1.2.[7]

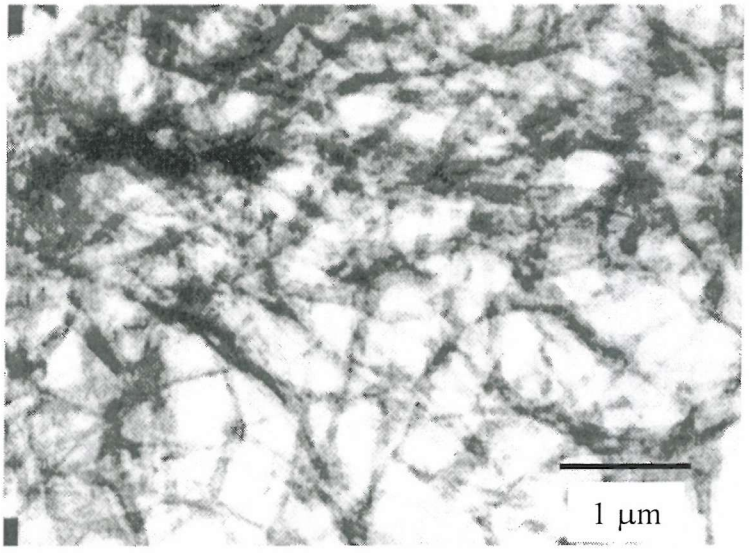

Figure 1.2.[7]This titania aerogel with its web-like morphology is considerably less dense than sintered powder porous materials.

The morphology of aerogels is best understood when considering the method of their synthesis. Synthesis of aerogels is done using an adaptation of sol-gel processing with the formation of a wet gel using a network forming precursor such as a metal alkoxide. The similarity ends here however, since instead of separating the solid components from the gel by a method such as filtration, the gel is allowed to undergo further polycondensation forming a cohesive but fragile network. The gel is then

carefully dried, preserving the condensed network. The manner in which the liquid phase is removed from the wet gel determines whether the dried solid is a highly porous aerogel or a denser xerogel. The latter is formed as a result of collapse of the wet gel's structure as the pore liquid is removed relatively quickly by evaporation. By drying the wet gel under supercritical CO_2 stresses associated with capillary pressure induced by evaporation of the pore water are removed, allowing the wet gel network structure to remain intact.[8] Unlike the older and more established technology of nanoparticulate electrodes, aerogels and xerogels have found only limited commercial application. Aerogels of silica are used as high surface area catalysts, catalyst supports and chromatographic stationary phases.[9] However, aerogels and xerogels are receiving increasing attention in the technical literature, particularly in the development of electrochemical applications such supercapacitors and lithium ion secondary batteries.[10]

1.2.3 Raney Metals

Nanoporous Raney metal coatings are fabricated by selective alkaline leaching of a Raney precursor alloy composed of a matrix metal (most commonly nickel) and a less noble metal (usually aluminium or zinc) where the mole fraction of nickel is below 0.5. Leaching of the precursor alloy such as $NiAl_3$ or Ni_5Zn_{21} proceeds with the selective dissolution of the less noble metal as indicated in Reaction 3, leaving a porous nickel structure.

$$NiAl_3 + 3OH^- + 9H_2O \rightarrow 3Al(OH)_4^- + 4\,1/2\,H_2 + Ni_{porous} \qquad (3)$$

Raney nickel has found application as the hydrogen evolving cathode in alkaline water electrolysis and the chlor-alkali process and as the fuel anode in some forms of the alkaline fuel cell. Raney nickel precursor alloys are commercially made by either cathodic co-deposition of a Ni/Zn alloy or by galvanostatic cathodic deposition of nickel from a $NiSO_4$ bath containing micrometer sized Ni/Al powder particles in the form of a slurry. The latter process produces deposits widely known as Raney nickel composite coatings.

The structure of Raney nickel consists of a matrix of small interconnected nickel crystals varying in size from 10 to 100 nm with pore diameters in the range 2 to 5 nm. This nanoporosity which contributes the vast majority of Raney nickel's catalytic activity is divided by larger micrometer sized cracks as illustrated in Figure 1.3. Porosity may vary from 20 to 50 %, with a corresponding variation of the specific area between 20 and 100 $m^2 g^{-1}$.[11] The pores in Raney nickel are not cylindrical but are characterised by a slit-like morphology. This porosity is not fractal, as reflected by a narrow pore size distribution. Despite the positive attributes of high surface area

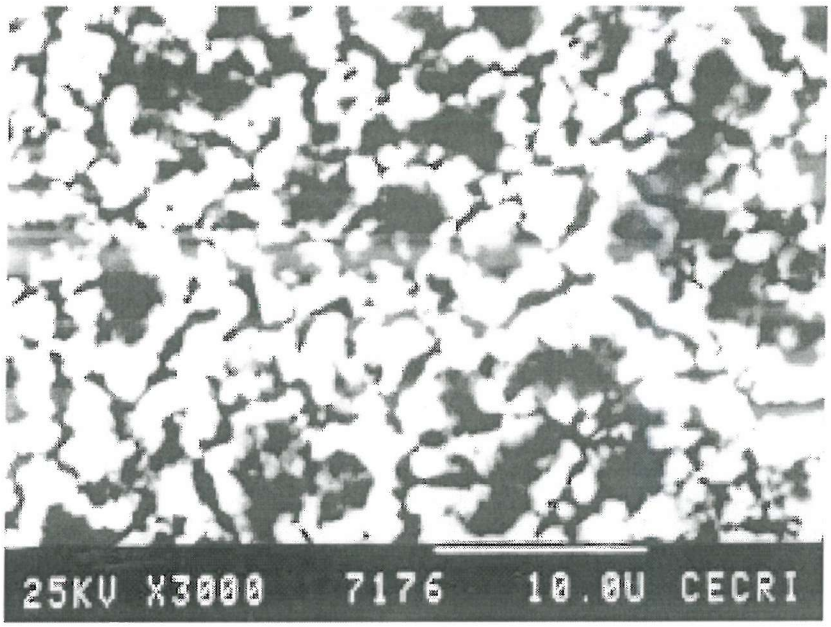

Figure 1.3.[12] The slit-like morphology of Raney metal porosity makes access to the entire surface area difficult for reacting species.

and large pore volume conveyed by the pore structure of Raney nickel, the structure of the pores also exposes the electrode to significant losses in catalytic activity upon anodic oxidation of the nickel which occurs often during operation. This loss in activity was attributed by Ewe and co-workers[12,13] to pore clogging by the more voluminous oxidation product $Ni(OH)_2$; these authors showed that only 40 % of the original catalytic activity is recoverable by cathodic reduction of the $Ni(OH)_2$ after oxidation.

1.2.4 Zeolites

Zeolites are porous aluminosilicate based materials consisting of a crystalline anionic cage framework, charge balanced by cations residing within the cavities or channels created by the framework. The composition of the framework oxide is represented by the general formula, $\{(Al_aM_bSi_c)O_d\}$ where M may be any of the elements P, Ga, Ge, B, Be, Zn, Ti, Fe, Co, Cr, Mn, V or Mg. The zeolite framework is constructed from TO_4 ($SiO_4$for example) tetrahedra such that each apical O atom is shared between 2 adjacent tetrahedra giving a framework O/T ratio of 2. Pure silicates with this structure do not contain framework charge since Si is tetravalent. However, due to the variation in charge of the framework atoms in aluminosilicates from +4, zeolites have negatively charged frameworks (1 negative charge per Al^{3+} framework atom). Consequently, zeolite frameworks require charge balancing by extra-framework positive ions. In naturally occurring zeolites these cations are either alkali metal (eg. Na^+) or alkaline earth (eg. Ca^{2+}) ions. Synthetic zeolite frameworks are capable of hosting a larger range of cationic species such as H^+ and organic cations such as quaternary ammonium ions.

The porosity of zeolites varies greatly, with pores of either circular or elliptical geometry forming one- two- or three-dimensional networks of channels or cages. Pore size distributions are extremely narrow since pore dimensions are defined by the bond lengths and angles between the framework atoms and the volume of the voids is usually less than 50 %. Approximately 60 naturally occurring zeolites are known, however many of the more industrially important examples such as ZSM-5 (Zeolite Socony Mobil material number 5) illustrated in Figure 1.4,[14] are synthetic. Pores sizes generally range from 2.5 Å to 8 Å[15] however diameters up to 14 Å have been reported.[16]

The industrial importance of zeolites and zeolitic materials is difficult to overstate. They have found use in a number of catalytic and separation applications including adsorptive separation of hydrocarbons, purification of gases and liquids and catalytic cracking of long chain hydrocarbons to form more valuable short chain homologues. Calcined zeolites such as ZSM-5 are capable of carrying out protonation reactions on usually unreactive organic molecules because of the presence of super-acid sites

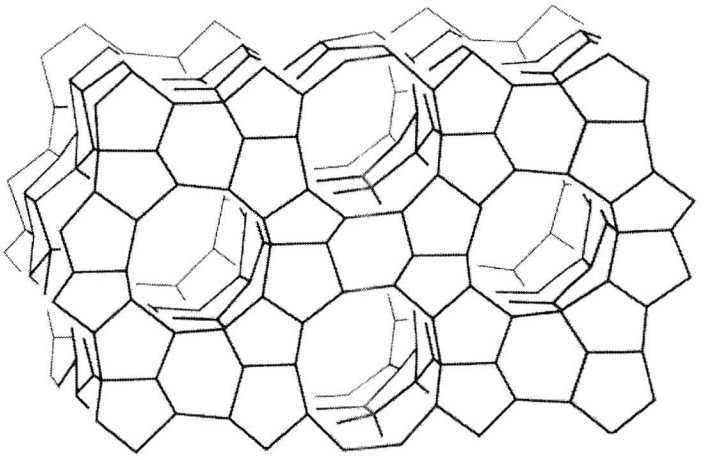

Figure 1.4[14] shows the atomic structure that gives the synthetic zeolite ZSM-5 its porosity.

within the channel structure and modification of reaction energetics due to the electronic confinement of guest species.[17] Here, the negative charge of the framework is balanced only by extremely reactive unsolvated protons such that even very weak bases like *n*-alkanes form reactive carbocations. Zeolites are also used in ion exchange and act as molecular sieves for dehydration of organic solvents. The utility of zeolites arises as a consequence of their channel/cavity structures which host metal cations, water and a vast range of potential guest species. Since the aluminosilicate cages are sufficiently robust, guest species may move in and out of the channels without disruption of the host framework. This utility is limited however by the small channel diameters of zeolitic materials, making operations such as sieving of biomolecules and cracking of the heavier fractions of crude oil impossible.

1.3 Lyotropic Liquid Crystalline Phases

1.3.1 Self Assembly of Surfactant Supramolecular Phases

Surface active agents or surfactants are molecular entities composed of both lyophilic (solvent loving) and lyophobic (solvent fearing) components. In those cases in which water is the solvent these components are referred to as hydrophilic and hydrophobic respectively. In aqueous solution surfactants exhibit characteristics of both hydrophilicity and hydrophobicity and as such surfactants are referred to as amphiphilic (loving both kinds) molecules.

In an aqueous solution containing surfactant molecules the system will seek to adopt a minimum energy configuration as dictated by the laws of thermodynamics. At very low surfactant concentrations this configuration is one in which the surfactant moves to the air-water interface (if one is present) and orients itself such that the hydrophobic component is protruding through the interface into the hydrophobic air side and the hydrophilic component remains within the water side of the interface.[18] As the concentration of dissolved surfactant increases in the solution, surfactant accumulates at the air-water interface until a complete monolayer forms corresponding to saturation of the interface. The surfactant concentration at this saturation point is known as the critical micelle concentration (cmc). Once the cmc has been reached, the saturated interface forces subsequently dissolving surfactant molecules to remain completely within the aqueous environment. As a result, these molecules adopt the next lowest energy configuration: the self assembled micellar solution (denoted L_I). Micelles are self-assembled spherical structures which minimise contact between the surfactant's hydrophobic component and water by sequestering the hydrophobic (non-polar) component within the interior of the structure and shielding it with an exterior shell composed of the hydrophilic (polar) component. Further increases in surfactant concentration are accommodated by the formation of more micelles which results in an increase in the viscosity of the solution. As the density of micelles in solution increases, the micellar packing geometry is forced to take on less random configurations and ultimately the cubic micellar phase (I_I) forms. The I_I phase consists of spherical micelles packed on a

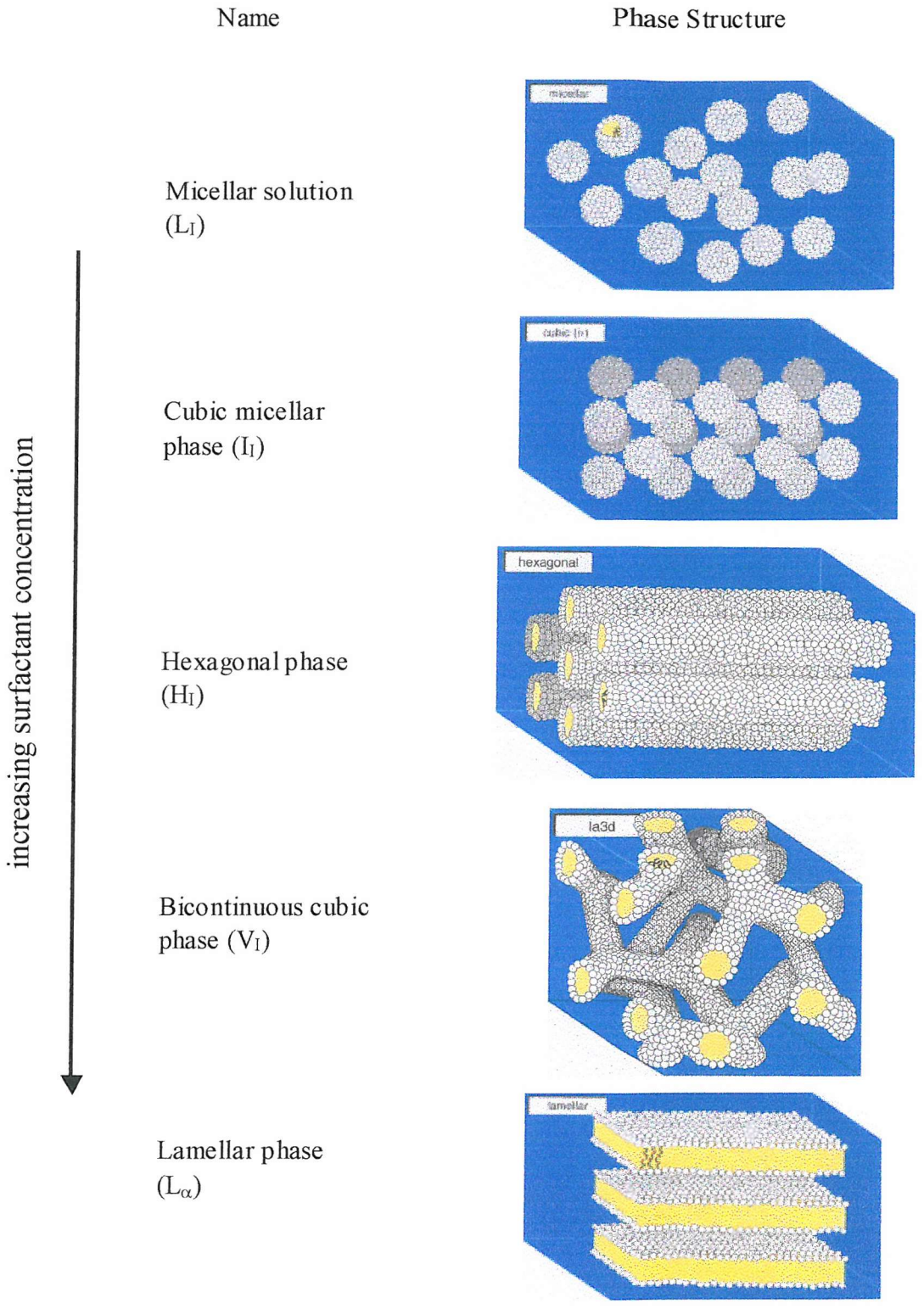

Figure 1.5[19] shows the generalised structural progression of liquid crystalline phases with increasing surfactant concentration.

body-centred cubic (bcc) lattice as illustrated in Figure 1.5, and is the first of the lyotropic liquid crystalline phases observed in surfactant-water systems. At higher surfactant concentrations spherical micelles coalesce to form rod-like structures in which the surfactant's hydrophobic segments are located within the centre of the rod. Self assembly of these cylindrical rods on an hexagonal array constitutes the hexagonal phase where surfactant rods are separated by a continuous aqueous phase. As the quantity of water in solution decreases further, another cubic morphology forms, composed of short surfactant rods which intersect to form a continuous network.[20] This is the bicontinuous cubic phase denoted V_I.[21] The V_I phase, unlike the H_I phase is structurally isotropic and possesses 3 axes of symmetry rather than 1. Under different conditions a sheet like structure called the lamellar phase (L_α) forms, consisting of surfactant molecules arranged in bilayers separated by layers of aqueous solution. These different lyotropic liquid crystalline phases are most easily recognised based on their texture under polarising light microscopy.[22]

One of the essential characteristic to consider in defining and characterising the phase behaviour of lyotropic liquid crystalline phases is the curvature of the mesophase surface. The curvature (and therefore the structure) of liquid crystalline phases may be understood and predicted to a greater extent if the surfactant packing parameter v/a_0l is considered, where a_0 is the interfacial area occupied by the head group and l and v are the alkyl chain (or more generally, the hydrophobic segment) length and volume respectively.[23] The surfactant packing parameter is inversely proportional to curvature in a liquid crystalline phase. For example, by increasing the head group size whilst keeping the hydrophobic portion of the molecule constant, the surfactant packing parameter decreases and the curvature of the phase increases. Consequently, the phase behaviour of surfactants with large head groups tends to be dominated by spherical or highly curved phases. This concept may be expressed in a more instinctive manner by noting that as the size and hence packing area occupied by the hydrophilic group is increased, surfactant packing considerations favour curved interfaces (spheres and cylinders) over planar ones (bilayers). The surfactant packing parameter also considers surfactant concentration effects since increasing surfactant concentration decreases a_0 due to the lower activity of water, and hence the reduced

hydration of each chain. Despite its apparent simplicity, the surfactant packing parameter has been successfully applied to explain the phase behaviour of polyoxyethylene surfactants.[24]

1.3.2 Different Types of Surfactants

There exists a vast array of surfactant species that are capable of self-assembling into liquid crystalline phases when mixed with water.[25] Of these, only selected non-ionic surfactants will be discussed here, that is, the polyoxyethylene family (with general formula C_xEO_y) and the tri-block copolymers. In the case of the former, the hydrophilic component of the surfactant is composed of polyethylene oxide (PEO) and the hydrophobic component of a hydrocarbon tail. The non-ionic triblock copolymers discussed here also possess PEO as their hydrophilic components but utilise polypropylene oxide (PPO) to provide the hydrophobicity. The family of tri-block copolymers consisting of the basic structural formula $(PEO)_x(PPO)_y(PEO)_x$, are commercially available (under the generic name poloxamers and the trade names Pluronics® and Synperonics®) and form micellar and lyotropic liquid crystalline phases in aqueous and other solvent systems. Where the solvent is relatively hydrophobic, micellar structure generally consists of a central dense core of PPO and an outer corona of hydrated PEO[26] as illustrated in Figure 1.6.

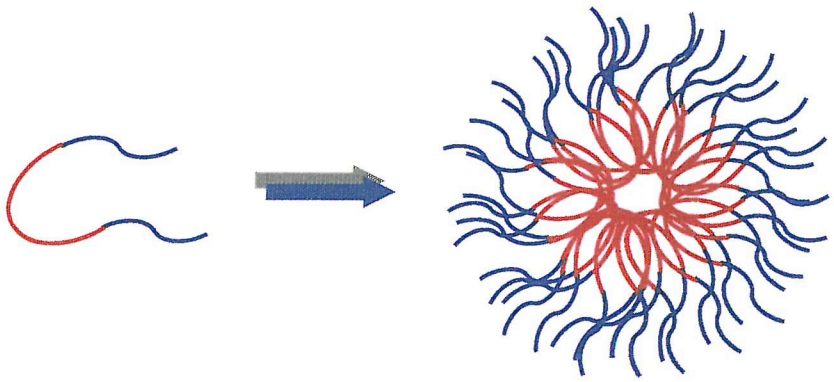

Figure 1.6 shows the shielding of a hydrophobic polymer core (red) from an aqueous solution by hydrophilic segments of a Pluronic® triblock copolymer (blue).

The Pluronic® surfactants have significantly more ideal lyotropic behaviour than the polyoxyethylene surfactants in that their phase behaviour is almost entirely dependent on interactions with the solvent[27] and almost independent of temperature, as indicated by the phase diagrams of Figure 1.7[28] and 1.8. Here it can be seen that trends in the phase behaviour of the triblock copolymer P105 are accurately modelled by trends in the surfactant packing parameter. As P105 concentration and surfactant packing density are increased, the area at the surfactant/water interface occupied by the head group is forced to decrease, and interfacial curvature in turn decreases, resulting in phase transitions from the spherical curvature of micelles to the lower planar curvature of the lamellar phase.

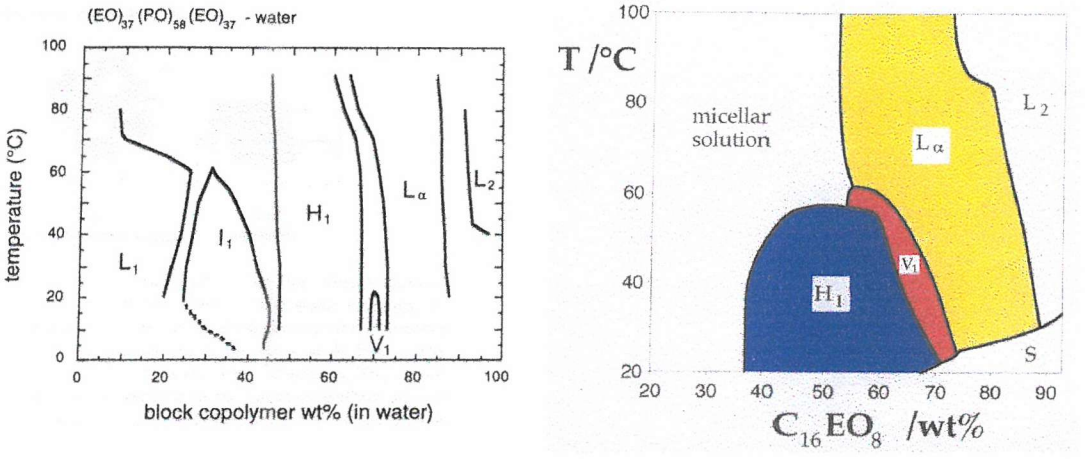

Figures 1.7[28] (left) and ***1.8***[19] (right) illustrate the phase behaviour of the triblock copolymer $(EO)_{37}(PO)_{58}(EO)_{37}$ (Pluronic® P105) and $C_{16}EO_8$ respectively in water.

Polyoxyethylene/water surfactant systems also follow this trend, however it is noted in Figure 1.8 that phase structure may also be changed significantly by variation in temperature at a constant mixture composition. In addition, the aqueous phase behaviour of Pluronic® surfactants is influenced to a much greater degree by the addition of polar solvents to aqueous surfactant mixtures[29,30] than are additions of polar solvents to non-ionic polyoxyethylene surfactant-aqueous systems.[31,32] One of the principal reasons for this difference in behaviour is the relative difference in polarity between each of the hydrophilic and hydrophobic surfactant components.

Unlike in the polyoxyethylene surfactant-water systems in which even relatively hydrophilic species such as large primary alcohols locate preferably in the hydrophobic phase, organic solvents in Pluronic® systems show a much greater tendency to partition in the hydrophilic phase.[33] Some solvents (for example ethanol) show amphiphilic behaviour and act as cosurfactants by positioning themselves at the hydrophilic/hydrophobic interface. This variation in phase behaviour with cosolvent addition has led the Pluronic® surfactants to possess the richest structural polymorphism of lyotropic liquid crystal forming species.[34]

This relative instability of the liquid crystalline phases of Pluronics® to co-solvent addition can be appreciated in knowing that the hydrophobicity of CH_2 groups in polyoxyethylene surfactants is 4-5 times greater than that of a propylene oxide group as reported by Wanka *et al.*[35] As a result, there is less lyotropic contrast between hydrophilic and hydrophobic segments in the Pluronic® surfactants and therefore less stabilisation of aggregate structures. As such, the addition of species of different polarity than those of the surfactant molecules may serve to lower the polarity difference across the interface even further, causing a phase change.

1.3.3 Alignment and Orientation

The orientation of liquid crystalline phases at solid surfaces has received much attention in the literature. Patrick *et al.*[36] reported that at a graphite surface, polyoxyethylene surfactants form hemicylindrical structures oriented parallel to the surface. Hemicylinders were supposedly formed due to hydrophobic association of the alkyl tails of the surfactant with the hydrophobic graphite surface. Here, graphite templated the adsorption of the hydrocarbon chains which occurred along one of the surface symmetry axes until a monolayer formed. Once formed, the monolayer of hemicylinders served to template subsequent adsorption such that additional layers of H_I cylindrical rods were also oriented parallel to the surface. The templating effect of graphite surfaces and formation of self-assembled structures has also been observed in interactions between graphite and alkanes and aliphatic alcohols which do not otherwise undergo self-assembly.[37]

The importance of surfactant aggregate structure at the interface is that, as indicated in the above example, the micellar orientation at a surface influences the phase structure in the bulk, however the range of this effect into the bulk and the extent of its continuity through liquid crystalline domain boundaries, if any, is unknown. Aggregate structure at the interface depends on the interactions between the surface and the surfactant groups. The non-ionic surfactant $C_{12}EO_8$ has been shown to form surface bound micelles when adsorbed at hydrophilic silica due to weak association of both the head group and the hydrocarbon tail with the hydrophilic surface, whereas adsorption at a hydrophobised silica surface results in the formation of a surfactant monolayer in which the hydrocarbon tails are strongly associated with the surface.[38,39] Miyata *et al.* carried out in-plane x-ray diffraction experiments investigating the orientation of mesochannels formed from the liquid crystalline phases of polyoxyethylene surfactants and a cationic surfactant on a polyimide polymer film.[40] This group demonstrated that mesochannel alignment was independent of the nature of the hydrophilic headgroups and was instead determined by hydrophobic interactions between the surfactant tail groups and the oriented polymer chains of the polyimide film.

Macroscopic alignment of liquid crystalline phases can be achieved by promoting interactions with surfaces or with the assistance of shear. Early literature reports suggested that on the application of a shear force, randomly oriented lamellar phases tend to align with the lamellae parallel to a glass surface while hexagonal phases also align with the rod axis parallel to the surface.[41]

1.4 Templated Materials

The application of porous materials such as those discussed in Section 1.1 is of considerable commercial interest particularly in separation, catalysis and power sources, in addition to the fundamental scientific interest in their synthesis and properties.[42] Despite this interest however, the application of basic scientific principles to the technological issues impeding the development of porous materials has been slow. Significant progress has been achieved in improving porous materials, however has been accomplished largely by manipulation of processing parameters rather than understanding of the chemical and physical mechanisms that influence porosity. As such, the development of porous materials has progressed by largely empirical means rather than by design.

The discovery and synthesis of zeolites first aroused inquiry into the possibilities of designing the structure of porous materials for specific applications. As discussed in Section 1.2.4 however, the pore sizes available in zeolitic materials do not penetrate the meso- range (2 to 50 nm). This deficiency was addressed by Kresge *et al.*[43] of Mobil Research and Development Corporation in a now much cited paper reporting the synthesis of mesoporous aluminosilicates using a self-assembled liquid crystalline template. The materials with variable pore diameters of 16 to 100 Å and a hexagonal pore arrangement (designated MCM-41) were synthesised by mixing a quaternary ammonium surfactant (< 20 wt. % of the total mixture) with alumina and a solution of silica precursor. The authors suggested a 'liquid-crystal templating' synthesis mechanism in which hexagonal arrays of cylindrical micelles formed as a result of electrostatic interactions between the cationic surfactant and anionic silicate species with subsequent condensation of the silica precursor within the aqueous domains of the liquid crystal. This seemed an obvious conclusion as suggested by the clear resemblance between the MCM-41 structure and the H_1 liquid crystalline phase found in surfactant-water mixtures. Davis *et al.*[44] supported by in situ ^{14}N NMR data proposed an alternative mechanism however, in which the synthesis mixture phase separates into a biphasic mixture of largely surfactant free aqueous solution and a small region rich in silicate encapsulated cylindrical micelles. The liquid crystalline phase is not present in the synthesis medium prior to or during formation of MCM-

41. It was suggested that phase separation occurs because the surfactant concentration is too low to permit formation of bulk liquid crystalline phases throughout the entire mixture. Stucky and co-workers supported this mechanism in which initially randomly ordered micelles interact with the silicate species, resulting in the condensation of 2 or 3 monolayers of silica around the external surface of the micelles.[45] These composite species were proposed to subsequently aggregate with further condensation as represented schematically in Figure 1.9[46] to give the characteristic long-range order of MCM-41 materials.

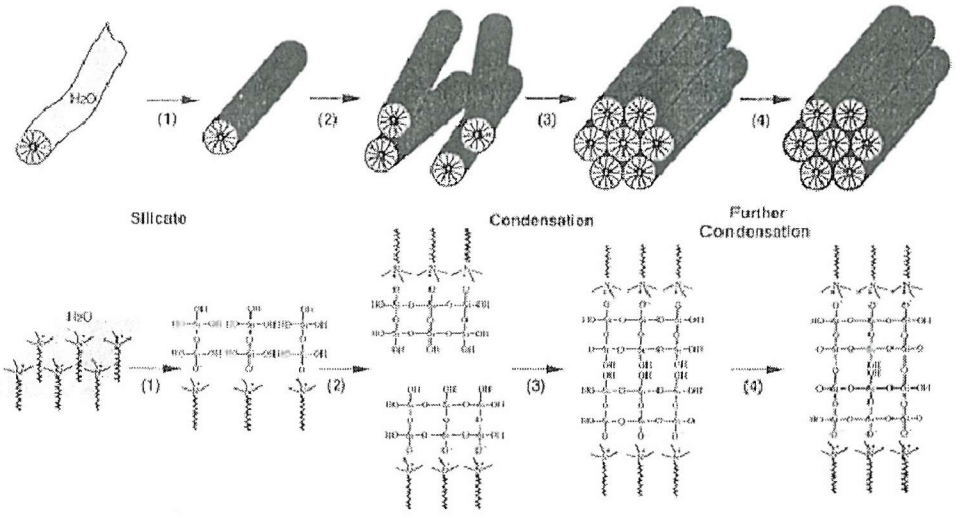

Figure 1.9.[46] In the 'MCM approach' liquid crystalline phases form only on association of inorganic precursor species with the surfactant micelles.

In an effort to increase to catalytic activity of MCM-41 silicates, Pinnavaia and co-workers used a template derived from a precursor containing 0.6 mole % primary amine to synthesise mesoporous silica based materials partially substituted with titanium.[47] Subsequent work by this group has used hydrogen bonding interactions (rather than electrostatic interactions) between non-ionic template forming species such as primary amine[48] and polyoxyethylene[49] surfactants and non-ionic inorganic precursors to facilitate the synthesis of mesoporous silicas and silica based materials. In such cases, the materials produced consisted of fine powders which were found to possess heterogeneous mesoporosity.

The use of non-ionic templates allows the templating of a wider range of materials than do electrostatic templating methods using ionic surfactants. In addition, the thicker pore walls obtained using non-ionic templates marginally improve the poor thermal and hydrothermal stability of the mesopore framework.[50] Stucky and co-workers[51,52] extended the use of non-ionic surfactant templates to the synthesis of a range of mesoporous transition metal oxides using the Pluronic® block copolymer surfactants with the general formula $(PEO)_x(PPO)_y(PEO)_x$. Previous syntheses of mesoporous materials used low molecular weight surfactants for the assembly of the mesostructures and thus produced pore sizes no greater than 4 nm. Where these materials were mesoporous metal oxides, the pore walls were relatively thin and exclusively amorphous. However, the Pluronic® synthesis route, which exploits block copolymer assembly induced by complexation of the inorganic metal species and hydrophilic copolymer moieties has produced materials with pore diameters as large as 14 nm. Here, careful calcination treatments were required to avoid structural collapse of the mesopores and even then only semi-crystalline pore walls were obtained.

Cheng *et al.* used a Pluronic® surfactant based template to synthesise mesoporous tungsten oxide for possible application as an electrochromic material.[53] Although the mesoporous material compared favourably with its sol-gel derived counterpart in applications testing, the mesoporosity of the templated material was shown to be disordered, and the mesopore structure collapsed during calcination at 400 °C due to crystallisation of the framework walls. Ozin and co-workers reported the fabrication of mesoporous nickel-yttria-zirconia composites deposited using a quaternary ammonium surfactant for fuel cell applications.[54,55] An impressive thermal stability threshold of 800 °C was reported.

An alternative surfactant templating route devised by Attard *et al.* used template mixtures with high surfactant concentrations (typically > 30 wt.% surfactant) to produce mesopore morphologies identical to the M41S family structures.[56] However, unlike the previously mentioned routes, Attard and co-workers demonstrated the ability to fabricate monolithic structures. This method is termed 'direct liquid crystal templating' (DLCT) because unlike previously mentioned routes in which the

formation of the mesoporous material is directed by micellar aggregates, deposition of the mesoporous material occurs within a preformed, ordered liquid crystalline mesophase. As a result of the existence of the template prior to deposition of the material, the formation of the template does not rely on hydrogen bonding or electrostatic interactions between the surfactant and inorganic precursor or polymerisation of inorganic species on micellar aggregates. Therefore, the DLCT route could possibly tolerate a greater range of deposition chemistries than the low surfactant concentration routes. In addition, the presence of the template prior to deposition introduces a greater degree of predictability into the deposition process, since the mesopore morphology of the deposited material has been shown to reflect that of the surfactant template.

Deposition of mesoporous silica by Attard *et al.* was carried out using a sol-gel reaction localised in the aqueous domains of the liquid crystal phases of polyoxyethylene surfactants, as represented schematically in Figure 1.10. After condensation of the silica phase, the template was removed by calcination.

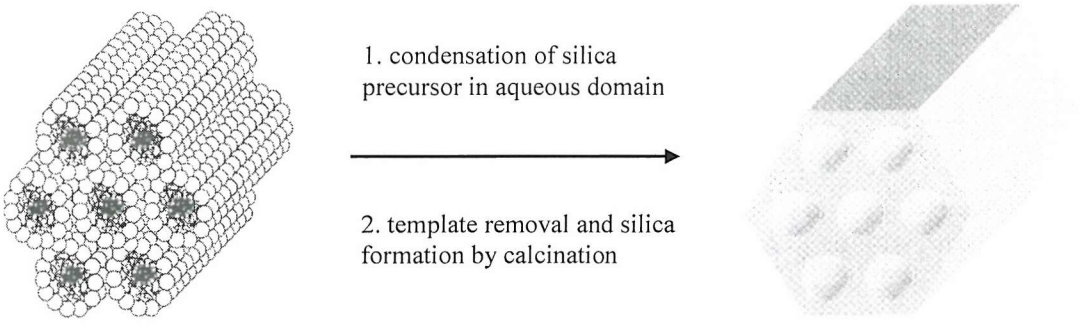

Figure 1.10.[19] Silica condensation is preceded here by the formation of a liquid crystalline phase of H_I morphology.

The versatility of the DLCT route was shown by Templer and co-workers with demonstration of the synthesis of high surface area platinum powder by reduction of hexachloroplatinic acid with the aqueous domains of a H_I liquid crystalline phase.[57] The templated platinum powder was characterised by a specific surface area of ~ 60

m^2 g^{-1} as compared to 35 m^2 g^{-1} characteristic of platinum black materials. The application of mesoporous platinum to fuel cell applications was not investigated.

Attard *et al.* reported an extension of the DLCT route in which hexachloroplatinic acid confined within the aqueous domains of a polyoxyethylene surfactant was electrochemically reduced to platinum metal at the surface of an electrode immersed in the mixture.[58,59] During this process a thin monolithic platinum film was deposited in regions occupied by the aqueous domains of the surfactant with the same morphology as materials produced by the chemical reduction route.[60] This process

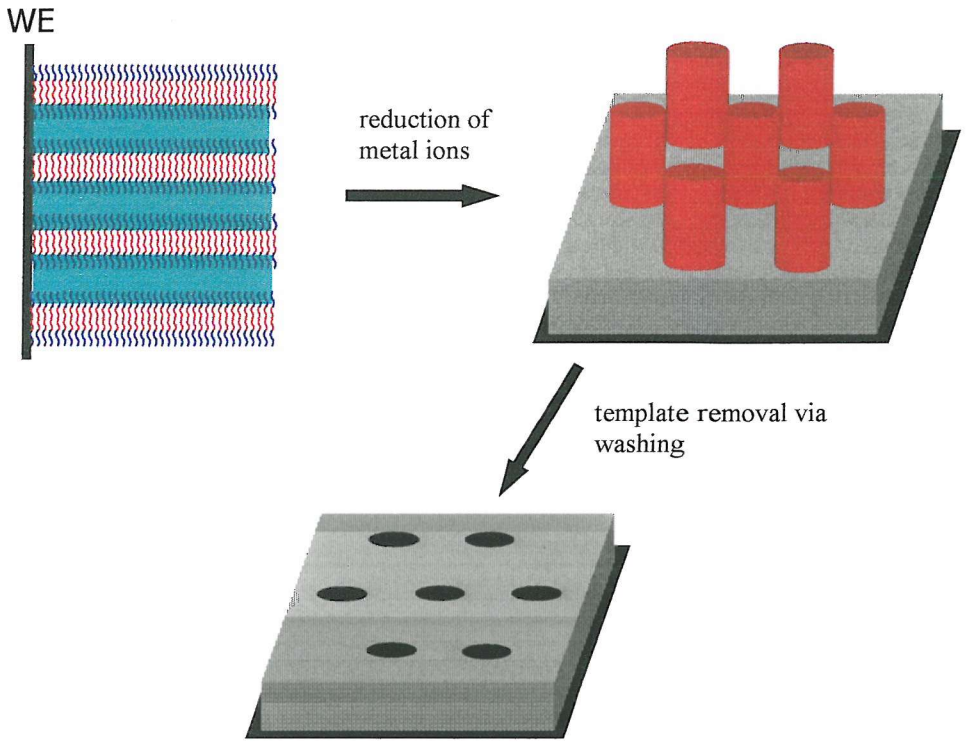

Figure 1.11 illustrates the electrodeposition of metal films (grey) within the aqueous domains of an H_I liquid crystal. Mesoporosity is created on removal of the surfactant template (red).

and subsequent removal of the surfactant template to produce a porous structure are represented schematically in Figure 1.11. These electrodeposited films were shown to possess high surface areas and more importantly, high electrochemically accessible

surface areas as demonstrated by surface activity in sulphuric acid and toward methanol oxidation.[61,62]

Since these reports a number of studies have been conducted concerning the electrodeposition of mesoporous materials using liquid crystalline templates. Bartlett *et al.* deposited mesoporous palladium[63] and cobalt[64] with H_I morphologies from the corresponding phase of a polyoxyethylene surfactant. Nandhakumar *et al.* electrodeposited H_I selenium also using a template mixture based on polyoxyethylene surfactant and selenium dioxide.[65]

Huang and co-workers obtained cuprite (Cu_2O) nanowires by electrodeposition within the aqueous domains of a reverse hexagonal phase liquid crystal.[66] Nanowires tens of micrometers in length were grown, assisted by electric field alignment of the ionic surfactant template between the electrodes. Whitehead *et al.* deposited mesoporous tin from the H_I phase of a polyoxyethylene surfactant.[67] Although the structures obtained in this work appeared to possess some mesoporosity, this porosity was disordered as reflected by the poor cyclability when used as a lithium battery negative electrode material. Elliott and co-workers electropolymerised poly(1,2-diaminobenzene) within the aqueous domains of a polyoxyethylene surfactant template.[68] The thin film electrodes obtained demonstrated a significant degree of ion permselectivity, which was attributed to the operation of a Donnan exclusion mechanism in the pores of a H_I structure, however no direct evidence was presented to support the existence of the ordered H_I morphology.

Martin and co-workers have used a significantly different templating route for the preparation of a variety of meso- and microporous materials.[69] This process consists of depositing a desired material within the voids of a porous membrane and subsequent removal of the template, leaving a direct cast of the template's pore network. The membranes contain cylindrical pores of uniform diameter in the range 5 nm to 1 μm, such that a nanocylinder of the desired material is obtained on removal of the template. Depending on interactions between the pore wall and the deposited material, this cylinder may be either a solid nanofibril or a hollow nanotubule. Both polymeric (usually polycarbonate) filtration membranes and porous alumina membranes prepared by the anodisation of aluminium have been used as templates

however in the case of the former, the pore density is relatively low in comparison with the latter template and lyotropic liquid crystals. This process has been used in conjunction with a number of deposition methods including electrochemical deposition,[70] electroless deposition,[71] chemical polymerisation,[72] sol-gel deposition[73] and chemical vapour deposition[74] have been used to prepare an even greater array of materials including metals, oxides, polymers and porous carbons.

Nesper and co-workers developed a novel templating mechanism using neutral surfactant molecules such as primary amine surfactants together with vanadium alkoxide precursors to fabricate crystalline vanadium oxide nanotubular materials with a wall structure consisting of concentric shells rolled around a hollow centre.[75] Tubes were typically up to 15 μm long with inner and outer diameters in the range 5 to 50 nm and 15 to 150 nm respectively. The amine surfactants template the formation of the 'nanorolls' by intercalating between the crystallising layers of vanadium oxide such that the distances between the layers corresponds to the length of the alkylamine molecule.[76] Later work by the same group used pre-existing vanadium pentoxide gels as a host for the intercalation of a primary amine during the hydrothermal synthesis of vanadium oxide nanorolls.[77]

1.5 Industrial Applications of Nickel Electrodes

1.5.1 Alkaline Water Electrolysis

Cathodic hydrogen evolution is catalysed efficiently by the platinum group metals and to a lesser extent by iron, cobalt and nickel.[78] Of the transition metals, only nickel is stable in concentrated alkaline solution at the hydrogen equilibrium potential.[79] Due to this fact and the relatively low cost of nickel compared to the platinum group metals, Raney nickel coatings are used as efficient electrocatalysts in the cathodic evolution of hydrogen in the alkaline electrolysis of water. While possessing high surface area however, the porosity of Raney nickel is not ideal for this application. During operation, the larger micrometer sized cracks become gas blanketed, effectively limiting exposure of the adjoining nanopores to the electrolyte. This effect limits utilisation of the electrode to around 10 %.[80] Performance is further retarded by the mass transport limitations of product hydrogen in the nanopores due to the absence the of convective mass transport usually provided by the presence of hydrogen gas cavities (bubbles). The non-existence of H_2 bubbles is rationalised considering the Laplace equation (4),[81]

$$P = \frac{2\gamma}{r} \qquad (4)$$

where P is the pressure within a gas cavity in a liquid with units of N m^{-2}, γ is the surface tension of water (7×10^{-2} N m^{-1}) and r is the bubble radius in m. For Raney nickel the gas bubble pressure in a pore of 2 nm diameter would amount to almost 1400 atmospheres, corresponding to a H_2 concentration of approximately 1.25 M using Henry's Law:[82]

$$m_H = k_H \times P_H \qquad (5)$$

where m_H is the concentration of hydrogen, k_H is the Henry's Law constant for hydrogen[83] (8.86×10^{-4} M atm^{-1}) and P_H is the partial pressure of H_2 in the cavity.

As a result, hydrogen remains dissolved in solution in the nanopores with no gas cavity formation. Therefore, those nanopores which are exposed to the electrolyte must be considered to be operating with only diffusive mass transport of hydrogen, that is, without the convection provided by movement of gas cavities.

1.5.2 Electrochemical Oxidation of Organic Species

Raney nickel coatings are also commonly used in alkaline solutions for the electrochemical hydrogenation of organic species.[84] A small body of literature has described the oxidation of organic species on nickel electrodes, the majority of these involving the oxidation of alcohols. Ethanol oxidation has received the most attention, due to its high miscibility with aqueous solutions and relatively well known reaction mechanisms.[85] Ethanol oxidation on nickel electrodes proceeds not by direct electron transfer but by chemical reaction with the catalyst NiOOH as shown in Reactions 4 and 5,

$$2NiOOH + CH_3CH_2OH \rightarrow CH_3CHO + 2Ni(OH)_2 \qquad (4)$$

$$CH_3CHO + 2NiOOH \rightarrow CH_3COOH + 2Ni(OH)_2 \qquad (5)$$

with subsequent electrochemical regeneration of NiOOH at suitable potentials.[86] The reduction of glucose to sorbitol at a nickel surface has also been studied.[87] The application of nickel electrodes in organic electrosynthesis has been most successful however in the process developed by La Roche Limited which involves the oxidation of diacetone-L-sorbose (DAS) to diacetone-2-keto-L-gulonic acid (DAG), one of the steps in the synthesis of vitamin C.[88]

1.5.3 Lithium Batteries

Lithium batteries have found wide application as energy storage devices because of their ability to reversibly store lithium with high energy densities. There reliance on non-aqueous rather than aqueous electrolytes enables operating voltages greater than 3 V to be achieved, so that energy densities are greater than in aqueous batteries.

Lithium batteries function by storage of lithium ions in an electrode material either by intercalation, alloying or the formation of ionic bonds. Figure 1.12 shows the movement of Li^+ ions (pink) through an electrolyte (green) between two electrode materials (yellow) capable of hosting such ions in their interlayer cavities.

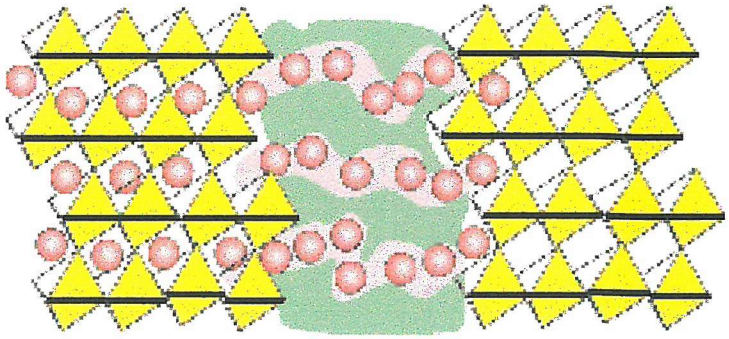

Figure 1.12.[89] Lithium batteries accommodate guest lithium ions between layers or within cavities in the electrode structure as indicated here and in doing so provide a means of store charge.

Positive electrode materials usually consist of lithiated transition metal oxides, while the most popularly researched negative electrode materials are carbon and tin based materials.

Of the transition metal oxides, $LiCo_2$, $LiNiO_2$ and $LiMn_2O_4$ have received the most attention as possible positive electrode materials in lithium ion batteries. $LiNiO_2$ exhibits the highest energy density of these candidates and has an innate advantage over $LiCoO_2$ because of the lower cost of nickel. Despite this, $LiNiO_2$ has not to date been commercially successful, since the desired β-phase is difficult to prepare using popular synthetic routes such as high temperature solid state reaction. Oxygen atmospheres or partial substitution with cobalt (forming $LiNi_{1-y+}Co_yO_2$) are required to stabilise Ni(III) against the more stable Ni(II) at the temperatures of synthesis (~700 °C). $LiNiO_2$ is also susceptible to cationic disordering and as such its formula is often written as $Li_xNi_{2-x}O_2$ (with $0 \leq x \leq 1$) where NiO is formed at the lower extreme of lithiation. Here, as x decreases an increasing amount of Ni^{2+} is resident within the van der Waals gap between the NiO_2 layers. This decreases the capacity of

the electrode for lithium storage and decreases lithium ion mobility since the amount of lithium ions in the structure is reduced. Electrochemical performance is further reduced as a consequence of cationic disorder because the lower diffusion rates in a disordered electrode increase polarisation.

Low temperature synthetic routes in inorganic chemistry[90] are receiving increasing attention in the technical literature because they offer access to metastable compositions and structures as well as to thermodynamically stable low temperature phases that otherwise decompose at higher temperatures. This interest has also been driven by commercial issues since high temperature fabrication processes require high capital cost outlays for fabrication equipment in addition to significant ongoing expense in terms of energy usage.

The structure of $LiNiO_2$ consists of edge sharing NiO_6 octahedra connected to form NiO_2 sheets. On complete delithiation $LiNiO_2$ forms NiO_2. Due to its high open circuit voltage NiO_2 immediately oxidises atmospheric moisture to form the reduced phase NiOOH. Recognising the close structural relationship that couples NiOOH and NiO_2 (β-NiOOH and $LiNiO_2$ are isostructural with the rock-salt α-$NaFeO_2$)[91] has enabled investigators to pursue low temperature routes to $LiNiO_2$. The majority of these efforts have proceeded with attempts to exchange H^+ with Li^+ ions in a NiOOH structure. The interlayer spacing in γ-NiOOH is 7.2 Å while in β-NiOOH and $LiNiO_2$ this spacing is 4.7 Å. As a result, while the only species resident between the layers of β-NiOOH are protons, γ-NiOOH is capable of accommodating a range of species such as H^+, H_2O and alkali metal ions. Consequently, in low temperature ion exchange reactions, the well ordered β-phase of NiOOH is preferred rather than the disordered, impurity containing γ-phase as the starting material.

$LiMO_2$ layered compounds (where M is a transition metal) are widely known to exchange H^+ for Li^+ in acidic media. However until recently, no investigations had achieved the reverse reaction:

$$MOOH + Li^+ \rightarrow LiMO_2 + H^+ \qquad (6)$$

Dahn and co-workers in 1993 were perhaps the first to demonstrate the synthesis of positive electrode materials using an ion exchange process.[92] They successfully lithiated MnOOH using $LiOH.H_2O$ at low temperatures. Amatucci *et al.* ion exchanged the protons in CoOOH to form $LiCoO_2$ using $LiOH.H_2O$ at 100 °C, however the resulting materials contained impurity species whose presence severely retarded lithium storage capacity and reversibility.[93] Only on heating the powders to 250 °C were the impurities removed and electrochemical performance improved.

Using a modification of the ion exchange syntheses discussed above, Murata *et al.* reported the low temperature synthesis of lithium nickelate positive electrodes by chemical oxidation of $Ni(OH)_2$ in an aqueous solution containing an oxidising agent and LiOH at temperatures close to 100 °C.[94] In their 'direct oxidation method' the oxidation of $Ni(OH)_2$ and a subsequent ion exchange reaction took place in the same medium, allowing the authors to obtain almost pure β-phase material. Capacities as high as 310 mAh g^{-1} were reported which was attributed to storage capacity derived from both the Ni^{2+}/Ni^{3+} and Ni^{3+}/Ni^{4+} redox couples. This impressive capacity was attributed to the potential difference between these two couples which was shown to be significantly less than in materials synthesised at high temperature, while the capacity of the Ni^{2+}/Ni^{3+} redox couple was also much greater.

Most of the research efforts in lithium battery electrode materials have focussed on improving the performance of the positive electrode since its mass specific capacity is much less than that of negative electrode materials. Nevertheless, new innovations in negative electrode material structures and compositions have been pursued feverishly in attempts to replace carbonaceous materials currently used with metal based chemistries. Li and Martin[95] demonstrated a nanoporous SnO_2 based negative electrode made by deposition of the electrode material within the pores of a polycarbonate membrane. Very high capacities of 700 mAh g^{-1} were recorded and the electrodes were shown to have excellent stability to rapid cycling. Studying the mechanism of lithium ion storage in metal based negative electrodes, Courtney and Dahn[96] were the first authors to present evidence for reversible lithium storage by the conversion of a metal oxide to an electrode composed of the metal in a matrix of lithia, upon insertion of lithium ions. They suggested that the high lithium storage

capacities observed for tin-based anodes (these compounds react with 4-7 atoms of lithium for each atom of tin) could not be due to normal intercalation processes in which 1 or 2 atoms of lithium per metal atom are typically stored reversibly. Tarascon and co-workers observed a similar mechanism of reversible lithium storage at low voltages versus lithium, albeit involving transition metal oxides rather than tin.[97,98] This chemistry had been reported previously by Ikeda and Narukawa[99] as an irreversible mechanism of discharge in a primary Li-CuO cell.

1.5.4 Supercapacitors

1.5.4.1 The Market and Need for Supercapacitors

The requirement for electrical energy storage is present in a myriad of applications such as telecommunication devices, implantable medical devices and electric and hybrid vehicles. Storage of electrical energy may be achieved using electric fields (capacitors), by means of chemical reactions (batteries) or as hydrogen generated by the electrolysis of water which may be subsequently converted to electricity in a fuel cell. By virtue of the different physical and chemical processes utilized, each of these

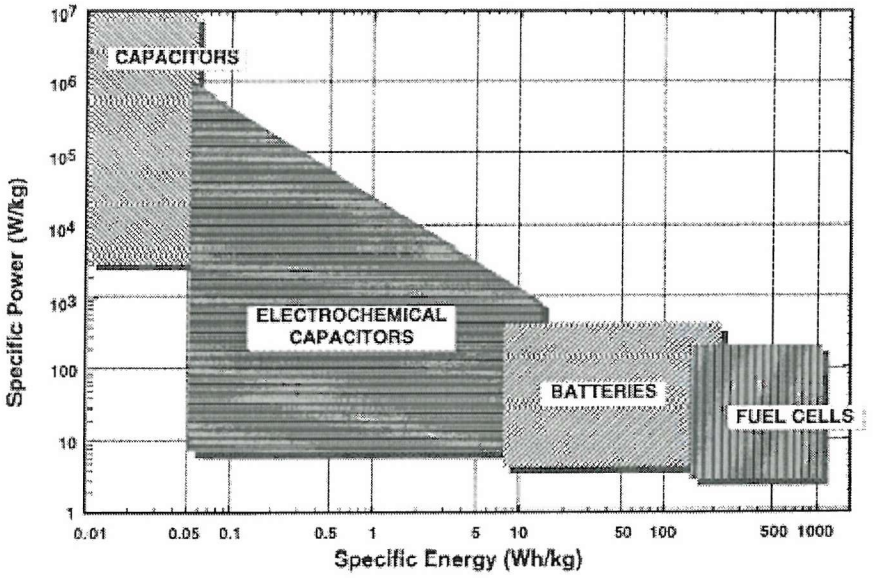

Figure 1.13[100] compares energy and power densities of various electrochemical charge storage devices in a Ragone Plot.

methods are characterised by different energy and power densities as illustrated in the Ragone plot of Figure 13.[100] The choice of which method to use, is dictated by the application. This choice is seldom easy though, since the power and energy requirements of a particular device can vary considerably during operation. The most common electrical energy storage device is the battery. Batteries are capable of storing large amounts of energy in a relatively small mass and volume while retaining the ability to satisfy moderate power demands. In recent times however, power requirements in many applications traditionally reliant on batteries have increased markedly, exceeding the capability of battery systems. The global system for mobile communications (GSM) format for example, requires current pulses of about 0.5 ms duration every 5 ms.[101] The pulse power is about 10 times greater than the average power requirement. Batteries are typically the storage method of choice for GSM applications, however in order to satisfy this high power demand, battery systems (which are considered to have low power and high energy density) must be over dimensioned such that the available energy far exceeds device requirements. In addition, exposure of batteries to such variable loads reduces their lifetimes dramatically. The application of fuel cells to emerging electric vehicle technologies has encountered similar problems.

Fuel cells, while being able to efficiently accommodate the energy needs of electric vehicles, have insufficient power density to satisfy the power requirements of an accelerating vehicle. A solution to this problem is to separate the energy and power demands of a particular application such that peak power is provided by a pulse power device (capacitor) that is charged periodically by a primary energy storage unit (fuel cell or battery). In this way, the total mass of the energy storage unit may be decreased by optimising its size for a particular application, and since the load placed on the primary energy storage unit is less variable, its lifetime is extended significantly.

Traditional (dielectric) capacitors with planar metal plate electrodes have capacitances in the range of pico- to nanofarads per square centimetre and are obviously incapable of storing significant amounts of energy in their given mass and volume. Hence, these devices are unable to satisfy demand from applications

requiring significant amounts of energy in pulse form. For this reason, the development of high energy density electrochemical capacitors (also called supercapacitors and ultracapacitors) has been undertaken.

1.5.4.2 Supercapacitors and Batteries Compared

Capacitors store energy by charge separation. Here, capacitance usually arises from the coverage of a solid electrode surface by solution-borne electroactive adatoms or the charging of the double layer that is formed at the interface of a solid electrode surface and a liquid electrolyte. These processes, the latter illustrated in Figure 1.14[102], are two-dimensional in nature in that atoms in the electrode bulk do not

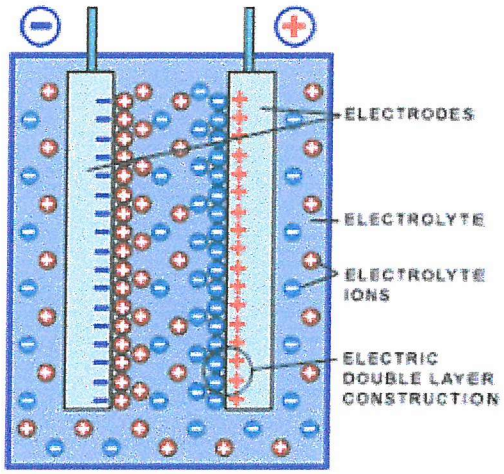

Figure1.14.[102] Double layer capacitors store charge by accumulation of electrolyte ions within the electrical double layer established at the surface of polarised electrodes.

contribute to the capacitance. In addition, no chemical charge transfer reactions are involved. The electrode potentials of these 'ideally capacitive' systems are a continuous function of the degree of charge of the electrode which is in turn controlled by the extent of surface coverage of the electrode.[103] Consequently, charging and discharging currents are constant with linear variation of the potential. The charging behaviour of an ideal system is illustrated in Figure 1.15. From the plot it can be seen that the energy ΔG, stored in a capacitor is calculated using equation 6,

$$\Delta G = \tfrac{1}{2} QV \qquad (6)$$

where V is the potential at which the charge Q is discharged from the device. The factor ½ in this equation arises due to the fact that the average potential at which an ideal capacitor charges and discharges is only half that of the maximum operating voltage. Charge storage using two-dimensional surface processes is typically highly reversible and since bulk diffusion is not involved time constants for charging and discharging are very small resulting in high power densities, particularly for devices with high surface area electrodes. The corollary of charge storage by charge

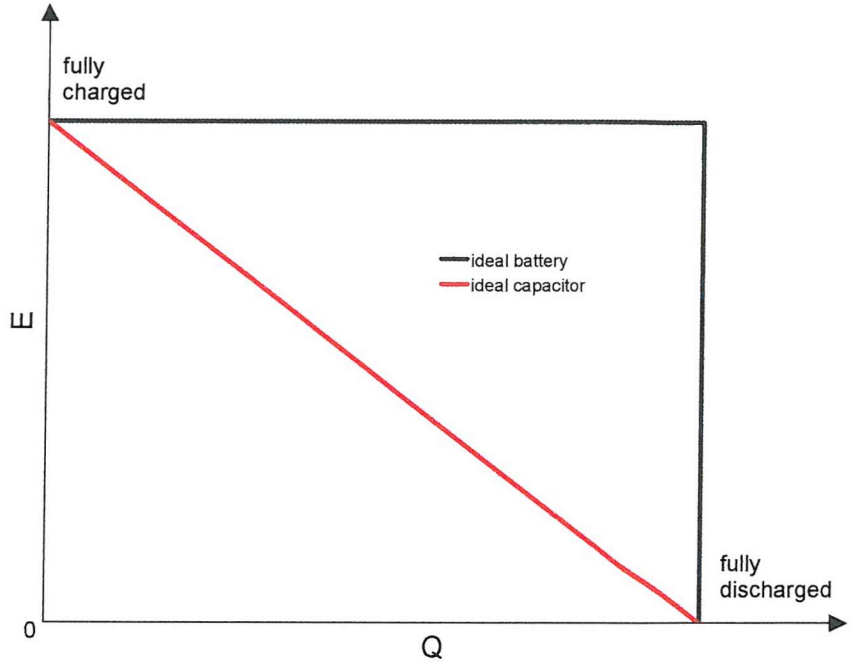

Figure 1.15 compares the voltage profile of an 'ideal' battery and supercapacitor as a function of state of charge.

separation and the lack of electrode bulk activity is that capacitor cycling is highly reversible, such that device lifetimes are typically in the range of 10^4-10^6 cycles.

By contrast, charge storage in batteries relies on charge transfer reactions occurring both in the electrode bulk and on the electrode surface. As a consequence of this reliance on redox processes, the state of charge of a battery is controlled by thermodynamic behaviour in which charge is stored at a defined redox potential at or near the maximum operating voltage of the device, as illustrated in Figure 1.15. Thus, the energy stored in a battery may be calculated using equation 7:

$$\Delta G = QV \qquad (7)$$

This reliance on bulk redox processes ensures that batteries possess a significantly higher energy density than supercapacitors which utilize only their surface. However, the three-dimensional nature of the battery energy storage mechanism also means that the rates of these processes are limited by bulk diffusion of electroactive species within the electrode and hence power densities are low. In addition, there is an inherent irreversibility associated with redox reactions, especially those occurring in the electrode bulk. As such, the cycle life of batteries is significantly less than that of capacitor devices.

1.5.4.3 The Various Types of Supercapacitors

Electrochemical capacitors or supercapacitors may be divided into two broad groups based on their means of charge storage. Double layer capacitors store energy by charge separation in the double layer, and as the first of the two broad groups, most closely resemble the ideal capacitors described in the section above. The second group of supercapacitors, also called pseudocapacitors, also utilize charge separation in the double layer as a means of storing energy, however a significant amount of their capacity is derived from faradaic reactions occurring at or near the electrode surface. Three types of charge transfer reactions have been utilized in the development of supercapacitors. These include surface adsorption of ions from the electrolyte, redox reactions involving ions from the electrolyte and the doping and undoping of conductive polymer materials.

1.5.4.3.1 Double Layer Capacitors

Double layers capacitors based on carbon are the most developed of all supercapacitors. Carbon is used for a number of reasons, principally, its low cost, high surface area, availability and established production technologies. Capacitance in double layer devices is a function of the surface area and pore size distribution and specific capacitance is calculated using the formula: $C=C_aA$, where specific capacitance is expressed in F g^{-1}, the area specific capacitance, C_a is expressed in F cm^{-2} and electrode surface area is expressed in cm^2 g^{-1}. The area specific capacitance of carbon is typically in the range 15-30 μF cm^{-2} and as such for a surface area of 1000 m^2 g^{-1}, we could expect a specific capacitance of 150-300 F g^{-1}. The reality is that although carbons with surface areas up to 2500 m^2 g^{-1} are obtainable, specific capacitances of carbon electrodes rarely reach values higher than 75-150 F g^{-1} for aqueous electrolytes and 40-100 F g^{-1} for organic electrolytes.[104] Even though double layer capacitors using organic electrolytes give lower capacitances than those employing aqueous electrolytes, the operating potential range of organic electrolytes may be up to 3.5 V as opposed to the 1.2 V limit imposed on aqueous electrolytes by the electrochemical instability of water. This offers supercapacitors using organic electrolytes a significant advantage in terms of energy density over those using aqueous electrolytes since the energy stored in a capacitor is given by the expression $\Delta G=1/2CV^2$. The increase in energy density however is accompanied by a decrease in power density since the electrolyte conductivity and therefore the maximum rate of discharge is significantly lower in organic systems. The reason for the lower than expected specific capacitance values observed in carbon based systems is that most of the activated carbons available for use in supercapacitors were developed for filtration applications. In these poorly structured materials, a large fraction of the nanopore volume (up to 90 %) results from pores that are too small to permit the electrolyte ions to freely diffuse in and out of the structure. Hence, only a fraction of the surface is capable of generating deliverable capacity and a significant fraction of the ionic electrode resistance is due to pore resistance. This effect is more pronounced in devices using organic electrolytes since the size of the ions is much greater than in aqueous electrolytes. Figure 1.16[105] shows the effect of variation in pore diameter on

surface area and electrode capacity. The critical pore diameter at which capacity begins to fall is dictated by the choice of ions in the electrolyte and the pore size distribution. By appropriate matching of these two parameters capacity may be optimized. Poor ionic resistance has a significant effect on the high frequency response of carbon based supercapacitors. Carbonaceous materials with small pores (< 1 nm) exhibit a significant decrease in capacitance at discharge rates greater than 100 mA cm^{-2}, especially when organic electrolytes are used. In contrast, materials with larger pore sizes can be discharged at rates greater than 500 mA cm^{-2} without significant decay in capacity.

At present, the majority of research efforts are focusing on increasing the relatively poor energy density of carbon based supercapacitors. The highest energy densities are

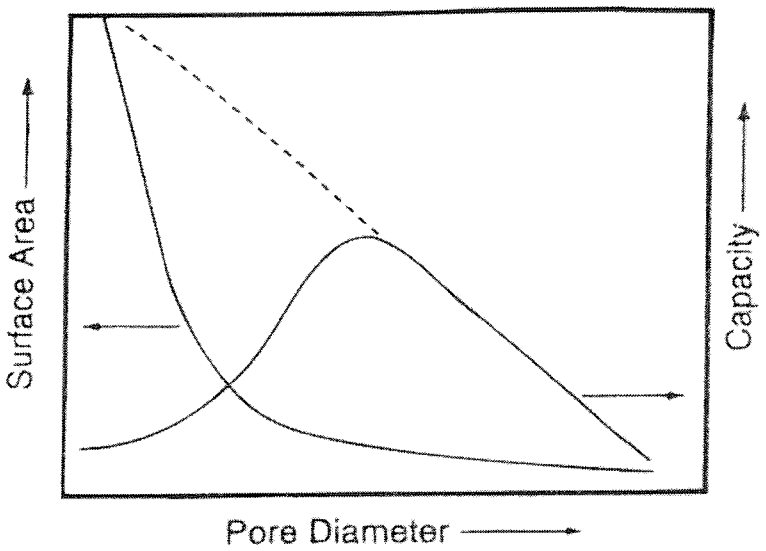

Figure 1.16[105] shows that as pore diameter in supercapacitor electrode materials decreases a greater proportion of the electrode surface area becomes inaccessible to the electrolyte.

in the vicinity of 5-6 W h kg^{-1} however there is a strong correlation between energy density and the RC time constant with the higher energy density devices having large time constants of at least 2 s. This translates to low power densities of around 500 W kg^{-1}. Devices with RC time constants as low as 0.1 s are available, translating to power densities above 1.5 kW kg^{-1} however these typically have energy densities

around 1 W h kg^{-1}. The reason for the lower energy density in high power supercapacitors is that in order to achieve high power, electrodes are made significantly thinner than those of higher energy devices causing the ratio of active material mass to the inactive component (separator, current collector and packaging) mass in a device to decrease.

Recently, a new type of nanoporous carbon was proposed for use in supercapacitor devices by an industrial developer.[106] These carbons are made via the temperature chlorination of carbide powders such as SiC, TiC and Mo_2C.[107] The resultant powders possess high surface areas with a narrow pore size distribution the mean size of which is dependent on the base carbide used. The developers claim pore size may be controllably varied between 0.8 and 3 nm such that all of the pore structure is accessible to an electrolyte and pore size may be tailored to the size of the ions. Specific capacitances of 320 F g^{-1} and 160 F g^{-1} for the active material utilizing aqueous and organic electrolytes respectively have been claimed. When incorporated into a practical device these materials yielded energy and power density values of 11 Wh kg^{-1} and 10 kW kg^{-1} respectively. Comparison with energy and power specifications of other commercial and developing supercapacitors in Figure 1.17 shows that these values if truly achievable, represent a substantial step forward in supercapacitor development.

1.5.4.3.2 Pseudocapacitors

Despite their relatively high energy density in comparison with dielectric devices, double layer capacitors at present are not capable of producing the performance characteristics to satisfy the requirements of future power intensive applications. This has led researchers to investigate charge storage systems more closely related to batteries. In many cases, these systems utilize double layer charge storage, however derive most of their capacity from redox reactions (hence the term 'pseudocapacitance') occurring at the surface or in the bulk of the electrode. Despite their reliance on thermodynamically defined potential dependent reactions, pseudocapacitors generally display uniform charge/discharge current behaviour similar to that of ideal capacitors. This is usually due to the presence of a sequence of

World-wide research and development activities on ultracapacitors

Country	Company or lab	Funding	Description of the technology	Device characteristics	Energy density (W h/kg)	Power density (W/kg)	Status/availability
Carbon particulate composites							
Japan	Panasonic	Private	Spiral wound, particulate with binder, organic electrolyte	3 V, 800–2000 F	3–4	200–400	Commercial
France/US	Saft/Alcatel	US DOE/private	Spiral wound, particulate with binder, organic electrolyte	3 V, 130 F	3	500	Packaged prototypes
Australia	Cap xx	Private	Spiral wound and monoblock, particulate with binder, organic electrolyte	3 V, 120 F	6	300	Packaged prototypes
Japan	NEC	Private	Monoblock, multi-cell, particulate with binder, aqueous electrolyte	5–11 V, 1–2 F	0.5	5–10	Commercial
Russia (Moscow)	ELIT	Russian Government/private	Bipolar, multi-cell, carbon with sulfuric acid	450 V, 0.5 F	1.0	900–1000 > 100,000 cycles	Commercial
Carbon fiber composites							
United States	Maxwell	US DOE/private	Monoblock, carbon cloth on aluminium foil, organic electrolyte	3 V, 1000–2700 F	3–5	400–600	Commercial
Sweden/Ukraine	Superfarad	Private	Monoblock, multi-cell, carbon cloth on aluminum foil, organic electrolyte	40 V, 250 F	5	200–300	Packaged prototypes
Aerogel carbons							
United States	PowerStor	US DOE/private	Spiral wound, aerogel carbon with binder, organic electrolyte	3 V, 7.5 F	0.4	250	Commercial
Conducting polymer films							
United States	Los Alamos National Lab	US DOE	Single-cell, conducting polymer (PFPT) on carbon paper, organic electrolyte	2.8 V, 0.8 F	1.2	2000	Laboratory prototype
Mixed metal oxides							
United States	Pinnacle Research Institute	US DOE/private	Bipolar, multi-cell, ruthenium oxide, on titanium foil, sulfuric acid	15 V, 125 F 100 V, 1 F	0.5–0.6	200	Packaged prototypes
United States	US Army, Fort Monmouth	US DOD	Hydrous ruthenium oxide, bipolar, multi-cell, sulfuric acid	5 V, 1F	1.5	4000	Unpacked lab prototype
Hybrid							
United States	Evans	Private	Double-layer/electrolytic, single cell, monoblock, ruthenium oxide/ tantalum powder dielectric, sulfuric acid	28 V, 0.02 F	0.1	30,000	Packaged prototype
Russia (Moscow)	ESMA	Russian Government/private	Double-layer/Faradaic, monoblock, multi-cell modules, carbon/nickel oxide/KOH	1.7 V cells/17 V modules/20 A h (50,000 F)	8–10	80–100 (95% discharge effic.) cycle life 10–20 K cycles	Commercial

Figure 1.17[104] compares performance characteristics of supercapacitors using various chemistries and at various stages of research and commercial development.

overlapping redox couples or adsorption onto the electrode surface of ions from the electrolyte.

The most well known pseudocapacitive systems are those based on metal oxides. RuO_2 is by far the most thoroughly characterised of these and to date has exhibited the highest performances. Crystalline RuO_2 has a high capacitance of approximately 150 to 260 μF cm^2 due to the reversible oxidation and reduction of the surface via a mechanism involving proton exchange with the electrolyte[108]:

$$RuO_x(OH)_y + \delta H^+ + \delta e^- \leftrightarrow RuO_{x-\delta}(OH)_{y+\delta} \qquad (7)$$

This value is approximately 10 times greater than that of carbon and has enabled investigators to fabricate single electrodes with a specific capacitance of 380 F g^{-1}.[109] Although charge/discharge currents are constant with voltage, the cyclic voltammetry is not purely a consequence of double layer charging but is also of a sequence of redox reactions involving the Ru(III) to Ru(VI) oxidation states within a potential window of approximately 1.4 V as indicated in Reaction 7 above.[110] Other investigators[111,112] have subsequently discovered that the amorphous phase of hydrous ruthenium oxide $RuO_2.xH_2O$, is capable of delivering even higher capacitances than the anhydrous crystalline form due to the involvement of proton insertion into the electrode bulk as well as the surface. Single electrode capacitances of 720 F g^{-1} and 760 F g^{-1} have been calculated using cyclic voltammetry, however due to the reliance on bulk derived capacity these impressive performance figures are only achievable at the low scan rate of 2 mV s^{-1}. Trasatti and co-workers[113] discussed the variation in charge storage capacity in hydrous ruthenium oxide as a function of scan rate and were able to separate charge contributions of the 'outer' surface from those of the 'inner' surface where charge/discharge rates and charge capacity were modelled assuming semi-infinite linear diffusion.

At present, the development of ruthenium oxide capacitors has proceeded only to the product development stage with packaged prototypes despite impressive performance. This is a direct consequence of the extremely high raw materials cost of

ruthenium which will probably ensure that commercial applications are restricted to military and aerospace markets.

Several attempts have been made to reduce the cost of ruthenium based supercapacitors. The simplest of these have imitated the development of Pt containing electrodes used in proton exchange membrane fuel cells by depositing RuO_2 onto inexpensive conducting supports. Miller *et al.* reported the deposition of ruthenium nanoparticles onto carbon aerogel supports.[114] The oxidised nanoparticles increased the mass specific capacity of the carbon single electrodes from 95 F g^{-1} to 206 F g^{-1}. Using a similar methodology Takasu *et al.* used a dip-coating process to fabricate ultrafine ruthenium oxide particles supported on high surface area vanadium oxide electrodes.[115] The authors achieved charge densities of 162 mC cm^{-2} for 1 μm thick electrodes. In other work, ruthenium was diluted by incorporation into an ABO_3 perovskite structure with Ru in the B position.[116] Capacities of 20 to 30 F g^{-1} were reported for single electrodes.

Other work on metal oxide pseudocapacitors has focussed on using less expensive transition metals. The majority of these works used nickel oxide as the electrode material formed by thermal treatment of a sol-gel precipitate or electrodeposited film. Thermal treatment is carried out to destroy the hydrous structure of the $Ni(OH)_2$, forming NiO and in doing so restricting any charge transfer reactions in the KOH electrolyte to the surface of the electrode. This exclusion of the bulk H^+ intercalation process (8),

$$Ni(OH)_2 + (OH)^- \leftrightarrow NiOOH + H_2O + e^- \qquad (8)$$

that endows Ni-MH battery systems with their high energy densities reduces greatly the capacity of the electrode in favour of obtaining more 'ideal' capacitive cycling behaviour. However, because all of the charge is derived from surface reactions, power density is increased. Respectable performance figures have been attained using this chemistry. Liu *et al.* reported a sol-gel derived NiO capacitor with a specific capacitance ranging from 200 F g^{-1} to 256 F g^{-1} for a single electrode.[117] Using an electrochemical route Srinivasan and Weidner[118, 119] fabricated a NiO based

supercapacitor with a single electrode capacitance of 236 F g^{-1}. To a lesser extent cobalt oxide has been used as a pseudocapacitive material. Lin *et al.*[120] used a sol-gel process to synthesise a $Co(OH)_2$ xerogel single electrode of high surface area capable of a specific capacitance of 291 F g^{-1}. Despite the fact that their preparation route preserved the hydrous electrode structure in the device, they claimed that all of the observed charge was derived from surface processes. Molybdenum nitride was also investigated as a relatively low cost alternative material to RuO_2.[121] Success was limited however, with authors demonstrating a low discharge charge density of 6 mC cm^{-2} and an operating voltage limited to 0.7 V by anodic decomposition of the Mo_xN film.

Electrochemical capacitors using carbon double layer materials in one electrode and an oxide pseudocapacitive material in the other have been proposed and developed by Beliakov *et al.* of the Russian company ESMA.[122] In principle, if one of the electrodes of a supercapacitor were not polarisable, or only to a small extent while the potential of the other electrode was variable with the degree of charge, then the capacitance of the device would be doubled. Indeed, this has led to the ESMA hybrid capacitor devices composed of a high surface area carbon negative electrode with a NiOOH positive electrode displaying the highest observed energy density in any supercapacitor of 8 – 10 Wh kg^{-1}. The magnitude of this value which is closer in order to the energy densities of Ni-MH batteries than other supercapacitors, can be appreciated in knowing that charge storage in the ESMA supercapacitor utilises both surface and bulk redox activity. Consequently, power density is lower than in a pure double layer electrode device since at high discharge current densities ionic resistance and the redox reaction time constant become significant. As such, the performance of this device more closely resembles that of a high power battery. Information concerning the extended cycle life of this device required in supercapacitor applications is scarce but it is expected that this will present a significant technical hurdle in the development of this device.

Park *et al.*[123] have attempted to retain some of the high capacity associated with hybrid capacitors while enhancing the power density. Their combination of a pure double layer carbon negative electrode with a composite NiOOH/activated carbon

positive electrode displayed a single electrode capacity of 530 F g^{-1}, however galvanostatic cycling of the assembled device was only carried out at 1 mA cm^{-2}, making a true description of the power capabilities difficult.

Conducting polymers have been investigated as electrochemical capacitor materials because of their high capacities as compared with carbon based systems and their low cost in comparison with ruthenium oxides.[124,125] Electronic conductivity is derived from their π-conjugated structure and polymers may be positively or negatively charged by ion insertion into the electrode bulk. Polyaniline[126] and polypyrrole may only be p-doped (positively charged) however polythiophene and its derivatives may be both p- and n-doped. It is the latter that has received the most attention in the literature and capacitances of up to 450 F g^{-1} have been reported.[127] The performance characteristics of polymer supercapacitors continues to increase, however there are still many problems associated with their development, particularly those related to limited cycle life and high rates of self-discharge.

1.6 The Electrodeposition of Nickel

Nickel electrodeposited from acetate baths is characteristically harder and contains lower internal stresses than deposits from the more commonly used sulphate and sulphamate deposition baths. This is because in general, nickel deposits obtained from acetate solutions contain significantly less hydrogen than those obtained using chloride, sulphate or sulphamate based solutions. Hydrogen incorporation may be effectively considered a defect in the metal lattice since it significantly undermines the mechanical properties of a deposit. Gamburg *et al.*[128] studied the incorporation of hydrogen into nickel during electrodeposition from acetate solutions and concluded that hydrogen is present in the nickel predominantly as a solid solution. The extent of hydrogen incorporation in nickel deposited from acetate solutions is lower than in previously mentioned solutions such as those containing chloride because the basicity of the acetate ion increases the pH of acetate solutions relative to the other anions which are weaker conjugate bases. As a consequence, hydrogen evolution is shifted to lower potentials in acetate solutions, allowing the cathodic deposition of nickel to occur without appreciable superposition with the hydrogen evolution reaction (HER). The cathodic electrodeposition of nickel proceeds via a number of intermediate steps, as indicated below:

$$Ni^{2+} + H_2O \leftrightarrow NiOH^+ + H^+ \qquad (9)$$

$$NiOH^+ + e^- \rightarrow NiOH_{ads} \qquad (10)$$

$$NiOH_{ads} + H^+ + e^- \leftrightarrow Ni + H_2O \qquad (11)$$

In this process, Reaction 10, that is, the reduction of $NiOH^+$ to the adsorbed intermediate $NiOH_{ads}$ has been postulated as the rate determining step.[129,130] The rate of nickel deposition is thus controlled by the electrode kinetics of Reaction 10 and the concentration of the reactant species $NiOH^+$ which is indirectly influenced by the concentration of H^+. Control of pH is therefore critical in controlling the rate of electrodeposition of nickel, not only because of the importance of H^+ concentration in Reaction 9, but as a consequence of the superposition of nickel electrodeposition with

the HER. In addition to the production of hydrogen, the HER generates hydroxyl ions via

$$H_2O + e^- \rightarrow \frac{1}{2}H_2 + OH^- \qquad (12)$$

increasing solution pH, especially in areas close to the electrode surface. This local pH rise has detrimental effects on the deposition of nickel since $Ni(OH)_2$ precipitates

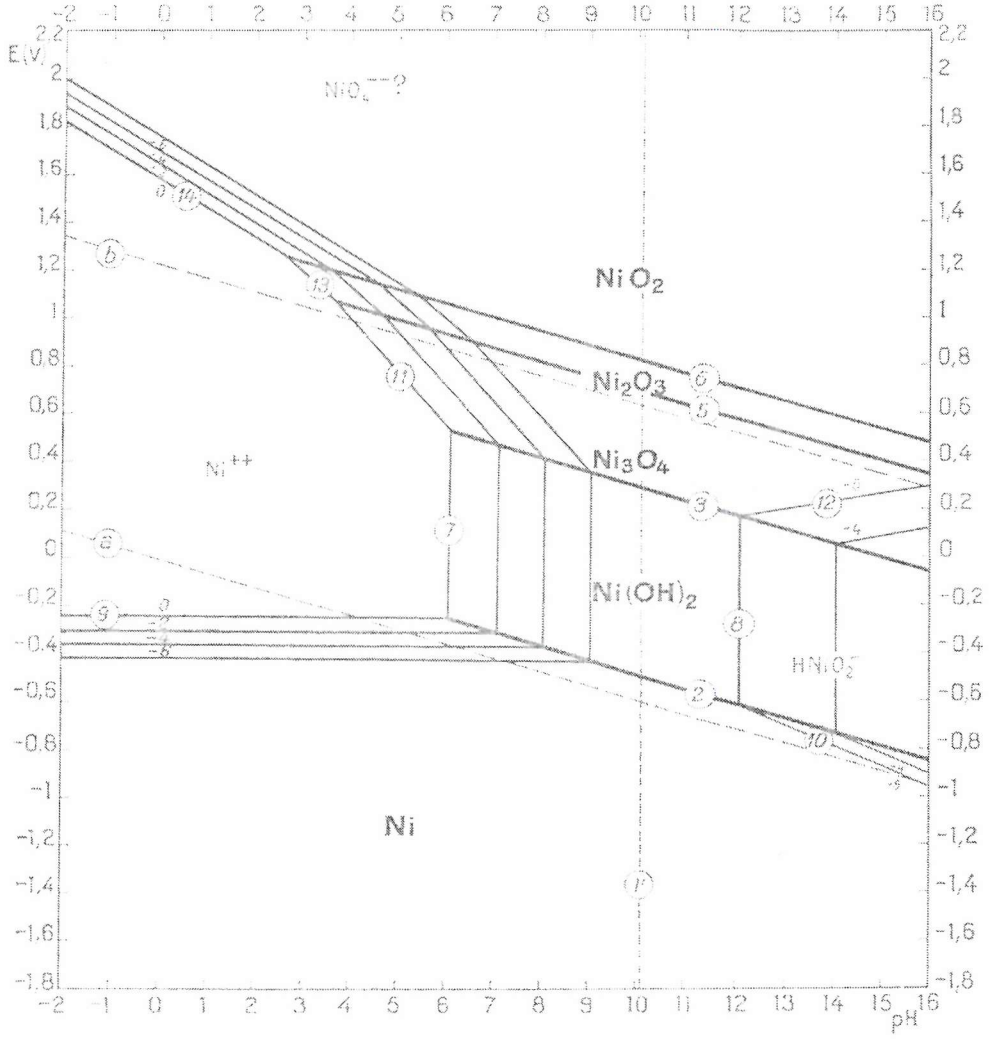

Figure 1.18.[132] The Pourbaix diagram of nickel shows the stability windows of the various redox states and species as a function of potential and pH.

at pH ≈ 6.6[131] as indicated in the Pourbaix diagram of electrochemical equilibria of Figure 1.18.[132] The precipitated $Ni(OH)_2$ which forms locally on the electrode surface reduces the rate of further deposition by passivating the electrode against nickel reduction and is occluded into the growing deposit, reducing its mechanical properties.[133]

The sensitivity of nickel electrodeposition to pH has led to the addition of buffering reagents, typically boric acid to most commonly used deposition solutions. Tsuru *et al.*[134] showed that the addition of boric acid to nickel plating solutions enables suppression of hydrogen evolution during electrodeposition, thus minimising hydrogen incorporation, passivation by $Ni(OH)_2$ and variation in the deposition rate. The mechanism of this suppression is not simple however.

Boric acid cannot buffer the solution by a simple proton dissociation mechanism because the practical pH range of a buffer is $pK_a \pm 1$, which in the case of boric acid is 9.2 ± 1. This is clearly too high a value given the fact that the bulk pH of nickel plating baths is between 4.0 and 6.5. Tilak *et al.*[135] addressed this inconsistency by suggesting that boric acid buffers nickel plating solutions through a weakly bound nickel borate complex which is thought to be $Ni[B(OH)_4]^+$. Indeed, the ability of boric acid to suppress hydrogen evolution is observed only in the presence of nickel ions, indicating the involvement of some kind of mutual interaction between boric acid and nickel ions or nickel-containing intermediates formed during the deposition process.

1.7 Nanoparticulate versus Nanoarchitectured Electrodes

High power capability in electrochemical devices such as those described above requires large electrode surface areas providing high current densities as discussed in Section 1.1. The benefits of large surface areas are negated however if those species in solution facilitating the reaction are not able to move rapidly to the reaction sites within a high surface area electrode. For example, Springer *et al.* found that PEM fuel cell performance incurred substantial losses as a result of poor diffusive mass transport of O_2 through the high surface area air cathode.[136] They found that the effective tortuous path length for gas diffusion was approximately 2.6 times the cathode thickness. Therefore, in addition to possessing a high roughness factor, high power porous electrodes must also have a structure capable of facilitating rapid diffusion. Another requirement for both high power and energy density is low electronic and ionic resistance in the electrode structure itself. Electronic electrode resistance is manifest as a voltage drop during operation, and in high power devices such as supercapacitors, this limits the maximum attainable power output. Ionic electrode resistance limitations are equally important for high power operation in devices such as lithium-ion batteries which function by insertion processes. Ions must diffuse through the electrode structure to undergo reaction and as such resistance to this diffusion results in power and energy losses.

Porous electrodes composed of nanoparticles attempt to address these requirements. Such materials possess high surface areas by virtue of their finely divided nature as illustrated in Figure 1.19. Since the particles are of nanometre dimensions, the distance ions must diffuse through the bulk to the interface is extremely small, as depicted schematically in Figure 1.20, and hence the time constant for bulk diffusion is low and reactions may be carried out rapidly.

The structure of nanoparticulate electrodes has negative attributes however. The aggregate structure contains a high density of grain boundaries and consequently, ionic and electronic electrode resistances are high. Also, because of the random nature of nanoparticle packing in the electrode, the pore structure is not uniform and consists of non-linear channels of varying diameter with necking at particle-particle

boundaries. Thus, species moving within the electrode encounter significant tortuosity. As a result of these negative attributes, power losses in nanoparticulate

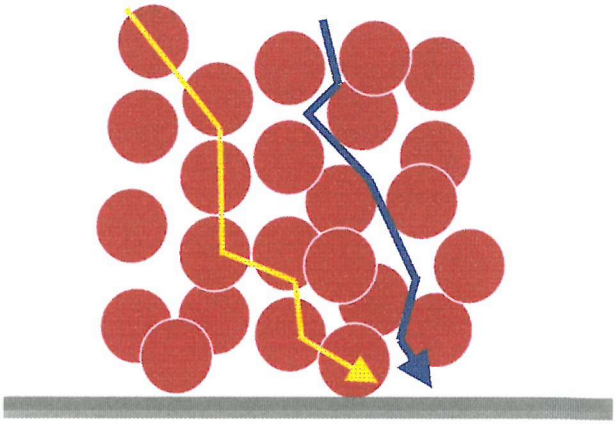

Figure 1.19. Intercalated ions and electrons (yellow) and solution bound species (blue) must traverse a considerably tortuous path in order to move through a nanoparticulate electrode.

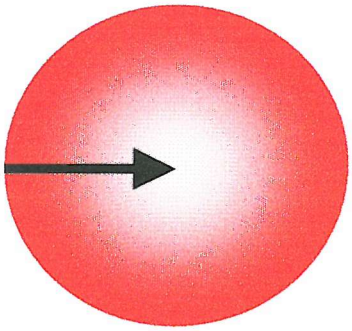

Figure 1.20. For complete utilisation of an active material an ion may have to diffuse a distance equal to the particle radius.

electrodes tend to be considerable and their high surface areas are only fully utilised when processes are conducted at low rates.

Templated materials as discussed in Section 1.4 also possess high surface areas however their pore structures offer a number of advantages over nanoparticulate electrodes in high power applications as illustrated in Figure 1.21. The ordered pore

system conveyed by the self-assembly of the template enables faster diffusion of species through the pore network so that the inherent capability of high current density which comes with high surface area is realised by high rates of mass transfer. This non-tortuous pore network works in concert with the monolithic electrode structure, in which there is an absence of the grain boundaries that cause power losses

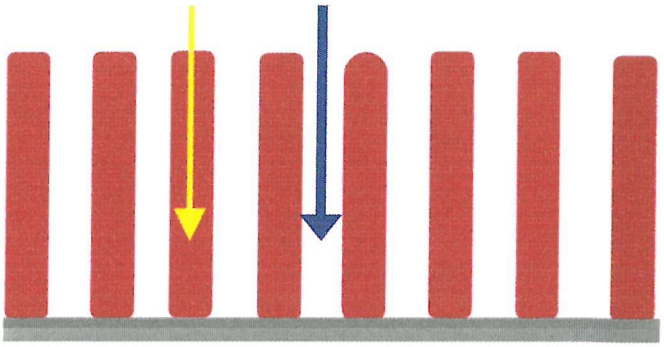

Figure 1.21. Ionic and electronic movement within templated electrodes encounters relatively low impedance due to the continuity and uniformity of the structure.

in nanoparticulate systems due to increased ionic and electronic resistance. Templated electrodes may also offer increased resistance to decrepitation associated with stresses induced by electrode volume expansion and contraction in comparison to nanoparticulate systems because of their more uniform structure.

1.8 References

[1] N. L. Wu, L. F. Wu, Y. C. Yang and S. J. Huang, J. Mater. Res., 1996, 11, 813.

[2] H. Rensmo, K. Keis, H. Linstrom, S. Sodergren, A. Solbrand, A. Hagfeldt, S. E. Lindquist, L. N. Wang and M. Muhammed, J. Phys. Chem. B, 1997, 101, 2598.

[3] N. N. Greenwood and A. Earnshaw, Chemistry of the Elements, First Edition, Pergamon Press, Oxford, 1985.

[4] C. J. Brinker and G. W. Scherer, Sol-Gel Science, Academic Press, New York 1990.

[5] T. J. Barton, L. M. Bull, W. G. Klemperer, D. A. Loy, B. McEnaney, M. Misono, P. A. Monson, G. Pez, G. W. Scherer, J. C. Vartuli and O. M. Yaghi, Chem. Mater., 1999, 11, 2633.

[6] M. K. Nazeeruddin, A. Kay, I. Rodicio, R. Humphry-Baker, E. Muller, P. Liska, N. Vlachopolous and M. Gratzel, J. Amer. Chem. Soc., 1993, 115, 6382.

[7] D. R. Rolison and B. Dunn, J. Mater. Chem., 2001, 11, 963.

[8] K. E. Swider, C. I. Merzbacher, P. L. Hagans and D. R. Rolison, Chem. Mater., 1997, 9, 1248.

[9] R. K. Iler, The Chemistry of Silica, Wiley, New York, 1979, 578-599.

[10] D. B. Le, S. Passerini, J. Guo, J. Ressler, B. B. Owens and W. H. Smyrl, J. Electrochem. Soc., 1996, 143, 2099.

[11] P. Fouilloux, App. Catalysis, 1983, 8, 12.

[12] H. H. Ewe, E. W. Justi, A. W. Kalberlah and A. F. Schmitt, Energy Conversion, 1972, 12, 1.

[13] M. Bauer, H. H. Ewe and E. W. Justi, Energy Conversion, 1972, 12, 149.

[14] J. L. Atwood, J. E. D. Davies, D. D. MacNicol and F. Vogtle, Comprehensive Supramolecular Chemistry, Pergamon Press, Oxford, 1996, 7, 226.

[15] M. E. Davies and R. F. Lobo, Chem. Mater., 1992, 4, 756.

[16] P. B. Moore and J. Shen, Nature, 1983, 306, 356.

[17] C. M. Zicovich and A. Corma, J. Phys. Chem., 1994, 98, 10863.

[18] Anionic surfactants: physical chemistry of surfactant action, E. H. Lucassen-Reynders, Editor, Marcel Dekker, New York, 1981.

[19] N. R. B. Coleman, PhD thesis, University of Southampton, 1999.

[20] V. Luzzati and P. Spegt, Nature, 1967, 215, 701.

[21] L. E. Scriven, Nature, 1976, 263, 123.

[22] N. H. Hartshorne, The Microscopy of Liquid Crystals, Microscope Publications Ltd., London, 1974.

[23] J. N. Israelachvili, D.J. Mitchell and B. W. Ninham, J. Chem. Soc. Faraday Trans. 2, 1976, 72, 1525.

[24] D. J. Mitchell, G. J. T. Tiddy, L. Waring, T. Bostock and M. P. McDonald, J. Chem. Soc., Faraday Trans. 1, 1983, 79, 975.

[25] R. G. Laughlin, The Aqueous Phase Behaviour of Surfactants, Academic Press, London, 1996.

[26] K. Mortensen and Y. Talmon, Macromolecules, 1995, 28, 8829.

[27] R. Ivanova, B. Lindman and P. Alexandridis, Langmuir, 2000, 16, 958.

[28] R. Ivanova, B. Lindman and P. Alexandridis, Adv. in Colloid and Interface Science, 2001, 89-90, 351.

[29] P. Holmqvist, P. Alexandridis and B. Lindman, Macromolecules, 1997, 30, 6788.

[30] P. Holmqvist, P. Alexandridis and B. Lindman, J. Phys. Chem. B, 1998, 102, 1149.

[31] T. Iwanaga, M. Suzuki and H. Kunieda, Langmuir, 1998, 14, 5775.

[32] K. Aramaki, U. Olsson, Y. Yamaguchi and H. Kunieda, Langmuir, 1999, 15, 6226.

[33] R. Ivanova, P. Alexandridis and B. Lindman, Coll. Surf. A, 2001, 183-185, 41.

[34] P. Alexandridis, U. Olsson and B. Lindman, Langmuir, 1998, 14, 2627.

[35] G. Wanka, H. Hoffmann and W. Ulbricht, Macromolecules, 1994, 27, 4145.

[36] H. N. Patrick, G. G. Warr, S. Manne and I. A. Aksay, Langmuir, 1997, 13, 4349.

[37] J. P. Rabe and S. Buchholz, Science, 1991, 253, 424.

[38] F. Tiberg, J. Chem. Soc. Faraday Trans., 1996, 92, 531.

[39] L. M. Grant, F. Tiberg and W. A. Ducker, J. Phys. Chem. B, 1998, 102, 4288.

[40] H. Miyata, T. Noma, M. Watanabe and K. Kuroda, Chem. Mater., 2002, 14 (2), 766.

[41] G. J. T. Tiddy, Physics Reports, 1980, 57(1), 1.

[42] C. N. R. Rao and A. K. Cheetham, J. Mater. Chem., 2001, 11, 2887.

[43] C. T. Kresge, M. E. Leonowicz, W. J. Roth, W. C. Vartuli and J. S. Beck, Nature, 1992, 359, 710.

[44] C. Y. Chen, S. L. Burkett, H. X. Li and M. E. Davis, Microporous Mater., 1993, 2, 27.

[45] A. Monnier, F. Schuth, Q. Huo, D. Kumar, D. Margolese, R. S. Maxwell, G. D. Stucky, M. Krishnamurty, P. Petroff, A. Firouzi, M. Janicke and B. F. Chmelka, Science, 1993, 261, 1299.

[46] A. Corma, Chem. Rev., 1997, 97, 2373.

[47] P. T. Tanev, M. Chibwe and T. J. Pinnavaia, Nature, 1994, 368, 321.

[48] P. T. Tanev and T. J. Pinnavaia, Science, 1995, 267, 865.

[49] S. A. Bagshaw, E. Prouzet and T. J. Pinnavaia, Science, 1995, 269, 1242.

[50] N. Coustel, F. Di Renzo and F. Fajula, J. Chem. Soc. Chem. Comm., 1994, 967, 1994.

[51] P. Yang, D. Zhao, D. I. Margolese, B. F. Chmelka and G. D. Stucky, Nature, 1998, 396, 152.

[52] P. Yang, D. Zhao, D. I. Margolese, B. F. Chmelka and G. D. Stucky, Chem. Mater., 1999, 11, 2813.

[53] W. Cheng, E. Baudrin, B. Dunn and J. I. Zink, J. Mater. Chem., 2001, 11, 92.

[54] M. Mamak, Neil Coombs and G. Ozin, J. Am. Chem. Soc., 2000, 122, 8932.

[55] M. Mamak, Neil Coombs and G. Ozin, Chem. Mater., 2001, 13, 3564.

[56] G. S. Attard, J. C. Glyde and C. G. Goltner, Nature, 1995, 378, 366.

[57] G. S. Attard, C. G. Goltner, J. M. Corker, S. Henke and R. H. Templer, Angew. Chem., Int. Ed. Engl., 1997, 36, 1315.

[58] G. S. Attard, P. N. Bartlett, N. R. B. Coleman, J. M. Elliott, J. R. Owen and J. H. Wang, Science, 1997, 278, 838.

[59] J. M. Elliott, G. S. Attard, P. N. Bartlett, N. R. B. Coleman, D. A. S. Merckel and J. R. Owen, Chem. Mater., 1999, 11, 3602.

[60] G. S. Attard, P. N. Bartlett, N. R. B. Coleman, J. M. Elliott and J. R. Owen, Langmuir, 1998, 14, 7340.

[61] J. M. Elliott, P. R. Birkin, P. N. Bartlett and G. S. Attard, Langmuir, 1999, 15, 7411.

[62] J. M. Elliott, G. S. Attard, P. N. Bartlett, J. R. Owen, N. Ryan and G. Singh, J. New Mater. for Electrochem. Systems, 1999, 2, 239.

[63] P. N. Bartlett, B. Gollas, S. Guerin and J. Marwan, *Phys. Chem. Chem. Phys.*, 2002, 4, 3835.

[64] P. N. Bartlett, P. N. Birkin, M. A. Ghanem, P. de Groot and M. Sawicki, J. Electrochem. Soc., 2001, 148, C119.

[65] I. Nandhakumar, J. M. Elliott and G. S. Attard, Chem. Mater., 2001, 13, 3840.

[66] L. Huang, H. Wang, Z. Wang, A. Mitra, D. Zhao and Y. Yan, Chem. Mater., 2002, 14, 876.

[67] A. H. Whitehead, J. M. Elliott, J. R. Owen and G. S. Attard, Chem. Comm., 1999, 331.

[68] J. M. Elliott, L. M. Cabuche and P. N. Bartlett, Anal. Chem., 2001, 73, 2855.

[69] J. C. Hulteen and C. R. Martin, J. Mater. Chem., 1997, 7, 1075.

[70] C. A. Foss, G. L. Hornyak, J. A. Stockert and C. R. Martin, Adv. Mater., 1993, 5, 135.

[71] V. P. Menon and C. R. Martin, Anal. Chem. 1995, 67, 1920.

[72] R. V. Parthasarathy, K. L. N. Pharni and C. R. Martin, Adv. Mater., 1995, 7, 896.

[73] B. B. Lakshmi, P. K. Dorhout and C. R. Martin, Chem. Mater., 1997, 9, 857.

[74] G. Che, B. B. Lakshmi, E. R. Fisher and C. R. Martin, Nature, 1998, 393, 346.

[75] M. E. Spahr, P. Bitterli, R. Nesper, M. Muller, F. Krumeich and H. U. Nissen, Angew. Chem. Int. Ed., 1998, 37, 1263.

[76] F. Krumeich, H. J. Muhr, M. Niederberger, F. Bieri, B. Schnyder and R. Nesper, J. Am. Chem. Soc., 1999, 121, 8324.

[77] M. Niederberger, H. J. Muhr, F. Krumeich, F. Bieri, D. Gunther and R. Nesper, Chem. Mater., 2000, 12, 1995.

[78] S. A. S. Machado and L. A. Avaca, Electrochim. Acta, 1994, 39(10), 1385.

[79] J. van Muylder, in Comprehensive Treatise of Electrochemistry, vol. 4, J. O'M. Bockris, B. E. Conway, E. Yeager and R. E. White, Plenum Press, New York, 1981.

[80] S. Rausch and H. Wendt, J. Electrochem. Soc., 1996, 143(9), 2852.

[81] P. W. Atkins, Physical Chemistry, Oxford University Press, Oxford, 1978, 193.

[82] K. J. Laidler and J. H. Meiser, Physical Chemistry, 2nd Edition, Houghton Mifflin Company, Boston, 1995, 194.

[83] W. Stumm and J. J. Morgan, Aquatic Chemistry, 2nd Edition, John Wiley and Sons, New York, 1981, 109.

[84] J. P. Orchard, A. D. Tomset, M. S. Wainwright and D. J. Young, J. Catal., 1983, 84, 189.

[85] M. Fleischmann, K. Korinek and D. Pletcher, J. Electroanal. Chem., 1971, 31, 39.

[86] M. Amjad, D. Pletcher and C. Smith, J. Electrochem. Soc., 124(2), 203.

[87] V. Anantharaman and P. N. Pintauro, J. Electrochem. Soc., 1994, 141(10), 2729.

[88] P. M. Robertson, P. Berg, H. Reimann, K. Schleich and P. Seiler, J. Electrochem. Soc., 1983, 130(3), 591.

[89] J. R. Owen, University of Southampton, 1997.

[90] A. Stein, S. W. Keller and T. E. Mallouk, Science, 1993, 259, 1558.

[91] M. Figlarz, B. Gerand, A. Delahaye-Vidal, B. Dumont, F. Harb and A. Coucou, Solid State Ionics, 1990, 43, 143.

[92] J. Reimers, E. Fuller, E. Rossen and J. Dahn, J. Electrochem. Soc., 1993, 140, 3396.

[93] G. G. Amatucci, J. M. Tarascon, D. Larcher and L. C. Klein, Solid State Ionics, 1996, 84, 169.

[94] J. Murata, H. Yasuda and M. Yamachi, J. Power Sources, 2000, 90, 89.

[95] N. Li and C. R. Martin, J. Electrochem. Soc., 2001, 148(2), A164.

[96] I. A. Courtney and J. R. Dahn, J. Electrochem. Soc., 1997, 144(6), 2045.

[97] P. Poizot, S. Laruelle, S. Grugeon, L. Dupont and J. M. Tarascon, Nature, 2000, 407, 496.

[98] S. Grugeon, S. Laruelle, R. Herrara-Urbina, L. Dupont, P. Poizot and J. M. Tarascon, J. Electrochem. Soc., 2001, 148(4), A285.

[99] H. Ikeda and S. Narukawa, J. Power Sources, 1983, 1983, 9, 329.

[100] Kotz, R. and Carlen, M., Electrochim. Acta., 2000, 45, 2483.

[101] Huggins, R. A., Solid State Ionics, 2000, 134, 179.

[102] http://www.esma-cap.com

[101] Conway, B. E., J. Electrochem. Soc., 1991, 138(6), 1539.

[104] Burke, A., J. Power Sources, 2000, 91, 37.

[105] Sarangapani, S., Tilak, B. V., Chen, C. P., J. Electrochem. Soc., 1996, 143(11), 3791.

[106] Skeleton Technologies at www.skeleton-technologies.com.

[107] Kotina, I. M., Lebedev, V. M., Ilves, A. G., Patsekina, G. V., Tuhkonen, L. M., Gordeev, S. K., Yagovkina, M. A., Ekstrom, T., J. Non-Crystalline Solids, 2002, 29-302, 815.

[108] Trasatti, S., Buzzanca, G., J Electroanal. Chem., 1971, 29, 1.

[109] Raistrick, I. D., The Electrochemistry of Semiconductors and Electrodes, Processes and Devices, 1992, McHardy and Ludwig , New Jersey, USA, p. 297

[110] Hadzi-Joredanov, S., Angerstein-Kozlowska, H., Vukovic, M., Conway, B. E., J. Electrochem. Soc., 1978, 125, 1471.

[111] Zheng, J. P., Cygan, P. J., Jow, T. R., J. Electrochem. Soc., 1995, 142(8), 2699.

[112] Jow, T. R., Zheng, J. P., J. Electrochem. Soc., 1998, 145(1), 49.

[113] Ardizzone, S., Fregonara, G., Trasatti, S., Electrochim. Acta, 1990, 35(1), 263.

[114] Miller, J. M., Dunn, B., Tran, T. D., Pekala, R. W., J. Electrochem. Soc., 1997, 144(12), L309.

[115] Takasu, Y., Nakamura, T., Ohkawauchi, H., Murakami, Y., J. Electrochem. Soc., 1997, 144(8), 2601.

[116] Wilde, P. M., Guther, T. J., Oesten, R., Garche, J., J. Electroanal. Chem., 1999, 461, 154.

[117] Liu, K. C., Anderson, M. A., J. Electrochem. Soc., 1996, 143(1), 124.

[118] Srinivasan, V., Weidner, J. W., J. Electrochem. Soc., 1997, 144(8), L210.

[119] Kalu, E. E., Nwoga, T. T., Srinivasan, V., Weidner, J. W., J. Power Sources, 2001, 92, 163.

[120] Lin, C., Ritter, J. A., Popov, B., N., J. Electrochem. Soc., 1998, 145(12), 4097.

[121] Liu, T-C., Pell, W. G., Conway, B. E., Roberson, S. L., J. Electrochem. Soc., 1998, 145(6), 1882.

[122] Beliakov, A. I., Brintsev, A. M., in Proceedings of the 7th International Seminar on Double Layer Capacitors and Similar Energy Storage Devices, Florida Educational Seminars, Dec 8-10 1997.

[123] Park, J. H., Park, O. O., Shin, K. H., Jin, C. S., Kim, J. H., Electrochem. and Solid State Letters, 2002, 5(2), H7.

[124] Naoi, K., Suematsu, S., Manago, A., J. Electrochem. Soc., 2000, 147(2), 420.

[125] Suematsu, S., Naoi, K., J. Power Sources, 2001, 97-98, 816.

[126] Fusalba, F., Gouerec, P., Villers, D., Belanger, D., J. Electrochem. Soc., 2001, 148(1), A1.

[127] Rudge, A., Davey, J., Raistrick, J., Gottesfield, S., Ferraris, J. P., J. Power Sources, 1994, 47, 89.

[128] Y. D. Gamburg, N. P. Nga, S. V. Vashchenko and T. E. Tsupak, Elektrokhimiya, 1985, 21, 1403.

[129] I. Epelboin and R. Wiart, J. Electrochem. Soc., 1971, 118, 1577.

[130] J. Matulis and R. Slizys, Electrochim. Acta, 1964, 9, 1177.

[131] K. M. Yin, J. H. Wei, J. R. Fu, B. N. Popov, S. N. Popova and R. E. White, J. Appl. Electrochem., 1995, 25, 543.

[132] M. Pourbaix, Atlas D'Equilibres Electrochimiques, Gauthier-Villars, Paris, 1963, 333.

[133] K. M. Yin and B. T. Lin, Surface and Coatings Tech., 1996, 78, 205.

[134] Y. Tsuru, M. Nomura and F. R. Foulkes, J. Appl. Electrochem., 2002, 32, 629.

[135] B. V. Tilak, A. S. Gendron and M. A. Masoiu, J. Appl. Electrochem., 1977, 7, 495.

[136] T. E. Springer, T. A. Zawodzinski, M. S. Wilson and S. Gottesfeld, J. Electrochem. Soc., 1996, 143(2), 587.

Chapter 2

The Preparation of Mesoporous Nickel

2.1 Background and Objectives

Prior to the work discussed here, the direct liquid crystal templating (DLCT) of electrodeposited metals with high quality mesoporosity was restricted to platinum and palladium using expensive, high purity polyoxyethylene surfactants such as $C_{16}EO_8$. Although platinum and palladium are efficient electrocatalysts for a number of processes, the high raw materials cost of these metals has impeded their widespread use in electrochemical technologies. Attempts to prepare less expensive metals of greater industrial relevance via the DLCT route with high quality mesoporosity using the cheaper, less pure Brij® polyoxyethylene surfactants have received little effort with the exception of mesoporous tin.[1]

The subject of the work described in this chapter is the preparation and characterisation of high quality mesoporous nickel using the Brij® and Pluronic® surfactant systems. The objectives of the work are described below:

1. To find an appropriate liquid crystal deposition medium and characterise its phase behaviour. Here, compatibility between the surfactant and a dissolved nickel salt were necessary such that the mixture gave access to important liquid crystalline phases such as the hexagonal (H_I) and bicontinuous cubic (V_I) phases.

2. To investigate methods of preparing mesoporous nickel via an electrodeposition route, to characterise this deposition process and to make comparisons with the non-templated electrodeposition of nickel. This is important not only for understanding the deposition process, but in order to elucidate means of rapid production of mesoporous nickel, whilst retaining high quality mesoporosity.

3. To prepare mesoporous nickel of varying pore sizes with both H_I and V_I pore geometry. The ability to vary pore size and geometry is important in successfully tailoring a mesoporous material to a particular application.

4. To characterise mesoporous nickel both structurally and electrochemically. Structural characterisation includes investigation of both macro- and mesoscale morphology and structural regularity, while electrochemical characterisation includes surface area analysis and investigation of relevant electrochemical rate capabilities.

5. The final objective of this chapter will be to compare the properties of templated mesoporous nickel with those of non-templated electrodeposited samples.

2.2 Experimental

Experimental work in this chapter is divided into four sections. The first gives details of the methods used in elucidation of the phase behaviour of the templating media, while the second section details the characterisation of the deposition process. Sections three and four then discuss methods used in the structural and electrochemical characterisation respectively of mesoporous nickel.

2.2.1 Phase Behaviour of Liquid Crystalline Templating Mixtures

The non-ionic polyoxyethylene surfactants Brij® 56 ($C_{16}[EO]_n$ where n~10) and Brij® 78 ($C_{18}[EO]_n$ where n~20) are trademarks of ICI America and were obtained from Aldrich and used as received. The Pluronic® (a trademark of BASF Corp.) block copolymer surfactant P123 (with formula $[EO]_{20}[PO]_{70}[EO]_{20}$) was a gift from BASF Corp. (Mt. Olive, New Jersey) and was also used as received. The precursor solution used in the electrodeposition consisted of nickel(II) acetate tetrahydrate (Fluka, >99%), sodium acetate trihydrate (Fluka, >99.5%) and boric acid (BDH Chemicals, >99.5%). All solutions were prepared using deionized water and glassware was cleaned by soaking in a 3 % solution of Decon 90 (Hogg) for 24 h. followed by soaking in dilute HCl and subsequent rinsing with deionized water.

The templating media used in the electrodeposition of mesoporous nickel were binary systems comprising either Brij® 56, Brij® 78 or Pluronic® P123 surfactants and an aqueous solution consisting of 0.2 M nickel acetate, 0.5 M sodium acetate and 0.2 M boric acid. In preparing the mixtures, the surfactants were heated to ~60 ° C (above their melting points) in a glass vial and mixed manually using a glass rod on addition of the aqueous solution. Compositions of the binary mixtures were calculated on a weight basis. Mixing times of ~10 minutes were required to obtain an homogeneous mixture. Complete mixing was confirmed by homogeneity of the liquid crystal's colour and by the absence of macroscopic surfactant particles under the non-polarizing light of an optical microscope.

Phase diagrams of the templating media in the composition range 30-85 wt. % Brij®/Pluronic®, were investigated using an Olympus BH-2 polarizing microscope equipped with a Linkam TMS 90 heating/cooling stage accurate to ± 0.1 °C. Here, thin films of the liquid crystals were prepared by sandwiching the mixture between a

glass microscope slide and cover slip. Liquid crystalline phases were identified based on their optical texture[2], viscosity and the shape of the air bubbles present in the mixture.

In identifying hexagonal/lamellar phase transitions the change in optical texture was not always a reliable indication of the transition. As such, the characteristic decrease in mixture viscosity accompanying this phase change was used as a more reliable indication of the transition. This transition was made easier to recognise by rotating the glass cover slip 180° while the mixture was in the hexagonal phase. Rotating the cover slip caused air bubbles in the sample to adopt a long arced shape. The bubbles were able to retain this highly stressed shape only because of the high viscosity of the hexagonal phase, however on moving to the less viscous lamellar phase, the stressed bubbles relaxed immediately to circular bubbles, making the transition easily recognisable.

2.2.2 The Electrodeposition Process

The electrochemical deposition of mesoporous nickel was conducted in a

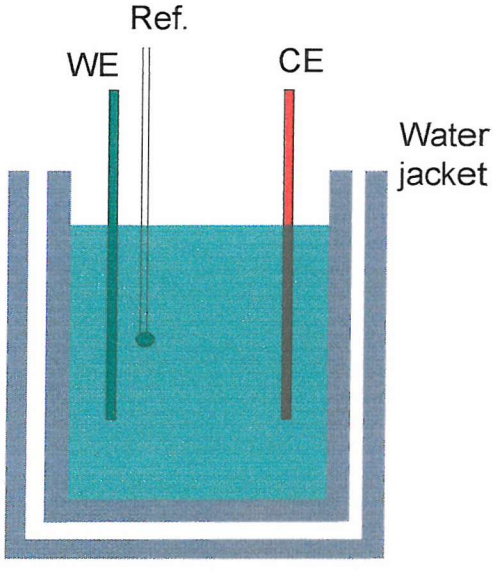

Figure 2.1. This schematic shows the electrodeposition cell consisting of a three electrode cell contained within a glass water jacket used in the deposition of mesoporous nickel.

potentiostatic regime using either a purpose-built potentiostat or a Perkin-Elmer VMP Multistat. Deposition cells were of a three-electrode configuration consisting of a gold

working electrode, a saturated calomel reference electrode (SCE) and a platinum gauze counter electrode. These electrodes were inserted into the liquid crystalline plating electrolyte containing dissolved nickel (II) salts as illustrated in Figure 2.1. All deposition experiments were carried out potentiostatically at –0.9 V *vs.* SCE and 25 °C (unless otherwise stated) with varying deposition charge densities. Mesoporous nickel deposited from the H_I Pluronic® template used a 50 wt. % P123 based template, while H_I nickel deposited from Brij® 56 and 78 used 65 wt. % surfactant templates. Deposition of V_I nickel from the Brij® 56 based template also used a 65 wt. % surfactant template however the deposition temperature was 35 °C.

Cells were contained in Pyrex water-jacketed vessels. Cell temperature was maintained at the deposition temperature with an accuracy of ± 0.1 °C using a Grant ZD thermostated water bath. Prior to the commencement of electrodeposition, the liquid crystalline electrolyte was heated to approximately 50 °C (into the less viscous micellar solution or lamellar phase regions) and then allowed to cool without assistance for 15 min. followed by a further 15 min. cooling period assisted by a water bath held at the deposition temperature. This process essentially annealed the liquid crystal, allowing internal stresses in the mesophase to be relieved. In combination with the 30 min. cooling period, this annealing resulted in the formation of a more continuous and ordered phase structure. This process will be discussed in detail in Chapter 6. In addition to assisting ordered phase formation, the annealing process also allows larger air bubbles to be removed from the solution by virtue of their buoyancy in the less viscous electrolyte at 50 °C. The removal of air bubbles ensures that the deposition of metal films is homogeneous over the entire electrode surface.

Films grown for transmission electron microscopy (TEM) and x-ray diffraction (XRD) analysis were deposited onto approximately 3 cm^2 thin film gold electrodes made by evaporation of gold onto chromium-coated glass microscope slides. These electrodes were cleaned in an ultrasonic bath of isopropanol for 60 minutes prior to deposition, then rinsed with de-ionised water and dried under ambient conditions. Films used in electrochemical characterization were deposited onto either 200 μm or 1 mm diameter gold discs encased in an epoxy insulator. These were cleaned by first polishing consecutively on 25 μm, 1 μm and 0.3 μm alumina (obtained from Buehler) embedded microcloths then electrochemically cleaned by cycling the electrodes between –0.6 V and 1.4 V *vs.* a saturated mercury sulphate reference electrode

(SMSE) at 200 mVs^{-1} in a 2 M H_2SO_4 solution. An example voltammogram is presented in Figure 2.2. With each cycle, a layer of gold oxide was formed at potentials above 0.75 V *vs.* SMSE and subsequently stripped from the electrode surface as indicated by the peak centred at 0.45 V.[3] Hydrogen and oxygen evolution currents dominated the voltammetry at the lower and upper limits respectively.

Experiments investigating the variation of the deposition current density with deposition potential in the non-templating nickel deposition solution were carried out potentiostatically using 25 μm gold disc microelectrodes. Steady state currents were used in analysis of the data.

After deposition working electrodes were removed from the cell and washed in isopropanol for 24 h. in order to remove the template electrolyte from the pores of the deposit.

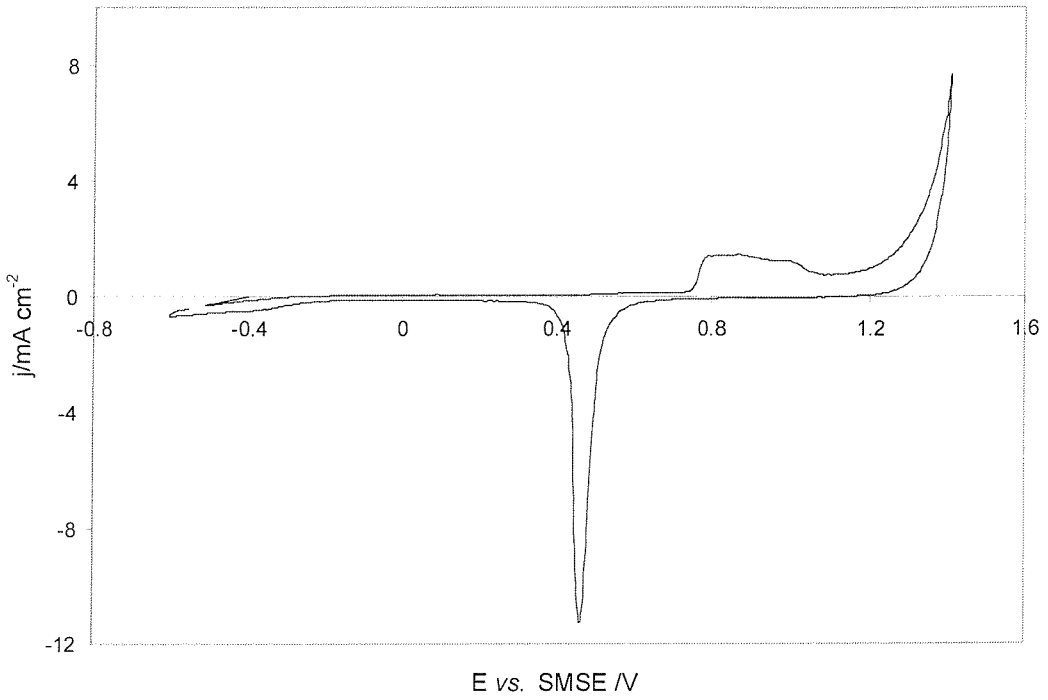

Figure 2.2 shows the voltammetry of a polished gold disc electrode cycled in 2 M $H_2SO_{4(aq)}$ at 200 mV s^{-1} indicating a clean, deposition ready surface.

The efficiency of the electrodeposition process was measured using an anodic stripping voltammetry treatment on deposited electrodes. This procedure is described in Chapter 6.

2.2.3 Structural Characterisation

Structural characterization of the films was carried out in order to confirm the templating effect of the liquid crystal on the deposit morphology. Transmission electron microscopy (TEM) was performed on a JEOL 2000FX TEM working at 200 kV. Samples were prepared by scraping particles from a mesoporous nickel film supported on a deposition substrate into ethanol. Particles of mesoporous nickel were then removed from the ethanol by pipette and dispersed on Cu TEM grids with evaporation of the ethanol.

Both small angle x-ray scattering (SAXS) and wide angle x-ray scattering (WAXS) were carried out using a Siemens D-5000 diffractometer (Cu-K_α radiation) with a scan rate of 5° min^{-1}.

2.2.4 Electrochemical characterisation

Electrochemical characterisation of electrodeposited nickel films was carried out in order to determine the surface area of the films and to determine their rate capabilities in charging and discharging reactions. Potential step and cyclic voltammetry experiments were conducted using a purpose built potentiostat and triangular waveform generator interfaced with a PC via a National Instruments data acquisition card. Experiments were carried out in three electrode cells consisting of the nickel working electrode, a platinum gauze counter electrode and a mercury/mercury oxide (using 6 M KOH) reference electrode (Hg/HgO) immersed in 6 M KOH purged with N_2 or Ar gas. Cyclic voltammetry was conducted between the potential limits of –1.06 V and 0.6 V *vs.* Hg/HgO. Determination of the amount of charge associated with the cyclovoltammetric peaks of the $Ni(OH)_2$/NiOOH redox couple in alkaline solution was done by integration of the entire peak area in the case of the cathodic process. Charge associated with the anodic peak was calculated by integration of the peak and using the potential intercept of the linear portion of the trailing edge (falling current) of the peak as the upper potential limit of integration. This enabled exclusion of the oxygen evolution current from the calculated anodic charge value.

2.3 Results and Discussion

2.3.1 Phase Characterization

The ability of three surfactants, namely Brij® 56, Brij® 78 and Pluronic® P123 to form self-assembled liquid crystalline phases on addition of aqueous solution was used to create supramolecular templates for the electrodeposition of porous nickel. Study of the phase behaviour of a liquid crystalline phase containing a Ni(II) aqueous solution was important in determining the correct experimental parameters needed to obtain the desired template geometry. The following sections describe the phase behaviour of the liquid crystalline electrolytes used in the deposition of mesoporous nickel.

2.3.1.1 Brij® 56

The Brij® 56 liquid crystal templating mixture was found to exhibit a variety of structural phase morphologies. The phase diagram of Brij® 56 with the nickel(II) acetate deposition solution is shown in Figure 2.3, and indicates relatively complex lyotropic phase behaviour. Although polyoxyethylene systems are considered lyotropic, there is also some thermotropic behaviour observable in Figure 2.3 as evidenced by the occurrence of phase transitions with variation of the temperature.

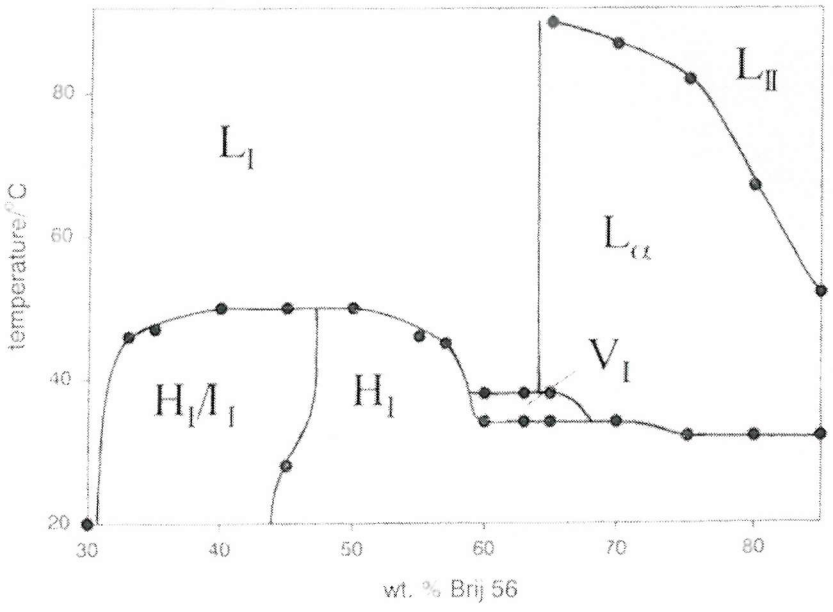

Figure 2.3 shows the phase behaviour of the Brij® 56/0.2 M nickel acetate deposition solution mixture over a wide temperature and composition range.

In general, only the hexagonal (H_I) and bicontinuous cubic (V_I) phases were of interest in our liquid crystal templating syntheses since only these phases are capable of producing materials with continuous pore networks and adequate mechanical stability. Figure 2.3 shows a large stable H_I domain, enabling fabrication of H_I structures over a range of temperatures and compositions using this templating system. The synthesis of V_I nickel is somewhat more restricted in that its fabrication is limited to surfactant concentrations between 60 and 65 wt. % in the temperature range 34-38 °C.

Figures 2.4, 2.5 and 2.6 illustrate the optical textures of the H_I, V_I and L_α phases

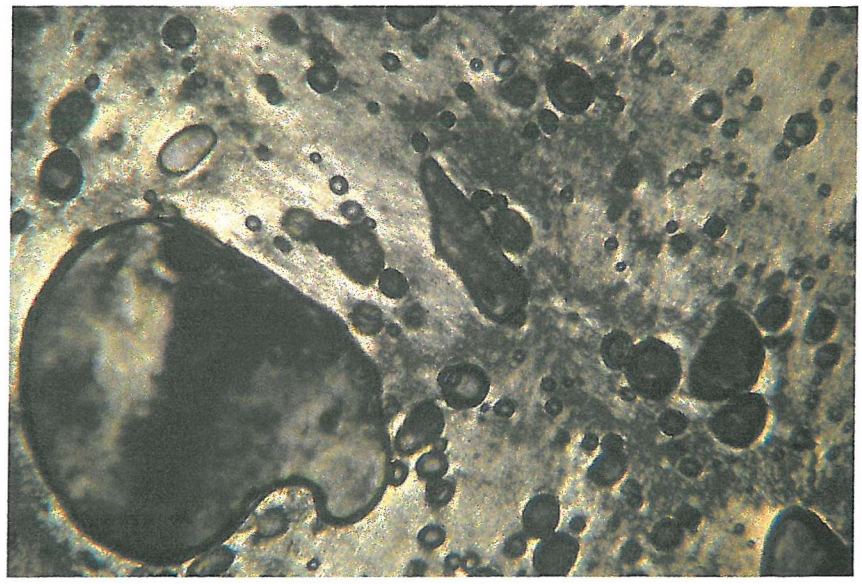

Figure 2.4. The charcoal-like appearance of this cross polarising optical micrograph identifies the H_I phase of the Brij® 56/0.2 M nickel acetate deposition solution system.

respectively under cross-polarising light. The H_I phase of Figure 2.4 is clearly identified by its optical texture, which resembles that of a charcoal drawing. The H_I phase is also identified by the irregular geometry of the air bubbles present in the mixture. In addition to the V_I and I_I cubic phases, the hexagonal phase is one of 3 phases having sufficient viscosity to allow air bubbles in the mixture to sustain an irregular geometry. Of these 3 viscous phases however, only the H_I phase displays a birefringence pattern under cross polarizing light. The V_I bicontinuous phase of Figure 2.5 clearly demonstrates an irregular air bubble geometry, however since this phase is structurally isotropic, it does not show a birefringence derived optical texture

under polarizing light. The V_I phase differentiates itself from the I_I phase by virtue of its higher viscosity and its relative proximity (with regard to surfactant concentration) to the H_I phase. Like the H_I phase, the L_α

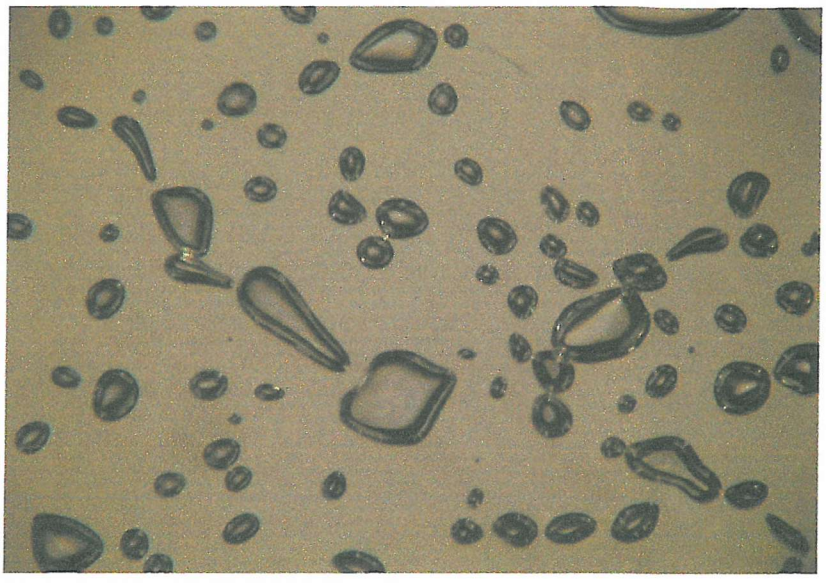

Figure 2.5. Lack of birefringence patterns and the presence of irregularly shaped bubbles in this micrgraph indicate the V_I phase of the Brij® 56/0.2 M nickel acetate templating electrolyte.

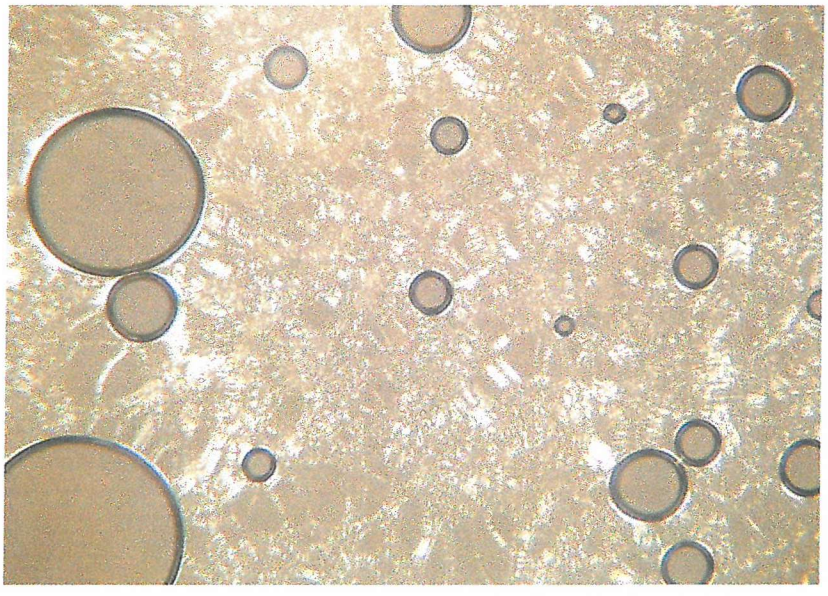

Figure 2.6. The L_α phase of the Brij® 56 based template is clearly evidenced here by the presence of optical birefringence and round bubbles.

phase of Figure 2.6 also possesses a birefringence pattern composed of mixed light and dark areas. The L_α phase may be differentiated from the H_I phase by the presence of round air bubbles in the mixture. This bubble geometry is a consequence of the relatively low viscosity of the L_α phase, which allows the bubbles to assume their preferred round shape.

Phase transitions occur via the formation of a biphasic mixture on the phase boundary. Unlike the $C_{16}EO_8$-aqueous system in which phase transitions are relatively sharp, phase transitions in liquid crystal systems based on the less pure Brij® surfactants often span 3-4 °C or wt. % surfactant. The lines representing phase boundaries in Figure 2.3 then, would be more correctly draw much thicker than they are actually depicted. As a consequence, attempts to template mesoporous nickel in an area of the phase diagram close to a phase boundary have proven difficult and often resulted in poorly formed mesoporosity as manifest by lower than expected surface areas. For example, deposition from a 50 wt. % Brij® 56/Ni(II) deposition solution mixture at 40 °C produced electrodeposits with surface areas not significantly greater than that of a nickel film deposited in the absence of the surfactant templating electrolyte.

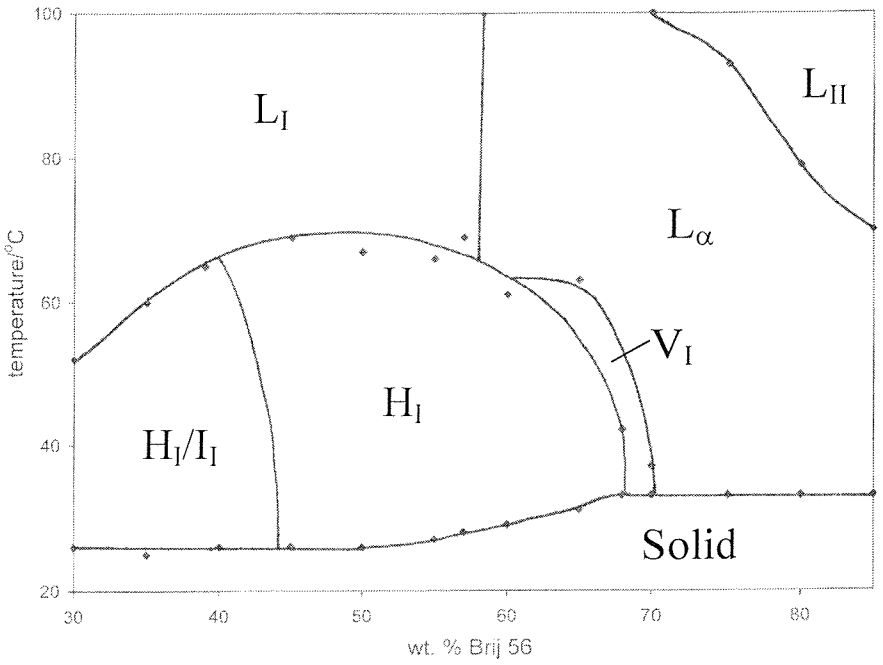

Figure 2.7 shows the phase behaviour of the Brij® 56/water system with an extended bicontinuous cubic phase region.

In comparison with the phase behaviour of the Brij® 56/water system[4] presented in Figure 2.7, the micellar (L_1) phase region of the Brij® 56 templating mixture is enlarged slightly at the expense of the H_1 and hexagonal/cubic micellar (H_1/I_1) phase regions, which are only stable to 48 °C in this system as opposed to 67 °C in the water mixture. The L_1 phase also extends to higher surfactant concentrations at the expense of the L_α phase which is stable to 66 wt. % Brij® 56 in the Ni(II) containing mixture as opposed to 57 wt. % Brij® 56 in the water system. The introduction of the deposition solution ions to the Brij® 56/water system also results in the stabilisation of the small V_1 domain at lower temperatures than that observed in the Brij® 56/water system. Where the V_1 phase is stable between 32 °C and 60 °C over the composition range 60 to 70 wt. % Brij® 56 in the water system, it is only stable over a 4 °C range in this composition range in the Ni(II) template system.

Prior to the elucidation of the Brij® 56/nickel (II) acetate phase diagram a number of nickel(II) salts were examined for their compatibility with this surfactant in forming liquid crystalline phases. The Brij® 56/nickel (II) sulphate system was found to be unsuitable due to phase separation (the formation of a viscous aqueous phase was observed in addition to a surfactant rich phase) in the liquid crystal mixture. Nickel (II) sulphamate was also investigated for compatibility with Brij® 56 however the phase diagram of this system was found to be dominated by biphasic regions, with only a small range of temperatures and compositions over which the desired H_1 phase was stable.

2.3.1.2 Brij® 78

The Brij® 78 templating system is somewhat simpler in its phase behaviour than the Brij® 56 system. Figure 2.8 shows an enlarged H_1 domain stable over an approximately 30 wt. % range over the entire range of temperatures measured (20 °C to 90 °C).

As expected, phase regions at lower surfactant concentrations than that required to form the H_1 phase are inhabited by the L_1 and I_1 micellar solutions. A small inverse phase, L_{II} is present at temperatures and surfactant concentrations above the stability domain of the H_1 phase. Perhaps of greatest note is the absence of the L_α phase, which occupies a significant proportion of the Brij® 56 phase diagram. This absence is not surprising when comparing the structures of Brij® 56 and Brij® 78 and considering the

effect of the surfactant packing parameter (see Chapter 1). The difference in hydrocarbon tail length in Brij® 56 and 78 is only two carbon units and is thus expected to have little effect on changes in the phase behaviour. In contrast, the area

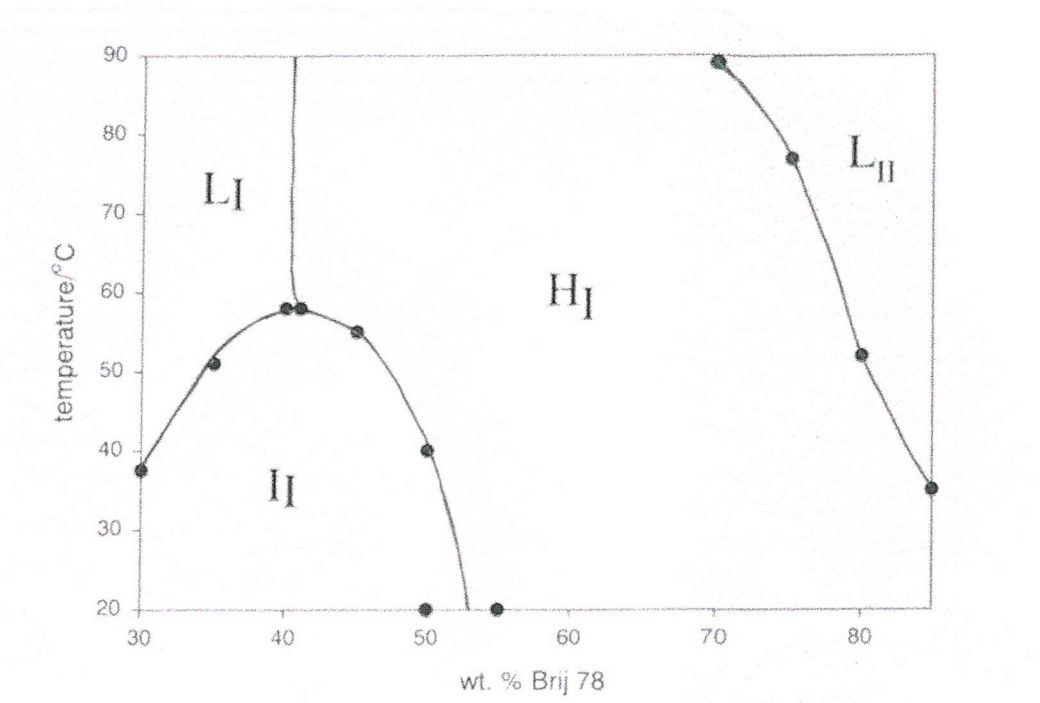

Figure 2.8 shows the phase behaviour of the Brij® 78/0.2 M nickel acetate deposition solution mixture over a wide temperature and composition range.

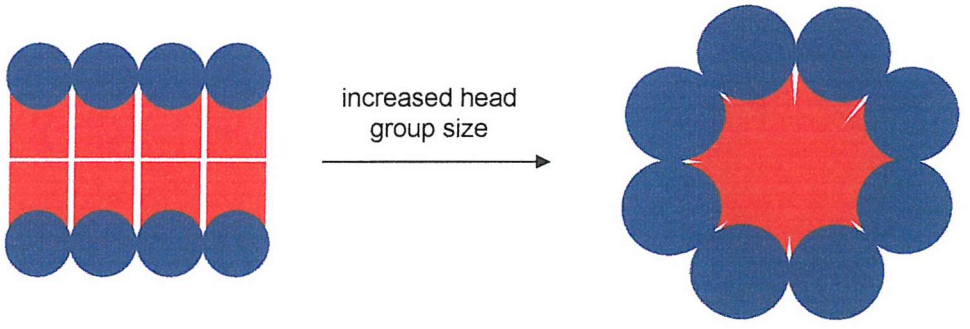

Figure 2.9. Increasing head group size relative to tail group size induces strain and results in the formation of phases of higher curvature as indicated in this two-dimensional representation of a L_α to H_I transition.

occupied by the head group, which is twice as great in Brij® 78 has a large effect on phase behaviour, as predicted by the surfactant packing parameter. With the enlarged head group of Brij® 78, the surfactant packing parameter favours the formation of

highly curved phases such as the H_I and micellar phases over the L_α phase which ideally possesses no curvature, as illustrated schematically in Figure 2.9.

The phase behaviour of the Brij® 78 based liquid crystalline system was found to be less sensitive to the addition of the deposition solution ions than was the Brij® 56 system in that the phase diagram of the Brij® 78 templating solution varied only slightly from that of the Brij® 78/water system presented in Figure 2.10.

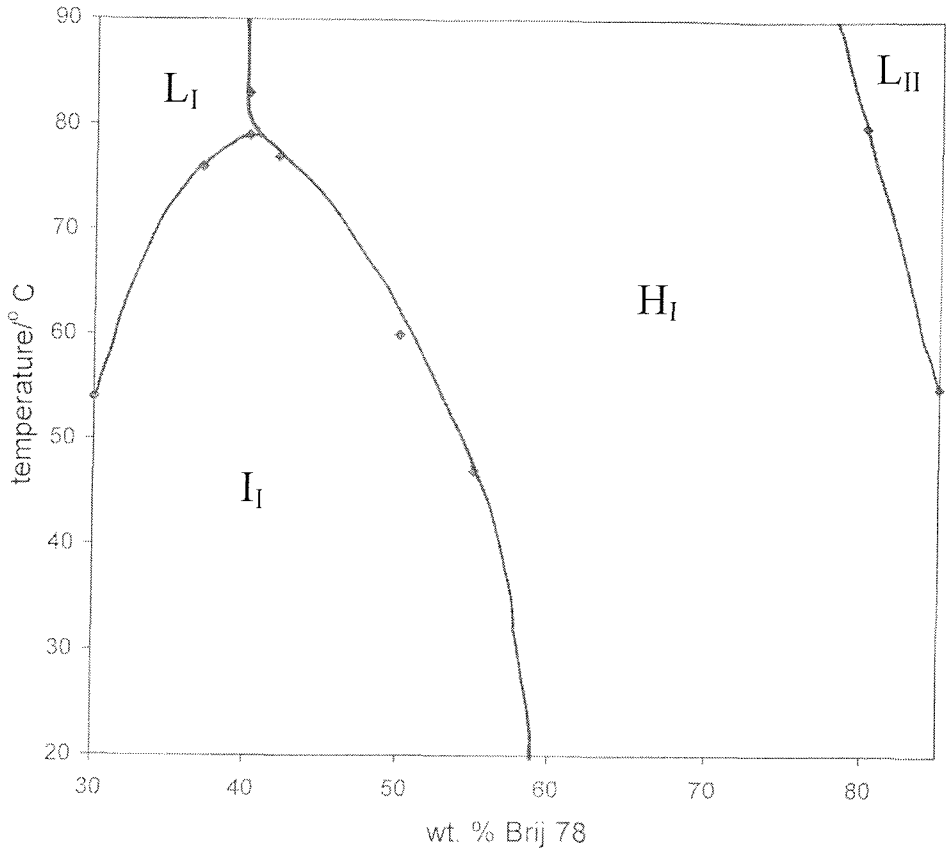

Figure 2.10 shows the relatively simple phase behaviour of the Brij® 78/water liquid crystal mixture.

2.3.1.3 Pluronic® P123

The phase behaviour of the Pluronic® P123/nickel (II) acetate deposition system is relatively simple as compared with polyoxyethylene surfactant systems. The phase diagram of the P123 template is presented in Figure 2.11. A large H_I phase existing at low temperatures between 30 and 58 wt. % P123 is surrounded by a phase of indefinable mesopore geometry.

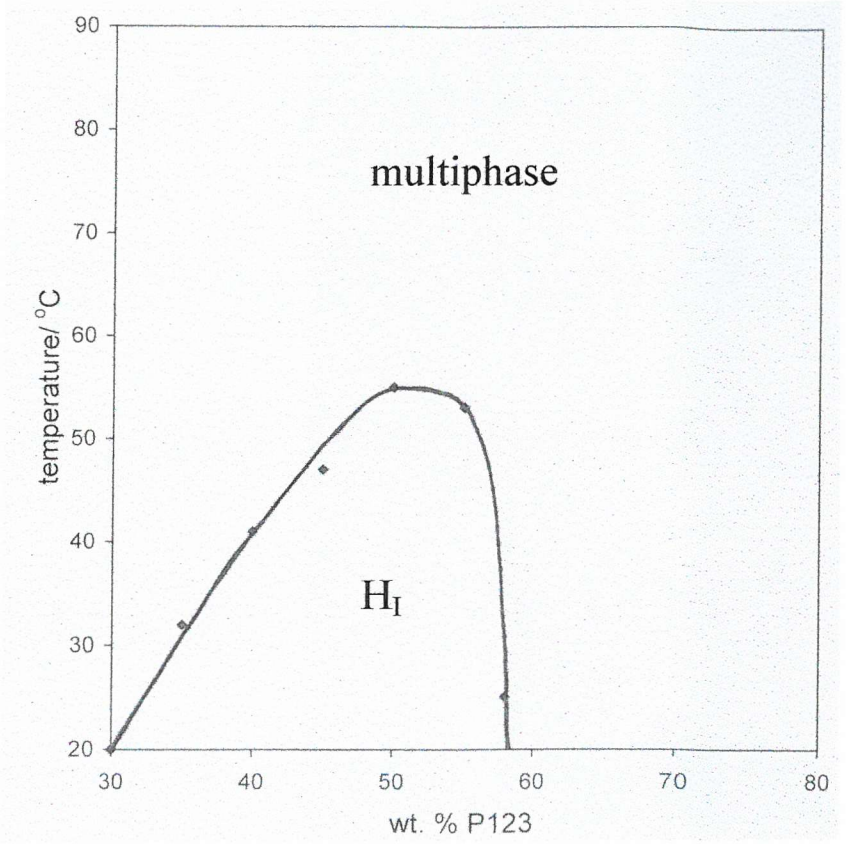

Figure 2.11 illustrates the phase behaviour of the Pluronic® P123/0.2 M nickel acetate deposition solution system that is dominated by a large H_I domain.

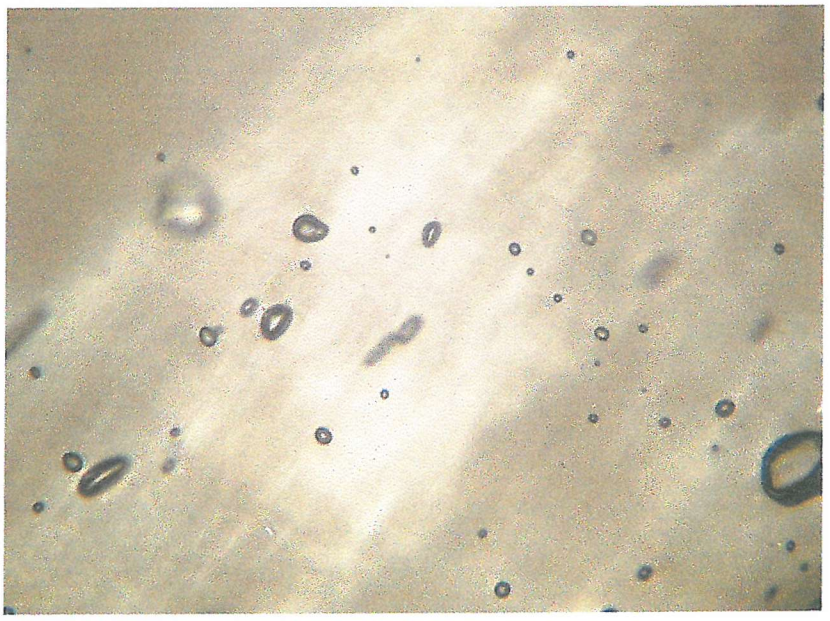

Figure 2.12 shows the birefringence pattern obtained from the H_I phase of the Pluronic® P123 H_I nickel deposition template.

Figure 2.12 shows a cross-polarising optical micrograph of the H_I liquid crystalline phase of the P123 template system. The contrast between light and dark areas of the micrograph is not as high as is in micrographs of the Brij® 56 H_I phase, making identification of phase transitions in the Pluronic® system more difficult. The presence of irregularly shaped air bubbles as observed in Brij® mixtures is obvious however, making assignment of the H_I phase possible. At temperatures above 54 °C in the 50 wt. % P123 electrolyte, the H_I phase transforms into a mixture which appears to be biphasic in nature as illustrated in Figure 2.13. On first appearance there appears to be no optical texture with the exception of the light areas at the air bubble

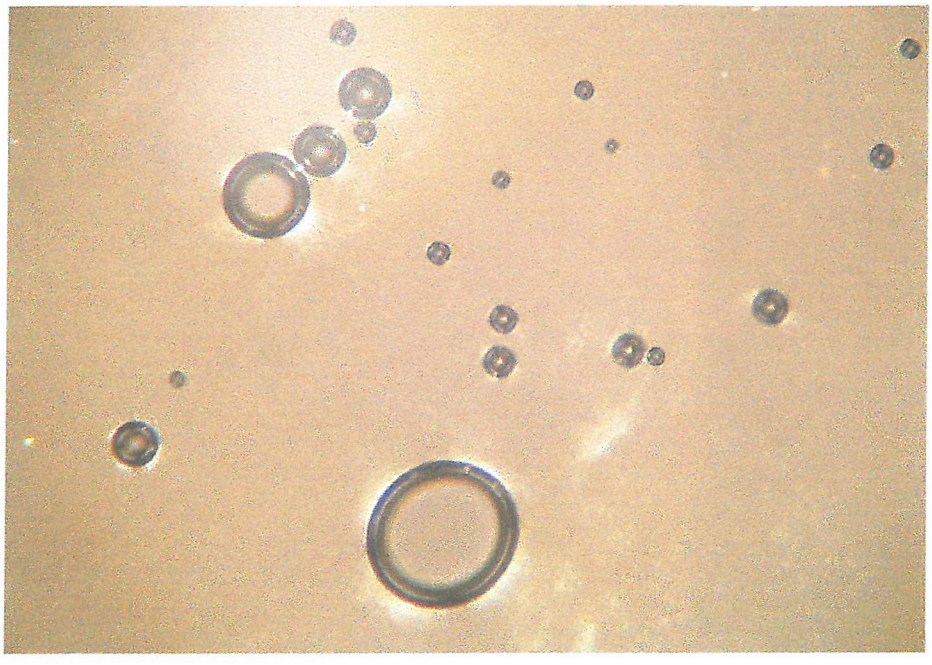

Figure 2.13. Optical microscopy reveals the complicated birefringence pattern of the P123 template's biphasic morphology.

edges. This textural patterning and the presence of double walled air bubbles is characteristic of the H_I/I_I biphasic regions seen in Brij® 56 based mixtures. On application of a mechanical force to the mixture by pressing the sample however, faint streaks momentarily appear indicative of an L_α phase. The round shape of the air bubbles is also further evidence of the L_α phase. Literature accounts of this anomalous phase in Pluronic® mixtures are numerous and it is usually referred to as a

multiphase.[5] As a result of these observations, the phase of this mixture cannot be definitively assigned.

2.3.2 The Deposition Process

The solution used in the electrodeposition of nickel was a well established formulation consisting of 0.2 M nickel acetate, 0.5 M sodium acetate and 0.2 M boric acid. In this solution, sodium acetate functions both as a supporting electrolyte and buffer, while boric acid provides additional buffering against pH change. All deposition experiments were conducted potentiostatically at –0.9 V *vs.* SCE.

2.3.2.1 Deposition from the Non-Templating Electrolyte

A cyclic voltammogram of the deposition of metallic nickel on a gold surface by electroreduction of the Ni(II) acetate solution is presented in Figure 2.14. On the negative going sweep currents are negligible until the onset on nickel deposition at ~-0.8 V *vs.* SCE. Thereafter, the cathodic current is seen to increase rapidly as the nucleation of nickel clusters on the electrode surface proceeds with concurrent

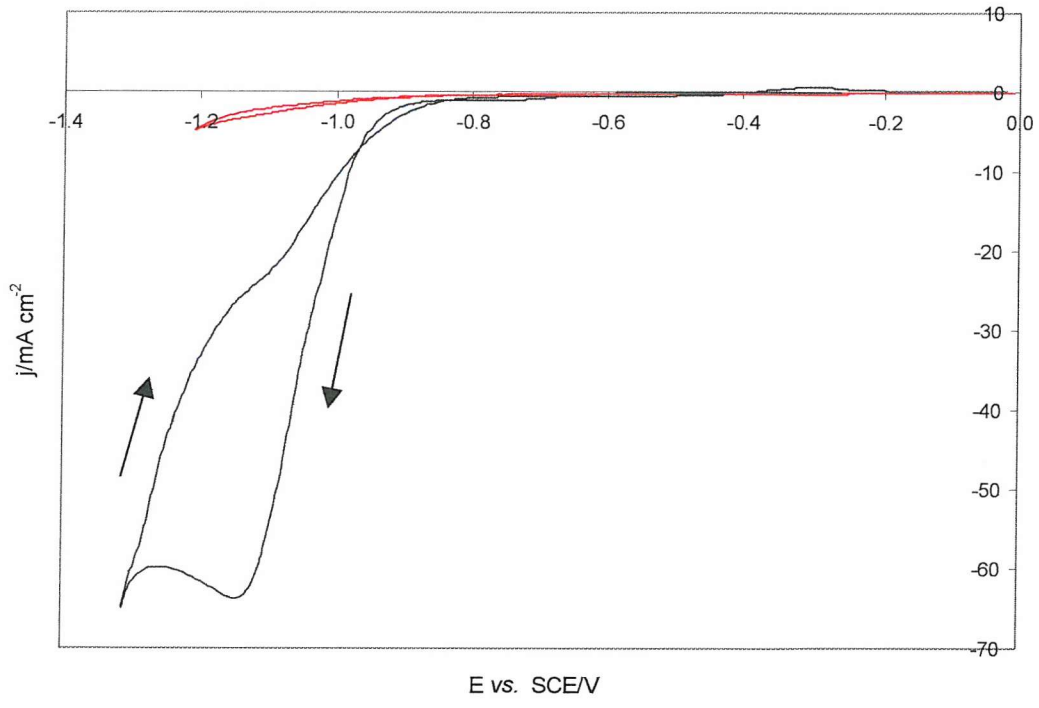

Figure 2.14 shows the first scan of the cyclic voltammetry of nickel metal deposition in a 0.2 M $Ni(ac)_2$ based deposition solution (blue) in addition to cyclic voltammetry of the 0.2 M $Ni(ac)_2$-free solution (red) on a 200 μm gold disc at 50 mV s^{-1}.

growth of existing cluster sites. Mass transport limitation occurs at ~-1.12 V as indicated by the decrease and subsequent plateau of the cathodic current. At lower potentials the hydrogen evolution reaction (HER) current becomes more significant and imposes its magnitude on the now diffusion limited electroreduction of Ni(II). On reversal of the potential sweep, the cathodic current decreases as the rate of nucleation and growth of nickel clusters slows. The scan completes a small nucleation loop at low deposition overpotentials indicating a faster rate of nickel deposition on the positive going sweep. This is expected here since there is no requirement for a nucleation threshold potential on the reverse sweep and there are more nickel clusters on which deposition can occur. A small anodic peak between –0.2 V and –0.4 V completes the scan. This oxidation current corresponds to the conversion of some of the deposited nickel atoms to the passivating $Ni(OH)_2$. This is expected, since at the solution pH of 6.73, $Ni(OH)_2$ formation is favoured as an anodic process over the dissolution of nickel metal to Ni(II) species which occurs at lower pHs. Furthermore, anodic processes involving nickel dissolution would be expected to produce significantly larger currents than those observed and at potentials in the vicinity of -0.8 V.[6] Included in Figure 2.14 is the cyclic voltammetry of a 0.5 M sodium acetate, 0.2 M H_3BO_3 solution on a gold electrode surface, that is, the nickel deposition solution without 0.2 M nickel acetate. Examination of the voltammogram does not reveal any significant electrochemical activity (such as that derived from the reaction of solution ions) until onset of hydrogen evolution at ~-0.8 V. From Figure 2.14 it can be seen that the use of the boric acid buffer is justified since the potential range in which the electroreduction of Ni(II) occurs is superimposed on the hydroxyl ion generating HER potential region. It must be noted here that the magnitude of the hydrogen evolution currents in the Ni(II) free solution of Figure 2.14 cannot be used as an accurate indication of the magnitude of these currents in the nickel deposition solution. Immediately after the nucleation of nickel deposits on the gold electrode surface in the first cycle, the electrode surface becomes a nickel-gold composite. Since nickel catalyses the reduction of water more efficiently than does gold, it would be expected that the extent of hydrogen evolution in the nickel deposition solution of Figure 2.14 would be greater than that indicated by the Ni(II) free solution. Nevertheless, anodic stripping voltammetry experiments detailed in Section 5.3.3.1 have shown that the nickel deposition efficiency at –0.9 V *vs.* SCE is 90 % in the

nickel deposition solution, indicating that at this relatively low deposition potential the reduction of water does not contribute significantly to the cathodic current.

The potential step deposition of nickel from the acetate solution was investigated with a deposition potential of –0.9 V *vs.* SCE. As illustrated in the potential step transient of Figure 2.15, application of the cathodic deposition potential immediately results in double layer charging of the gold electrode as manifest by the current spike of almost 12 mA cm^{-2} in the initial time interval. The current then decreases rapidly as the double layer is fully charged and in response to the decrease in Ni(II) concentration close to the electrode surface which is in turn a consequence of nickel cluster nucleation and subsequent growth. The system achieves a steady state current density of 1.84 mA cm^{-2} after approximately 70 s, indicating control of the deposition reaction by kinetic rather than mass transport processes.

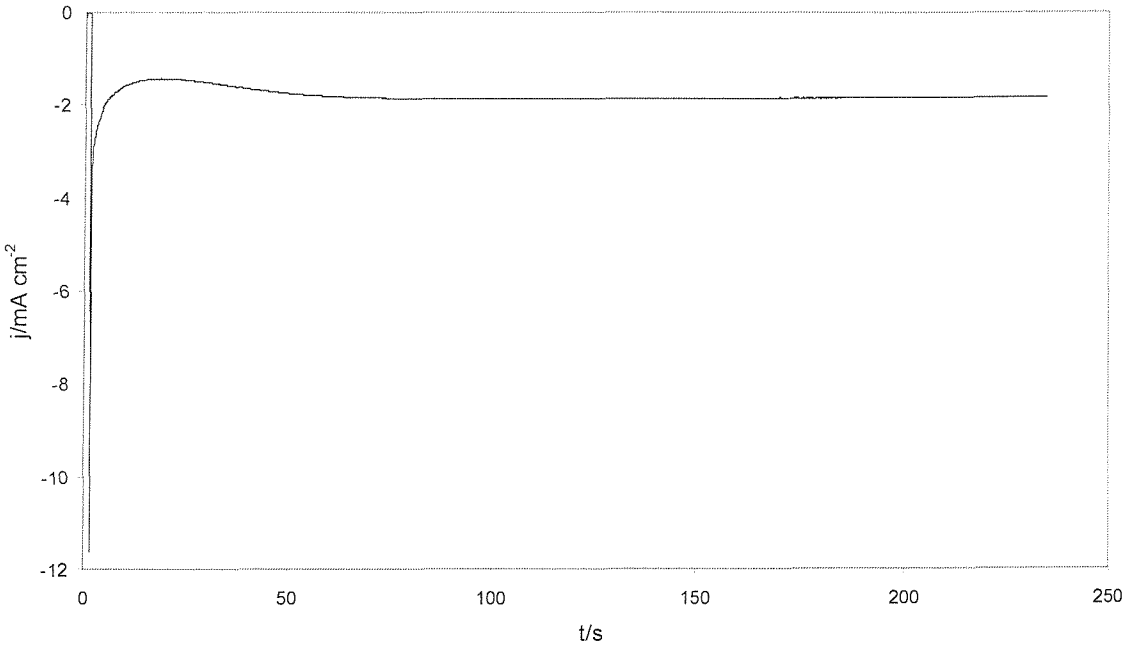

Figure 2.15 shows the potential step deposition transient for nickel deposition carried out at –0.9 V *vs.* SCE using a 200 μm gold disc working electrode in a non-templating 0.2 M $Ni(ac)_2$ based deposition solution.

The steady state current density in the kinetically controlled process of Figure 2.15 allows a rate constant k, of 4.8×10^{-5} cm s^{-1} for the reduction of Ni(II) to be calculated using Equation 1,

$$j = -nFkc_o \qquad (1)$$

where c_o is the concentration of Ni(II) species in moles cm^{-3}. It must be noted however that since hydrogen evolution also makes a small contribution to the kinetically controlled current density of Figure 2.15, this rate constant is a composite of the two processes.

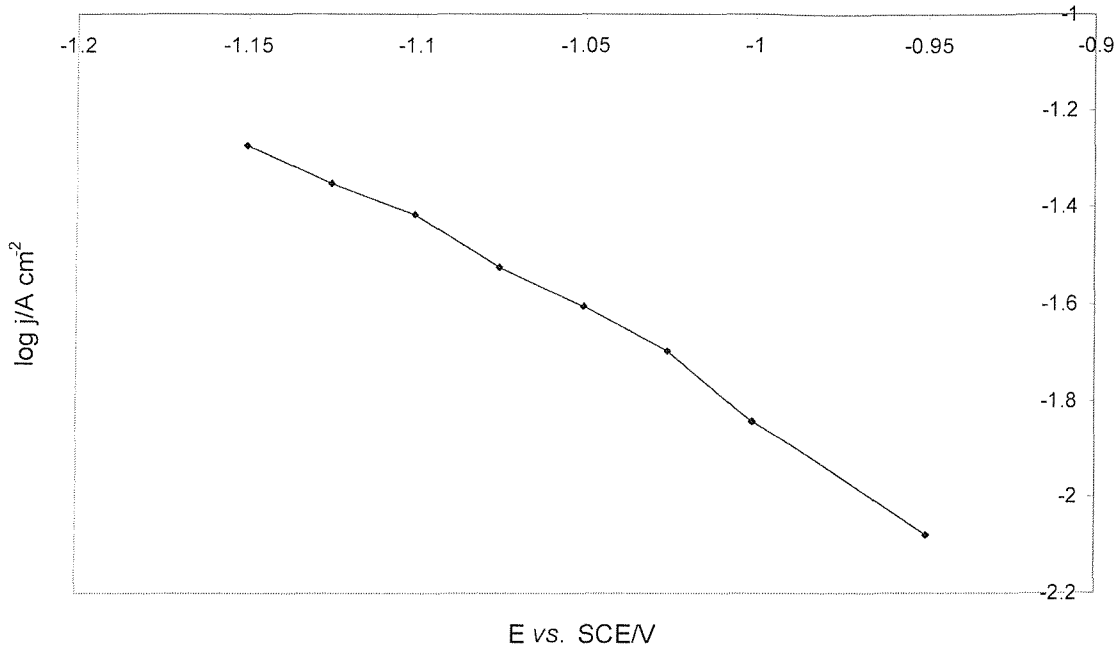

Figure 2.16 shows the log current density *vs.* deposition potential plot for the reduction of the $Ni(ac)_2$ deposition solution in the absence of templating species at 25 °C. Currents are steady state values obtained potentiostatically using a 25 μm gold disc microelectrode.

A plot of the logarithm of the deposition current density versus the deposition potential for the electrodeposition of nickel from the acetate solution is presented in Figure 2.16. The plot shows the magnitude of the deposition current to be increasing exponentially with increasing magnitude of the potential up to approximately –1.25 V *vs.* SCE, indicating a kinetically controlled cathodic process in this region. This confirms that the steady state behaviour observed in the -0.9 V *vs.* SCE potential step of Figure 2.15 is indeed kinetically controlled and not a diffusion controlled process in which the current density versus $t^{1/2}$ relationship is not observable at short times. Figure 2.16 reveals a slope of approximately 200 mV/decade. This value is somewhat

higher than those observed in nickel deposition baths incorporating sulphate or chloride rather than acetate ions, which vary between 70 to 130 mV/decade depending on bath composition and substrate.[7] In addition, examination of the current densities in Figure 2.16 reveals that these are somewhat lower than those observed using other plating bath compositions with 0.2 M $Ni^{2+}_{(aq)}$. These results suggest slower deposition kinetics and a higher activation barrier for nickel deposition. This is probably due to the effects imparted by anionic species present in the deposition solution. As discussed in Section 1.5, boric acid acts as a surfactant adsorbing on the surface of the electrode. This adsorption may block sites for nickel deposition or form an adlayer through which Ni(II) species must move before being reduced. Both of these processes would retard the rate of nickel electrodeposition and the latter could have effects on the cathodic slope of Figure 2.16. Unlike the anions of other common nickel deposition solutions such as chloride or sulphate ions, the acetate anion forms a complex with Ni(II) ions in aqueous solution with the composition $Ni(CH_3COO)_2$.[8] Boric acid derived borate ions also form complexes with Ni(II) ions as discussed in Section 1.5. As a consequence of this solution chelating effect, reduction of Ni(II) species to nickel metal does not occur by a simple direct two electron transfer as in other plating solutions, but involves a chemical step prior to the electrochemical reduction step.[9] This step involves the breakdown of the Ni(II) complex and thus introduces additional kinetic limitations on the deposition process as evidenced by the slow rates of nickel electrodeposition and the large slope of Figure 2.16.

At potentials lower than –1.025 V in Figure 2.16 the plot deviates from linearity as the reaction behaviour enters a mixed kinetic-mass transport control regime.

2.3.2.2 Deposition from Surfactant Template Electrolytes

A cyclic voltammogram of the electrochemical reduction of nickel ions to metallic nickel within the aqueous domains of a Brij® 56 based H_I template is presented in Figure 2.17. The superimposed voltammogram is that of a Brij® 56 based H_I template containing both 0.5 M sodium acetate and 0.2 M H_3BO_3, that is, the voltammetry of the Brij® 56/Ni(II) template in the absence of nickel acetate. This voltammogram reveals that the electrochemical activity observed in Figure 2.17 is due only to the redox activity of nickel containing species, with the exception of a small contribution from hydrogen evolution at lower potentials. Figure 2.17 is the second scan in a series and is representative of subsequent scans, however does not show the nucleation of

nickel clusters on the gold electrode surface only observable in the initial sweep. In the negative going sweep significant nickel deposition is observed to commence at ~-0.85 V *vs.* SCE, rapidly increasing in magnitude thereafter until the onset of

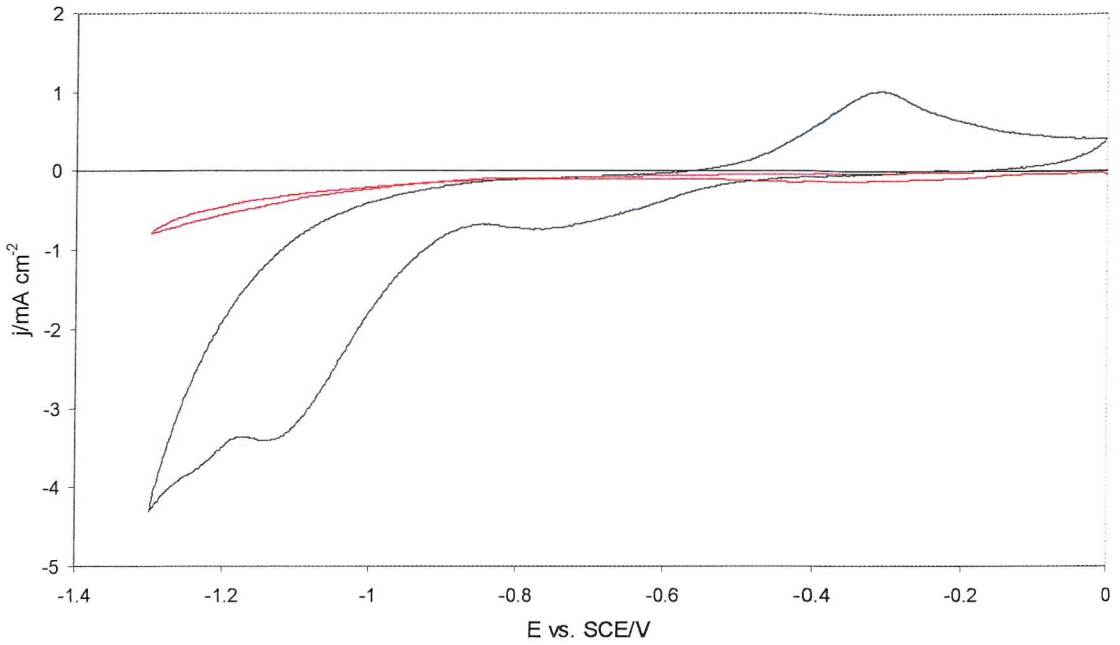

Figure 2.17 compares the second scan of the voltammetry of the Brij® 56 templating electrolyte with (blue) and without (red) Ni(II) ions on a 200 μm gold disc at 50 mV s^{-1} and 25 °C.

diffusion limitation at ~-1.1 V indicated by the decrease and brief plateau in cathodic current. The cathodic current subsequently increases prior to the reversal of the sweep as hydrogen evolution becomes significant at more reducing potentials.

On the positive going sweep the surface of the electrodeposited nickel is seen to oxidise to $Ni(OH)_2$ at potentials above –0.55 V as indicated by the anodic peak. This oxidative current is not thought to be due to nickel dissolution since the pH of the templating electrolyte is 7.03, making $Ni(OH)_2$ the preferred Ni(II) species according to the Pourbaix diagram that is Figure 1.18. Furthermore, as in the case of the non-templating electrolyte discussed in Section 2.3.2.1, this peak is observed at potentials some 0.4 V higher than that expected for nickel dissolution. The magnitude of the $Ni(OH)_2$ formation peak in the templating electrolyte relative to the nickel deposition current is significantly greater than that observed in the non-templating electrolyte. Since $Ni(OH)_2$ formation may be considered a surface process, this indicates a

significantly greater surface area to volume ratio in the templated nickel. The subsequent reduction of $Ni(OH)_2$ is observed at higher potentials of the negative going sweep as indicated by the cathodic peak centred at ~-0.75 V. Comparison of the relative peak areas reveals that the magnitude of the charge associated with this peak is seen to be approximately equal to the charge associated with the formation of $Ni(OH)_2$.

Comparison of Figures 2.17 and 2.14 reveals a significantly lower nickel deposition limiting current in the templating electrolyte as compared with the surfactant free solution. The reduced rate and limiting current of nickel deposition from the templating electrolyte is probably due to slower diffusion kinetics of Ni(II) species within the confined aqueous domain structure of the viscous liquid crystal, as compared with the more rapid diffusion rates observed in bulk aqueous solution. The slow deposition rates observed may also be due to blocking of the electrode surface by the surfactant species and solution chelating of the Ni(II) reactant species by surfactant moieties.

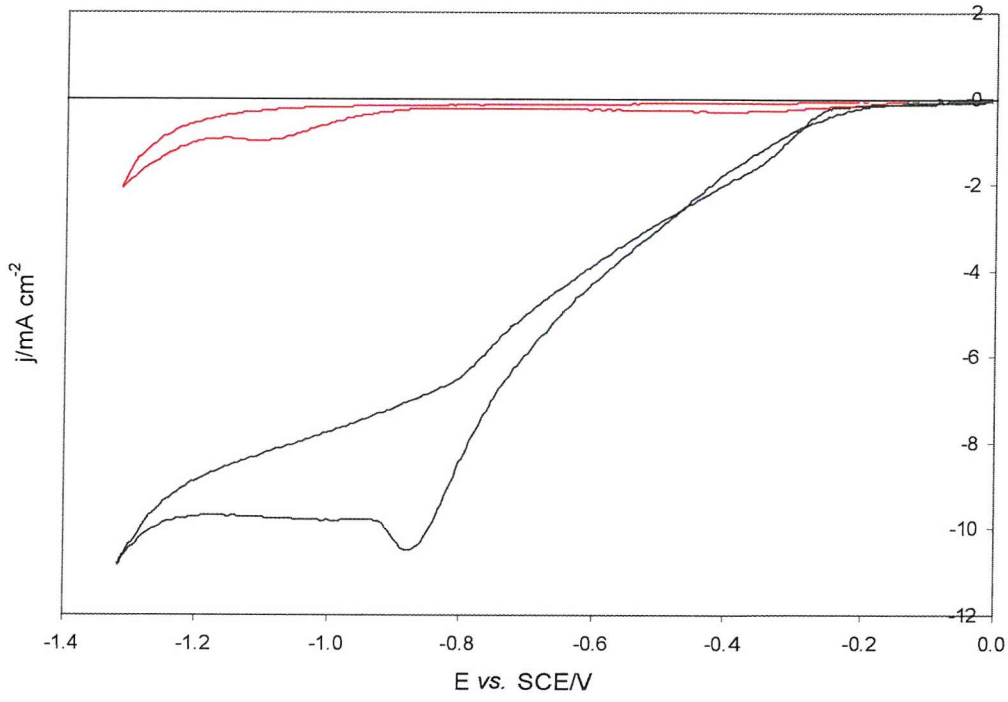

Figure 2.18 compares the cyclic voltammetry of a 50 wt. % Pluronic® P123/$Ni(ac)_2$ deposition solution (second scan, in blue) with that of the background solution (red) at 50 mV s^{-1} and 25 °C.

Cyclic voltammetry characterising the deposition of nickel metal from a 50 wt. % Pluronic® P123 H_I template is presented in Figure 2.18. The deposition behaviour has both similarities and differences with that of the Brij® 56 based electrolyte. In Figure 2.18, which like Figure 2.17 is also the second scan, there is no indication of the anodic currents associated with $Ni(OH)_2$ formation or nickel dissolution. Indeed, since the pH of the P123 templating electrolyte is 6.60 we could expect either of these processes to occur. The absence of anodic currents however, leads to the conclusion that either these processes are prevented from occurring, or that these anodic processes are occurring albeit concurrently with a cathodic process such that there is a net cathodic current. The former explanation is suggestive of some kind of interaction between the surfactant and the nickel surface such that the metal is protected from oxidation. The latter explanation suggests that there is an electroactive species in the templating electrolyte that is able to undergo electroreduction at potentials above that

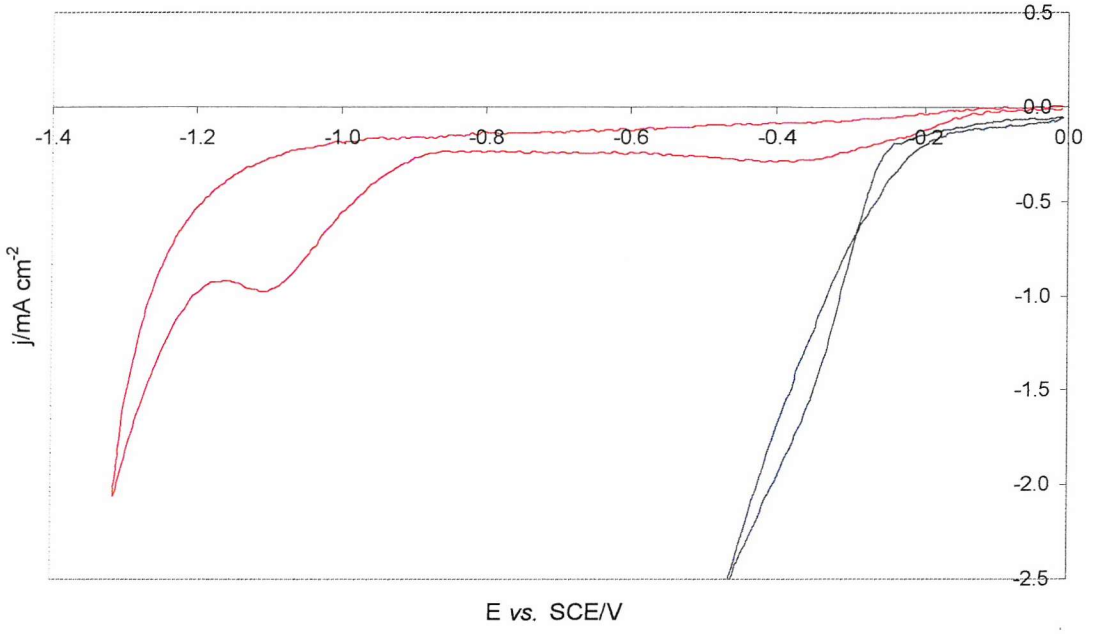

Figure 2.19 shows electrochemical activity occurring at the lower current densities of Figure 2.18.

required for nickel electrodeposition (~-0.6 V *vs.* SCE). This hypothesis is supported by Figures 2.18 and 2.19 which indicate the operation of a cathodic process at potentials below –0.2 V. The rate of this reduction on the gold electrode surface is relatively slow in the nickel(II)-free solution (indicated by the red line) with the magnitude of the current density not greater than 0.5 mA cm^{-2} at higher potentials.

The magnitude of the current density is significantly higher in the nickel deposition template however. This difference in the rate of the cathodic process at potentials above that of the E_0 for nickel(II) reduction is possibly due the fact that the reduction of the electroactive species occurs more rapidly on a nickel electrode surface (after the first scan the electrode surface consists of electrodeposited nickel metal) than on gold. Another possibility is that nickel(II) species in the deposition solution chemically oxidise species in the surfactant solution (with reduction of the nickel(II) to nickel metal as in the 'polyol' process) to produce a product which is easily electroreduced on the nickel cathode surface. Both of these explanations are feasible due to the relative impurity of Pluronic® surfactant materials which are characterised by broad molecular mass distributions and contain not only triblock copolymer surfactant but side-products of their syntheses.

The other noticeable difference in the voltammetry of the Brij® 56 and P123 templates is the much larger limiting current density of deposition in the P123 system as compared with the former system. The higher diffusion limited current is probably due to the larger aqueous channels of the P123 H_I phase as compared with the H_I phase of Brij® 56 and the resulting increased rate of flux of nickel(II) to the cathode surface.

The differences between the Brij® 56 and Pluronic® P123 deposition electrolytes are further illustrated when comparing the steady state behaviour of these two systems. Figure 2.20 shows a potential step transient of Ni(II) reduction in the H_I phase of a 65 wt. % Brij® 56 template on a 1 mm gold disc electrode. The potential step deposition was carried out at –0.9 V *vs.* SCE. Examination of Figure 2.20 shows current density decreasing with time, indicative of a diffusion limited or mixed kinetic/mass transport limited process. The initial current density decays rapidly, first as the double layer becomes fully charged, then as the concentration of Ni(II) at or close to the electrode surface decreases. Equation 2 describes the variation in deposition current density with time either in a mixed kinetic/mass transport limited regime, or more broadly, in a diffusion limited regime in which a significant resistive component exists (that is, a charge transfer resistance or possibly an electrolyte resistance in this case). Adherence of the deposition transient data of Figure 2.20 to the behaviour described by Equation 2,

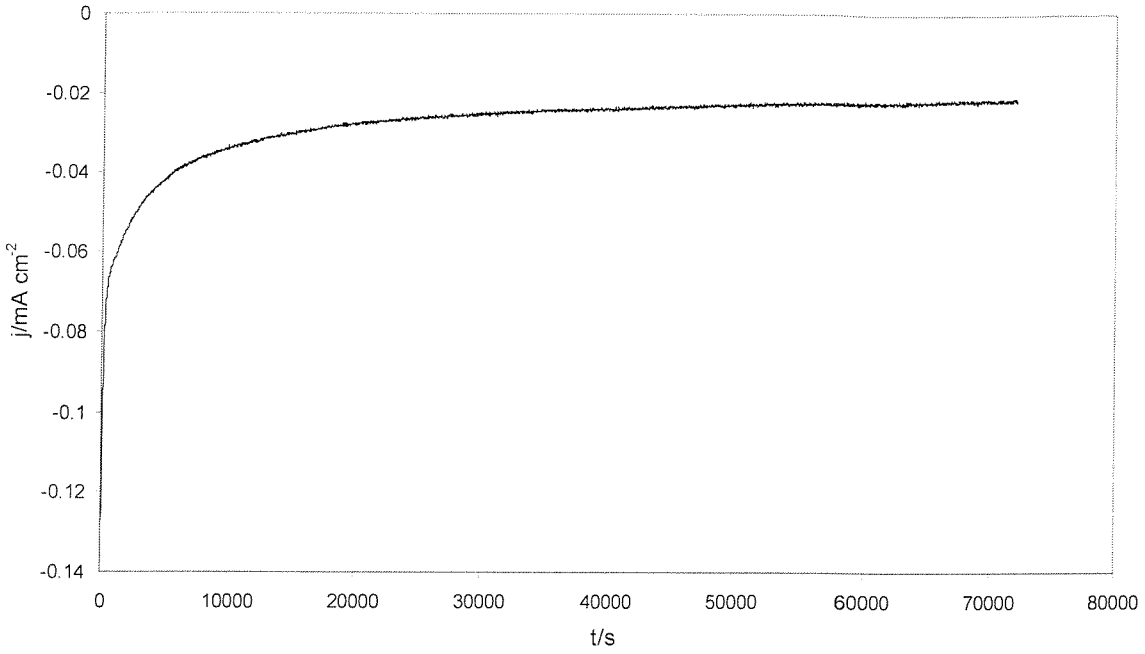

Figure 2.20 shows the electrodeposition of mesoporous nickel from the H_I phase of a 65 wt. % Brij® 56 based templating electrolyte at –0.9 V *vs.* SCE and 25 ° with 2.0 C cm^{-2} deposition charge.

$$j = -nFkc_o^{\infty} \exp\frac{k^2 t}{D} erfc\frac{kt^{1/2}}{D^{1/2}} \qquad (2)$$

where k is the rate constant for Ni (II) reduction (in cm s^{-1}), c_o^{∞} is the bulk concentration of Ni (II) (in moles cm^{-3}) and D is the diffusion coefficient of Ni (II) species in the Brij® 56 H_I template is evidenced in Figure 2.21. Figure 2.21 was obtained by successive simultaneous iteration of the values of D and k until the data of Figure 2.20 produced a suitably straight line plot using Equation 2. The value of the diffusion coefficient obtained using this method was 1.2×10^{-8} cm^2 s^{-1}. This value is significantly lower than the value of 10^{-5} cm^2 s^{-1} expected for the diffusion of ions in an aqueous, surfactant free solution but is significantly higher than the value of 10^{-11} cm^2 s^{-1} typical of solid state ionic diffusion. As the name suggests, the liquid crystalline electrolyte is essentially a high viscosity liquid with the mechanical and rheological properties of a liquid/crystalline solid hybrid. It is not surprising then that

the value of the diffusion coefficient obtained here is between that of ions in aqueous solution and solid state media. The relative positioning of the diffusion coefficient for the liquid crystal system between these extremes is unexpected however. Considering that the aqueous domain occupies 77 % of the volume (see Appendix 1) in a 65 wt. % Brij® 56 H_I structure (and therefore only 77% of the volume is available to support Ni (II) diffusion), it might be reasonable to expect a decrease in the value of the diffusion

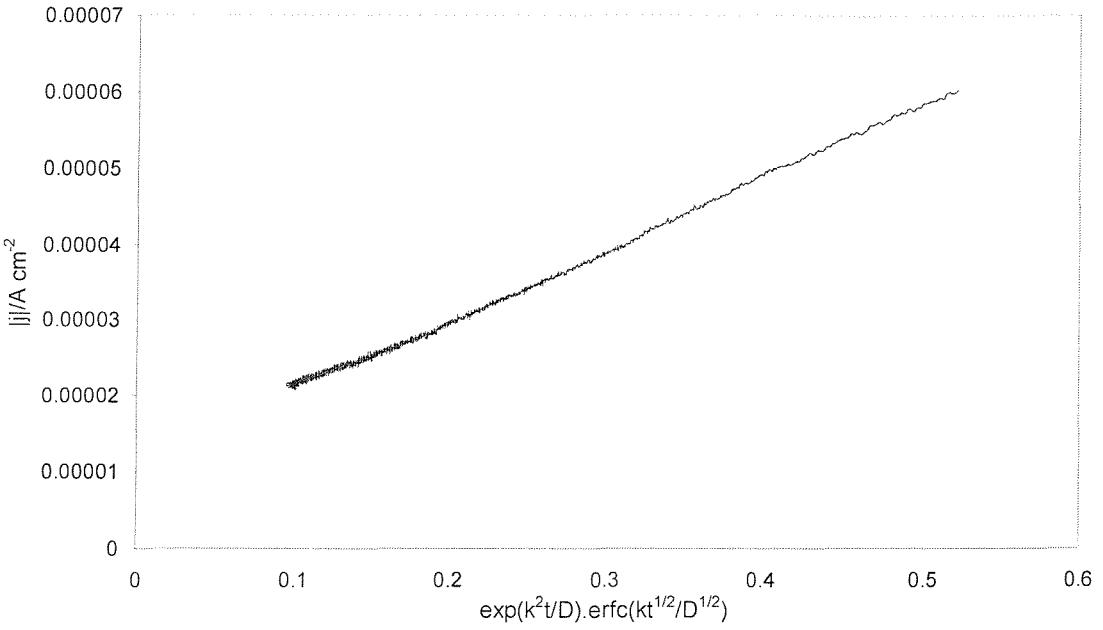

Figure 2.21. An error function analysis provides evidence for operation of a mixed kinetic/mass transport rate limitation in the data of Figure 2.20 using the Equation 2 operator.

coefficient of similar magnitude. The observed decrease in D of 10^3 times certainly cannot be justified using this argument. There are a number of possible explanations for this discrepancy. It is likely that in moving through the H_I structure Ni (II) species undergo numerous collisions with the surfactant rods and in doing so lose kinetic energy resulting in a decreased rate of diffusion. Attractive electrostatic interactions between the positively charged Ni (II) species and the polyether head groups of the surfactant may also contribute to a reduction of the velocity of Ni (II) species moving through the structure. Finally, it possible that in moving to the electrode surface to undergo reduction, Ni (II) species must tunnel through an adsorbed layer of surfactant on the electrode surface.

The value of the intercept in Figure 2.21 was found to be -1.2×10^{-5} A cm^{-2}. Equation 2 however, suggests that this value should be zero. This discrepancy is rationalised in knowing that during the potential step experiment there is a contribution to the current density from the reduction of the solvent. The value of this H_2 evolution current density is -1.2×10^{-5} A cm^{-2} and is not diffusion limited, therefore remaining constant throughout the experiment and not affecting the value of the slope. Equation 3 also permits the determination of the rate constant for the reduction of Ni (II) species within the Brij® 56 templating electrolyte. This has a value of 2.3×10^{-6} cm s^{-1} and is considerably lower than the value of 4.8×10^{-5} cm s^{-1} calculated from Figure 2.14 for the reduction of Ni (II) in a surfactant free electrolyte. As indicated above in the comparison of the cyclic voltammetry of these two systems, the faster rate of kinetics in the surfactant free deposition may be due to a number of factors including variation in pH, variation of overpotential (as a result of variation in E_0) or the involvement of the surfactant in a solution chelating or electrode blocking phenomenon.

The potential step transient of the reduction of Ni (II) within the aqueous domain of a 50 wt. % H_I Pluronic® P123 liquid crystalline template is presented in Figure 2.22. The chronoamperometric behaviour is markedly different from that of the mixed mass

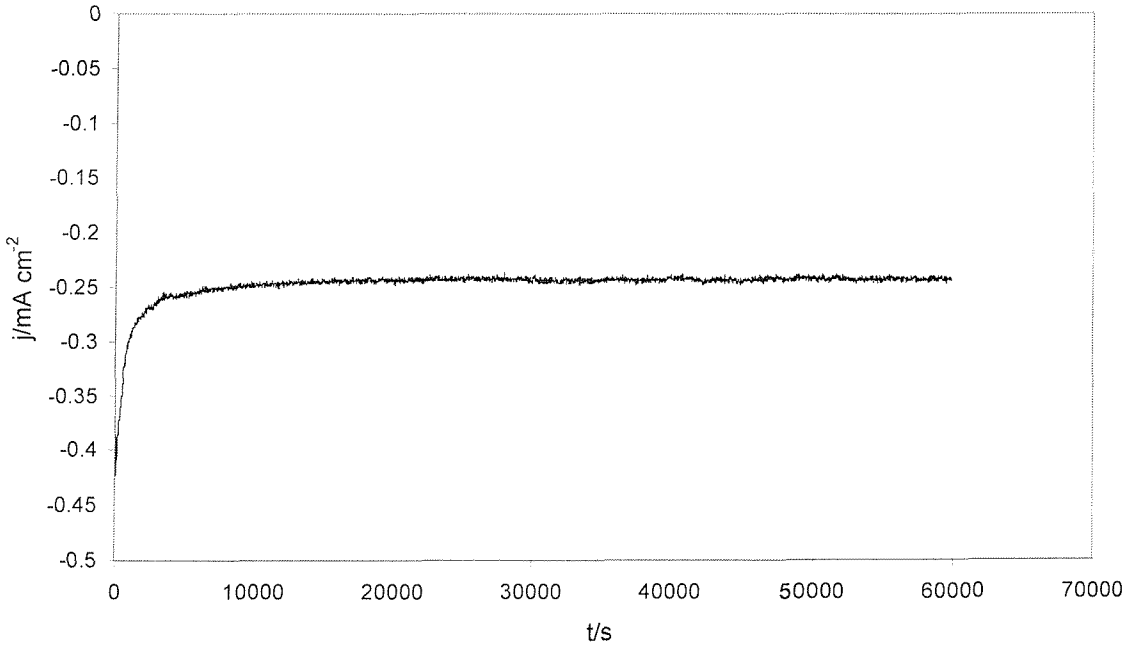

Figure 2.22 shows the kinetically controlled potential step transient for the deposition of mesoporous nickel at –0.9 V *vs.* SCE from the H_I phase of the Pluronic® P123 based deposition template at 25 °C with a deposition charge of 16.0 C cm^{-2}.

transport/kinetically limited behaviour observed within the Brij® 56 electrolyte of Figure 2.20, with a kinetically controlled current density reaching a constant value of 240 μA cm^{-2}. Using Equation 2, a value of the rate constant for the reduction of Ni(II) species of 6.2×10^{-6} cm s^{-1} is obtained. This value is between that measured in the Brij® 56 and surfactant free deposition systems discussed above, reflecting the difference in pH, extent of hydrogen evolution and surfactant-electrode and surfactant-Ni(II) interactions.

2.3.3 Structural Characterisation

2.3.3.1 Transmission Electron Microscopy

The porosity of liquid crystal templated nickel was investigated using TEM. Figure 2.23 shows the mesostructure of nickel templated from the H_I phase of a Brij® 56 liquid crystal template. Interaction of the TEM electron beam with matter is represented by lighter areas of the micrograph. The lightest area at the bottom of Figure 2.23 indicates a section of the sample too thick for sufficient transmission of

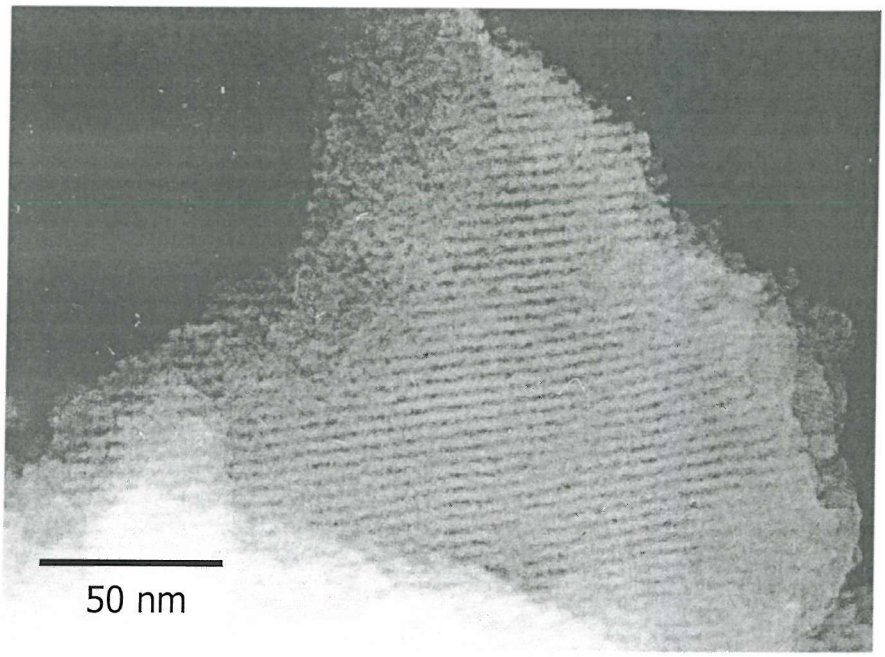

Figure 2.23. This TEM image gives a lateral view of the H_I mesopore morphology deposited from the H_I phase of a Brij® 56 based templating electrolyte at –0.9 V *vs.* SCE and 25 °C.

the electron beam flux, resulting in a signal of insufficient strength for formation of a well resolved image. Darker areas of the micrograph contain either no sample or more importantly, indicate lower density (porosity) in the material bulk.

The parallel lines running across the image show the projection of a two-dimensional pore network composed of channels of uniform diameter running laterally through the sample, although there is no direct evidence of an hexagonal mesostructure. Indeed, the image could be construed as showing lamellar structure. This is considered to be highly unlikely however, since the formation of the lamellar phase of the template

requires higher concentrations of surfactant and significantly higher temperatures, as indicated in the phase diagram of Figure 2.23. In this case, direct observation of the H_I pattern of channels "end-on" was not possible because of imaging difficulties derived from the ferromagnetism of nickel.

However, the TEM image is consistent with previous observations of hexagonally oriented channels in other H_I materials prepared by electrodeposition, in which the images of neighbouring pores were superimposed if the pores were not exactly parallel to the beam axis.[10] This concept is illustrated schematically in Figure 2.24. In the extreme case in which particles are oriented such that the beam is aligned 90 ° to the pore axis, the same pattern as that observed in Figure 2.23 may be expected.

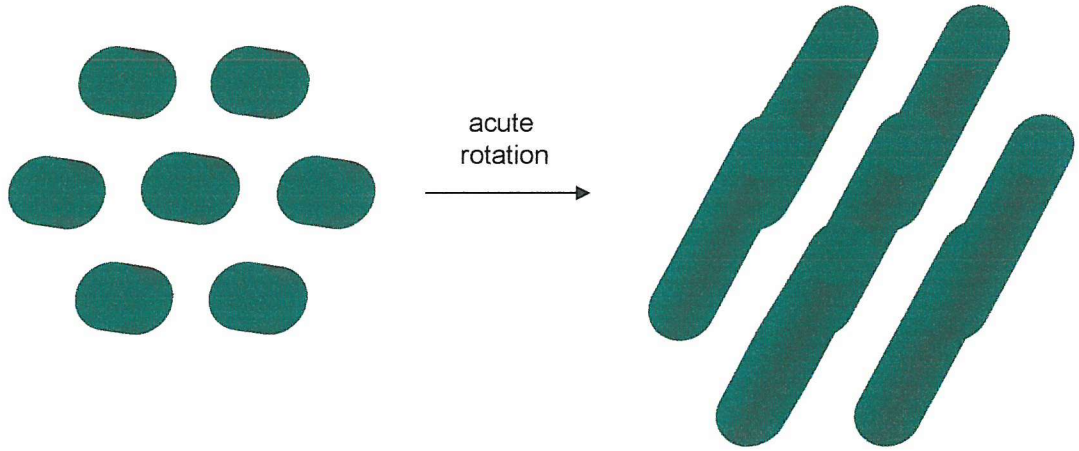

Figure 2.24 shows that overlapping induced by rotation of an axially oriented H_I structure produces an image like that of an axially viewed L_α structure.

Figure 2.23 reveals a centre-to-centre pore spacing of 5.2 nm ± 1.0 nm and wall thickness is seen to be approximately equal to pore diameter. Pore diameter may therefore be estimated at approximately 2.6 ± 0.5 nm. Figure 2.23 also shows pore walls that are not entirely flat, however quantification of this roughness is not possible with the resolution obtained. The mesoporosity of the nickel structures produced from the Brij® 56 surfactant is well ordered and channels have long range continuity. There are no visible necks or blockages in the channels which might retard mass transport within the pores and limit the electrochemically accessible surface area.

Attempts to image mesoporous nickel templated from the H_I phase of Pluronic® P123 were not successful due to the ferromagnetism of the material. Sample particles interacting with the electron beam vibrated vigorously and were frequently ejected from the Cu grid by this force.

2.3.3.2 Small Angle X-ray Scattering (SAXS)

Small angle x-ray scattering results from Brij® 56 templated nickel support the TEM data of Figure 2.23. Figure 2.25 shows a typical SAXS pattern for mesostructured nickel using the H_I mesophase of Brij® 56 as the structure-directing agent. The strong, sharp peak indicates well-defined mesoscopic order with a *d* spacing of 7.0 nm ± 0.7 nm, corresponding to a pore to pore distance of 8.1 ± 0.8 nm and a pore diameter of

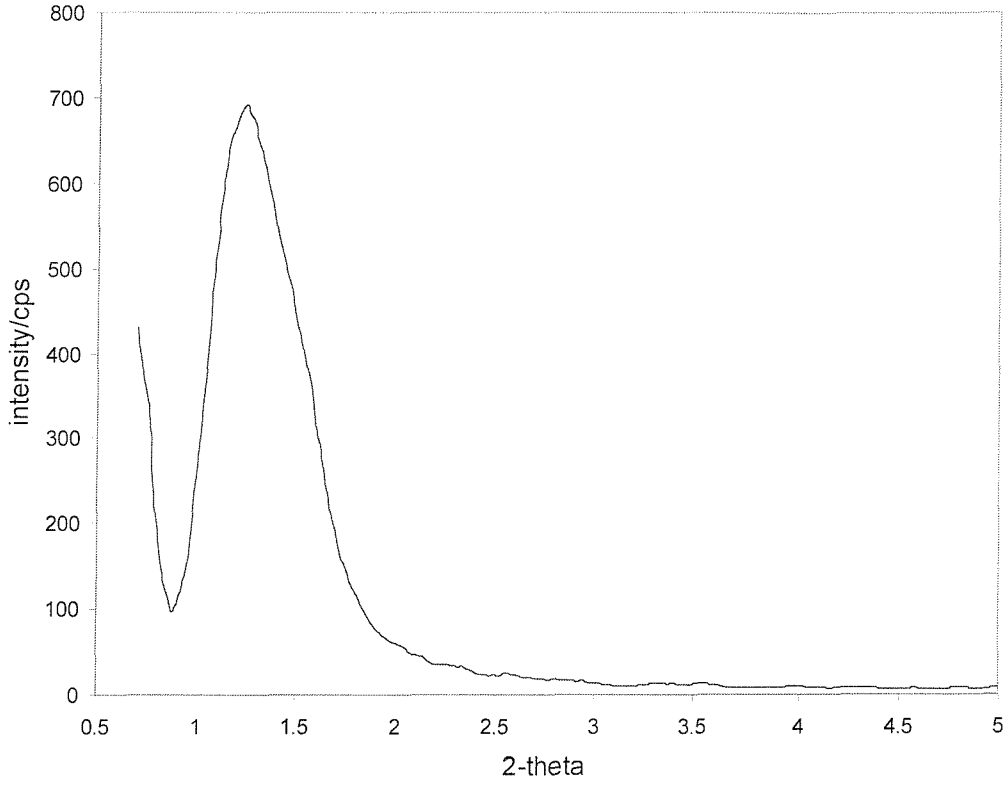

Figure 2.25. Small angle x-ray scattering analysis reveals a relatively intense reflection from mesoporous nickel deposited from the H_I phase of a 65 wt. % Brij® 56 based templating electrolyte at –0.9 V *vs.* SCE and 25 °C.

approximately 4.1 ± 0.4 nm. This value is larger than that determined by TEM, and is as yet unexplained but is in accordance with previous work on mesoporous cobalt.[10]

Nickel mesostructures templated from the H_I phase of a Brij® 78 liquid crystal showed similarly sharp SAXS patterns indicating well-developed mesostructural architecture. Figure 2.26 shows a typical SAXS pattern of nickel templated from the

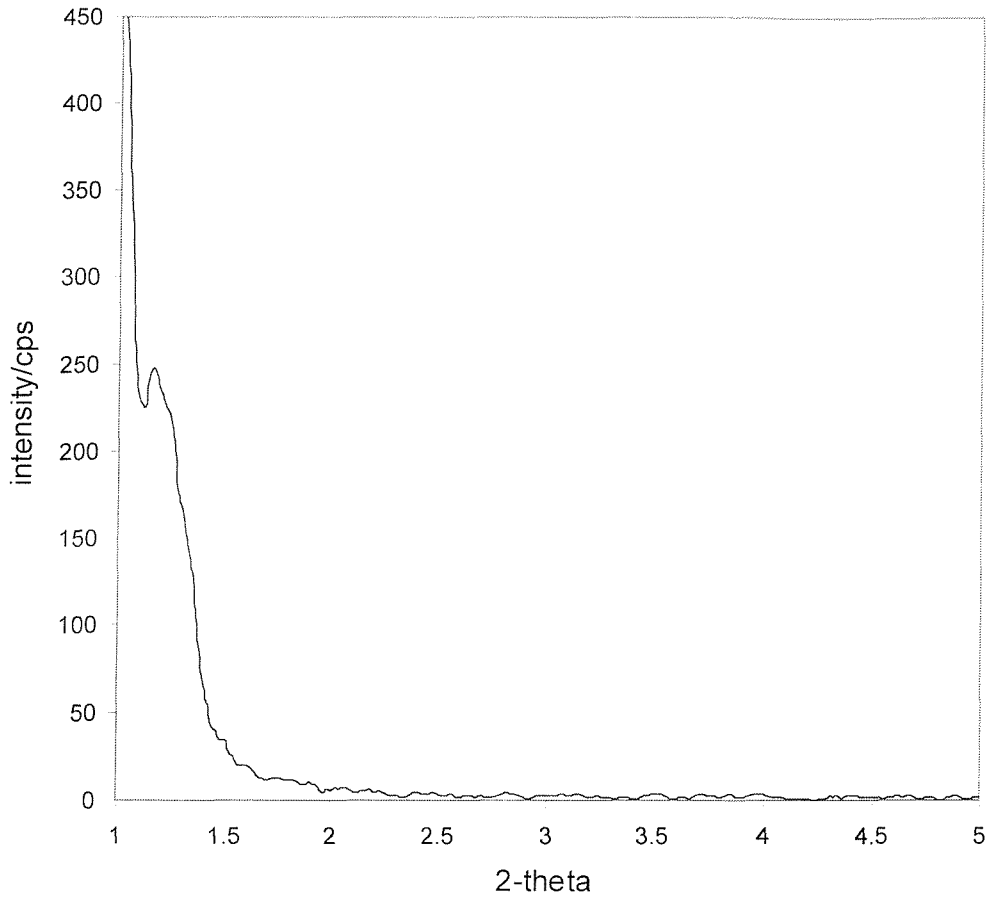

Figure 2.26. The small angle x-ray reflection peak of mesoporous nickel deposited from the H_I phase of a 65 wt. % Brij® 78 based templating electrolyte at –0.9 V *vs.* SCE and 25 °C appears at lower angles than that of Brij® 56 templated nickel. It is shown here partially superimposed on the background signal.

H_I mesophase Brij® 78. It reveals a *d* spacing of 7.7 ± 0.7 nm corresponding to a pore to pore separation of 8.9 ± 0.8 nm. As expected, the use of a surfactant molecule larger than Brij® 56 ($C_{18}[EO]_{\sim 20}$ as compared with $C_{16}[EO]_{\sim 10}$) causes an increase in the periodicity of the resulting mesostructure. The magnitude of the increase in the periodicity relative to the size of the template surfactants suggests that dimensional

changes in the structure are controlled by variation in the hydrocarbon tail size of the template surfactant more so than changes in head group size.

The lower intensity of scattering in Figure 2.26 as compared with that in Figure 2.25 is most likely due to decreased sample thickness in the former case such that a lower proportion of the interrogating x-rays are scattered to the detector. The higher background signal of Figure 2.26 is a typical result of sample surface roughness or imperfect alignment, both of which become problematic at very low angles.

SAXS measurements on mesoporous nickel templated from the H_I phase of a Pluronic® P123 based template showed strong scattering at low angles indicating the presence of a well ordered mesostructure. Figure 2.27 allows calculation of a *d* spacing of 14.7 ± 1.4 nm which corresponds to a pore to pore distance of 17.0 ± 1.6 nm, assuming the mesostructure has an H_I structure. Since the thickness of the pore

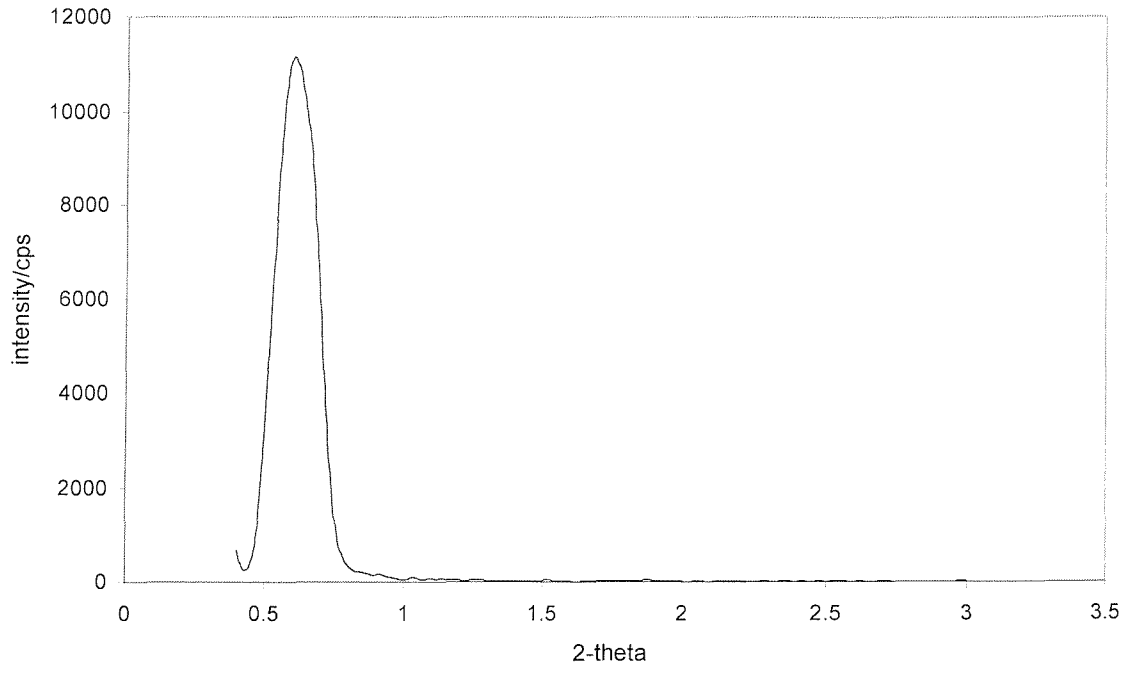

Figure 2.27 shows a particularly strong small angle reflection peak derived from x-ray scattering analysis of mesoporous nickel deposited from a 50 wt. % Pluronic® P123 based electrolyte at –0.9 V *vs.* SCE at 25 °C.

walls in Pluronic® P123 templated materials is known to be slightly greater than the pore diameter,[11] we expect a pore diameter of approximately 7-8 nm. It should be noted however that although the well ordered, periodic mesostructured material

confirmed by Figure 2.27 was deposited from the H_I phase of a Pluronic® liquid crystal, there is no direct evidence for this pore geometry as usually provided by TEM.

The scattering peak in Figure 2.27 is significantly stronger than that of the Brij® templated materials. This is quite likely due to the fact that the Pluronic® templated sample was significantly thicker than the Brij® templated samples as a result of faster deposition of the former material.

Figure 2.28 shows the small angle x-ray scattering of mesoporous nickel deposited from the V_I phase of a 65 wt. % Brij® 56 template at 35 °C. The diffractogram clearly shows a more complicated scattering behaviour than depicted in Figure 2.25 for the H_I mesopore geometry. This increased complexity is derived from the three-dimensionality

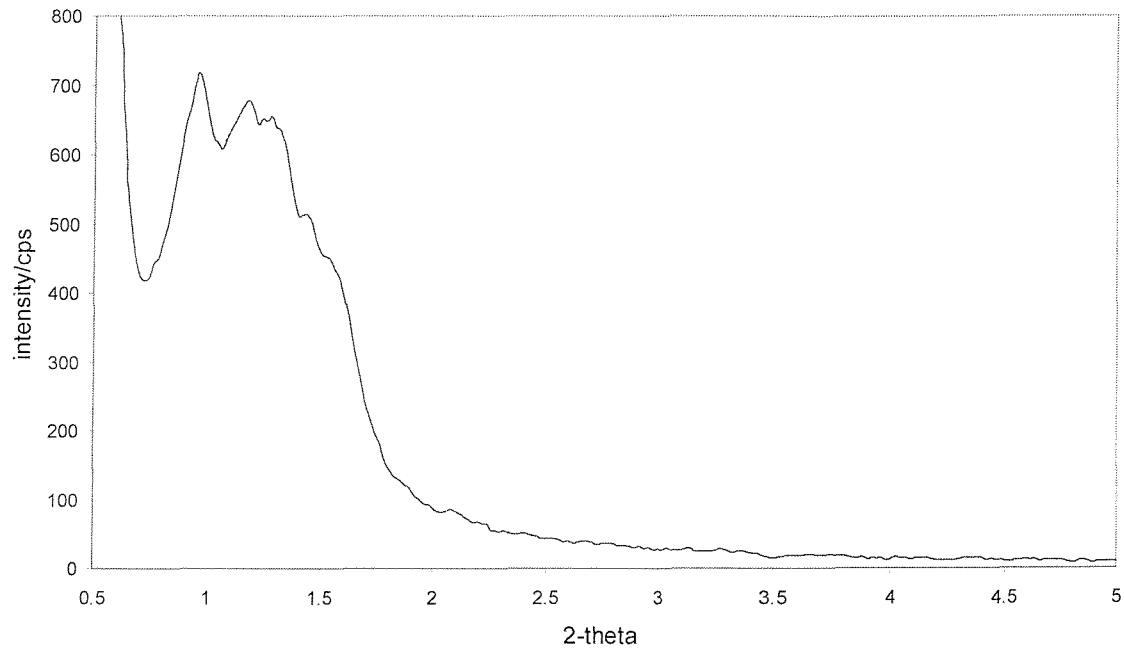

Figure 2.28. Small angle x-ray scattering analysis of mesoporous nickel deposited from the V_I phase of a 65 wt. % Brij® 56 at –0.9 V *vs.* SCE and 35 °C shows a complicated signal indicative of three-dimensional mesopore geometry.

of the V_I mesopore structure as compared with the two-dimensional periodicity associated with the H_I phase. At an angle of 0.96 2θ a strong peak appears corresponding to periodicity of 9.2 nm. Subsequently, peaks appear centred at 1.23

and 1.44 2θ (corresponding to d values of 7.2 and 6.1 nm respectively) however the superposition of these prevents a proper determination of the number of peaks contained within this range and the 2θ values of their maxima. Nevertheless, using these values it is possible to make a crude evaluation of the mesopore geometry. Taking the peak at 0.96 2θ as the principal peak, the corresponding d values of the three peaks are spaced according to the ratio $\sqrt{2}:2:\sqrt{5}/\sqrt{6}$. As detailed in Appendix 2, these spacing ratios indicate a *Pm3n*, *Im3n* or *Ia3d* space group.

The lack of clarity in the diffractogram of Figure 2.28 indicates a degree of disorder in the structure. Since the template mixture was in close proximity to the H_I/V_I phase boundary during deposition, it is quite likely that the template and therefore the deposited mesoporous nickel consisted of a biphasic mixture of H_I and V_I phases. As such, the signals appearing at approximately 1.23 2θ in Figure 2.28 may be due to contributions from H_I material, agreeing with the periodicity of the H_I phase that was shown to be centred at 1.24 2θ in Figure 2.25.

2.3.3.3 Wide Angle X-ray Scattering (WAXS)

Wide angle x-ray scattering experiments confirmed the presence of cubic nickel metal in samples electrodeposited from the H_I phases of Brij® 56 and 78 and Pluronic® P123 however these data were undermined by the presence of the gold deposition substrate. Figure 2.29 shows x-ray scattering from a Pluronic® templated material. The peak at 38.1 ° represents the {111} reflection of the gold film beneath the nickel electrodeposit. The smallest of the 3 peaks at 51.9 ° indicates the {200} reflection of cubic nickel, while the peak at 44.4 ° is a superposition of the gold {200} and nickel {111} reflections.

The low intensity of the peaks and their superposition with those of gold prevented a Scherrer line broadening analysis being performed to ascertain crystallite size in the sample. Samples electrodeposited from the Brij® templates gave nickel WAXS signals of even lower intensity than in Figure 2.29.

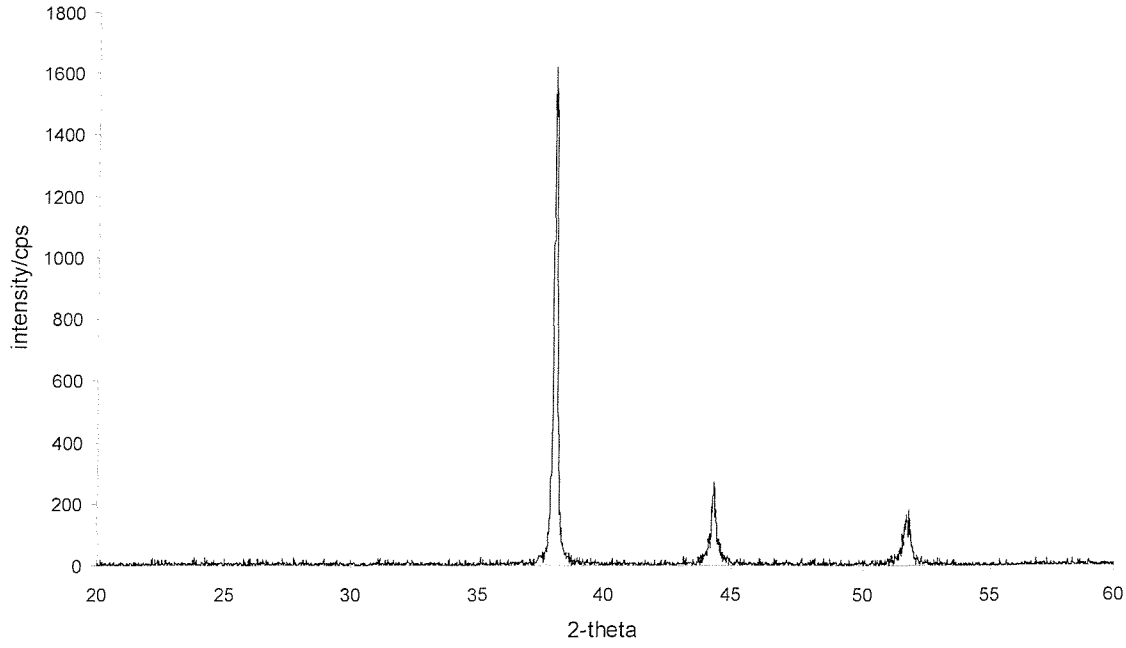

Figure 2.29. Wide angle x-ray scattering analysis of H_I mesoporous nickel deposited from the Pluronic® P123 template produces a signal difficult to differentiate from that of the gold substrate.

2.3.4 Electrochemical Characterisation

Non-templated and templated mesoporous nickel electrodes deposited from Brij® and Pluronic® surfactant templates were subjected to cyclic voltammetry and potential step experiments in alkaline solution in order to understand their electrochemical properties. Cyclic voltammetry enabled elucidation of elements of the electrode composition, roughness factors and the charging/discharging behaviour of mesoporous nickel in 6 M KOH.

2.3.4.1 Non-templated Nickel

Non-templated nickel electrodes were deposited potentiostatically onto gold disc electrodes from the 0.2 M $Ni(ac)_2$ deposition solution at –0.9 V *vs.* SCE at 25 °C. On immersion of the nickel electrodes in 6 M KOH the open circuit potential of all nickel films was found to be approximately –0.45 V *vs.* Hg/HgO when first transferred from the isopropanol/water wash. This result indicates an electrode surface consisting not of nickel metal but of its corrosion product (in alkaline solution) $Ni(OH)_2$. The presence of $Ni(OH)_2$ which has been observed by others[12] is not surprising since the deposited nickel metal undergoes rapid oxidation in the isopropanol wash (due to the presence of trace amounts of water), during the water wash and on exposure to air during transfer to the electrochemical cell.

Figure 2.30 shows the cyclic voltammetry of a 1 mm diameter nickel disc electrode in 6 M KOH electrodeposited from the non-templating electrolyte. Conversion of the nickel metal to $Ni(OH)_2$ according to

$$Ni + 2OH^- \leftrightarrow Ni(OH)_2 + 2e^- \quad (1)$$

is seen at low potentials immediately above hydrogen evolution.[13] As the potential is swept in the positive direction, the current density decreases but maintains a relatively constant non-zero value. This current corresponds to further conversion of the nickel electrode to the insulating $Ni(OH)_2$, which occurs by the field driven diffusion of OH^- ions across the $Ni(OH)_2$ layer. The current density remains constant here, despite the increase in the electrical field strength across the $Ni(OH)_2$ layer as the potential is

swept positive because the thickness of the layer increases as more $Ni(OH)_2$ is formed.

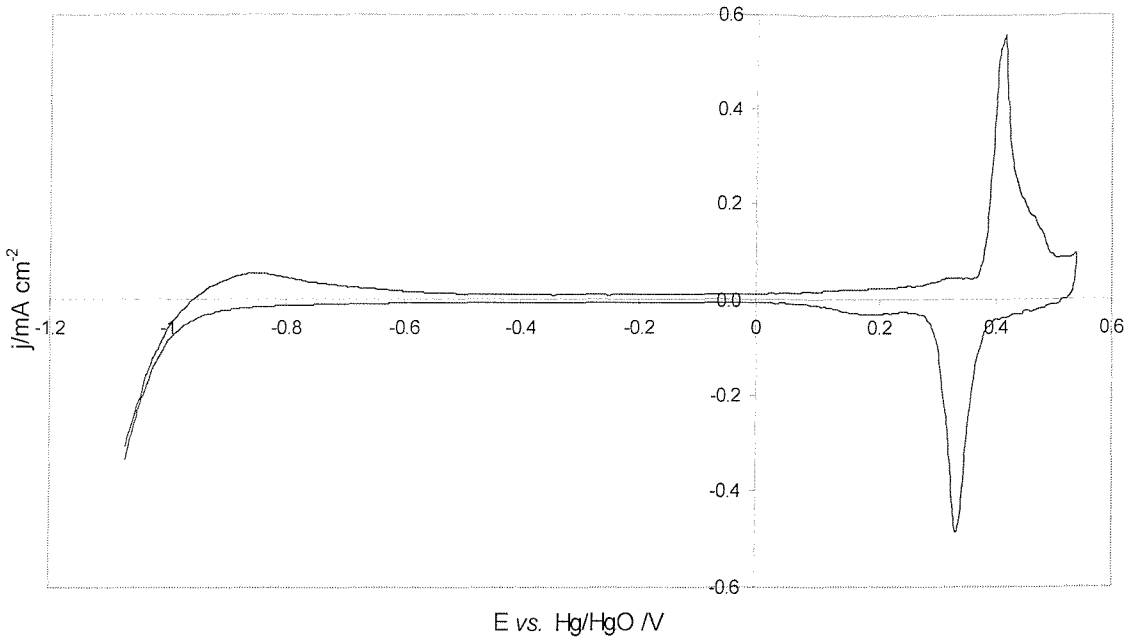

Figure 2.30 shows the electrochemistry (second scan) of an approximately 1 μm thick non-templated nickel on gold electrode in 6 M KOH with a scan rate of 20 mV s^{-1} at 25 °C.

At ~0.37 V *vs.* SCE the anodic current increases rapidly, indicating the oxidation of nickel hydroxide to nickel oxyhydroxide followed by the subsequent reduction of NiOOH on the reverse sweep according to

$$Ni(OH)_2 + OH^- \leftrightarrow NiOOH + H_2O + e^- \quad (2)$$

or,

$$Ni(OH)_2 \leftrightarrow NiOOH + H^+ + e^- \quad (3)$$

These reactions occur by the intercalation of either hydroxyl ions and water or protons between a layered structure consisting of NiO_2 sheets. The open structure of $Ni(OH)_2$ offers sites for possible OH^- and H_2O as well as H^+ incorporation, making both Reaction 2 and Reaction 3 plausible. Bode *et al.*[14] made the first attempts to elucidate

the charging/discharging behaviour of nickel electrodes in KOH and a number of others have since followed. The issue of whether the species which diffuses through the film is H^+, OH^- or both however remains controversial. Carbonio and Macagno proposed a model based on the OH^- diffusion mechanism of Reaction 2 and it is this model which has gained the widest acceptance.[15]

The anodic and cathodic peaks between 0.3 and 0.5 V *vs.* Hg/HgO in Figure 2.30 with an associated charge of approximately 1.5 mC cm^{-2} and 1.3 mC cm^{-2} respectively are typical of those found in the literature and attributed to the formation and subsequent reduction of a few monolayers of NiOOH.[16] Previous studies have referred to thickening of this active oxide layer with surface treatments and square wave cycling or potential pulse treatment[17,18], leading to charges of up to 30 mC cm^{-2} associated with the formation of additional NiOOH. Most authors, however, agree on a cathodic peak charge of approximately 0.7 mC cm^{-2} during the second and subsequent cycles on a smooth, clean, nickel surface.[19] It should be noted that this value was measured experimentally in 0.1 M KOH solution and is undoubtedly accompanied by a degree of error. The significance of this error is unknown. Assuming the number of NiOOH monolayers reduced in Figure 2.30 is the same as that reduced in Ref. 19, we can attribute the increased cathodic charge observed in Figure 2.30 to an approximately two-fold enhancement in the roughness of the electrode surface over that of the polished electrodes discussed in the literature. This is reasonable since electrodeposition is not expected to produce nickel films as smooth as those obtained by polishing treatments.

Figure 2.31 shows the reversible oxidation of nickel metal to $Ni(OH)_2$ with anodic currents centred at –0.57 V *vs.* Hg/HgO in 6 M KOH. Reduction of $Ni(OH)_2$ back to the metal is superimposed on hydrogen evolution currents, peaking at –0.93 V. This redox activity is derived from the cycling of the α-phase of $Ni(OH)_2$, one of the two crystallographic phases of $Ni(OH)_2$ (the other phase being the β-form). Their interrelationship and those with the β- and γ-phases of NiOOH complicate the cyclic voltammetry of nickel in alkaline solution and have been the subject of numerous debates in the literature. The generally accepted phase relationship is illustrated in Figure 2.32 as first suggested by Bode and co-workers.[20] α-$Ni(OH)_2.xH_2O$ as it is more correctly written, is not stable in 6 M KOH solution and ages to the dehydrated

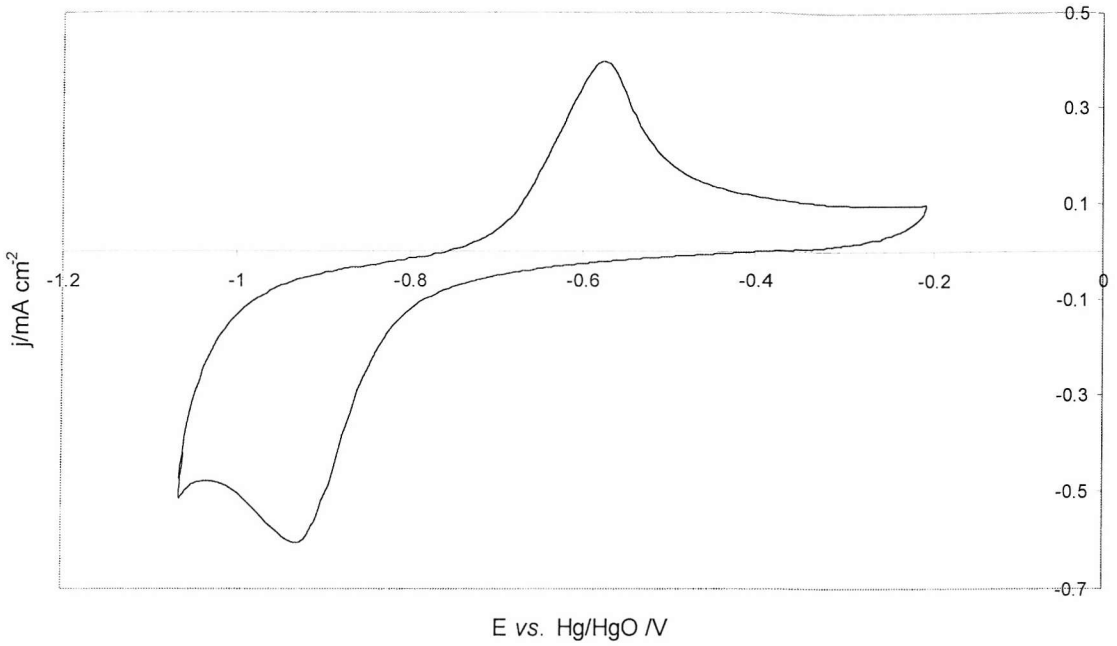

Figure 2.31 shows the reversible electrochemistry of nickel in 6 M KOH at 50 mV s^{-1} with restriction of the upper potential limit to –0.2 V *vs.* Hg/HgO.

β- phase in a recrystallisation process that is accelerated at higher temperatures.[21] The ageing of α-$Ni(OH)_2$ also occurs as a function of potential such that the transformation to β-$Ni(OH)_2$ is total at potentials at and above approximately 0 V *vs.* Hg/HgO (6 M KOH). The β-phase of $Ni(OH)_2$ possesses a higher degree of

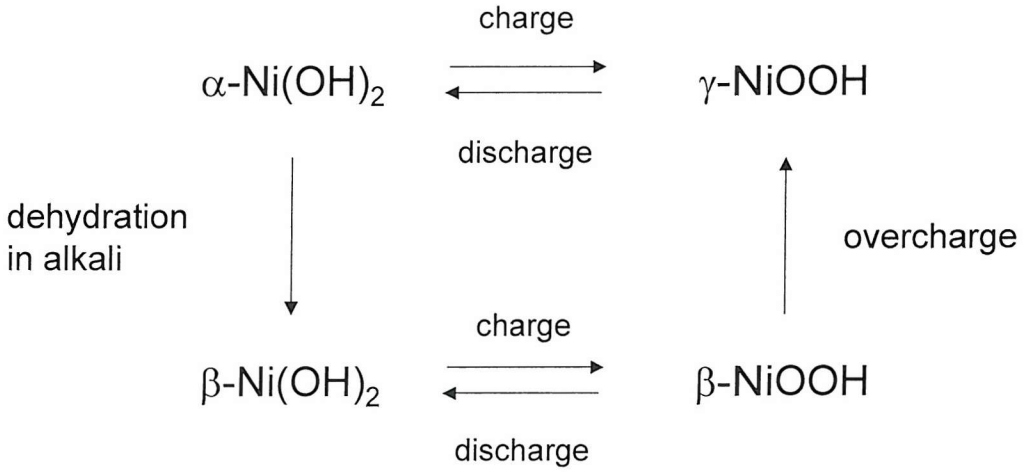

Figure 2.32 shows the complex relationship between phases and redox couples developed from nickel electrodes in alkaline solution.

crystallinity than the α-phase and is manifest as larger and less disordered crystallites. As such, the electrode surface area exposed to the electrolyte on cathodic reduction is smaller and the diffusion pathways are significantly extended. Consequently, while α-$Ni(OH)_2$ is reversibly formed by the oxidation of nickel metal as indicated in Figure 2.31, the β-phase of $Ni(OH)_2$ is extremely difficult to reduce back to nickel by cathodic polarisation in 6 M KOH.[22] This irreversibility is evidenced by the absence of $Ni(OH)_2$ reduction currents at low potentials of Figure 2.30. Here, the α-$Ni(OH)_2$ formed at low potentials in the voltammogram has been irreversibly converted to β-$Ni(OH)_2$ during the initial sweep such that at low potentials the electrode surface is completely covered by β-$Ni(OH)_2$. Bode's diagram, thus indicates that the large anodic and cathodic peaks appearing at high potentials in Figure 2.30 are due to the formation and reduction of the β- phase of NiOOH. The conversion of β-NiOOH to γ-NiOOH occurs slowly and irreversibly. The rate of conversion is a function of the upper potential limit in cyclic voltammetry, with overcharge conditions promoting γ-phase formation. Cycling of the hydrated γ-NiOOH phase, which has a more disordered structure than β-NiOOH is known to cause mechanical deformation and results in electrode capacity loss.[23]

The complex phase relationship proposed by Bode *et al.* has been supported by studies discussing the structure of the nickel electrode in alkaline solution. Using cyclic voltammetry coupled with *in-situ* ellipsometry, de Souza *et al.*[24] determined the structure of the oxidised nickel electrode at various stages of the voltammetry. They deduced that with the first anodic peak at low potentials a compact film of α-$Ni(OH)_2$ is formed from the oxidation of nickel metal. This layer grows at a diffusion limited rate during the initial forward sweep and is converted to β-$Ni(OH)_2$ at higher

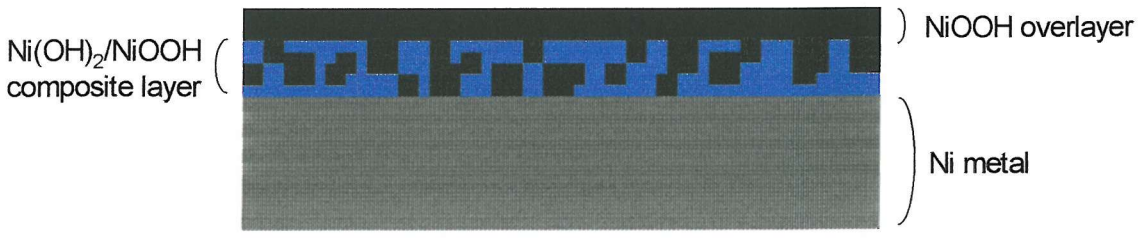

Figure 2.33. After treatment in alkaline solution, nickel electrodes possess a multi-layered structure containing the nickel species of numerous redox states.

potentials of the Ni(II) stability window. On subsequent oxidation at higher potentials the redox active layer was shown to consist of a base mixture of $Ni(OH)_2$ and NiOOH with an overlayer of NiOOH, as proposed by Crocker[25] and illustrated schematically in Figure 2.33. NiO is also known to be formed in small amounts by electrochemical oxidation of Ni electrodes in alkaline solution.[26] The NiOOH overlayer represents the reversible capacity of the electrode and was shown to be completely reduced by cathodic reduction, while that NiOOH embedded in the $Ni(OH)_2$/NiOOH composite layer was only partially reduced to $Ni(OH)_2$. This limited irreversibility in the reduction of the lower layer of NiOOH explains the charge imbalance of 0.2 mC cm^{-2} observed in Figure 2.30. Jeong *et al.* offered an alternative and less popular explanation, concluding that the reason for the anodic to cathodic charge ratio being above 1 was either excess capacity derived from the underpotential oxidation of OH^- ions as they are inserted into the nickel hydroxide layers or the formation of Ni(IV) species.[27]

2.3.4.2 Mesoporous Nickel from the Brij® 56 and Brij® 78 H_I Templates

The voltammogram of mesoporous nickel deposited from the Brij 56® H_I liquid crystal template is shown in Figure 2.34. On the first scan the voltammetry shows the formation of the anodic oxidation product $Ni(OH)_2$ with a small peak centred at -0.65 V *vs.* Hg/HgO. The magnitude of this peak is relatively small because the electrode surface already largely consists of $Ni(OH)_2$ as a result of exposure to air and water during washing. At higher potentials of the first cycle the large anodic peak beginning at 0.40 V, with an associated charge of 120 mC cm^{-2}, and the cathodic peak centred at 0.34 V with a charge of 61 mC cm^{-2} indicate the formation and subsequent reduction of β-NiOOH. The charge imbalance of 59 mC cm^{-2} indicates an incomplete reduction of the NiOOH formed during the forward sweep. At low potentials below –0.8 V there is no evidence of the reduction of $Ni(OH)_2$ to nickel metal, indicating the presence of the β-phase of $Ni(OH)_2$. On the second and third cycles there is a distinct absence of the anodic currents corresponding to $Ni(OH)_2$ formation from the metal, providing further evidence for electrode coverage by the irreversibly formed β-phase of $Ni(OH)_2$. On the second and third cycles the high potential charging/discharging behaviour observed at higher potentials of Figure 2.34 is noticeably different in

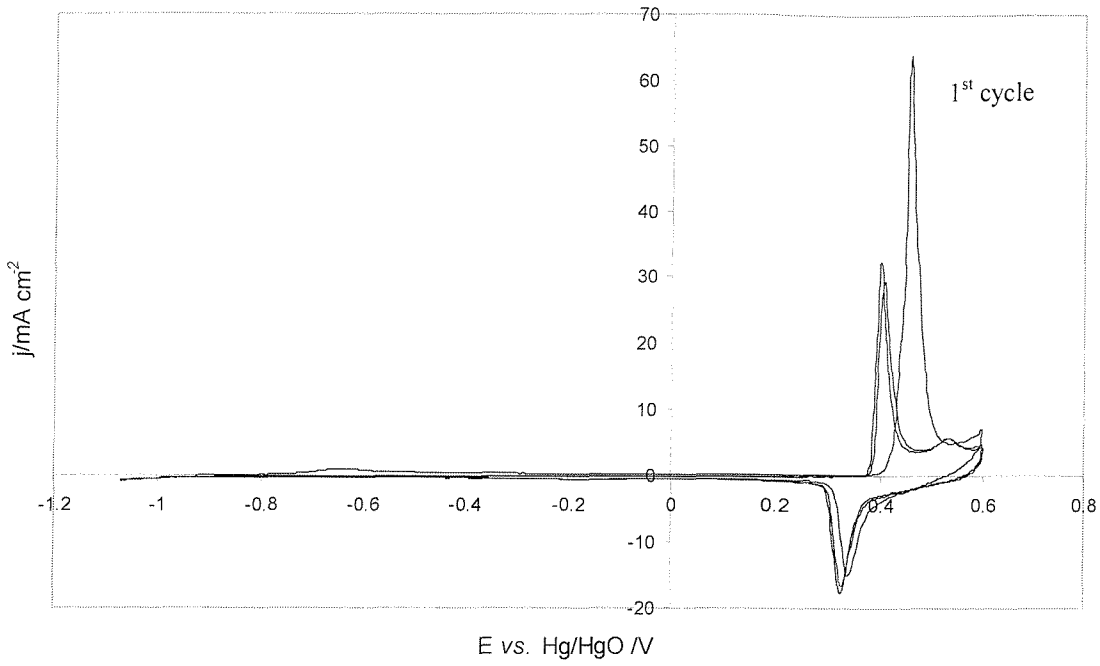

Figure 2.34 shows the first and two subsequent voltammetric cycles of an H_I mesoporous nickel electrode (deposited with a charge density of 1.8 C cm^{-2}) in 6 M KOH at 20 mV s^{-1}.

comparison to the initial cycle. NiOOH formation begins at the lower potential of 0.37 V and the amount of charge cycled changes after the initial cycle, remaining constant over the second and third cycles at 70 mC cm^{-2} and 65 mC cm^{-2} for the anodic and cathodic processes respectively. The positive displacement of the anodic peak during the initial cycle is due to the energy requirement for the nucleation of NiOOH growth sites on the $Ni(OH)_2$ electrode. The requirement for this nucleation energy is avoided on subsequent cycles because of the presence of NiOOH within the electrode structure prior to the anodic peak, which results from the incomplete reduction of NiOOH during the previous cycle. The anodic peaks of the second and third cycle are also considerably smaller than the peak of the initial cycle. The larger charge of the initial anodic peak is due to NiOOH formation establishing both the reversible overlayer, and layers below this which are not entirely reversibly formed, as discussed in Section 2.3.4.1. The second and third cycle anodic currents are due to the re-oxidation of the reversible overlayer in addition to a much smaller irreversible charge contribution of approximately 5 mC cm^{-2}. This additional irreversible charge increases slightly the thickness of the NiOOH layers beneath the overlayer, however

is significantly less than that observed in the first cycle. As such, it is concluded that the increase in NiOOH sub-layer thickness is significantly less than the total sub-layer thickness.

Based on the charge associated with the reversibly formed NiOOH overlayer (65 mC cm^{-2}), it is possible to make approximate estimates of the roughness factor and surface area of the mesoporous electrode. Considering there was no surface treatment leading to oxide thickening, it may be assumed that the average overlayer thickness in the mesoporous electrode was approximately the same as that of the non-templated sample discussed in Section 2.3.4.1. Consequently, the increased cathodic charge is interpreted as confirmation that the surface area available during the 20 mV s^{-1} sweep is enhanced by a factor of about 50 times over that of the non-templated sample due to the large internal area of the porous electrode.

Unlike the case of the mesoporous platinum films reported previously,[13] in which the measured charge in cyclic voltammetry experiments was correlated with the adsorption of precisely one monolayer of hydrogen to obtain an estimate of the surface area, the electrochemical determination of surface area in this case is complicated by uncertainty regarding the degree of surface oxidation of nickel. Nevertheless, the measurement of large charge density confirms the expected activity due to the mesoporosity shown by TEM.

The charge associated with the cathodic charging peak was used to quantify the surface area of the mesoporous nickel films. Using the value of 0.7 mC cm^{-2} obtained by Amjad *et al.* (in 0.1 M KOH), the absolute surface of the mesoporous nickel deposit of Figure 2.34 was calculated as 0.73 cm^2. This value corresponds to a surface area value of ~440 m^2 cm^{-3} or 64 m^2 g^{-1} using the mass of the deposit as determined by anodic stripping voltammetry (see Chapter 5) and the calculated pore volume of 23 % (see Appendix 1). The value of 440 m^2 cm^{-3} is significantly higher than the calculated value of 224 m^2 cm^{-3} for a perfect hexagonal structure (see Appendix 1 for theoretical surface area calculations) with wall thickness and pore diameter of 4.05 nm, as deduced from SAXS measurements discussed in Section 2.3.3.2. It is however closer to the theoretical surface area of 349 m^2 cm^{-3} calculated on the basis of TEM data, which indicated a smaller pore diameter and wall thickness of 2.6 nm. Although this comparison appears to lend support to the relative accuracy of TEM data over SAXS derived spacings, there still remains a large discrepancy between the electrochemically derived surface area estimate and those of both TEM and SAXS

based calculations. This discrepancy is probably due to the internal roughness of the pores, which is easily visible in the TEM micrograph of Figure 2.23 and of which the theoretical calculation takes no account of. Since this internal roughness cannot be quantified, the electrochemically derived surface area estimate cannot be used to establish the relative accuracy of the TEM and SAXS data. Nevertheless, on the basis of this surface area comparison we can conclude that the quality of the mesoporosity must be very high since the theoretical estimates are significantly exceeded.

The cyclic voltammetry of mesoporous nickel deposited from the H_I phase of a Brij® 78 template is presented in Figure 2.35. Here, on the first cycle of the voltammogram 62 mC cm^{-2} and 30 mC cm^{-2} of charge are passed in the anodic and cathodic peaks respectively, corresponding to the oxidation of $Ni(OH)_2$ to NiOOH and reduction back to the same. The cathodic charge here indicates a 23 fold enhancement in the roughness of the templated electrode over that of the non-templated electrode discussed in Section 2.3.4.1. Figure 2.35 demonstrates a lower charge capacity than

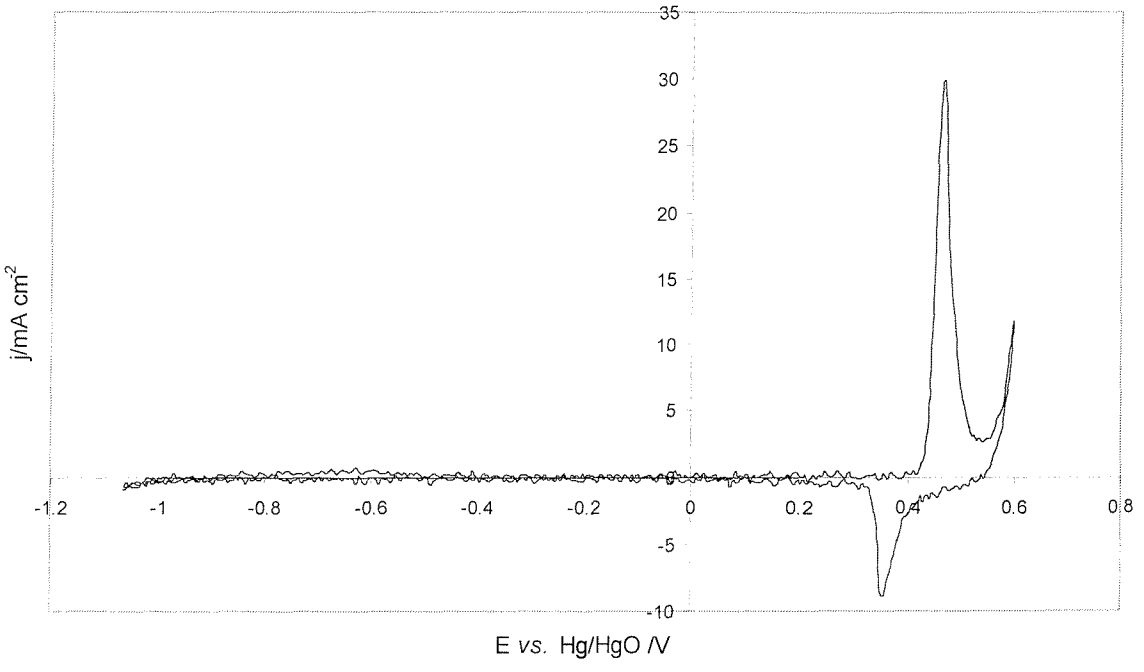

Figure 2.35. The first cycle of mesoporous nickel deposited from a Brij® 78 based template (with a charge density of 1.1 C cm^{-2}) in 6 M KOH shows substantial charge capacity at 20 mV s^{-1}.

that of the Brij® 56 templated mesoporous nickel discussed above. This is in part due to the lower specific surface areas expected from Brij® 78 templated nickel as a

consequence of the larger pore sizes obtained. Where we expect 224 m^2 cm^{-3} from the Brij® 56 template, a theoretical specific surface area of 202 m^2 cm^{-3} (using SAXS derived spacings) is expected from the Brij® 78 template (see Appendix 1). Another contribution to the lower charge capacity however is the simple fact that the thickness of the templated electrode of Figure 2.35 is lower than that of the Brij® 56 templated sample. In order to make a direct comparison, the volume specific surface areas relative to the theoretical surface areas are compared. The volumetric surface area of the Brij® 56 templated nickel was 440 m^2 cm^{-3}, 80 % higher than the theoretical value. The Brij® 78 templated sample however showed an electrochemically derived volumetric surface area of 190 m^2 cm^{-3} or 28 m^2g^{-1}, lower than that of the theoretical (SAXS derived) value. Assuming that the internal pore roughness is the same in both samples it must therefore be concluded that the lower charge capacity seen in Figure 2.35 is due to a lower quality mesopore structure in the Brij® 78 sample. The reason for this is thought to be the inability to perform annealing of the liquid crystal prior to deposition. The absence of low viscosity phases at high temperatures in the Brij® 78 phase diagram did not allow annealing to be carried out. As shown in Chapter 5, this is an important step in the deposition of high surface area mesoporous structures from Brij® surfactant templates.

2.3.4.3 Mesoporous Nickel from the Brij® 56 V_I Template

Mesoporous nickel electrodes were deposited from the V_I phase of a 65 wt. % Brij® 56 liquid crystalline electrolyte at 35 °C. The cyclic voltammetry of the template free electrode in 6 M KOH is presented in Figure 2.36. The characteristics of the voltammetry are indifferent to that seen in the previous Section for H_I phase mesoporous nickel. The charge density associated with the anodic and cathodic peaks for the second cycle of this relatively thin deposit were calculated as 28 mC cm^{-2} and 25 mC cm^{-2} respectively. The value of the cathodic charge density corresponds to a roughness factor of 19 compared with that of a nickel electrode deposited from a non-templating electrolyte. Using the value of 0.7 mC cm^{-2} given by Amjad *et al.* volume and mass specific surface area estimates are calculated as 125 m^2 cm^{-3} and 18 m^2 g^{-1} respectively. The value of 125 mC cm^{-2} is again significantly lower than that of mesoporous nickel deposited from the Brij® 56 H_I template. Although it is not accurate to directly compare these values because the geometry of the H_I and V_I

mesostructures is different, this does serve as a useful approximation of the mesostructure quality. The significantly lower surface area of the V_I templated nickel

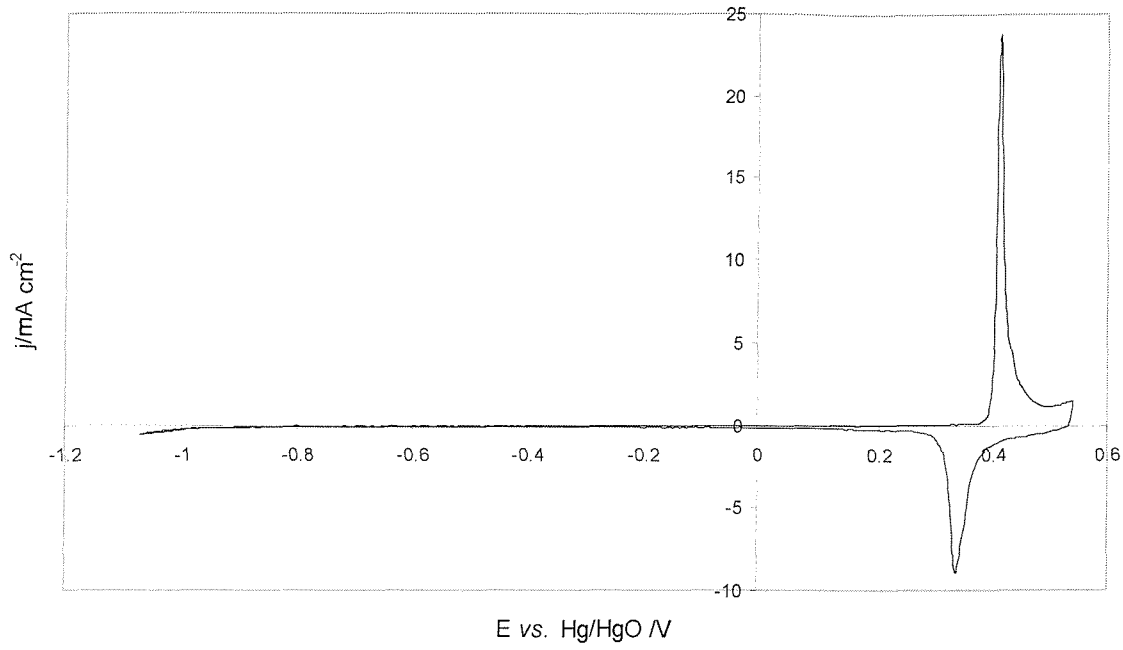

Figure 2.36. Large charging/discharging current densities in 6 M KOH at a scan rate of 20 mV s^{-1} indicate high surface area in mesoporous nickel electrodes deposited from the V_I phase of a Brij® 56 based template with a deposition charge density of 1.4 C cm^{-2}.

(deposited from an annealed template) is probably due to incomplete formation of the V_I template under the conditions of the deposition.

As was established in Section 2.3.1.1 the V_I phase region in the Brij® 56 phase diagram is extremely narrow in terms of both composition and temperature. In addition, the polydispersity of the Brij® surfactant narrows even more the window of stability of the V_I monophase such that the phase boundaries as they are depicted in Figure 2.3 are actually much thicker than the narrow lines with which they are represented. The liquid crystalline phases associated with these phase boundaries are biphasic mixtures of the two phases on either side of the boundary. These biphasic mixtures are probably disordered and act as poor templates for the deposition of high surface area nickel. This poor templating ability was confirmed by depositions of mesoporous nickel from the 65 wt. % Brij® 56 liquid crystalline electrolyte at both

34.5 °C and 35.5 °C. In both cases the resulting mesostructures demonstrated low surface areas in cyclic voltammetry experiments.

2.3.4.4 Mesoporous Nickel from the Pluronic® P123 H_I Template

The cyclic voltammetry of mesoporous nickel deposited from the H_I phase of a 50 wt. % Pluronic® P123 liquid crystalline template is presented in Figure 2.37. The P123 templated nickel shows anodic and cathodic charge densities of 148 mC cm^{-2} and 93 mC cm^{-2} respectively. The value of the cathodic charge density enables a roughness

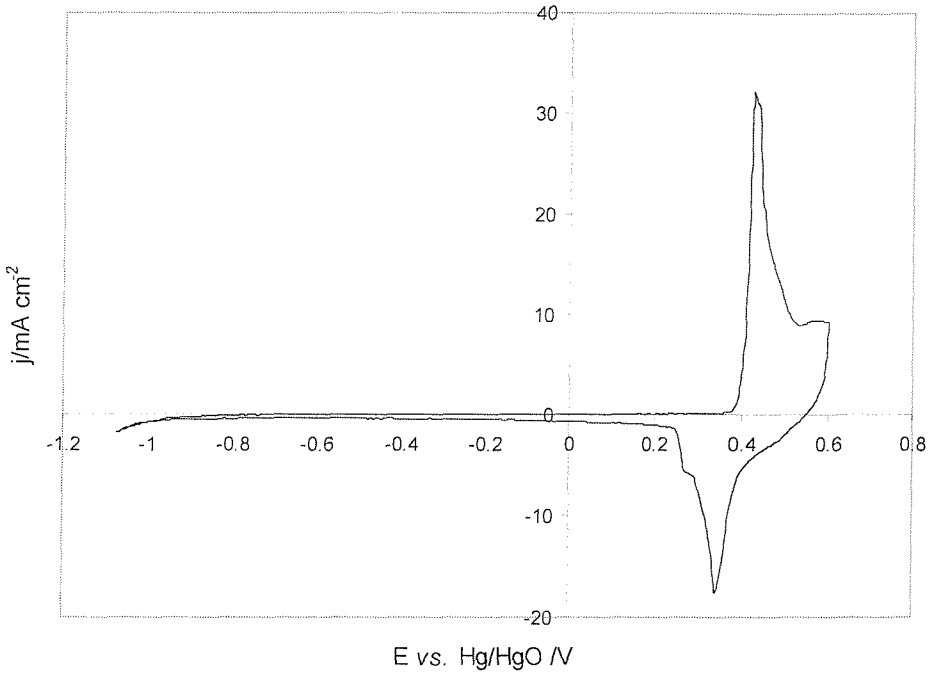

Figure 2.37. Cyclic voltammetry (second scan) conducted at 20 mV s^{-1} on mesoporous nickel templated from a Pluronic® P123 electrolyte (with a deposition charge density of 18.9 C cm^{-2}) shows substantial charge density.

factor of 72 to be calculated, representing the surface area enhancement over that of a non-templated nickel electrode. Using the 0.7 mC cm^{-2} conversion factor of Amjad *et al.*, taking into account a deposition charge of -149 mC and a faradaic deposition efficiency of 78 % (this is discussed in Chapter 5), a value of 21 m^2 cm^{-3} is calculated as an estimate of the volumetric surface area. This value is somewhat lower than the value of 100 m^2 cm^{-3} calculated assuming a perfect H_I structure with the structural periodicity obtained from SAXS experiments. The most obvious reason for this is that the mesostructure in P123 templated nickel does not possess the long range continuity

and periodic ordering that is present in the Brij® templated nickel discussed above. The general lower quality of the P123 templated materials and therefore of the P123 H_I liquid crystalline phase is possibly a consequence of the impurity of the surfactant. GPC analysis of Pluronic® surfactants has shown considerable variation in the molecular mass of these commercial surfactants.[28] Variation in the molecular mass of a surfactant templating agent can have considerable effects on the quality of thus derived mesostructured materials. For example, and as will be demonstrated in Chapter 5, only with thermal treatment of the H_I phase of the surfactant Brij® 56 does the quality of mesostructured material derived from this phase approach that obtainable using the more pure surfactant templating surfactant $C_{16}EO_8$.

The cyclic voltammetry shown in Figure 2.37 possesses an unusual feature in both the anodic and cathodic peaks. A shoulder is observable at 0.49 V and 0.27 V *vs.* Hg/HgO respectively in these peaks. This shoulder is attributed to the formation of γ-NiOOH and its reduction product α-$Ni(OH)_2$ which are usually observed after periods of extended cycling or overcharge of the nickel electrode in alkaline solution.[29] The

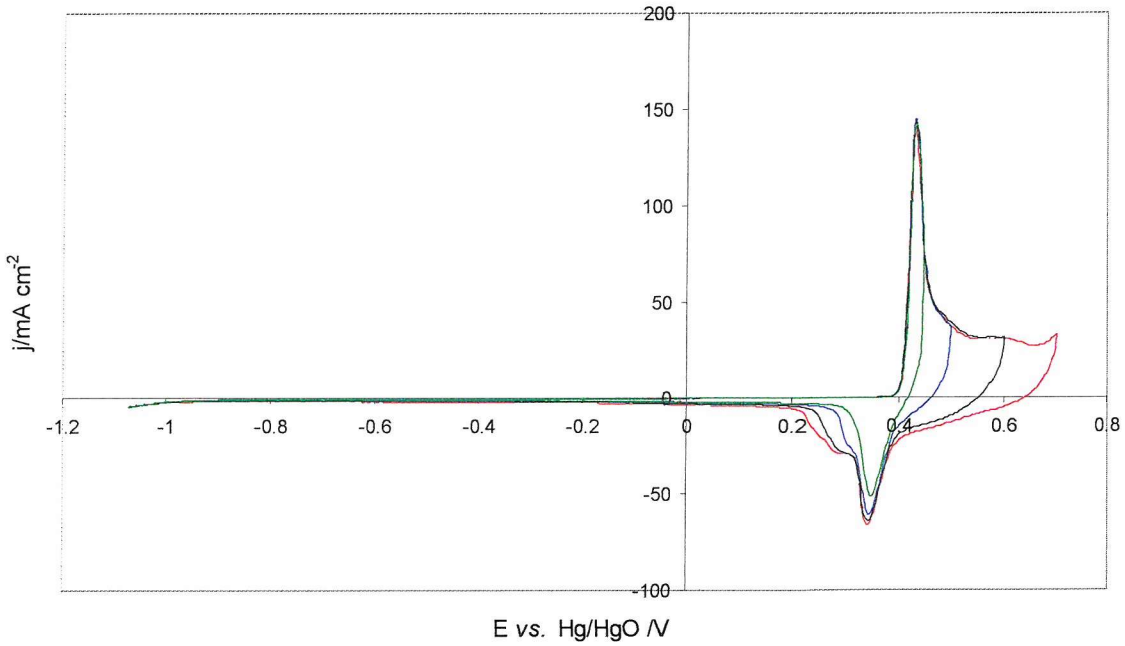

Figure 2.38 shows the evolution of the cathodic peak with variation of the upper potential limit for Pluronic® P123 templated mesoporous nickel (with a deposition charge density of 18.9 C cm^{-2}) in 6 M KOH at 100 mV s^{-1}.

reason for their presence here, in the second voltammetric cycle and without exposure to overcharge is unknown. Figure 2.38 clearly shows the formation of the β- and γ-phases of NiOOH at different potentials in the forward sweep and the corresponding reduction of these phases to β- and α-$Ni(OH)_2$ respectively in the reverse sweep. With restriction of the upper potential limit to 0.45 V there is no observable formation or subsequent reduction of γ-NiOOH. On increasing the upper potential limit to 0.50 V however, the cathodic shoulder indicating reduction of γ-NiOOH appears, growing with further increase of the upper potential limit. With an upper potential limit of 0.70 V, a second smaller shoulder appears on the side of the cathodic peak at potentials of approximately 0.23 V. This redox activity is possibly due to the reduction of a Ni(IV) species which is known to be formed at potentials required for oxygen evolution,[30] the beginnings of which are observed in Figure 2.38.

2.3.4.5 Limitations in Charge /Discharge Kinetics of H_I Mesoporous Nickel

The sharpness of the peaks in Figure 2.34 indicates extremely rapid charge transfer, which is only possible with a highly accessible pore structure in which the diffusion of ions is rapid and unhindered.

Figure 2.39 shows the effect on the charging/discharging current density of mesoporous nickel with variation of the scan rate in 6 M KOH. With increase of the scan rate from 2 to 500 mV s^{-1} both the anodic and cathodic currents are observed to increase. On comparison of the cathodic charge associated with the 20 mV s^{-1} scan (592 mC cm^{-2}) with that of the non-templated nickel electrode discussed in Section 2.3.4.1 (1.3 mC cm^{-2}), a roughness factor of 455 is calculated for the mesoporous nickel electrode of Figure 2.39. The linearity and scan rate independence of the leading edge of the anodic peaks suggests that the rate of charging is limited by a non-variable resistive parameter. The slope of the leading edges suggests a resistance limitation of about 0.3 Ω cm^2 which can be attributed to the spreading resistance from the disc surface to a bulk electrolyte of conductivity 1 S cm^{-1}. That is, the rate of charging in this initial period is limited only by the conductivity of the electrolyte solution. The progressive movement of the anodic current peak to higher potentials with increasing scan rate indicates a diffusion limited process. Diffusion limitation is

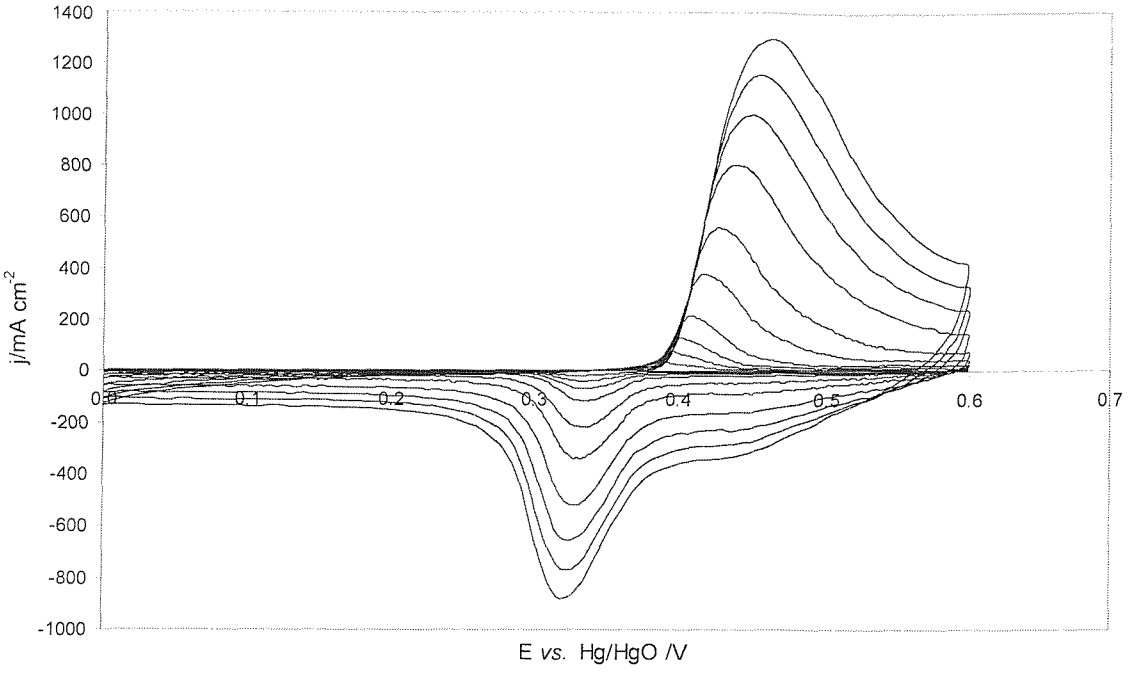

Figure 2.39 shows the effect of variation of scan rate (2, 5, 10, 20, 50, 100, 200, 300, 400 and 500 mV s^{-1}) on the charging and discharging currents of H_I mesoporous nickel deposited for a 48 h. period from a Brij® 56 template (with a deposition charge of 10.5 C cm^{-2}) in 6 M KOH at 25 °C.

confirmed by the absence of a straight line in the plot of anodic and cathodic peak charge values versus scan rate presented in Figure 2.40. Here, both anodic and cathodic charge decrease with scan rate from values initially approaching 900 and 800 mC cm^{-2} respectively. These values contain contributions from both double layer capacity and that derived from the $Ni(OH)_2$/NiOOH redox couple. Plotting Q^{-1} against $v^{1/2}$ gives a straight line as indicated in Figure 2.41. The non-zero intercept of Figure 2.41 equates to the maximum available capacity of the electrode, that is, the capacity obtained in the absence of any diffusion limitation. In Figure 2.41 this value is 824 mC cm^{-2} for the approximately 0.65 μm thick electrode.

Double layer capacitive behaviour is visible in the cathodic sweep of Figure 2.39 prior to the onset of redox activity at 0.33 V *vs.* Hg/HgO but disappears at lower potentials where the electrode is composed of the insulating $Ni(OH)_2$. A plot of current versus scan rate (using the current at 0.42 V) in this segment of the voltammogram yields a

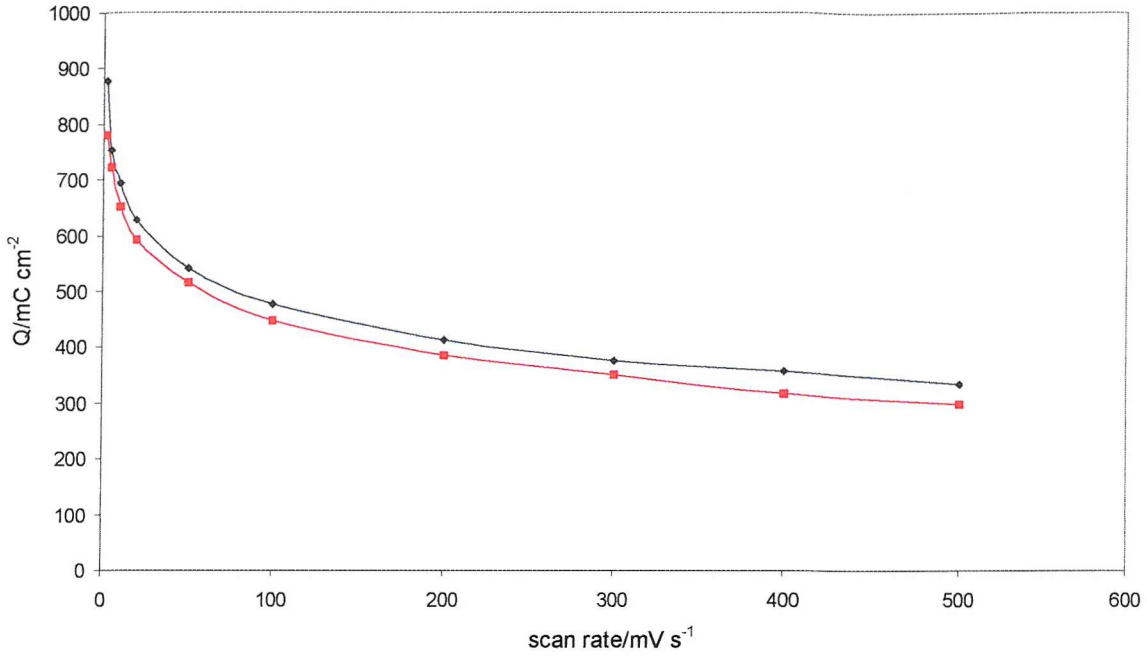

Figure 2.40 shows the scan rate dependence of anodic (blue) and cathodic (red) charge densities during cyclic voltammetry in 6 M KOH using 200 μm H_I mesoporous nickel disc electrode of approximately 0.65 μm thickness.

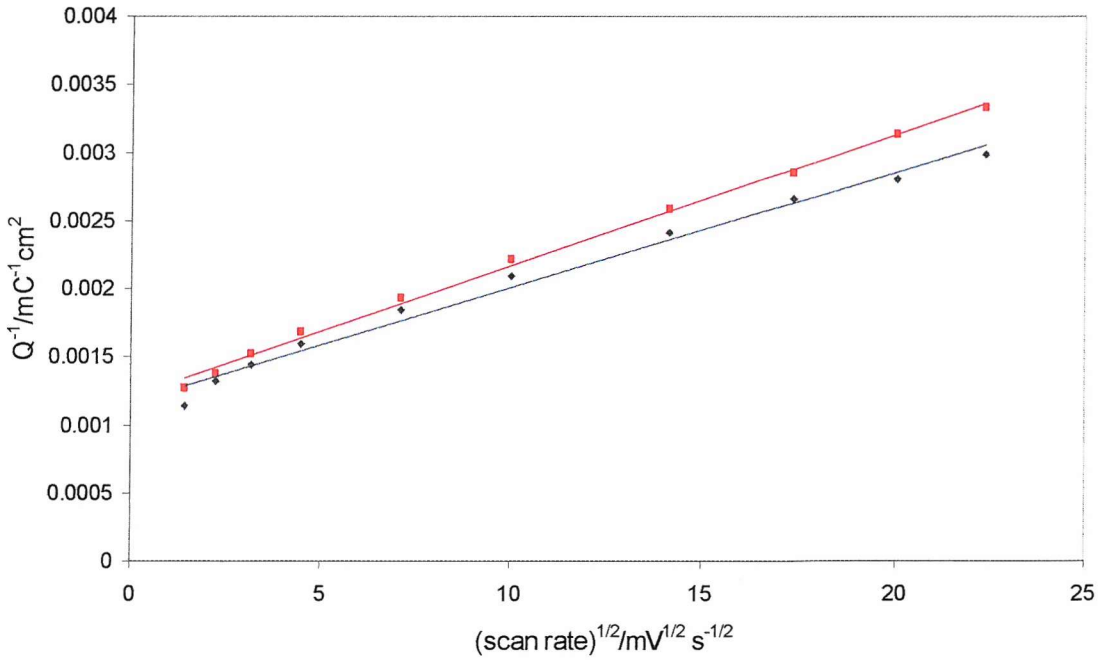

Figure 2.41 shows variation in the reciprocal of the charge density with the square root of the scan rate for the anodic (blue) and cathodic (red) processes occurring in a mesoporous nickel disc in 6 M KOH.

straight line as indicated in Figure 2.42. This relationship demonstrates that the discharge currents observed in this segment of relatively constant current are due to a surface process, most likely double layer discharge. The slope of the plot in Figure 2.42 indicates a double layer capacitance of 726 F g^{-1} using an electrode mass calculated based on the known deposition efficiency of 34% (for a 24 h deposition) and the deposition charge.

The shape of the cathodic peaks of Figure 2.39 are markedly different from those of the anodic peaks. The potential at which the cathodic peaks reach their maxima varies only slightly with scan rate and the cathodic peaks are largely symmetrical about their maxima. In contrast, the anodic peak maxima are significantly displaced to higher

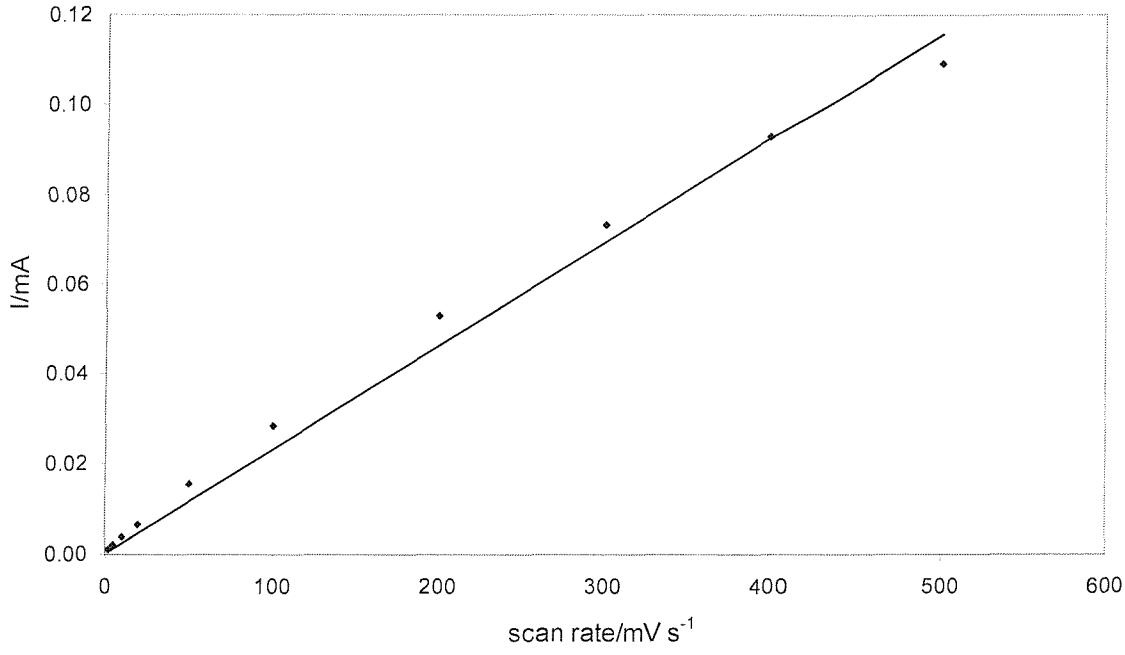

Figure 2.42. A plot of current *versus* scan rate at 0.42 V (*vs.* Hg/HgO) during the cathodic sweep on cycling mesoporous nickel in 6 M KOH shows double layer capacity.

potentials with increasing scan rate while the peak shapes are skewed toward lower potentials. In the case of the cathodic peaks, this generally indicates a kinetically controlled process, that is, the currents are a function of potential and are not mass transport controlled. This is contrary to the data presented in Figure 2.41 however, which demonstrated a charge density-scan rate relationship characteristic of a diffusion limited process. Despite this apparent contradiction, both of these observations are correct. Although the cathodic currents are kinetically controlled, the

cathodic charge is limited by the amount of charge passed during the anodic sweep. As such, in this way the cathodic charge is limited by the diffusional process that limits the anodic process. The nature of this diffusion limitation is unknown, however is probably due to either the solid state diffusion of H^+/OH^- species in the $Ni(OH)_2/NiOOH$ layer or the diffusion of OH^- ions within the 6 M KOH filled mesopores.

In order to absolutely quantify the rate at which mesoporous nickel electrodes could be charged and discharged in alkaline solution, potential step charging/discharging experiments were carried out. Figure 2.43 shows the results of such an experiment in

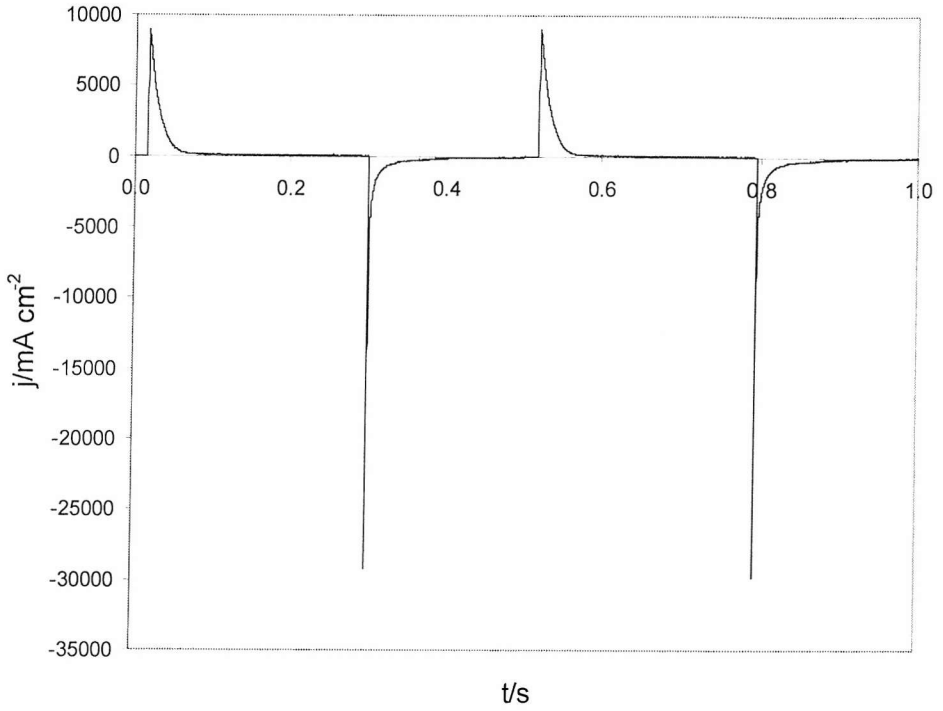

Figure 2.43. Potential step charging/discharging of Brij® 56 templated H_I mesoporous nickel (same electrode as in Figure 2.39) in 6 M KOH produces extremely large current densities.

which the potential of a 500 nm thick mesoporous nickel electrode was stepped between 0 V and 0.6 V *vs.* Hg/HgO. On stepping to the upper potential, an anodic current spike of ~9 A cm^{-2} was observed which quickly decayed to zero current as the electrochemically accessible $Ni(OH)_2$ was completely converted to NiOOH. During the step 124 mC cm^{-2} of charge was passed, the majority of which passed in the initial

50 ms. On the cathodic step to 0 V, 103 mC cm^{-2} of charge was passed in a spike with a maximum current density of ~30 A cm^{-2}. As with the anodic process, the majority of this charge was passed in the first 50 ms. The latter charge value corresponds to that stored in the NiOOH overlayer.

A potential step experiment of this nature was also carried out on a 1.0 μm thick mesoporous nickel electrode as a part of characterisation of a mesoporous nickel/mesoporous palladium supercapacitor as discussed in Chapter 3. In the configuration used, the rate of charge and discharge was found to be limited by the performance of the mesoporous nickel electrode such that the electrochemical response of the cell could be used to quantify this performance. In this experiment, the majority of the charge released on discharge was passed within 50 ms as in the case above, despite the fact that the quantity of charge was much greater than in Figure 2.43. This suggests that the diffusion path-length responsible for the diffusion limitation during discharge is of equal length in both experiments. Given that the electrodes are of differing thickness, the diffusion limitation cannot be due to the diffusion of OH^- in the mesopores of an H_I electrode in which the pores are oriented perpendicular to the substrate surface, since in this case the diffusion path-lengths are different for the thin and thick electrodes. In an electrode of this mesopore orientation only the solid state diffusion path-lengths are equal. In an H_I mesoporous electrode in which the pores are oriented parallel to the substrate surface however, both modes of ion transport are possible rate limiting processes. Consequently, the data discussed above does not reveal the nature of the diffusion limitation in the charging reaction, but only excludes OH^- mesopore diffusion in an H_I structure in which pores are oriented perpendicular to the substrate.

2.4 Conclusions and Further Work

This Chapter has demonstrated the ability to synthesise mesoporous nickel with high quality mesoporosity using liquid crystalline phases of the inexpensive Brij® surfactants. This mesoporous nickel has been made in a range of pore geometries and sizes, parameters that may be controlled by appropriate selection of the surfactant and deposition conditions. Deposition from the template based on the surfactant Brij® 56 was shown to be a diffusion limited process.

These mesoporous nickel electrodes were characterised structurally and the charge storage properties were examined in alkaline solution. These investigations showed large charge densities coupled with extremely rapid charge transfer rates limited only by the conductivity of the alkaline electrolyte.

Further to the work presented in this Chapter, it would be of interest to develop a synthesis route capable of producing mesoporous nickel with high quality porosity from templates based on the Pluronic® surfactants. The larger pore sizes of such materials would extend further the range of applications in which mesoporous nickel may be used.

2.5 References

[1] A. H. Whitehead, J. M. Elliott, J. R. Owen and G. S. Attard, Chem. Comm., 1999, 331.

[2] Mitchell, D. J.; Tiddy, G. J. T.; Waring, L.; Bostock, T.; McDonald, M. P. *J. Chem. Soc., Faraday Trans. I* **1983**, 79, 975.

[3] Angerstein-Kozlowska, H.; Conway, B. E.; Hamelin, A.; Stoicoviciu, L. *Electrochim. Acta.* **1986**, 31(8), 1051.

[4] N. R. B. Coleman, PhD thesis, University of Southampton, 1999.

[5] G. Wanka, H. Hoffmann and W. Ulbricht, Macromolecules, 1994, 27, 4145.

[6] A. Lachenwitzer and O. M. Magnussen, J. Phys. Chem. B, 2000, 104, 7424.

[7] A. J. Arvia and D. Posadas, Encyclopedia of Electrochemistry of the Elements, Marcel Dekker, New York, 1975, 211-421.

[8] D. Golodnitsky, N. V. Gudin and G. A. Volyanuk, J. Electrochem. Soc., 2000, 147, 4156.

[9] K. B. Yazimirski and L. I. Budarin, Zh. Neorg. Khim., 1962, 7, 1090.

[10] Bartlett PN, Birkin PR, Ghanem MA, et al. *J Electrochem.Soc.* **2001,** 148, C119-C123.

[11] P. Yang, D. Zhao, D. I. Margolese, B. F. Chmelka and G. D. Stucky, Chem. Mater., 1999, 11, 2813.

[12] A. Seghiouer, J. Chevalet, A. Barhoun and F. Lantelme, J. Electroanal. Cmem., 1998, 442, 113.

[13] Burke,L.D., and Twomey, T.A.M., J. Electroanal Chem **1984**, 162, 101-119.

[14] H. Bode, R. Dehmelt and J. Witte, Electrochim. Acta, 1966, 11, 1079.

[15] R. E. Carbonio and V. A. Macagno, J. Electroanal. Chem. 1984, 177, 217.

[16] B. Beden and A. Bewick, Electrochim. Acta, 1988, 33, 1695.

[17] Seghiouer, A., Chevalet, J., Barhoun, A., and Lantelme, F. J. Electroanal. Chem **1998**, 442, 113-123

[18] Vukovic,M., J.Applied Electrochem,**1994**, 24, 878-882.

[19] Amjad, M.; Pletcher, D.; Smith, C., *J. Electrochem. Soc.*, **1977**, 203.

[20] H. Bode, K. Dehmelt and J. Witte, Electrochim. Acta, 1966, 11, 1079.

[21] H. Bode, R. Dehmelt and J. Witte, Z. anorg. allg. Chem., 1969, 366, 1.

[22] H. H. Ewe, E. W. Justi, A. W. Kalberlah and A. F. Schmitt, Energy Conversion, 1972, 12, 1.

[23] W. Visscher and E. Barendrecht, J. Electroanal. Chem., 1983, 154, 69.

[24] L. M. M. de Souza, F. P. Kong, F. R. McLarnon and R. H. Muller, Electrochim. Acta, 1997, 42, 1253.

[25] R. W. Crocker and R. H. Muller, *Structural Transformation of Nickel Hydroxide Films During Anodic Oxidation, Electrochemical Society Meeting Extended Abstracts*, The Electrochemical Society, Pennington NJ, 1992, 92, 132.

[26] I. G. Cassella, M. R. Guascito and M.G. Sannazzaro, J. Electroanal. Chem., 1999, 462, 202.

[27] D. J. Jeong, W. S. Kim, Y. K. Choi and Y. E. Sung, J. Electroanal. Chem., 2001, 511, 79.

[28] M. Malmsten and B. Lindman, Macromolecules, 1992, 25, 5440.

[29] F. Hahn, B. Beden, M. J. Croissant and C. Lamy, Electrochim. Acta, 1986, 31, 335.

[30] P. W. T. Lu and S. Srinivasan, J. Electrochem. Soc., 1978, 125, 871.

Chapter 3

The All-Mesoporous Supercapacitor

3.1 Background and Objectives

Until now, supercapacitor devices have utilized nanoparticulate and xerogel materials such as those described in Section 1.1 in the fabrication of their electrode structures. However, the morphologies of these structures impose both significant resistive and diffusive limitations on the rate of charge and discharge of the devices. As such, the structural properties of these materials are far from ideal in an application where rapid charge and discharge with minimal power loss is required.

The electrochemical performance characteristics of present supercapacitor technologies also contribute to performance decay in such devices. Supercapacitors exhibiting an 'ideal' capacitive behaviour are in fact not ideal for application as pulse power devices. The linear dependence of state of charge on voltage characteristic of supercapacitor devices means that the energy density is only half of that of a battery-like system (storing the same amount of charge and with the same operating voltage range), which holds its charge close to or at the maximum operating voltage. The ideal pulse power device then would be more aptly described as a battery capable of charging and discharging very rapidly. This device could possess the energy density of a battery, but the power density characteristic of supercapacitors. In order to construct such a device, the associated redox processes would have to occur extremely rapidly, facilitated by extremely small bulk diffusion distances working in concert with high electrolyte conductivity and ideal pore geometry.

The work described in this Chapter follows from the more fundamentally grounded work of Chapter 2, which discussed the synthesis and characterisation of liquid crystal templated mesoporous nickel. In Chapter 2 it was demonstrated that mesoporous nickel with hexagonal pore geometry could be fabricated with a range of pore sizes depending on the templating surfactant used. By virtue of the designed structure of the material this mesoporous nickel was shown to be capable of facilitating extremely rapid charge transfer rates for the charging/discharging reaction in alkaline solution.

Here we discuss the application of liquid crystal templated mesoporous nickel to supercapacitor technology. We do not present new electrode chemical compositions but

attempt to demonstrate how supercapacitor/battery performance may be improved solely by designing the electrode structure. The objectives of the work are described below:

1. To synthesise and characterise liquid crystal templated mesoporous palladium with high surface area and high charge and discharge rate capability. This material functions as the negative electrode in the all-mesoporous supercapacitor. Characterisation involved electrochemical analysis of the palladium, particularly investigation of charging and discharging rates.

2. To fabricate and evaluate the performance of a supercapacitor device employing mesoporous nickel and mesoporous palladium as the positive and negative electrodes respectively. Performance evaluation included investigation of charging and discharging rates, operational voltage ranges, open circuit decay (self-discharge) and cyclability of the device.

3. To investigate the effects on the electrodes of supercapacitor operation. This involved both examination of compositional and structural changes in the electrodes.

3.2 Experimental

3.2.1 Synthesis of Mesoporous Electrode Materials

Mesoporous nickel was deposited potentiostatically at –0.9 V *vs.* SCE from the hexagonal (H_I) phase of a liquid crystalline mixture consisting of 65 wt. % Brij® 56/35 wt. % 0.2 M nickel acetate, 0.5 M sodium acetate and 0.2 M boric acid solution as described in Chapter 2. Mesoporous palladium films were also deposited potentiostatically from the H_I phase of a Brij® 56 based liquid crystalline solution at 0.1 V *vs.* SCE in a modified procedure based on that reported by Bartlett *et al.*[1] Modifications included the use of a templating solution consisting of 65 wt. % Brij® 56/35 wt. % 0.5 M ammonium tetrachloropalladate (Premion-99.998%, Alfa Aesar) solution and the use of isopropanol rather than water to remove the surfactant template after deposition. The presence of the H_I liquid crystalline phase in the palladium deposition template solution at 25 °C was confirmed using polarising light microscopy with an Olympus BH-2 polarizing microscope equipped with a Linkam TMS 90 heating/cooling stage accurate to ±0.1°C.

Mesoporous nickel and palladium electrodes were deposited with varying deposition charge densities onto 200 μm or 1 mm diameter gold discs encased in an epoxy insulator or approximately 1 cm^2 thin film gold electrodes made by evaporation of gold onto chromium-coated glass microscope slides. Gold disc electrodes were cleaned by first polishing consecutively on 25 μm, 1 μm and 0.3 μm alumina (obtained from Buehler) embedded microcloths then cycling the electrodes between –0.6 V and 1.4 V *vs.* a saturated mercury sulphate reference electrode (SMSE) at 200 mVs^{-1} for 5 min. in 2 M H_2SO_4 solution. With each cycle, a monolayer of gold oxide was formed and subsequently removed from the electrode surface.[2] Evaporated gold electrodes were cleaned in an ultrasonic bath of isopropanol for 60 min. prior to deposition, then rinsed with de-ionized water and dried under ambient conditions.

Deposition experiments were carried out using a Perkin Elmer VMP Multistat.

3.2.2 Electrochemical Characterisation

After deposition and washing in isopropanol for 24 h. to remove the surfactant template, deposited mesoporous electrodes were individually examined by cyclic voltammetry prior to assembly of the supercapacitor. This was done in a three electrode cell containing 6 M KOH or 2 M H_2SO_4 solution. The cell consisted of a Pyrex water-jacketed cell connected to a Grant ZD thermostated water bath which maintained a cell temperature of 25 °C, a mercury/mercury oxide (6 M KOH) reference electrode (Hg/HgO) and a large area Pt gauze counter electrode. In cases where 2 M H_2SO_4 solution was used, the reference electrode employed was a saturated mercury sulphate electrode (SMSE). All experiments were carried out at 25 °C and potentials in experiments involving a reference electrode are quoted against the Hg/HgO reference unless otherwise stated. Solutions were degassed by bubbling nitrogen or argon through the cell for 20 min. prior to the commencement of each experiment. Gasification of the solution by atmospheric oxygen during an experiment was prevented by maintaining a blanket of nitrogen or argon over the top of the solution for the duration of an experiment.

In order to study the performance and limitations of mesoporous nickel in a supercapacitor configuration, a negative electrode with higher capacity and power capability was needed. For this purpose, liquid crystal templated mesoporous palladium was used. The size of the mesoporous palladium electrode was made significantly larger than the mesoporous nickel electrode such that performance limitations would be due to limitations in the nickel electrode. Two-electrode supercapacitor testing without a separator was carried out using a 200 μm diameter mesoporous nickel positive electrode of approximately 1 μm thickness in conjunction with a 1 cm^2 mesoporous palladium electrode separated by 1 cm in degassed 6 M KOH solution.

The performance of porous separator materials was evaluated by measurement of the impedance of 10 mM KOH filled membranes. In these experiments surfactant modified PTFE Gore Alkaline Excellerator (30 μm thick from W. L. Gore and Associates), Celgard 3401 and 3501 (25 μm and 22 μm thick respectively from Celgard Inc.) and Whatman GF/F glass fibre (275 μm thick) membranes were subjected to 20 mV excitation voltage oscillations in a frequency range of 300 kHz to 100 Hz. The two

electrode cell assembly consisted of 9 mm diameter stainless steel discs between which the membrane was fixed with light pressure.

In experiments examining cycle life of the device the porous PTFE separator (Gore Excellerator) was used and both the mesoporous nickel and palladium electrodes were deposited onto approximately 1 cm^2 evaporated gold substrates and separated by the 6 M KOH filled membrane. The 6 M KOH solution was not degassed in this case because solution would rapidly become resaturated with atmospheric O_2 on assembly of the sandwich cell configuration. The device was cycled at 500 mV s^{-1} in the potential range 0 V to 1.2 V. All performance data are quoted in units with respect to the mass or geometric area of the nickel electrode.

The deposition charge in the synthesis of the 200 μm mesoporous nickel disc used in performance testing was –1.13 mC, which corresponds to a mass of 0.117 μg when taking into account a deposition efficiency of 34 %. The efficiency of the mesoporous nickel deposition process was quantified by anodic stripping voltammetry (see Section 5.3.3.2). This involved scanning the potential of an electrodeposited mesoporous nickel working electrode between –0.45 V and 0.9 V *vs.* a saturated calomel reference electrode (SCE) in 0.2 M HCl solution at 1 mV s^{-1}. The counter electrode was Pt gauze. The charge associated with the anodic dissolution of nickel and comparison of this charge with the deposition charge gave a deposition efficiency of 34 %. Anodic stripping voltammetry is described further in Chapter 5.

Cyclic voltammetry and potential step experiments were conducted using a custom made potentiostat and ramp generator in conjunction with a National Instruments data acquisition card with a maximum data acquisition rate of 200 kHz and LabVIEW software. Open circuit measurements were carried out using a Perkin Elmer VMP Multistat.

3.2.3 Structural Characterisation

Structural characterisation of mesoporous electrodes was carried before and after cycling in the supercapacitor configuration. Scanning electron microscopy (SEM) images were collected using a Philips XL-30 SEM with a field emission gun electron source. Small

angle x-ray scattering (SAXS) data was collected using a Siemens D-500 diffractometer emitting Cu-K_α x-radiation.

3.3 Results and Discussion

3.3.1 The Concept of the All-Mesoporous Supercapacitor

The all-mesoporous supercapacitor stores charge via a simple mechanism of proton shuttling between a mesoporous $Ni(OH)_2$ positive electrode and a hydrogen absorbing mesoporous palladium negative electrode as illustrated in the schematic of Figure 3.1. The mechanism is similar to that operating in nickel-metal hydride (Ni-MH) batteries where the palladium is replaced by another hydrogen absorbing material such as $LaNi_5$.

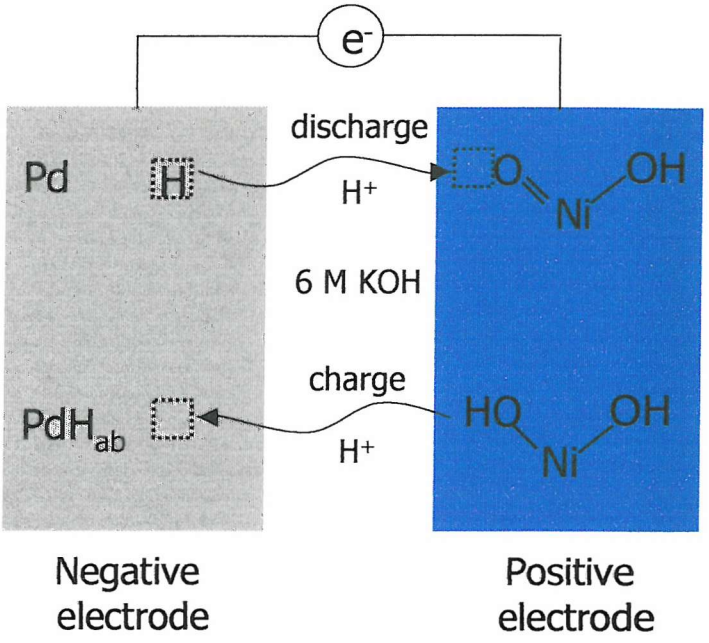

Figure 3.1 shows the relationship between proton movement and the $Ni(OH)_2/NiOOH$ and Pd/PdH_x redox couples that facilitate charge and discharge reactions in the mesoporous supercapacitor.

On charging the device, protons move from the $Ni(OH)_2$ into the palladium lattice, forming a palladium-hydrogen alloy according to the forward steps of Reactions 1 and 2 below

$$Ni(OH)_2 \leftrightarrow NiOOH + H^+ + e^- \qquad (1)$$

$$Pd + xH^+ + xe^- \leftrightarrow PdH_x \qquad (2)$$

3.3.2 Mesoporous Palladium

The work described in this Section did not seek to repeat the structural studies of Brij® 56 templated palladium as described previously by Bartlett *et al.*[1] but sought to fabricate and electrochemically characterise a high surface area palladium electrode capable of rapidly delivering and storing charge in alkaline solution. The rates of charge transfer were required to be sufficiently fast such that when combined with a mesoporous nickel electrode in the supercapacitor configuration as discussed above, the rate of charge transfer would be limited by the electrochemical rate limitations of the nickel electrode.

The cyclic voltammetry of H_I palladium deposited from a 65 wt. % Brij® 56 template in 6 M KOH is presented in Figure 3.2. Here, the lower potential limit is varied from –1.2 V to –1.3 V *vs.* Hg/HgO in order to better understand the relationship between anodic and

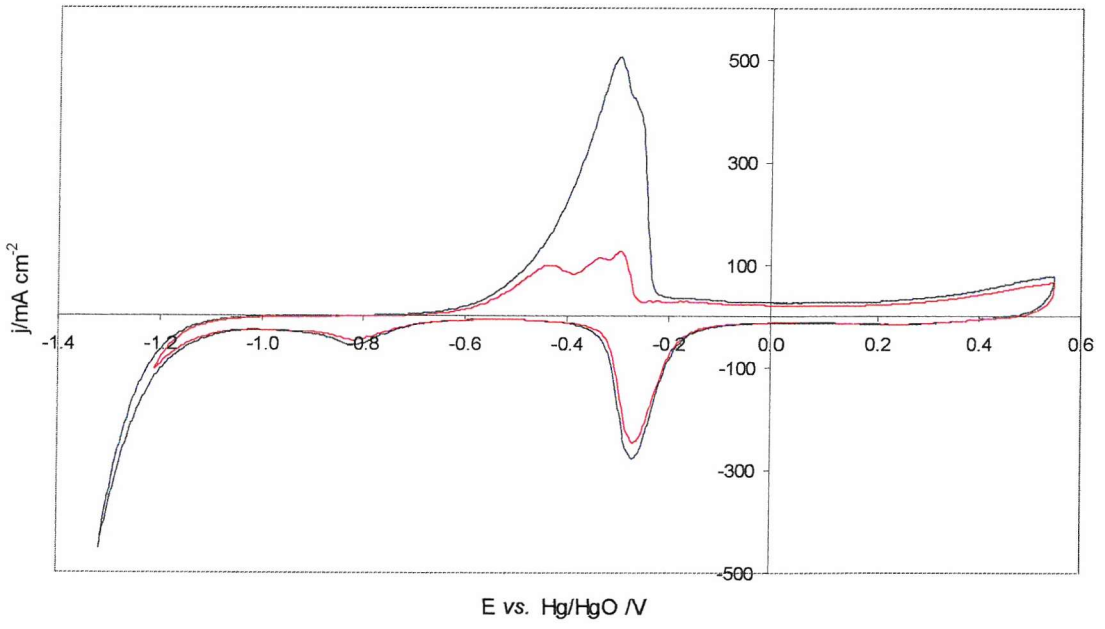

Figure 3.2 shows the effect on proton storage capacity at 200 mV s^{-1} of variation in the lower potential cycling limit between -1.3 V (blue) and –1.2 V *vs.* Hg/HgO (red).

cathodic currents at lower potentials. In comparison with the electrochemistry of nickel discussed in Chapter 2, the voltammetry of H_I palladium in 6 M KOH is more complex.[3] Anodic currents observed at positive potentials in Figure 3.2 are due to oxide formation, followed by subsequent stripping of this oxide with the cathodic peak at –0.25 V. At lower potentials the voltammetry is dominated by the hydrogen electrode reaction which proceeds on palladium surfaces via the Volmer-Tafel mechanism:[4]

$$H_2O + e^- \rightarrow H_{ad} + OH^- \quad (3)$$

$$2H_{ad} \rightarrow H_2 \quad (4)$$

where *ad* denotes the adsorbed state of a hydrogen atom. Hydrogen incorporation into the palladium bulk occurs in parallel to the Tafel process (4) according to the mechanism:

$$H_{ad} \rightarrow H_{ab} \quad (5)$$

Adsorption of hydrogen adatoms onto the palladium surface in Figure 3.2 by formation of the surface palladium hydride is indicated by the small cathodic peak at around –0.75 V *vs.* Hg/HgO. This is followed by the more substantial hydrogen absorption into the palladium lattice, indicated by the large current superimposed on the hydrogen evolution current at potentials below –1 V. On reversal of potential in the positive direction oxidation of absorbed hydrogen begins at approximately –0.7 V in both scans and peaks at –0.45 V and –0.29 V in scans **a** and **b** respectively. At higher potentials in both scans desorption of hydrogen adatoms occurs, as indicated by the peak centred at –0.3 V in scan **a** and the shoulder occurring at –0.26 V in scan **b**. Decreasing the lower potential limit as in scan **b**, has the effect of causing an increase in the anodic currents in the subsequent forward sweep. The larger anodic currents are a consequence of the greater extent of hydrogen occlusion observed in scan **b**. Close examination of the anodic peaks in Figure 3.2 reveals that the increased current can be attributed mainly to an increased amount of hydrogen oxidation rather than hydrogen adatom desorption, however the

superposition of peaks in scan **b** prevents quantification of this effect. The disproportionate increase in the extent of hydrogen absorption relative to adsorption is expected since the extent of hydrogen adsorption is limited to total coverage of the electrode surface regardless of the lower potential limit.

The surface area enhancement of H_I templated mesoporous palladium over that of non-templated palladium was quantified by comparison of the charge associated with the oxide stripping peak in 2 M H_2SO_4. Anodic currents in Figure 3.3 show the formation of a palladium surface oxide at potentials above 0.05 V *vs.* SMSE and subsequent reduction of the oxide with the cathodic peak centred at 0.03 V. The charge associated with the

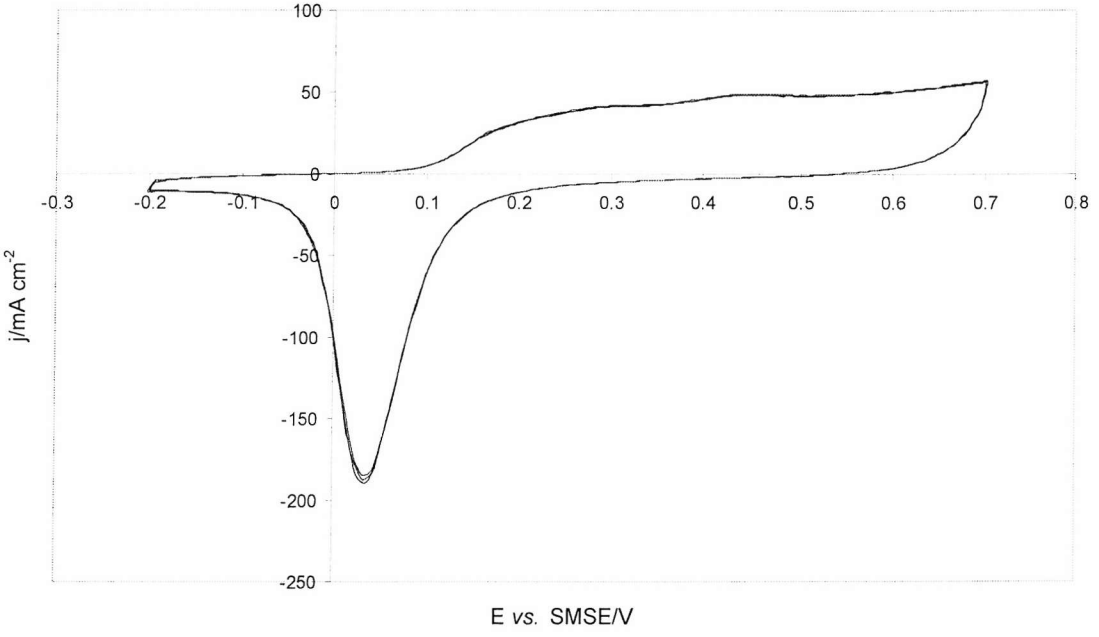

Figure 3.3. The charge associated with reduction of the palladium surface oxide in $H_2SO_{4(aq)}$ at 200 mV s^{-1} is used here to quantify electrode surface area.

cathodic peak was calculated as 112 mC cm^{-2} and when compared with the value of 424 μC cm^{-2} for an atomically flat palladium surface[5] in 2 M H_2SO_4 a roughness factor of 265 was obtained. This value confirms that the liquid crystal templating process described in Section 3.2.1 enables the fabrication of high surface area palladium electrodes. It does not however confirm the existence of the H_I pore geometry despite the fact that the palladium

was deposited from an H_I template. Nevertheless, the above results have demonstrated the synthesis of a high surface area mesoporous palladium electrode with the potential of producing high rates of charge transfer.

Variation in the charge density of the palladium discharge reaction (hydride oxidation and hydrogen desorption) with scan rate was investigated using the cyclic voltammetric conditions of Figure 3.2 above. The results shown here in Figure 3.4 indicate a rapid decrease in anodic charge density from a value of ~415 mC cm^{-2} as the scan rate is increased from 2 to 500 mV s^{-1}. A plot of the inverse of the charge density against the

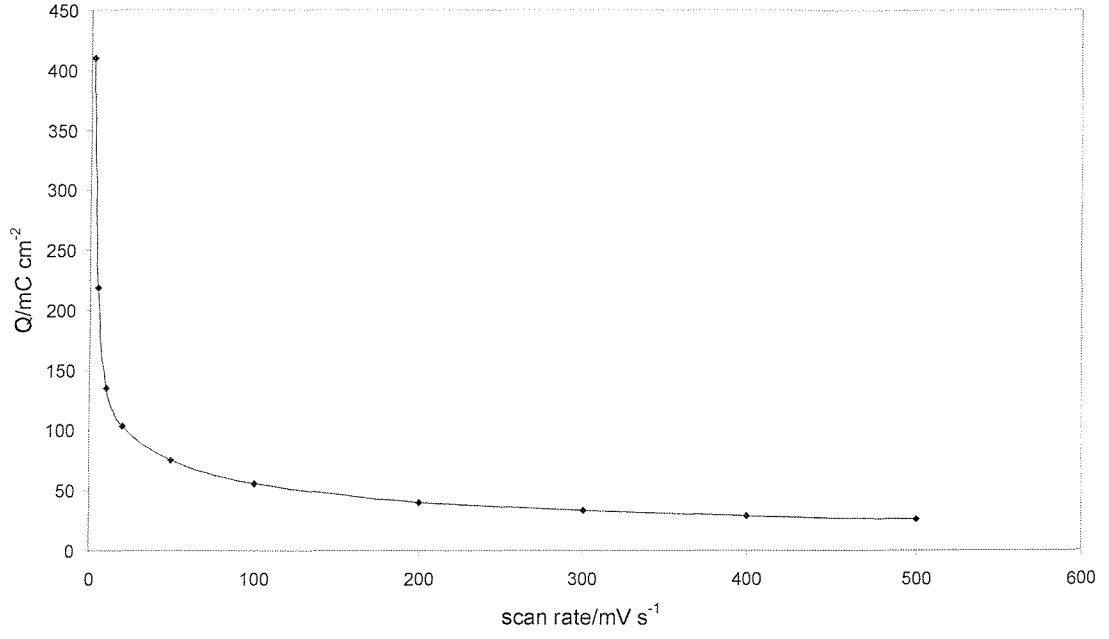

Figure 3.4 shows the decay in proton discharge capacity of mesoporous palladium in 6 M KOH at 25 °C on increasing scan rate from 2 to 500 mV s^{-1}.

square root of the scan rate reveals the straight line of Figure 3.5. This indicates that the palladium proton discharge in 6 M KOH is diffusion limited, which is not unexpected since the rate limiting step of the discharge reaction is expected to be the diffusion of hydrogen within the palladium bulk.

The discharge behaviour of mesoporous palladium was also investigated by potential step discharge in 6 M KOH solution. In this experiment mesoporous palladium was held at

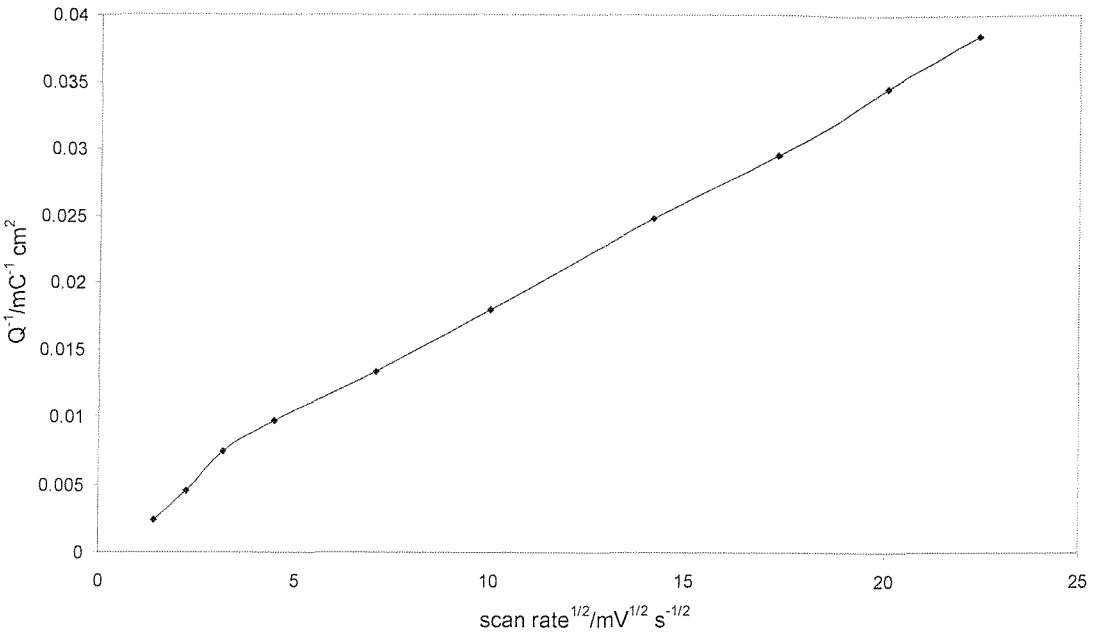

Figure 3.5. The proton discharge capacity of mesoporous palladium is shown here to be a diffusion limited process.

–1.1 V *vs.* Hg/HgO for 3 s in order to charge the palladium bulk with hydrogen (see Figure 3.2) followed by potential step to –0.8 V (during which no current flowed). This was followed by discharge of stored hydrogen with a step to 0 V. The discharge transient is presented in Figure 3.6 and shows an initial anodic spike of 4 A cm^{-2} followed by smaller current densities corresponding to the desorption of hydrogen adatoms from the high surface area palladium electrode and oxidation of hydrogen stored in the palladium bulk. A total of 16.4 mC of charge is passed from the 1mm diameter mesoporous palladium disc in Figure 3.6 and during the first 50 ms a charge density of 0.049 mC cm^{-2} is measured. A relatively thick (~1.5 μm) H_I mesoporous nickel disc with a diameter of 200 μm can be expected to pass, at most, approximately 0.094 mC (300 mC cm^{-2}) of charge in the first 50 ms of discharge (as will be demonstrated in Section 3.3.3). As such, the area of the mesoporous palladium electrode required to ensure that the supercapacitor rate limitation will be due to the nickel electrode is approximately 2 cm^2, assuming the same thickness as that of the sample discussed in the potential step of Figure 3.6.

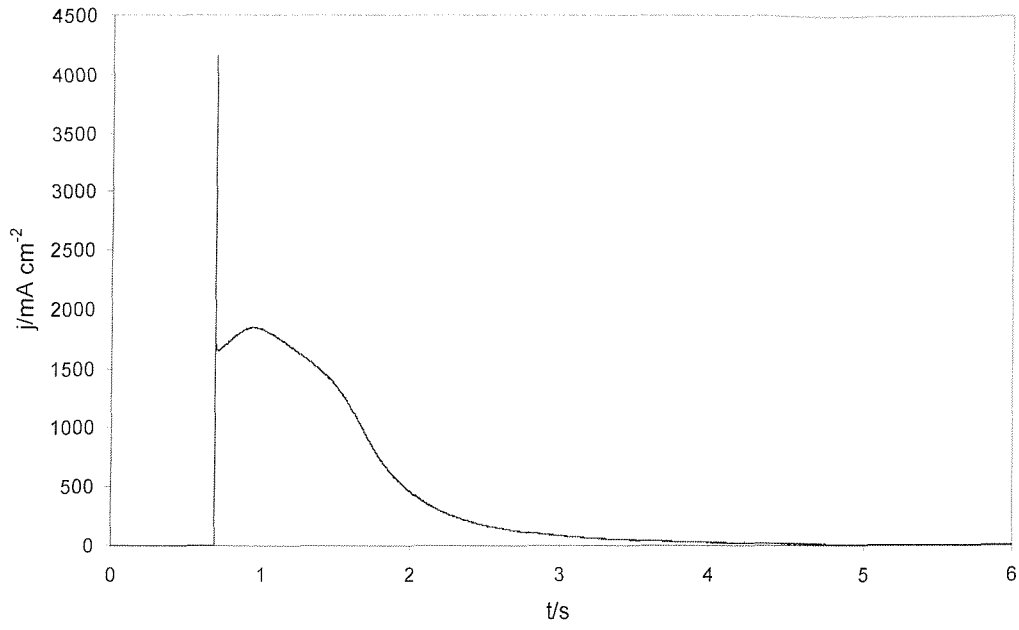

Figure 3.6. The potential step discharge of mesoporous palladium in 6 M KOH produces 16.4 mC here from double layer, hydrogen adatom and occluded hydrogen oxidation.

3.3.3 Electrochemical Testing of the All-Mesoporous Supercapacitor

In order to compare the electrochemical characteristics of mesoporous nickel and mesoporous palladium, the cyclic voltammograms of both these electrodes in 6 M KOH are overlaid in Figure 3.7. The anodic peak for nickel at 0.38 V *vs.* Hg/HgO shows oxidation of $Ni(OH)_2$ to NiOOH via Reaction (1) with subsequent reduction back to $Ni(OH)_2$ represented by the cathodic peak commencing at 0.4 V. The size of the latter

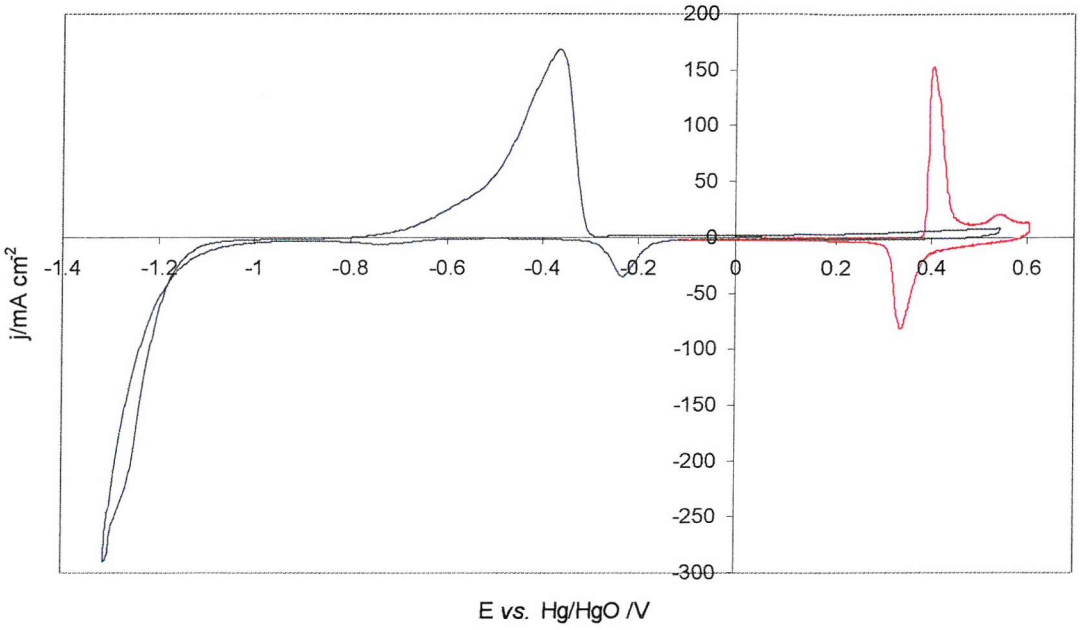

Figure 3.7 compares the electrochemical activity of H_I nickel and palladium in 6 M KOH at 20 mV s^{-1}.

peak represents the proton storage capacity of the electrode, that is, the reversible capacity of the electrode for proton storage.[6] In Figure 3.7, this is 295 mC cm^{-2}.

Based on a comparison of the voltammetry of mesoporous nickel and mesoporous palladium it could be expected that a charge storage device using these 2 electrodes would have a discharge voltage of approximately 1.2 V since this is approximately the potential difference between the onset of bulk hydrogen oxidation (resulting in the generation of protons) in palladium (-0.8 V *vs.* Hg/HgO) and the intercalation of protons into NiOOH (0.4 V *vs.* Hg/HgO). This discharge voltage is of course variable with the state of charge of the palladium which can vary between –0.8 V *vs.* Hg/HgO for a fully

charged electrode to –0.3 V *vs.* Hg/HgO where the palladium is fully discharged of hydrogen at 20 mV s^{-1}.

Figure 3.8 shows the cyclic voltammogram of a supercapacitor composed of a 200 μm mesoporous nickel positive electrode with a thick, 1 cm^2 mesoporous palladium negative electrode in 6 M KOH solution cycled in the potential range 0 V to 1.3 V. At approximately 1.22 V the device is charged, corresponding to the removal of protons

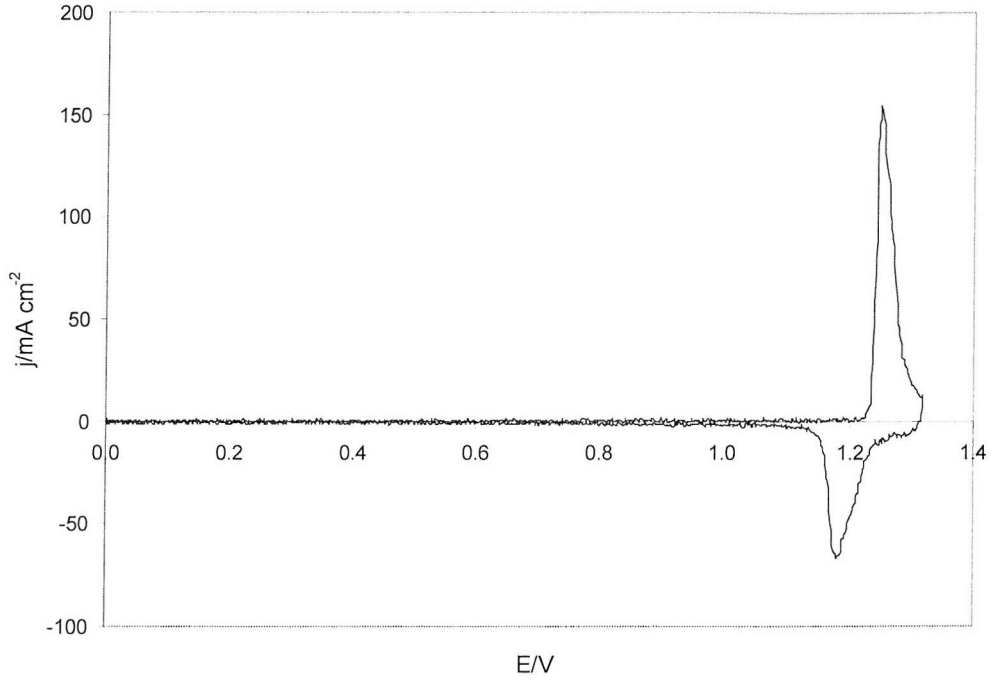

Figure 3.8. Potential cycling of a mesoporous palladium/nickel supercapacitor (with a 200 μm nickel electrode) separated only by 6 M KOH at 20 mV s^{-1} shows sharp charge/discharge peaks close to the maximum operating voltage.

from the $Ni(OH)_2$ and formation of NiOOH. Discharge occurs as protons from the palladium lattice move into the NiOOH structure reforming $Ni(OH)_2$ as indicated by the cathodic peak. The discharge current in this 20 mV s^{-1} cycle peaks at 67 mA cm^{-2} and the total charge passed is 257 mC cm^{-2}.

The shape of the voltammogram of Figure 3.8 more closely resembles that of a battery than a supercapacitor. Here, as is more clearly illustrated in Figure 3.9, 50 % of the charge on discharge is passed above 1.18 V in this 1.22 V device.

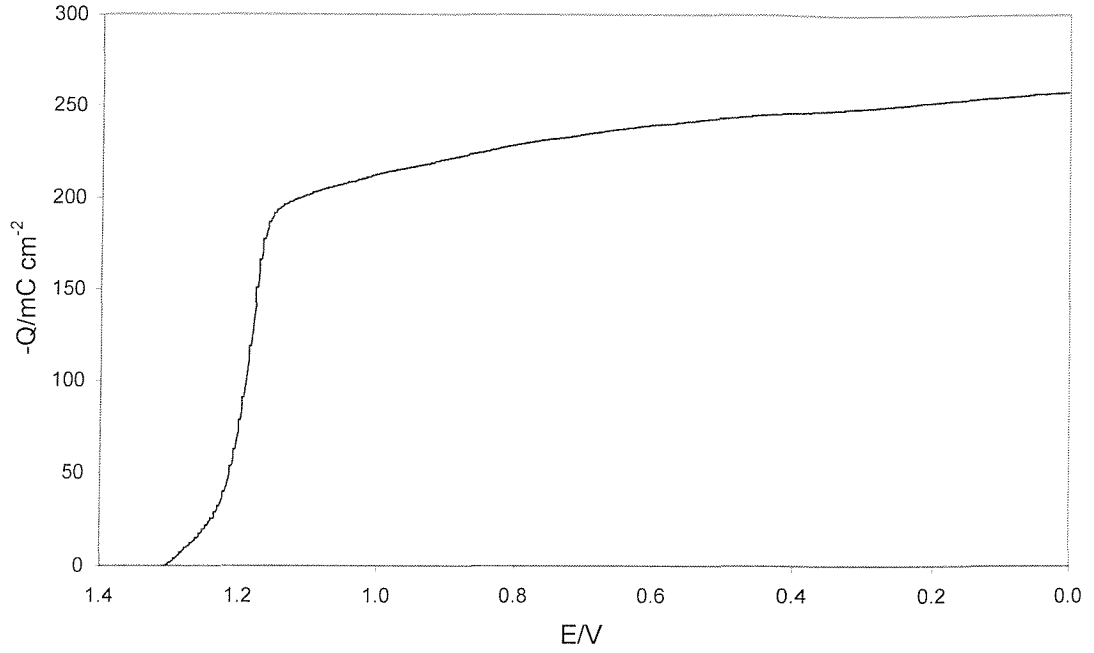

Figure 3.9 presents the integration (with respect to time) of Figure 3.8 showing the discharge voltage profile of the supercapacitor over its 1.22 V operating range in 6 M KOH.

This behaviour is in contrast with that of double layer supercapacitors and pseudocapacitive devices using transition metal oxides such as RuO_2, in which cell voltage falls linearly to 0 V with a constant discharge current. This illustrates an obvious advantage of the all-mesoporous supercapacitor over double layer and pseudocapacitive devices utilising aqueous electrolytes. That is, the former device is able to store a given quantity of charge at approximately twice the voltage of the latter devices which store their charge at a mean voltage corresponding to 50 % of the maximum operating voltage. Consequently, the energy density of an all-mesoporous device would be approximately twice that of a double layer/pseudocapacitive device of the same charge storage capacity. In order to determine how fast the supercapacitor could be charged and discharged the potential of the device was stepped between 0 V (discharged state) and 1.3 V (charged state) and the current response recorded. Figure 3.10 shows a single charge/discharge step sequence.

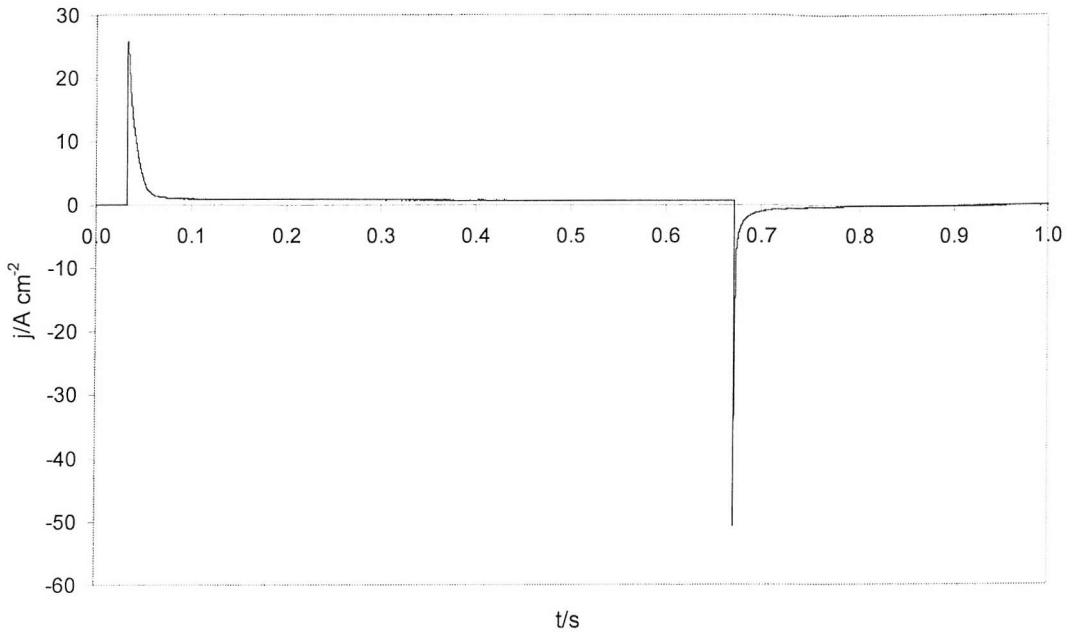

Figure 3.10. Potential step charging/discharging of the mesoporous supercapacitor separated only by 6 M KOH is characterised by large current spikes.

During the anodic spike, 800 mC cm^{-2} of charge is passed, 257 mC cm^{-2} of which is passed within the first 50 ms. Figure 3.9 showed that the charge capacity of the NiOOH electrode, that is, the capacity of the NiOOH to accept protons was exactly this amount. This initial charge can therefore be attributed to the movement of protons from the positive electrode to the negative electrode. The additional 543 mC cm^{-2} of charge observed in the anodic regime after the first 50 ms then, cannot be attributed to reversible charge storage since this is beyond the capacity of the nickel electrode. The reductive (with respect to the negative electrode) currents observed, which are relatively constant after this initial period are most likely due to the reduction of oxygen on the palladium electrode surface. This is possible since degassing may not have removed all of the solution dissolved oxygen prior to the experiment. Discharge of the device is represented by the large cathodic spike with a maximum amplitude of 50 A cm^{-2}, indicative of double layer discharge, superimposed on the rapid movement of protons from the palladium lattice into the NiOOH forming $Ni(OH)_2$. Here, 276 mC cm^{-2} is passed during the discharge step, 222 mC cm^{-2} (7×10^{-5} C over the 200 μm diameter or 166 mA h g^{-1}) of

which is passed in the first 50 ms. The latter charge density value probably corresponds to the charge storage capacity of the NiOOH overlayer discussed in Section 2.3.4.1. This capacity is rapidly accessible because of the direct contact between the overlayer and the electrolyte. The additional 54 mC cm^{-2} of charge is probably derived from the reduction of sub-overlayer pockets of NiOOH located deeper within the electrode structure (see Figure 2.33). Since this material lies beneath an insulating layer of $Ni(OH)_2$ after the initial 50 ms of the potential step, reduction occurs slowly as ionic species must diffuse through the insulator for reaction to occur.

Using the charge density value of 222 mC cm^{-2}, it is possible to make approximate calculations of the energy and power density with respect to the mass of the mesoporous nickel electrode. Taking the mean voltage of discharge as 1.18 V (the potential at which half the total charge has passed in Figure 3.9) we obtain an energy density of 706 kJ kg^{-1} of nickel using the formula

$$\Delta G = \frac{QV}{m_e} \qquad (5)$$

where m_e is the mass of the nickel electrode. Passing this quantity of energy in a 50 ms discharge gives a power density of 14.1 MW kg^{-1} according to

$$P = \frac{\Delta G}{\Delta t} \qquad (6)$$

where P is power density and Δt is the time of discharge. In comparing these values with existing supercapacitor electrode technologies it must be noted that these values are derived from whole device performance (not single electrode performance), but are quoted with respect to the mass of the nickel electrode and not the entire device or two electrode mass, since the mesoporous nickel is the material of interest in this study. With this in mind, comparison with the market leading supercapacitor material developed by Skeleton Technologies Group (a high surface area structured carbon) yields favourable results. The performance specifications of these materials quote a dry single electrode

capacitance (in organic electrolyte) of 160 F g^{-1} with a device voltage of 3 V and an RC time constant of 250 ms.[7] When considering the capacity of this material and its discharge characteristics (that of a double layer capacitor), a symmetrical device capacity, C_{total} of 80 F g^{-1} is calculated according to the equation

$$\frac{1}{C_{total}} = \frac{1}{C_1} + \frac{1}{C_2} \qquad (7)$$

where C_{total} is the device capacity with respect to the mass of a single electrode. This value gives an energy density of 360 kJ kg^{-1} using the equation

$$\Delta G = \frac{1}{2} C_{total} V^2 \qquad (8)$$

where V is the operating voltage of the device. This value is significantly lower than that of 706 kJ kg^{-1} calculated for the all-mesoporous supercapacitor nickel electrode discussed above. This comparison is particularly impressive when noting the large advantage endowed on the Skeleton Technologies device by virtue of its 3 V operating range. Typically, supercapacitors using aqueous electrolytes have substantially lower energy densities than those using organic electrolytes because of the operating voltage advantage, where energy density is proportional to V^2. The advantage of using aqueous electrolytes is in their higher electrolyte conductivities and therefore higher power densities (for a given energy density). This advantage is reflected in the time constants for discharge. The Skeleton Technologies material has a time constant of 250 ms, giving a power density of 1.44 MW kg^{-1} according to Equation 6. This value is almost 10 times lower than that of the all-mesoporous supercapacitor nickel electrode with a time constant of 50 ms and a power density of 14.1 MW kg^{-1}.

The high energy density derived from the all-mesoporous supercapacitor is due to two factors; i) the reliance on bulk redox capacity which fixes the average operating voltage close to the maximum operating voltage as discussed above, and ii) the high utilisation of the electrode mass for charge storage. This is achievable using the H_I templated electrode

structure. The percentage of atom utilisation in the electrode, that is, the percentage of nickel atoms participating in the charge storage process (assuming none of the charge is derived from double layer discharge) may be calculated based on the charge passed in the potential step experiment and the known mass of the mesoporous nickel electrode. This is

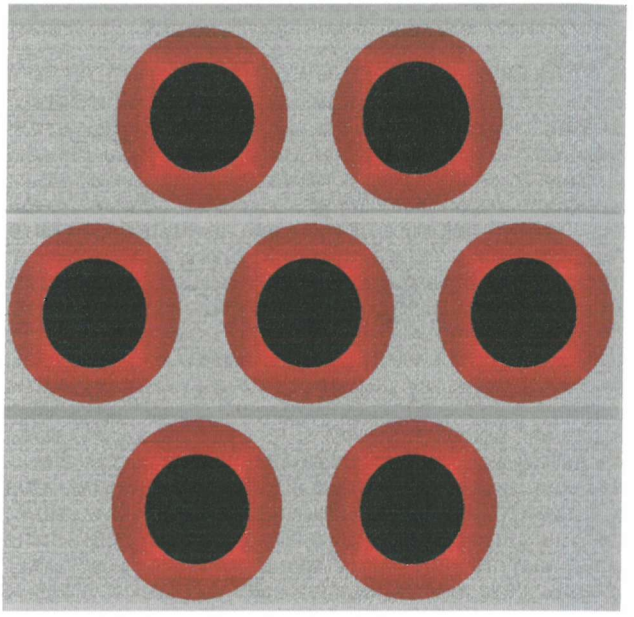

Figure 3.11 presents a schematic of the H_I mesoporous nickel electrode cross-section with 45 % of the material mass indicated (red) surrounding the pores (black).

calculated as 36 % atom utilisation in the first 50 ms and 45 % atom utilisation over the entire discharge. The proportion of electrode material used in the entire discharge process is illustrated schematically in Figure 3.11. Here, 45 % of the electrode mass is indicated in red. At this extent of atom utilisation in the perfect H_I structure of Figure 3.11, the oxidised active material lining the pores is not connected through the pore walls. As such, the continuous monolithic nickel metal phase that provides electrical conductivity within the electrode is not interrupted. The high power density of the all-mesoporous supercapacitor can also be attributed to the structure of the electrode. While the finely divided nature of the electrode ensures high levels of atomic utilisation, the structure also ensures that all of the electrode material is within 2 nm (according to SAXS data discussed in Section 2.3.3.2) of the electrolyte. Consequently, ionic species that must

diffuse through the electrode material to and from the electrolyte during cell operation have an extremely short diffusion path, enabling charge and discharge to occur rapidly. In addition, since the electrode structure is monolithic and contains no grain boundaries there is negligible ohmic loss during cycling. High power capability is also facilitated by the pore structure, which allows rapid diffusion of ionic species within the electrolyte.

3.3.4 Self-Discharge Characteristics

The open circuit potential (OCP) of a charged mesoporous supercapacitor was monitored in 6 M KOH solution as a function of time to assess the rate of self-discharge in the device. Self-discharge contributes to supercapacitor performance decay during periods of storage of a charged device or during operation when a charged device is awaiting the

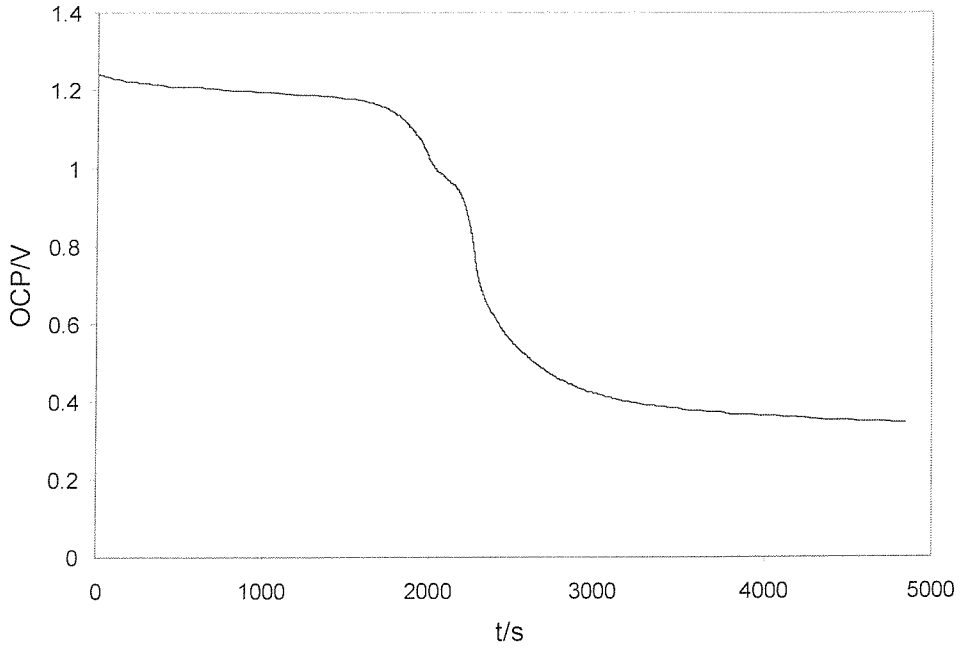

Figure 3.12 shows the open circuit decay of a charged mesoporous supercapacitor device in 6 M KOH at 25°C.

next discharge. Figure 3.12 shows the self-discharge transient of the all-mesoporous supercapacitor immersed in 6 M KOH solution. The OCP is initially 1.24 V, approximately equal to the stability window of aqueous solutions. Over 28 min. the OCP

decreases slowly to 1.16 V, showing self-discharge behaviour typical of aqueous battery systems. After this point however, the OCP decreases sharply levelling out into a plateau at approximately 0.35 V after 80 min. Two shoulders in the transient at 1.05 V and 0.90 V indicate a biphasic process of self-discharge, and possibly the involvement of absorbed and adsorbed hydrogen in/on the palladium electrode respectively. The mechanism by which the palladium electrode loses its charge was not investigated. It is possible that an impurity in the electrolyte reacted with the palladium causing it to lose charge.

The problem of self-discharge is well known to nickel-metal hydride (Ni-MH) battery systems. In their development of the Ni-MH battery, Matsushita Battery Industrial Co. observed significant self-discharge rates in their early battery systems. This was attributed to a surfactant species present in the electrolyte used to hydrophilise the hydrophobic polymer separators. The surfactant reacted with the metal hydride electrodes, generating a solution borne charge carrier. The absence of this problem in other Matsushita aqueous battery chemistries is testament to the susceptibility of Ni-MH systems to self-discharge.

3.3.5 Extended Cycling of the All-Mesoporous Supercapacitor

The cyclability of the nickel-palladium supercapacitor was investigated by continuously cycling a configuration consisting of 1 cm^2 mesoporous nickel and mesoporous palladium electrodes separated by a 6 M KOH filled porous membrane. This configuration in which the geometric area of each electrode was the same was used in order to represent a more realistic device.

A suitable separator was identified based on comparison of the impedance of a number of 10 mM KOH filled membranes. Minimisation of the separator and cell impedance was important here in minimising ohmic loss in the cell. The group of membranes tested consisted of a glass fibre membrane (GF/F), a porous polytetrafluoroethylene membrane (PTFE, W. L. Gore) and two porous polypropylene membranes of differing thickness and porosity (Celgard 3501 and 3401). The impedance spectra of these samples are presented in Figure 3.13. The impedance behaviour is clearly that of non-ideal resistor-capacitor

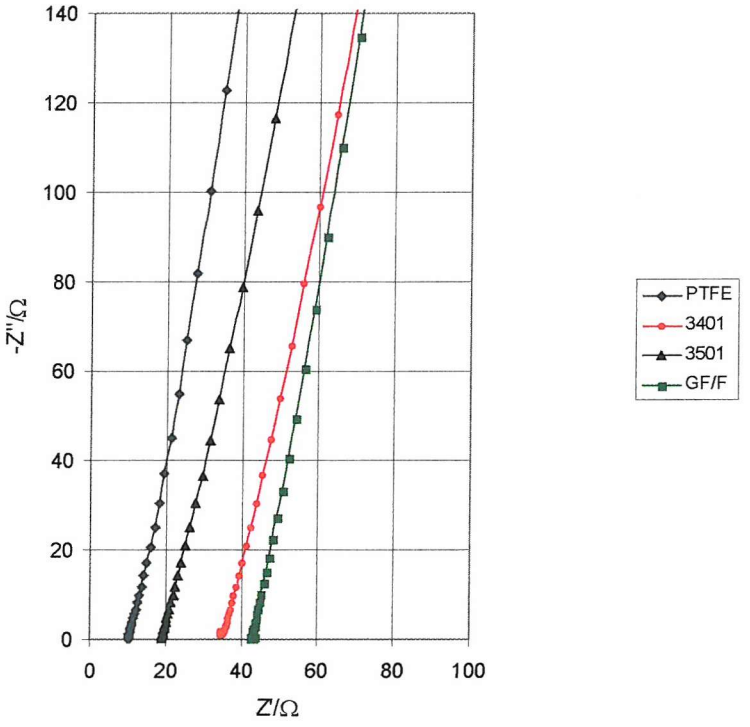

Figure 3.13 shows the Nyquist plot impedance spectra of the four 10 mM KOH filled supercapacitor separators.

series cells, however here only the high frequency real impedance intercept, that is, the resistance of each cell is important. These values, in addition to the calculated area

Membrane	R Ω	Thickness μm	ASR Ω.cm²
PTFE	**10.1**	**30**	**6.4**
3401	**34.0**	**25**	**21.6**
3501	**18.9**	**22**	**12.0**
GF/F	**42.2**	**275**	**26.8**

Table 3.1 summarises the performance data of the four 10 mM KOH filled separators as determined by ac impedance.

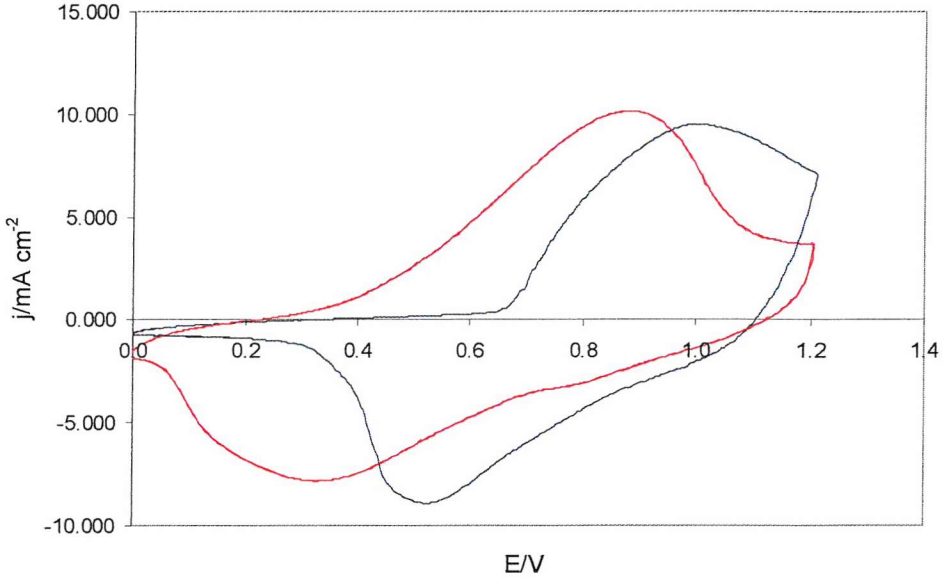

Figure 3.14 compares the first and 15000th cycles of a 1 cm^2 H_I mesoporous nickel/mesoporous palladium supercapacitor at 500 mV s^{-1}, incorporating a 6 M KOH filled GF/F separator.

specific resistances are presented in Table 3.1. Of the membranes studied, the PTFE membrane, although thicker than both of the polypropylene samples, showed the lowest impedance. This indicates that the PTFE membrane probably possessed a higher degree of porosity than the other membranes and possibly a less tortuous pore network.

The cyclic voltammogram of a 1 cm^2 mesoporous nickel-mesoporous palladium supercapacitor incorporating a PTFE separator (Gore) in presented in Figure 3.14. The shape of the voltammogram is considerably different to that of the configuration without

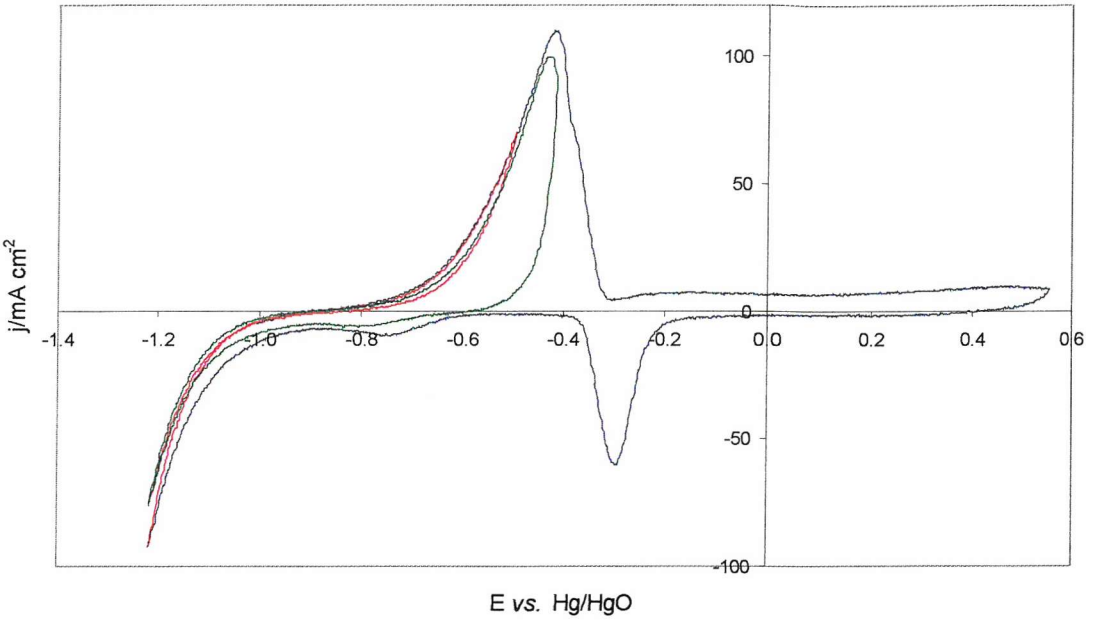

Figure 3.15. Variation of the upper potential limit from 0.55 V (blue) to –0.48 V (red) and –0.42 V (green) shows that hydrogen absorption does not occur more readily in mesoporous PdH_x than in mesoporous Pd in 6 M KOH at 20 mV s^{-1}.

a separator presented in Figure 3.8. The peaks are considerably broader and are separated by approximately 0.5 V as opposed to only 0.07 V in Figure 3.8. This is due to a combination of the IR limitation imposed on the cell with the introduction of the porous separator and the slow electrochemical response of the palladium, the capacity of which was not significantly larger than that of the $Ni(OH)_2$ electrode in this configuration. Figure 3.14 compares the first full 4.8 s cycle with the 15000th. The first and most obvious difference is that the latter voltammogram has been shifted to lower potentials by almost 0.2 V. This maybe explained by the gradual depletion of hydrogen in the palladium lattice with cycling, since in the potential range used it is more probable that oxygen reduction on the palladium surface rather than lattice replenishment by proton

insertion is occurring during charging. Oxygen reduction is observed in Figure 3.14 and not in Figure 3.8 since in the former case the 6 M KOH electrolyte is not degassed due to the configuration of the cell. Figure 3.2 established that significant hydrogen absorption into a palladium lattice empty of hydrogen does not occur at potentials above –1 V *vs.* Hg/HgO. It is not unreasonable however to suggest that the presence of absorbed or adsorbed hydrogen might increase the onset potential of hydrogen absorption into the palladium lattice, making it possible for proton insertion into the lattice to occur during supercapacitor cycling. As evidenced in Figure 3.15 however, the presence of hydrogen in a partially hydrogen depleted palladium lattice does not effect significantly the onset potential for hydrogen reduction. Figure 3.15 shows reversal of the potential at two different stages of hydride oxidation. With reversal of the forward sweep at –0.48 V *vs.* Hg/HgO, the voltammogram retraces itself with typical cathodic currents flowing below –1 V. With sweep reversal at –0.42 V the voltammogram shows hydrogen adsorption activity at –0.8 V followed again by hydrogen absorption and evolution currents at typical potentials. As such, the onset of hydrogen occlusion in a partially hydrogenated palladium lattice occurs at the same potential as that of a lattice devoid of hydrogen.

In the extreme case of complete depletion of the palladium lattice, both proton insertion and extraction processes become inactive in the potential range of supercapacitor operation. In this situation it is possible to envisage PdO formation as an alternative to proton extraction to explain the current flowing near 0 V in the aged cell of Figure 3.14.

Of most interesting note in Figure 3.14 however is that after 15000 cycles the discharge capacity increases by approximately 10 %. This result has two implications. The first is that the mesoporous electrodes seem to resist the decrepitation on cycling that is associated with capacity decay in other supercapacitor and battery systems that utilize insertion processes. This is not surprising since it is expected that a uniform monolithic structure such as that represented schematically in Figure 3.11 would withstand the strain of volume expansion and contraction better than those consisting of an aggregation of sintered particles of non-uniform size. The second implication addresses the fact that not only does the capacity of the mesoporous nickel electrode resist decay, but actually increases with cycling. This effect is rationalized by understanding that in 6 M KOH under potential cycling conditions the amount of $Ni(OH)_2$ in a nickel electrode may

increase with time as more of the nickel base metal is oxidized. In effect this increases the amount of active material in the electrode and hence the capacity. A number of groups have shown that the capacity of an electrodeposited nickel electrode may be increased by up to 30 times by application of the appropriate cycling conditions in alkaline solution.[8,9,10] Here, such a large increase in capacity cannot be expected since during initial cycling 45 wt. % of the electrode material is already being utilised. Fortunately, a large increase in capacity corresponding to complete conversion of the nickel base metal to the electrically non-conducting $Ni(OH)_2$ was not observed since this would destroy the continuous path of nickel metal in the mesoporous electrode that provides electrical conductivity and acts as a nanoscale current collector.

3.3.6 Structural and Compositional Effects of Cycling

Electrodes employing insertion processes as a means of charge storage typically undergo significant structural changes during their lifetime. As the result of the expansion and contraction accompanying insertion and extraction of ions respectively, electrode structures are subjected to severe stresses during operation, which often results in decrepitation of the electrode material. This causes capacity loss. As discussed in Section 3.3.5 above, capacity loss was not observed in the all-mesoporous supercapacitor. On the contrary, capacity was observed to increase on cycling. This was explained by an increase in the amount of active material in the electrode during cycling, that is, some of the electrochemically inactive nickel base metal present during the first cycle was converted to the active hydroxide during the experiment. This increase in capacity however does not discount the occurrence of decrepitation of the electrode structure. Indeed, decrepitation may have occurred, but the effects on capacity may have been disguised by increases in the amount of active electrode material.

In order to assess the relevant structural and compositional changes occurring within the

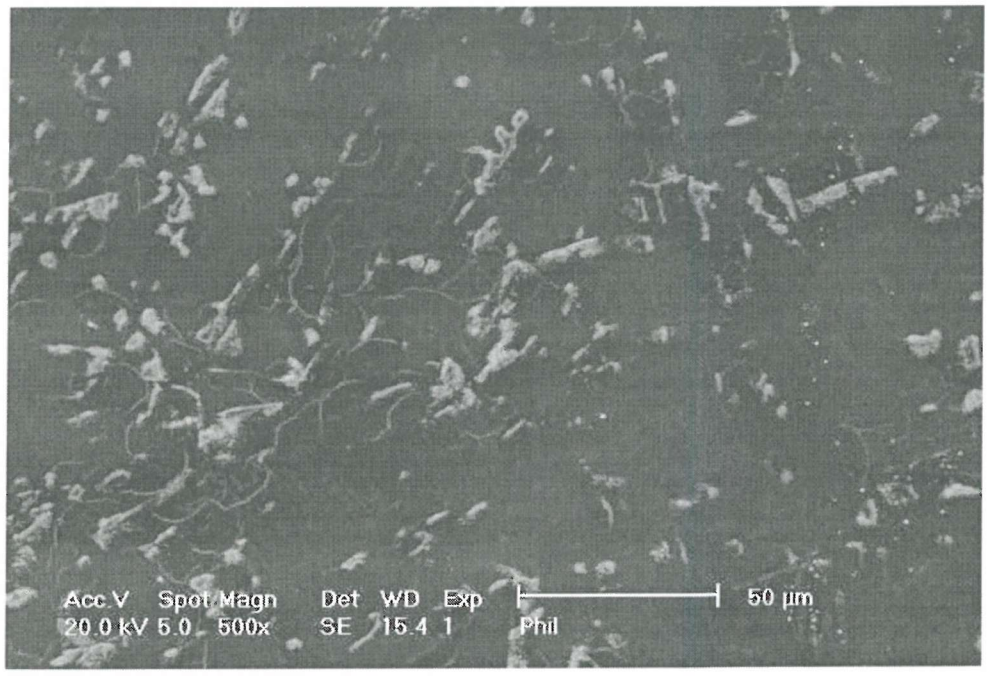

Figure 3.16 shows a freshly washed mesoporous nickel electrode surface largely consisting of the unoxidised metal.

mesoporous nickel electrode with extended cycling, SEM investigations using both secondary electron (SE) and back-scattered electron (BSE) imaging modes were used to compare cycled and uncycled nickel electrodes. Figure 3.16 shows the SE image of a freshly prepared mesoporous nickel film deposited from a 65 wt. % Brij® 56 templating electrolyte after washing in isopropanol. In SE mode, dark areas of the image represent material of high electronic conductivity, whereas lighter areas represent a more insulating material. In the latter areas interrogating electrons accumulate by virtue of the low electronic conductivity and appear brighter to the SE detector. Figure 3.16 then, shows an electrode surface consisting largely of nickel metal with dispersed areas of a more insulating material, probably $Ni(OH)_2$ which was shown in Section 2.3.4.2 to form spontaneously in air and/or during post-deposition washing. Images of the electrode of Figure 3.16 recorded using the topographical and compositional modes of BSE imaging lacked sufficient contrast to produce a well resolved image. Lack of contrast in topographical mode is consistent with a very smooth mesoporous nickel film and this

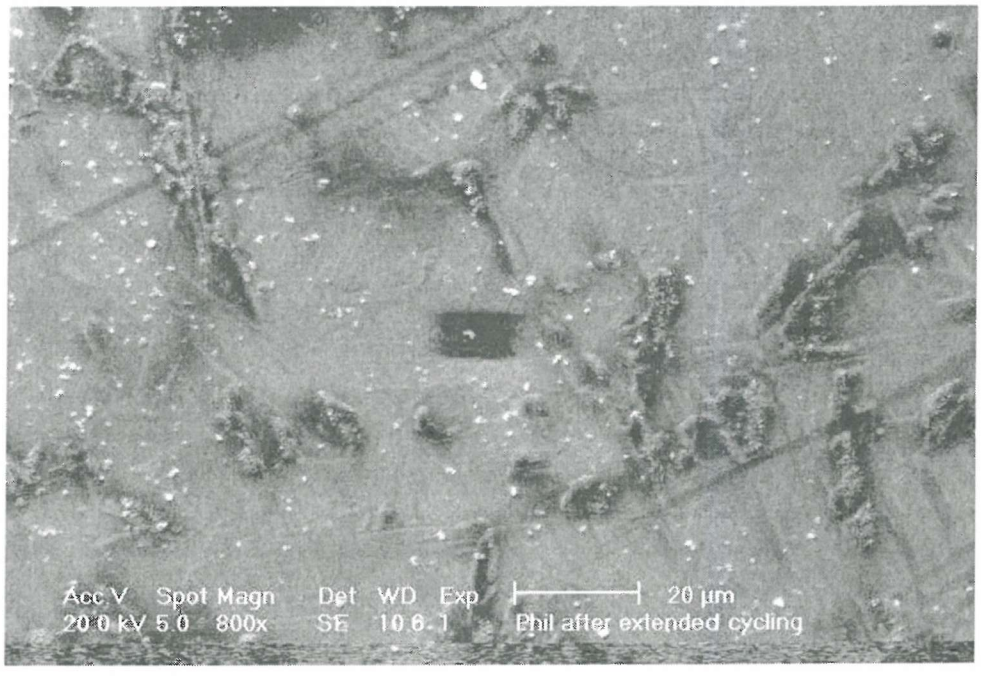

Figure 3.17. Secondary electron imaging shows that after cycling in 6 M KOH the mesoporous nickel electrode is predominantly composed of the insulating $Ni(OH)_2$.

result using compositional mode imaging indicates that the hydroxide materials identified in the SE image of Figure 3.16 are extremely thin and probably located only on the outer surface of the electrode.

The SE image of a mesoporous nickel electrode after 15000 cycles in the supercapacitor configuration is presented in Figure 3.17. In marked contrast to Figure 3.16, the majority of the surface appears to be composed of the insulating $Ni(OH)_2$ with dispersed areas of a more conductive material, which in this case is probably NiOOH. The presence of nickel metal is discounted here since surface nickel metal was shown in Section 2.3.4.1 to be completely oxidised during the first cycle in 6 M KOH. The darker areas of Figure 3.17 indicate not only the presence of NiOOH, but that this material is in electrical contact with the substrate. That is, either the NiOOH phase is continuous throughout the thickness of the electrode, or that it is in contact with the remains of the nickel base metal. Figure 3.17 appears to show a rougher surface than that of the uncycled sample. Roughening is indicative of the structural changes encountered by insertion electrodes on

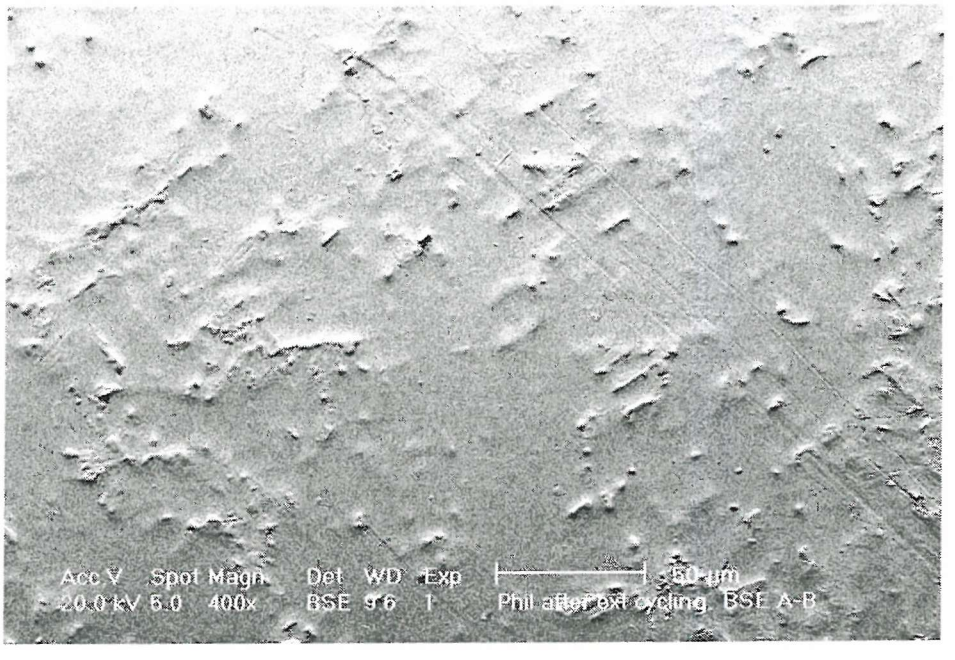

Figure 3.18. Topographical mode back scattered electron imaging shows a roughened mesoporous nickel electrode after cycling in 6 M KOH.

cycling including decrepitation, however it is impossible to quantify the extent of any decrepitation here.

Figure 3.18 shows the BSE image of a cycled mesoporous nickel electrode recorded in topographical mode. While the remnants of a smooth electrode are observable, the surface is punctuated by raised areas that are probably the result of expansion of material both on the electrode surface and within the bulk. This provides evidence that the effects of repeated electrode expansion and contraction on cycling a templated mesoporous electrode are not uniform in their resulting structural changes on the electrode. Figure 3.19 shows the BSE image of the same mesoporous nickel sample of Figure 3.18 recorded in the same sample position but in composition mode. Dark areas of the image

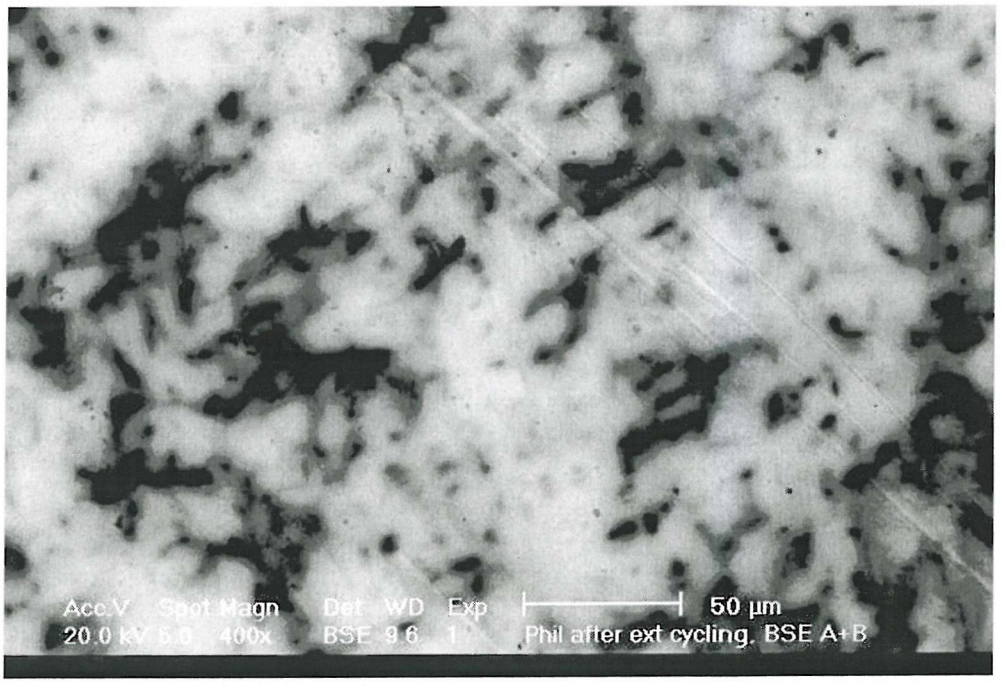

Figure 3.19. Compositional mode imaging reveals pockets of NiOOH within a matrix of $Ni(OH)_2$ in the cycled mesoporous nickel supercapacitor electrode.

again represent material of high electrical conductivity, that is, NiOOH, whilst light areas correspond to the more insulating $Ni(OH)_2$. Intermediate grey areas which appear most often at the borders of the dark NiOOH segments indicate sub-surface NiOOH deposits

covered by a thin layer of insulating $Ni(OH)_2$. Comparison of Figures 3.18 and 3.19 reveals that the areas in which NiOOH is present are also those areas constituting the most obvious areas of expansion in the topographical image.

3.4 Conclusions and Further Work

Chapter 3 has demonstrated the application of liquid crystal templated mesoporous nickel in a pulse power device. Very high power and energy densities have been observed in the device using a mesoporous palladium negative electrode. Although mesoporous palladium is not the preferred negative electrode material due to high cost, it has allowed the demonstration of the properties of an inexpensive and high performance positive electrode.

By designing and controlling the electrode structure it has become possible to take what is essentially a Ni-MH battery positive electrode material and fabricate an electrode with performance specifications closer to that of a high performance supercapacitor electrode.

The H_I electrode mesostructure is well designed for supercapacitor applications. When filled with electrolyte, the electrode can be thought of as a three-phase composite composed of an interconnected nickel current collector base, coated with the $Ni(OH)_2$ active material which is in contact with the electrolyte. All three phases are in either in intimate contact or within 2 nm of each other and the overall surface area of the 'phase boundaries' is extremely high.

3.5 References

[1] P. N. Bartlett, B. Gollas, S. Guerin and J. Marwan, *Phys. Chem. Chem. Phys.*, **4**, 3835 (2002).

[2] H. Angerstein-Kozlowska, B. E. Conway, A. Hamelin and L. Stoicoviciu, *Electrochim. Acta*, **31**, 1 (1986).

[3] N. Tateishi, K. Yahikozawa, K. Nishimura and Y. Takasu, *Electrochim. Acta*, **37**, 2427 (1992).

[4] M. Enyo, J. Electroanal. Chem., 1982, 134, 75.

[5] D. A. J. Rand and R. Woods, J. Electroanal. Chem., 1972, 35, 209.

[6] L. M. M. de Souza, F. P. Kong, F. R. McLarnon and R. H. Muller, *Electrochim. Acta*, **42**, 1253 (1997).

[7] www.skeleton-technologies.com

[8] M. Vukovic, *J. App. Electrochem.*, **24**, 878 (1994).

[9] L. D. Burke and T. A. M. Twomey, *J. Electroanal. Chem.*, **162**, 101 (1984).

[10] F. Hahn, B. Beden, M. J. Croissant and C. Lamy, *Electrochim. Acta*, **31**, 335 (1986).

Chapter 4

Application of Mesoporous Nickel to Lithium Battery Electrodes

4.1 Background and Objectives

As discussed in Section 1.5.3 there exists a considerable research effort focussed on the elucidation of low temperature synthetic routes to lithium containing transition metal oxides. The majority of the routes discovered thus far involve ion exchange of the parent oxide/oxyhydroxide protons with lithium ions. In this process it is desirable that the parent material be of the appropriate crystalline phase since at low temperatures there is little energy to force the intercalation of guest ions into a foreign host structure. In the case of nickel based electrodes the desired phase of the NiOOH parent material is the β- phase.

The cyclic voltammetry of mesoporous nickel in alkaline solution presented in Chapter 2 discussed the presence and formation of the β- and γ- phases of NiOOH. These data showed the exclusive presence of β-NiOOH during the initial stages of cycling.

It is on this basis that the work described in this Chapter was initiated. It was reasoned that if the synthesis of a high phase purity β-NiOOH was possible then perhaps a similar low temperature route to those described previously could be developed in order to fabricate mesoporous nickelate lithium battery electrodes with high rate capabilities. This work follows from that described in Chapter 3 in which the fabrication of a high energy and power density mesoporous supercapacitor based on aqueous chemistry was detailed. In essence, the work of this Chapter seeks to extend the concept of the mesoporous supercapacitor to lithium chemistries such that the attainable energy densities of mesoporous electrode charge storage devices may be extended even further. This Chapter does not seek to construct such a device as in Chapter 3, but demonstrates possible chemistries for such a device. The objectives of the work are described below:

1. To examine methods of low temperature lithium ion exchange in mesoporous Ni/NiOOH electrodes.

2. To investigate the lithium ion storage properties of materials made according to Objective 1.

4.2 Experimental

4.2.1 Ion Exchange Reactions

The mesoporous nickel electrodes used in this work were deposited from the H_I phase of 65 wt. % Brij® 56/0.2 M nickel(II) acetate deposition solution templates at 25 °C as discussed in Chapter 2 for 24 h. periods. Deposition was carried out on 2 cm^2 planar gold electrodes made by evaporation of gold onto chromium coated glass microscope slides. After deposition all electrodes were washed in isopropanol for 24 h. to remove the surfactant template. Prior to ion exchange treatments the mesoporous nickel was cycled in 6 M KOH between the limits –1.06 V and 0.6 V *vs.* Hg/HgO at 20 mV s^{-1}. This served to confirm the high surface area and charge storage capacity of the electrodes and to facilitate growth of the NiOOH active material in which ion exchange was to take place. After four cycles the mesoporous electrodes were removed from the solution under potential control (at 0.6 V) such that the surface layers were in the NiOOH state. The electrodes were then washed with water and dried in an evacuated Buchi furnace at 50 °C for 24 h. The dried mesoporous electrodes were then transferred to a dry box. Ion exchange was carried out inside the dry box by immersion of a cycled mesoporous nickel electrode in either 1 M $LiPF_6$ in propylene carbonate (PC) (purchased from Merck and used without purification) or 1 M $LiSO_3CF_3$ in PC at room temperature. 1 M $LiSO_3CF_3$ in propylene carbonate (PC) was made by drying $LiSO_3CF_3$ (used as received from Fluka) in an evacuated Buchi furnace at 60 °C for 48 h. followed by mixing with PC (as received from Aldrich) in a dry box. Alternatively, ion exchange was carried out in aqueous solution by cycling a freshly washed H_I mesoporous nickel electrode in 1.9 M $LiOH_{(aq)}$ at 80 °C with potential limits of –1.06 V and 0.6 V *vs.* Hg/HgO. After 10 cycles the electrodes were washed in water and dried in a Buchi furnace as above followed by transfer into a dry box.

4.2.2 Electrochemical Testing

After ion exchange all electrodes were assembled within the dry box into cells for electrochemical testing outside of the dry box. Cells consisted of air-tight Pyrex glass electrochemical vessels and contained the mesoporous working electrode with lithium counter and reference electrodes. The electrolyte solution was either 1 M $LiPF_6$ in PC

or 1 M $LiSO_3CF_3$ in PC. All aqueous solutions were prepared using deionised water and glassware was cleaned by soaking in a 3 % solution of Decon 90 (Aldrich) for 24 h., followed by soaking in dilute $HCl_{(aq)}$ for at least 6 h. and subsequent rinsing with deionised water.

Electrochemical experiments involving aqueous solutions were conducted using a purpose built potentiostat and ramp generator. Cell temperature was held at 25 °C for all testing experiments and was maintained with an accuracy of ±0.1°C using a Grant ZD thermostated water bath. Non-aqueous electrochemistry was conducted using a Solartron 1287 Electrochemical interface and Corrware software.

4.3 Results and Discussion

4.3.1 Mesoporous Nickel as a Positive Electrode Material

As discussed in Section 1.5.3 NiO_2 is a well known H^+ and Li^+ intercalation host used as a lithium battery positive electrode material. Similarly, NiOOH has a high capacity for H^+ storage and indeed this reaction is the basis of the $Ni(OH)_2$/NiOOH redox couple discussed in Chapters 2 and 3. To investigate NiOOH as a possible Li^+ intercalation host, mesoporous NiOOH formed electrochemically from the oxidation of mesoporous nickel in alkaline solution was ion exchanged by soaking in $LiPF_6$/PC at room temperature. Figure 4.1 shows the cyclic voltammetry of an ion exchanged electrode in 1 M $LiPF_6$/PC between 2 V and 4 V *vs.* Li at 20 mV s^{-1}. The voltammogram indicates no redox activity other than the beginnings of electrolyte decomposition above 3 V and the reduction of NiOOH below 2.5 V. The lack of activity here is probably due to the presence of small amounts of hydrofluoric acid in

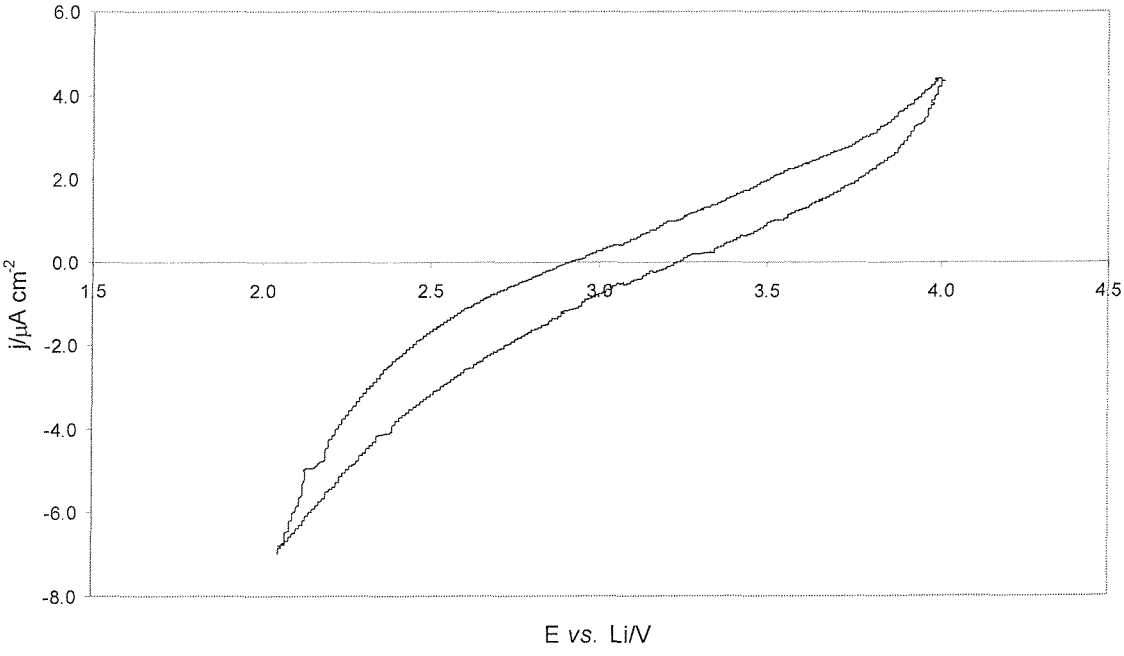

Figure 4.1. Cyclic voltammetry of 1 M $LiPF_6$/PC soaked mesoporous Ni/NiOOH in 1 M $LiPF_6$/PC at 25 °C and 20 mV s^{-1} shows no significant redox activity.

the electrolyte that exists in equilibrium with the PF_6^- ion. HF acts to destroy the metal-oxygen bonds, resulting in a decrease in the amount of active material in the electrode and ultimately a decrease in capacity.

An alternative electrolyte containing no residual HF was sought. Figure 4.2 shows the cyclic voltammetry of an ion exchanged H_I mesoporous Ni/NiOOH electrode in 1 M $LiSO_3CF_3$ in PC at 5 mV s^{-1}. In this case 1 M $LiSO_3CF_3$ in PC was also used as the ion exchanging solution rather than 1 M $LiPF_6$/PC. Figure 4.2 shows definite redox activity with two partially superimposed anodic peaks at 3.5 V and 3.9 V *vs.* Li

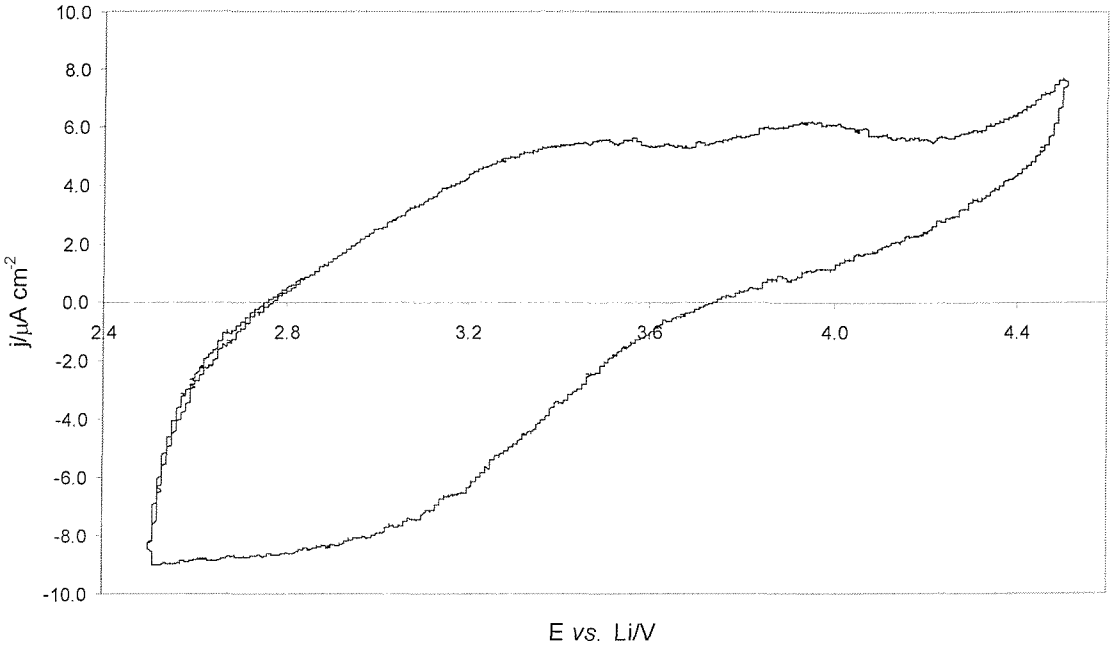

Figure 4.2. Replacement of the ion exchange and electrolyte solutions with 1 M $LiSO_3CF_3$/PC improves cycling performance as evidenced in this 5 mV s^{-1} scan.

followed by oxidation of the PC solvent above approximately 4 V. These peaks probably correspond to the removal of lithium ions from the mesoporous electrode structure, however this assignment cannot be definitively made. The negative-going sweep of Figure 4.2 shows cathodic activity below 3.6 V and down to the point of sweep reversal at 2.5 V. This cathodic feature is related to the anodic peaks both in magnitude and in position and as such these features are ascribed to a reversible redox couple, that is, the storage and release of lithium ions in the dehydrated mesoporous oxide structure. The current densities of Figure 4.2 are significantly lower than those attributed to H^+ storage/release within mesoporous Ni/NiOOH electrodes in aqueous alkaline solution as discussed in Chapter 2. The most likely reason for this is the incomplete ion exchange of intercalated ions with Li^+.

In an attempt to improve the effectiveness of the ion exchange process an alternative ion exchange process was used. This involved cycling the potential of freshly washed

mesoporous nickel electrodes in 1.9 M $LiOH_{(aq)}$ at 80 °C followed by drying of the electrode and incorporation into an air-tight cell for testing in non-aqueous lithium containing electrolyte. This process failed to produce significant currents for lithium intercalation.

4.3.2 Mesoporous Nickel as a Negative Electrode Material

During the investigations of Section 4.3.1 considerable redox activity was discovered on scanning to voltages lower than those conventionally used for positive electrode materials. Figure 4.3 shows this activity with the cyclic voltammogram of an ion exchanged (in 1 M $LiPF_6$/PC) mesoporous Ni/NiOOH electrode in 1 M $LiPF_6$/PC at 50 mV s^{-1}. The reduction and oxidation currents are probably due to a Li^+ ion storage and release mechanism. This behaviour has been observed previously[1] and was ascribed to the storage and release of Li^+ according to the following reversible mechanism:

$$Ni(OH)_2 + 2Li^+ + 2e^- \leftrightarrow Ni + Li_2O + H_2O$$

As indicated in Figure 4.3, this reaction occurs at a relatively high rate as expected from a mesoporous electrode, however there is a significant decrease in capacity with cycling. This decrease in capacity is probably due to destruction of the metal oxide by small amounts of HF as discussed in the previous Section. Interestingly, despite this corrosion problem, the current densities of Figure 4.3 are significantly higher than those of Figure 4.2 where corrosion does not influence capacity. This difference cannot be explained by the difference in scan rate or the fact that Figure 4.2 describes a one electron process whereas Figure 4.3 describes a two electron Li^+ ion storage mechanism. The difference in capacities is thought to be derived from the effectiveness of the ion exchange process. Where the functioning of the mesoporous electrode as a negative electrode material only requires the presence of $Ni(OH)_2$, capacity as a positive electrode material relies on a successful ion exchange reaction. This is clear evidence for the ineffectiveness of the ion exchange method described in Section 4.2 but also indicates the potential for increased capacity as a positive electrode material with the use of an efficient ion exchange method.

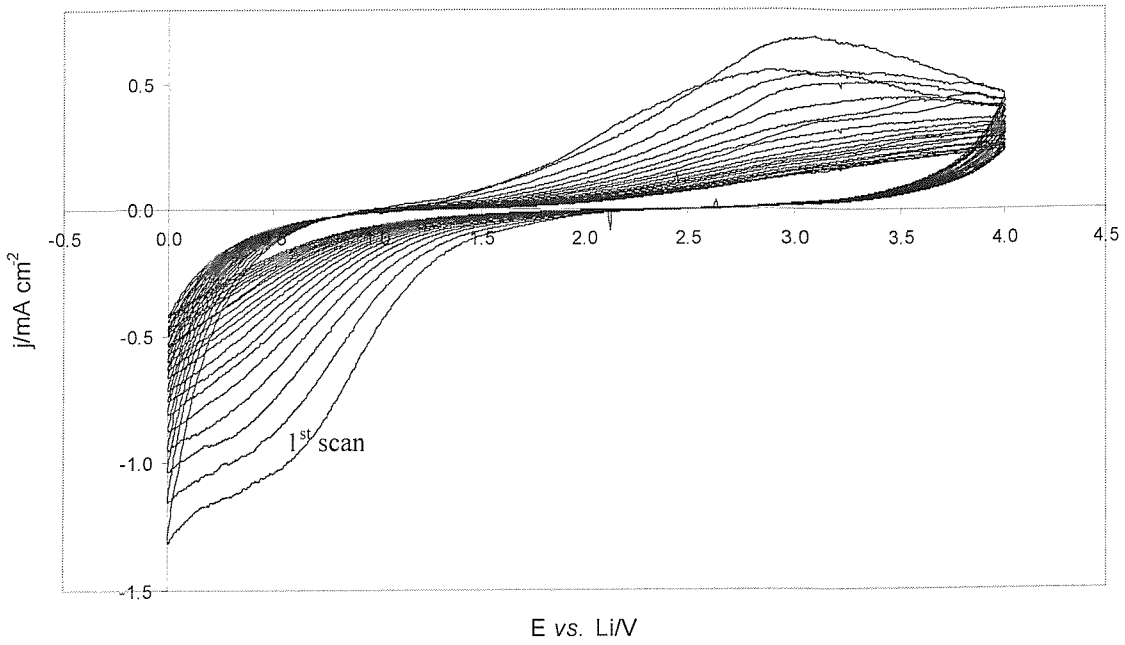

Figure 4.3 shows a decrease in capacity over 20 cycles of mesoporous Ni/NiOOH in 1 M $LiPF_6$/PC at 50 mV s^{-1}.

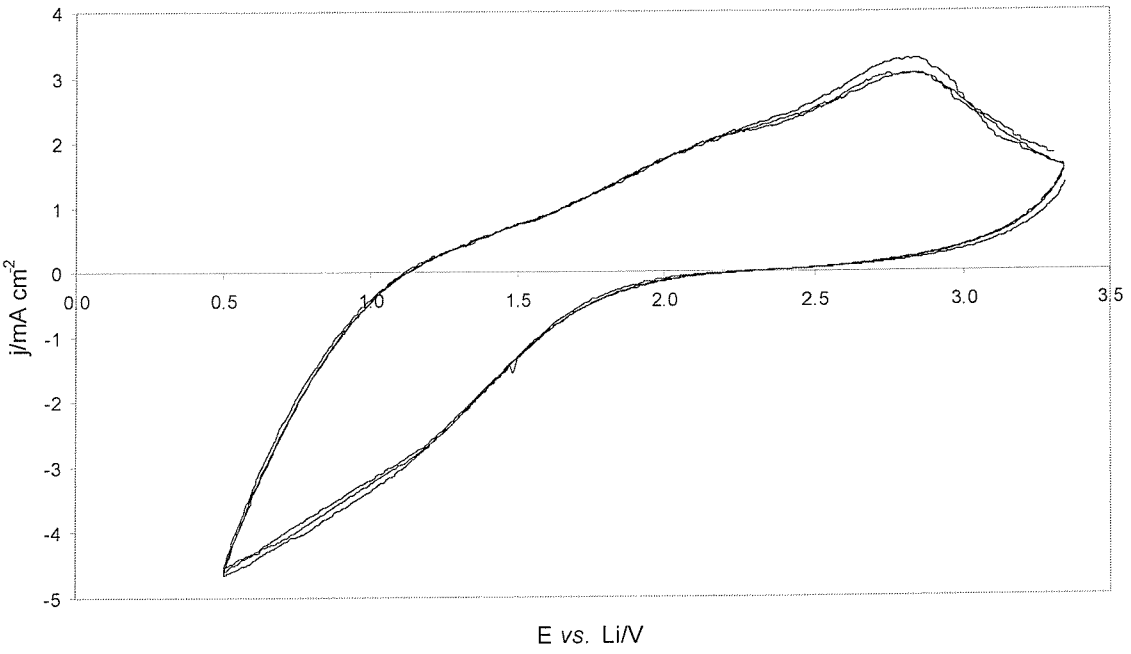

Figure 4.4. A dramatic improvement in cyclability is observed in this 100 mV s^{-1} voltammogram using 1 M $LiSO_3CF_3$/PC and a mesoporous Ni/NiOOH electrode soaked in the same solution.

To address the corrosion derived capacity loss observed with the use of $LiPF_6$, a dehydrated mesoporous Ni/NiOOH electrode was cycled as a negative electrode material in 1 M $LiSO_3CF_3$/PC as indicated in Figure 4.4. As can be seen, there is no decay in capacity over three cycles and in some cases capacity was observed to increase with cycling. Consequently, it is thought that the reason for the decay in capacity with cycling in Figure 4.3 was most certainly the destruction of metal-oxygen bonds by HF.

4.4 Conclusions and Further Work

This Chapter has demonstrated the possibility of deriving capacity from the storage of lithium ions in mesoporous nickel electrodes that have undergone an ion exchange process. Although these ion exchange reactions were not overtly successful, they are a useful basis for continued work on this subject.

Further work in this area must focus on the elucidation of a method of successfully converting a mesoporous Ni/NiOOH composite electrode into one consisting of $Ni/LiNiO_2$. In order to retain the mesostructure conventional high temperature ion exchange methods cannot be used.

4.5 References

[1] Poizot, P., Laruelle, S., Grugeon, L., Dupont, L., Tarascon, J-M., *Nature*, **2000**, 407, 496.

Chapter 5

Ionic Conductivity in Liquid Crystalline Phases and the Production of High Quality Mesostructures

5.1 Background and Objectives

Prior to the work discussed in this thesis, the direct liquid crystal templating (DLCT) of electrodeposited metals with high quality mesostructure had been carried out using only expensive, high purity polyoxyethylene based templates. The limited success of attempts at templating using inexpensive industrial grade polyoxyethylene materials was unexplained but thought to be due to the impurity of the surfactants. Indeed, industrial preparations of non-ionic surfactants are rarely monodisperse in either their hydrophilic or hydrophobic components. Industrial grade polyoxyethylene surfactants may contain mixtures of alkyl chain lengths and isomers, are usually polydisperse in the number of ethylene oxide groups and are not of high purity.[1] However Patrick and Warr reported that alkyl chain polydispersity in the polyoxyethylene surfactants does not have a dramatic effect on bulk phase behaviour.[2] This may indeed be true, however the effect of impurity contamination may influence the formation and structure of liquid crystalline phases on the molecular and supramolecular scales.
The basis of the work described in this chapter is the premise that liquid crystalline phases are exactly that: crystals. The crystallinity of liquid crystals however, is fundamentally different from conventionally denoted crystals such as metals. In the latter case, the ordering that endows crystallinity on the material is atomic scale ordering. Liquid crystals do not possess such disciplined atomic ordering but derive their crystallinity by virtue of the order created by self-assembly of supramolecular species. In addition, the energy of association that binds units together is lower than in conventional crystals with the result that liquid crystalline systems are considerably more dynamic. Nevertheless, in thinking and treating liquid crystalline phases as we do conventional crystals, we are more able to understand and control their properties.

This Chapter discusses the application of electrochemical techniques to the elucidation of a number of factors that influence the formation of liquid crystalline phases and the materials they are used to template. In addition, electrochemical transport phenomena within various liquid crystalline phases are investigated. In an effort to evaluate the feasibility of depositing thicker and larger mesoporous metal electrodes, the relationship between the electrode electrochemical performance and

bulk liquid crystalline domain structure is examined. The objectives of the work are described below:

1. To characterise the diffusion and conductivity of ionic species contained within the aqueous domains of the liquid crystalline phases of the polyoxyethylene surfactant Brij® 56. These experiments were used to identify ionic transport properties and relate these to phase transitions in the liquid crystalline electrolyte.

2. To apply knowledge gained from the fundamental electrochemical investigations of Objective 1 to the development of methods enabling the fabrication of high quality mesoporous nickel films.

3. To investigate the effect on the charge storage capacity of mesoporous nickel electrodes of increasing electrode thickness and geometric area. Trends will be related to electrode macroscopic domain structure imparted by the liquid crystalline template.

5.2 Experimental

5.2.1 Ionic Diffusion and Conductivity in Liquid Crystalline Phases

Ionic diffusion in the liquid crystalline phases of Brij® 56 based liquid crystalline phases was investigated using a 65 wt. % Brij® 56/10 mM $K_3(Fe[CN]_6)$ in 0.1 M $KCl_{(aq)}$ liquid crystalline mixture. The experimental apparatus used to collect diffusion data consisted of a glass electrochemical cell (~5 cm^3 volume) contained within a Pyrex water jacket for temperature regulation. A three electrode configuration was used, consisting of a glassy carbon random array microelectrode (GC-RAM donated by Stephen Fletcher of CSIRO Australia) as working electrode, a Pt gauze counter electrode and a saturated calomel reference electrode (SCE). The GC-RAM electrode consisted of an array of 10 μm glassy carbon microelectrodes embedded in epoxy resin oriented parallel and in plane with each other and connected to a common current collector. In this configuration in which there was no overlap of individual microelectrode diffusion fields, a characteristic diffusion limited current signal was obtained, albeit amplified by the contribution from all of the electrodes in the array. The diffusion limited currents were measured by cyclic voltammetry with a scan rate of 10 mV s^{-1}. Due to the instability of the ferricyanide solution under visible light, solutions were wrapped in aluminium foil and both aqueous and liquid crystal solutions were not kept for more than 12 h. after their making. In measuring the limiting current of the aqueous ferricyanide solution as a function of temperature it was found that the solution had to be changed at every temperature increment in order to prevent loss of significant amounts of water and thus erroneous results. This was not necessary in the liquid crystal system since the working electrode was buried deep within the solution and any water loss occurred from the uppermost layers of the electrolyte only. In addition, the cell was sealed in Parafilm for the duration of the experiment to minimise water loss.

Cell temperature was maintained with an accuracy of ± 0.1 °C using a Grant ZD thermostated water bath. The temperatures of phase transitions in the 65 wt. % Brij® 56/10 mM ferricyanide in 0.1 M $KCl_{(aq)}$ electrolyte were identified using an Olympus BH-2 polarizing microscope equipped with a Linkam TMS 90 heating/cooling stage accurate to ± 0.1 °C. Here, thin films of the liquid crystals were prepared by sandwiching the mixture between a glass microscope slide and cover slip. Liquid

crystalline phases were identified based on their optical texture[3], viscosity and the shape of the air bubbles present in the mixture.

The ionic conductivity of a Brij® 56 based electrolyte was measured in two electrode cells consisting of gold electrodes made by evaporation of gold onto chromium-coated glass microscope slides separated by a PTFE spacer. Electrodes were cleaned in an ultrasonic bath of isopropanol for 60 minutes prior to deposition, then rinsed with de-ionized water and dried under ambient conditions. The electrolyte consisted of a 65 wt. % Brij® 56/0.1 M sodium acetate mixture. Measurements were conducted using ac impedance spectroscopy with a Solartron Analytical 1260 frequency response analyser in conjunction with a 1287 Electrochemical Interface. In all experiments a 100 mV oscillation was used to perturb the system without dc potential bias.

5.2.2 Effects of Template Annealing and Post-deposition Washing Treatments

The effect of thermally annealing the H_I mesoporous nickel deposition template on the quality of the resulting electrodeposited mesostructure was evaluated by comparing the effect on charge storage capacity (and hence surface area) of materials deposited from annealed and unannealed templates. 65 wt. % Brij® 56/nickel acetate deposition solution mixtures used in the deposition of mesoporous nickel and described in Chapter 2 were thermally annealed by heating within the deposition cell to 50 °C and holding at this temperature for 10-15 min. On complete formation of the less viscous micellar (L_I) phase at this temperature, the three-electrode deposition configuration using a 1 mm gold disc working electrode was inserted into the mixture which was then slowly cooled to 25 °C. After a cooling period of 30 min., deposition of mesoporous nickel was carried out for a 2 h. period. Deposition conditions and post-washing surfactant removal using isopropanol were the same as those described in Chapter 2. Charge storage capacity in KOH solution was also determined in the same manner as described in Chapter 2, with the exception that this was done using 3 M rather than 6 M KOH and the appropriately different lower and upper potential limits in cyclic voltammetry of –1.25 V and 0.5 V *vs.* SCE respectively.

The effectiveness of using isopropanol and demineralised water in post-deposition washing treatments for surfactant removal was also investigated. As for the investigation of template annealing, the effectiveness of the two washing solutions

was determined by comparison of the charge storage capacity of mesoporous nickel deposited under the same conditions but washed in the respective solutions. Depositions were carried out for a 15 h. period, again using the template and deposition conditions described in Chapter 2. Freshly deposited mesoporous nickel was transferred immediately to the respective solution and washed with magnetic stirring for a 24 h. period. Charge storage capacity was determined by cyclic voltammetry in 3 M KOH using the same conditions as those described for the investigation of template annealing above.

5.2.3 Anodic Stripping Voltammetry

Anodic stripping voltammetry (ASV) was used in the determination of the mass of nickel deposited during deposition experiments. ASV experiments were carried out by cyclic voltammetry in 0.1 M $HCl_{(aq)}$ solutions at 25 °C. Freshly deposited and washed nickel electrodes (deposited onto gold disc substrates) were cycled from –0.45 V to 0.9 V *vs.* SCE at 2 mV s^{-1}. During this scan all of the nickel metal was oxidised to nickel (II) ions, leaving a clean gold electrode surface. The stripping charge was converted to a mass using Faraday's Law and the assumption that the dissolution of nickel atoms in the electrode yielded two electrons per atom. The efficiency of deposition experiments was determined by dividing the ASV stripping charge by the charge passed during the deposition experiments. The electrodeposition reaction was assumed to be a two electron electroreduction process.

5.2.4 Variation in Electrode Capacity with Electrode Thickness and Geometric Area

The relationship between the charge storage capacity of H_I mesoporous nickel electrodes (which is proportional to the electrode roughness factor) and electrode thickness and geometric area was investigated. Investigation of electrode thickness effects involved depositing H_I mesoporous nickel with varying deposition charge densities onto 1 mm gold disc electrodes using the procedure described in Chapter 2. Electrode thickness was calculated based on the known mass of nickel present as determined by ASV and the density of nickel (corrected for the 23 % porosity of the H_I structure- see Appendix 1). The investigation of electrode geometric area involved deposition of mesoporous nickel with the same charge density onto gold disc or

evaporated gold electrodes of varying geometric area. Charge storage capacity was determined by cyclic voltammetry in 6 M KOH. Potential scan limits of –1.06 V and 0.6 V *vs.* Hg/HgO were used with a scan rate of 5 mV s^{-1}. Charge storage capacity was determined by calculation of the charge associated with the cathodic peak at high potentials in the voltammogram, as detailed in Chapter 2.

The electrode thickness was calculated based on the deposition charge, the known efficiency of the deposition process, the radius of the electrode and the density of the H_I mesoporous nickel electrode material (corrected for the presence of porosity).

5.2.5 Light and Electron Microscopy

Optical microscopy was carried out in reflective mode using an Olympus BH-2 light microscope. Electron micrographs were recorded using a Philips XL-30 scanning electron microscope. In both cases, samples consisted of freshly washed H_I mesoporous nickel deposited from a 65 wt. % Brij® 56 template.

5.3 Results and Discussion

5.3.1 Diffusion in Liquid Crystalline Phases

Studies of ionic diffusion in the Brij® 56 liquid crystal system were carried out in order to examine the ion transport characteristics of the liquid crystalline phases and to determine whether any correlation between these characteristics and the phase morphology existed. Such studies were important in gaining a more thorough understanding of the electrodeposition process and in the development of more effective deposition techniques.

The relative rates of diffusion of $(Fe[CN]_6)^{3-}$ ions within the liquid crystalline phases of Brij® 56 were studied by measurement of the limiting current of reduction of $[Fe(CN)_6]^{3-}$ on a glassy carbon random array microelectrode (GC-RAM) in each of the phases. Figure 5.1 shows the diffusion limited reduction of a surfactant free aqueous ferricyanide solution on the GC-RAM electrode with a scan rate of 10 mV s^{-1}. The reduction of the ferricyanide redox probe is seen to become diffusion

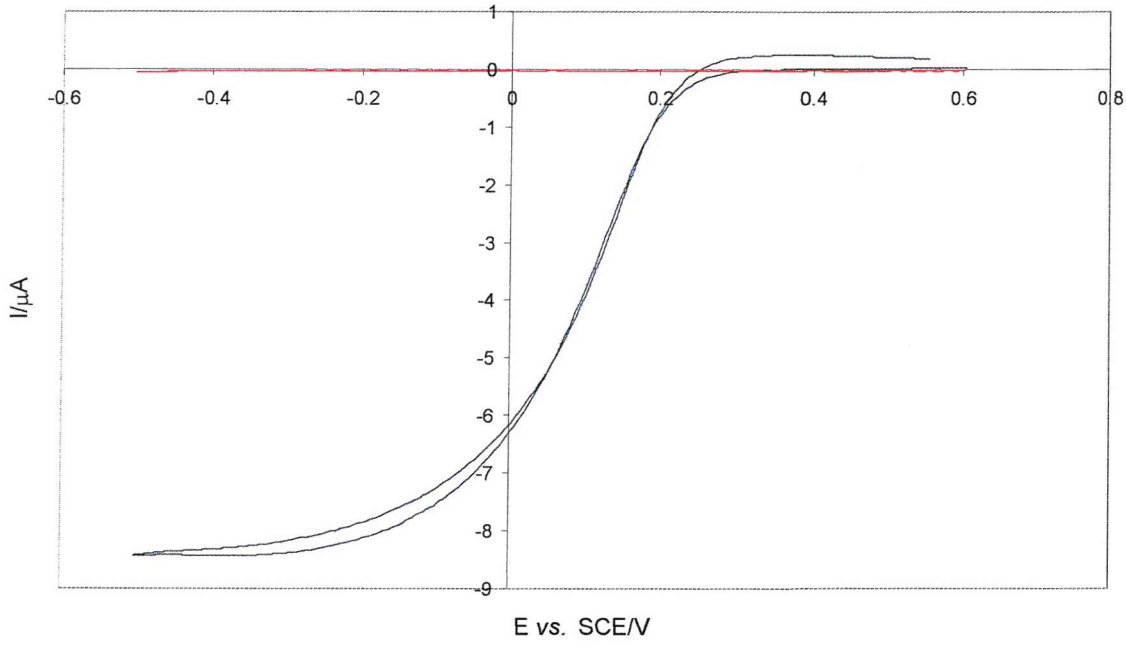

Figure 5.1 compares the cyclic voltammetry of an aqueous solution of 10 mM $K_3(Fe[CN]_6)$/0.1 M $KCl_{(aq)}$ (blue) with that of a 0.1 M $KCl_{(aq)}$ solution (red) on a GC-RAM electrode at 10 mV s^{-1} and 25 °C.

limited at ~ -0.4 V *vs.* SCE. The background cyclic voltammogram included in Figure 5.1 establishes the non-existence of any electrochemical activity other than that due to the reduction of the ferricyanide. Figure 5.1 shows a diffusion limiting current of approximately –8.3 μA. The value of the diffusion coefficient for $(Fe[CN]_6)^{3-}$ transport in the solution cannot be derived here from the diffusion limited current since the total electrode surface area is unknown. Nevertheless, trends in the diffusion coefficient may still be observed by comparison of the relative values of the diffusion limiting current.

Figure 5.2 shows the cyclic voltammogram of ferricyanide reduction in the H_I phase of a 65 wt. % Brij® 56 liquid crystal electrolyte. As in Figure 5.1, the background scan of Figure 5.2 indicates no significant electrochemical activity in the potential region in which ferricyanide reduction occurs. A limiting current of approximately –50 nA is reached at ~ -0.12 V *vs.* SCE. This diffusion limiting current of reduction is

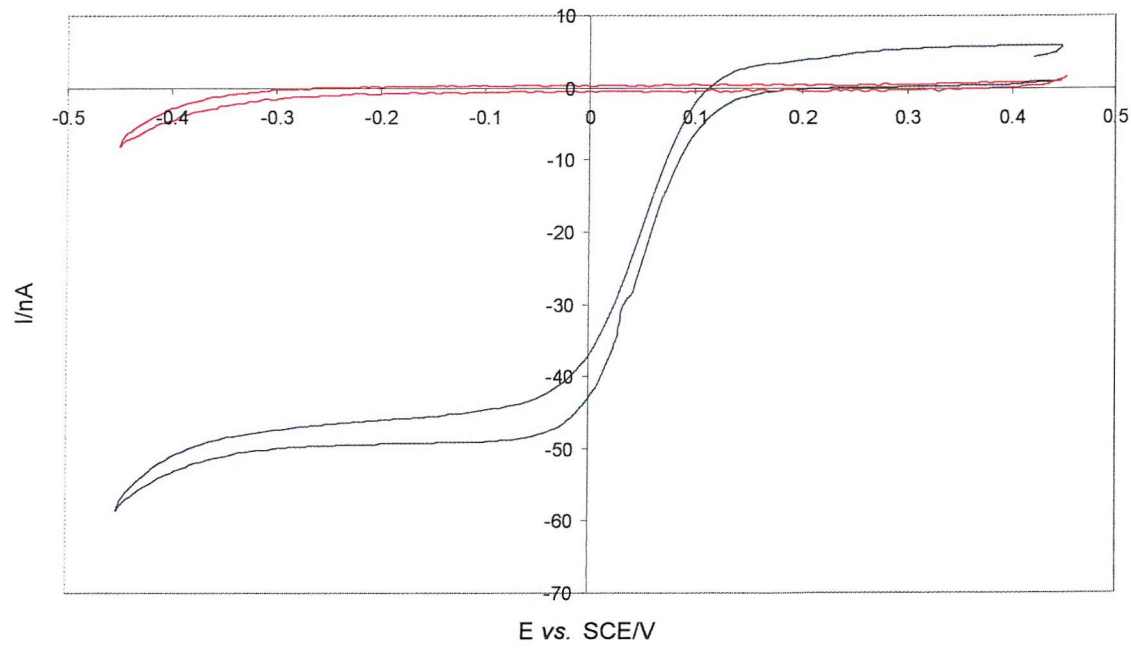

Figure 5.2 compares the cyclic voltammetry of H_I liquid crystalline mixtures containing 10 mM $K_3(Fe[CN]_6)$/0.1 M $KCl_{(aq)}$ (blue) and 0.1 M $KCl_{(aq)}$ (red) solutions on a GC-RAM electrode at 10 mV s^{-1} and 25 °C.

some 170 times lower than that observed in the aqueous solution, indicating the same difference in the values of the diffusion coefficient. The significantly reduced ionic

diffusion rate in the liquid crystalline template electrolyte cannot be solely due to the decreased cross-sectional area occupied by the aqueous domain of the electrolyte as compared with the aqueous solution since in the H_I phase the hydrophobic surfactant rods occupy only 23 % of the total volume. The reduced rate of ionic movement in the liquid crystal may however be a result of interactions between the diffusing ions and the surfactant walls of the aqueous channels within the electrolyte. These interactions may be collisional in nature or attractive forces resulting from the electrostatic interaction of the surfactant groups and the negatively charged $(Fe[CN]_6)^{3-}$ ions.

The limiting current of ferricyanide reduction was measured as a function of temperature in the 65 wt. % Brij® 56 based mixture. As indicated in Figure 5.3, the diffusion limited current increases approximately linearly with temperature as

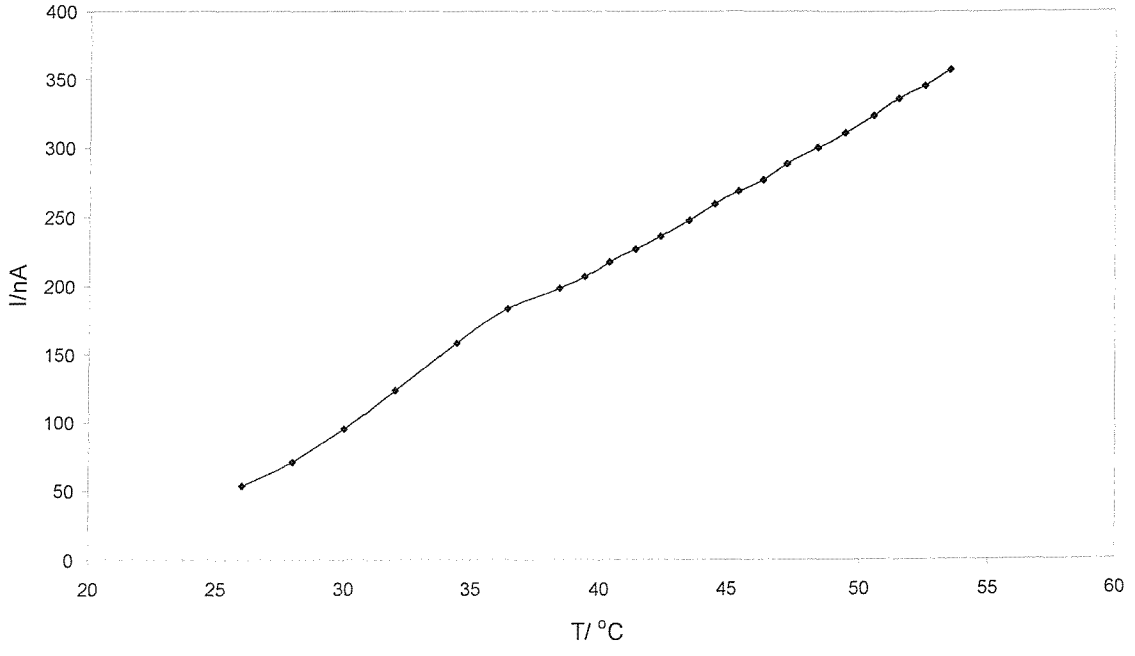

Figure 5.3 shows the variation of the limiting current of reduction of $(Fe[CN]_6)^{3-}$ on a GC-RAM electrode in a 65 wt. % Brij® 56 liquid crystal as a function of temperature.

observed in surfactant-free aqueous solutions. A small but broad shoulder centred at 36 °C corresponds to the melting point of the liquid crystal. The magnitude of this shoulder indicates that melting of the liquid crystal is not accompanied by significant structural changes in the system. Of most interesting note however is the absence of any feature corresponding to the H_I to V_I phase change that occurs at 45 °C. This is not surprising since the morphology of the aqueous domain does not change

significantly with the H_I to V_I phase transition and would therefore be expected to have little impact on the diffusion coefficient. A more pronounced change in transport properties would be expected in the hydrophobic domain with this transition. Indeed, Chen and co-workers[4] found that the diffusional anisotropy of hydrophobic redox probes within the micellar nematic phase of a lyotropic liquid crystal showed much greater variation during phase transitions than did hydrophilic redox probes.

5.3.2 Thermal Annealing and Structural Evolution in Liquid Crystalline Templates

In carrying out the studies investigating the diffusion of ionic species within the aqueous domain of an H_I Brij® 56 based liquid crystal, it was discovered that the diffusion limited current varies as a function of time at constant temperature. This effect however was observed over a period of hours and had no significant effect on the measurements of Section 5.3.1 above, which were carried out over a much shorter period. The change in ionic transport properties with time indicated the possible occurrence of some form of structural evolution albeit with retention of the overall H_I structure. This may have been derived from the liquid crystal mixing process. Mixing of the liquid crystalline precursor materials (aqueous solution and surfactant melt) is achieved using considerable shear forces. This process introduces significant internal stresses that probably cause deformation of the phase structure. With time, these stresses would be expected to relax as the phase structure approached a more ideal geometry. As with many properties of liquid crystals, the time constant for stress relaxation would be expected to be between that of a liquid (where stress relaxation is immediate) and a solid (where internal stresses can be permanently held).

To examine the effects on ionic transport properties of any structural changes in the liquid crystalline template ac impedance spectroscopy was used to monitor the ionic resistance of a 65 wt. % Brij® 56/0.1 M sodium acetate liquid crystal at 26 °C as a function of time. Ionic resistance is related to the diffusion coefficient through the Nernst-Einstein equation and is a useful diagnostic of the ionic transport properties within a liquid crystalline phase. Figure 5.4 shows the cell area specific resistance of an unannealed liquid crystal measured continuously at a frequency of 8250 Hz over a period of 5 h. 8250 Hz was chosen as the frequency of measurement because at this frequency the impedance of the cell was purely resistive. That is, and as is indicated in

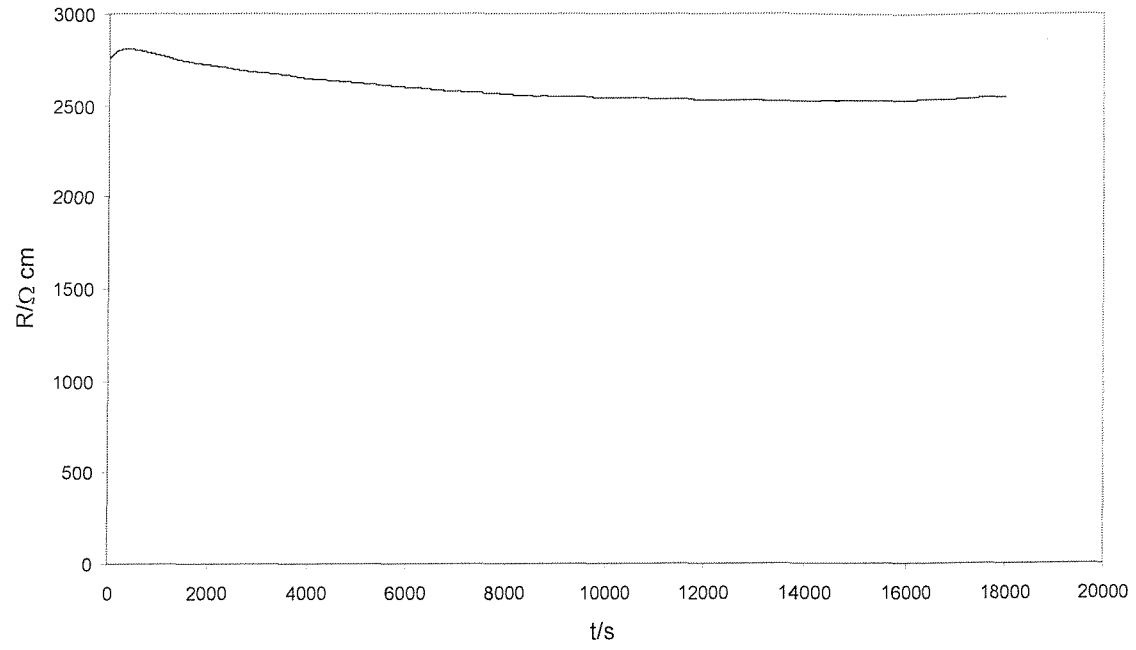

Figure 5.4 shows the variation in the area specific resistance of an unannealed H_I 65 wt. % Brij® 56/0.1 M sodium acetate liquid crystal with time at a constant temperature of 26 °C.

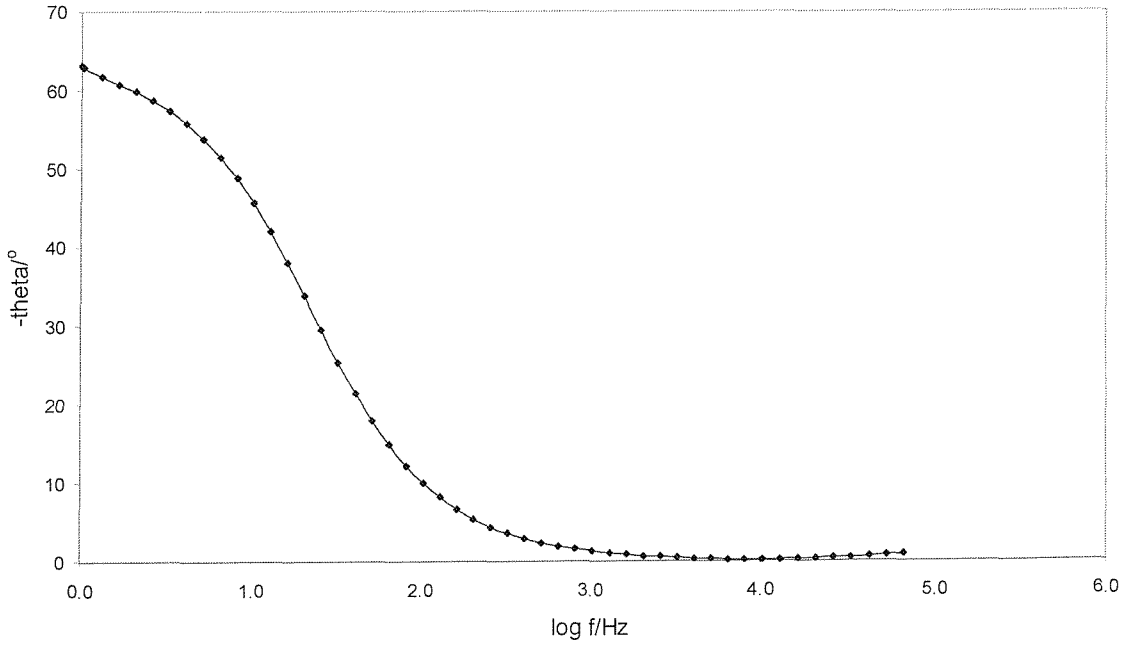

Figure 5.5. Ac impedance shows the frequency of lowest phase shift with the application of 100 mV oscillations to an unannealed H_I liquid crystal.

Figure 5.5, at 8250 Hz the impedance phase shift is approximately 0 ° such that the impedance value obtained at this frequency contains no capacitive or other component. 8250 Hz was also observed to give the lowest phase shift after the 5 h. measurement period.

After a small increase, the resistance of the H_I liquid crystalline phase decreases gradually over the entire measurement period to a value approaching 2500 Ω.cm. The reason for this gradual decrease in cell resistance remains a subject of speculation but is probably due to structural rearrangement of the surfactant rods of the H_I phase.

In order to release possible internal stresses within the freshly mixed H_I liquid crystal, the mixture was heated to 50 °C into the L_I phase. At this temperature and in the less viscous L_I phase it was anticipated that there would be sufficient template motion to allow the surfactant species to rearrange, dissipating shear stresses created during mixing and assume a more stress-free geometry closer to that of the ideal H_I structure. This process is called thermal annealing, a practise common in materials processing used to relieve internal stresses in materials that develop during their manufacture.

The ionic resistance of the annealed liquid crystalline phase was measured as a

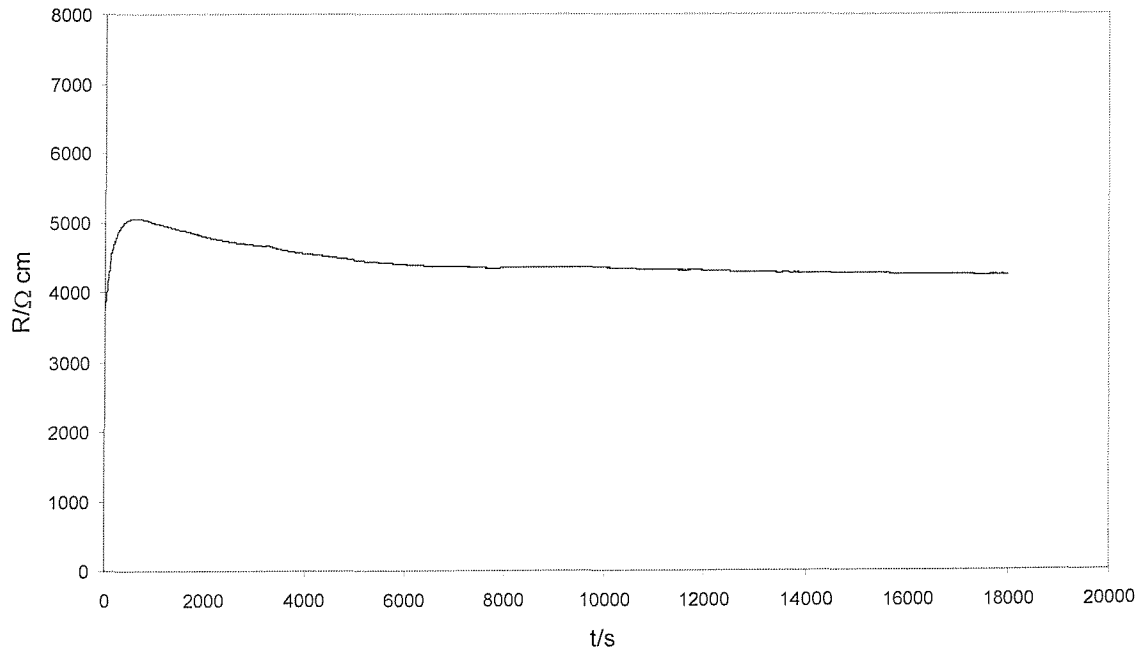

Figure 5.6 shows the variation in the area specific resistance of an annealed H_I 65 wt. % Brij® 56/0.1 M sodium acetate liquid crystal with time at a constant temperature of 26 °C.

function of time using ac impedance. Here, 5205 Hz was found to be the frequency at which an entirely resistive impedance was obtained. As indicated in Figure 5.6, the ionic resistance of the annealed liquid crystal rapidly increases from an initial value of approximately 4000 Ω.cm, followed by a slow decrease to an approximately steady state value approaching 4200 Ω.cm. The value of this steady state ionic resistance is considerably higher than the value of 2500 Ω.cm observed for the unannealed liquid crystal. The decreased resistance (or increased conductivity) observed in the unannealed liquid crystal indicates that the conduction pathways through this medium are perhaps less tortuous (since the volume fraction of the H_I rods is expected to be the same in both cases) than those of the annealed phase which is thought to possess a more ideal H_I structure. This is indirect evidence for the existence of a phase morphology consisting of broken and discontinuous surfactant rods in the unannealed phase. It is envisaged that in this case the diffusion path is less tortuous because instead of circumventing a surfactant rod as in an ideal H_I phase, ions moving through the phase may pass through breaks in the structure and therefore travel a more direct route. It must be stressed however that polarising microscope examinations have revealed that the liquid crystal remains in the H_I phase throughout the experiment during which structural evolution of the mesophase is speculated to occur.

The increased resistance of annealed templates correlates well with observations made during the deposition of mesoporous nickel. Here, it was noted that under the same deposition conditions those electrodes deposited with the lowest current density (potentiostatically) demonstrated the highest charge storage capacity during cyclic voltammetric testing in alkaline solution.

First attempts at the synthesis of mesoporous nickel from the H_I phase of a Brij® 56 based template resulted in films which showed only marginal improvement in charge storage capacity compared with that of non-templated nickel electrodes (typically 2-5 times charge storage capacity enhancement was observed). Transmission electron microscopy (TEM) and small angle x-ray scattering (SAXS) results however confirmed the existence of mesoporosity in the films. As such, it appeared likely that the electrochemical inaccessibility of the mesopore network was due to blockage of the pore structure. It was thought that pore blockage might have been caused by ineffective removal of the surfactant during post-deposition washing, or by a physical

discontinuity in the channels of the mesoporous material. In support of the latter case, and with the results of the above described experiments in mind, it was reasoned that as speculated, in mixing the aqueous solution and surfactant to form the liquid crystal template, appreciable strains are introduced into the templating mixture. This could result in a pore structure consisting of small domains of pore connectivity (hence the observation of an H_I phase in polarising optical microscopy and TEM) but an overall structure that was contorted and discontinuous.

Thermal annealing of the template was proposed as a solution to this problem since this would allow relaxation of any strain in the phase structure by virtue of the higher supramolecular mobility that exists in the less viscous L_I phase. To test the effect of template annealing on the quality of mesoporous nickel films, deposition experiments were conducted using a 65 wt. % Brij® 56/nickel (II) acetate deposition template as described in Chapter 2, annealed at 50 °C. After slow cooling to the deposition temperature, the liquid crystal was allowed to equilibrate for 15 min. prior to the start of electrodeposition. This latency period allowed the pore structure time to form completely after the transition from the L_I phase. In addition to internal stress relaxation, the annealing process removes the majority of air bubbles present in the

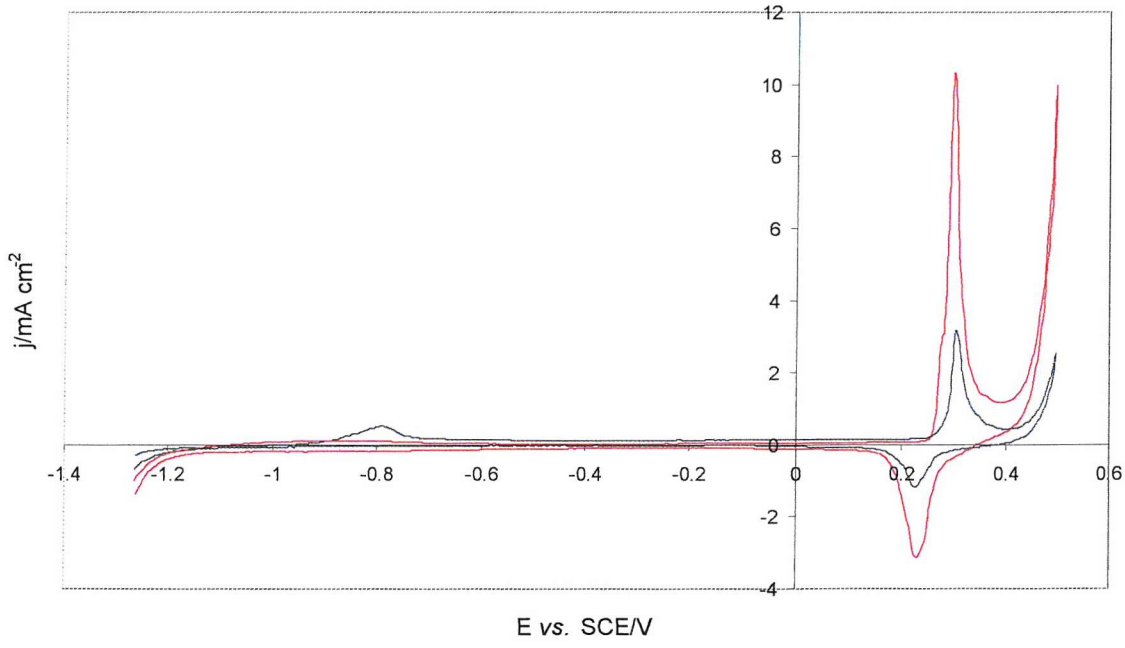

Figure 5.7 compares the voltammetry (third cycles) of nickel deposited from the annealed (red) and unannealed (blue) H_I phases of a Brij® 56 based liquid crystal in 3 M KOH at 20 mV s^{-1}.

mixture since in the less viscous L_1 phase air bubbles are mobile enough to move out of the mixture. Figure 5.7 shows the effect of the annealing process on the charge storage capacity of a mesostructured nickel electrode. The electrode that has been deposited from an annealed liquid crystal template shows significantly greater charge storage capacity compared with that deposited from an unannealed liquid crystal with the same deposition time. This indicates that pore connectivity is significantly enhanced in the material deposited from the annealed template.

The effects of annealing the liquid crystalline template on the template and deposited

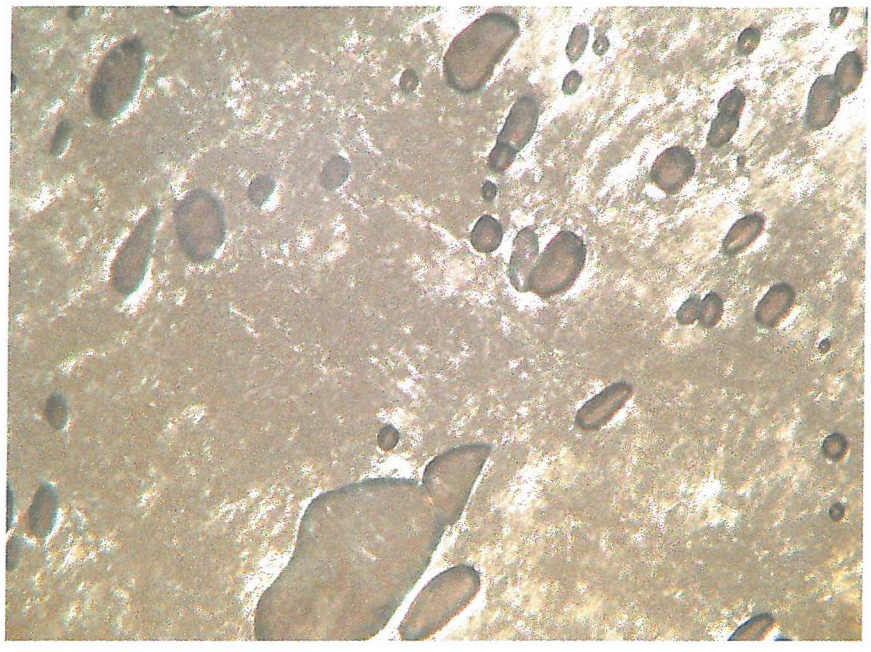

Figure 5.8. The appearance of the H_I phase of this 65 wt. % Brij® 56/0.2 M nickel(II) acetate deposition template is random and unstructured showing no microscopic ordering.

material morphology may also be seen visually using optical and scanning electron microscopy (SEM). Figure 5.8 shows a polarising optical micrograph of the unannealed H_I phase of a Brij® 56 based liquid crystal. The charcoal-like texture and presence of irregularly shaped air bubbles are clear evidence of an H_I phase, however there is no indication of any structural patterning on a larger scale as would be expected in the presence of a domain structure. The optical birefringence pattern of the annealed form of this liquid crystal is markedly different. Examination of Figure

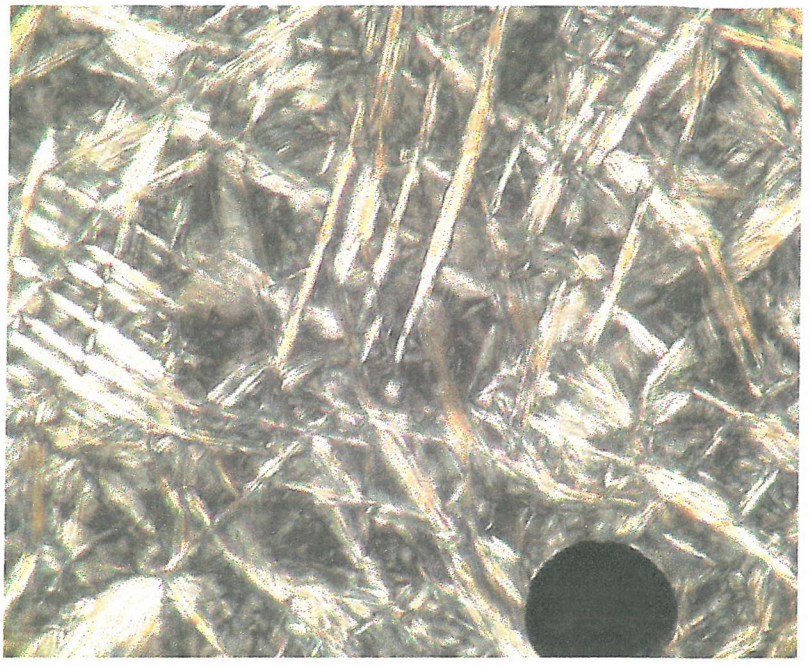

Figure 5.9. The microscopic structure of the annealed liquid crystalline template presented here bares a stark contrast to the unannealed form of Figure 5.8.

5.9 reveals the same general optical texture that characterises H_I phases, however the lighter streaks in the image suggest crystal-like ordering on a larger scale than that of the supramolecular assembly which defines the H_I phase. Therefore, the contrast in this image is probably derived from the presence of domains of ordered material. Liquid crystalline domains are commonly observed in polarising optical micrographs of the more pure polyoxyethylene surfactants. In the case of Brij® 56 however, thermal annealing is required for their formation. This is direct evidence that the annealing process enables a structural change in the liquid crystalline template and that this structural ordering enables the deposition of high quality mesoporous materials with continuous pore networks.

The domain structure observed in the optical micrographs of annealed liquid crystalline templates may also be seen in the materials deposited from them. Figure 5.10 shows an optical micrograph of the surface of a mesoporous nickel electrode deposited from an annealed H_I Brij® 56 based template. The majority of the surface is covered with a thin oxide layer, the reflection through which produces a colouring effect. Silvery-white areas are those with little or no passivating oxide coverage. The mosaic-like pattern that divides the electrode into domains separated by boundary

Figure 5.10. Light microscopy of a freshly washed mesoporous nickel electrode film shows a surface divided into domains.

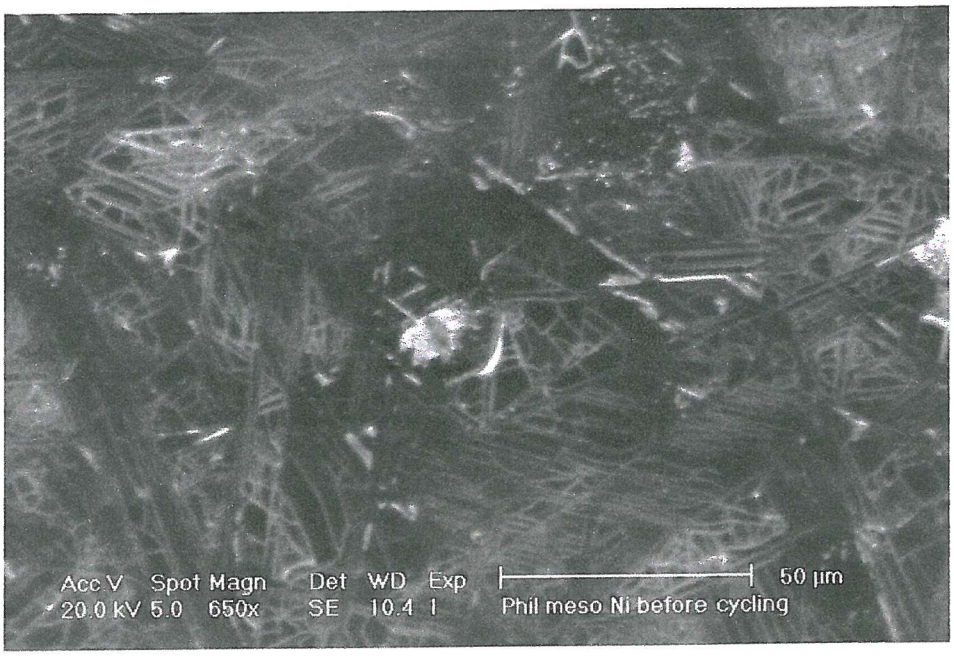

Figure 5.11. Contrast in this SEM image shows the domain boundaries of a freshly washed H_I mesoporous nickel film. The structure is very similar to that observed in Figure 5.10.

regions is similar to that observed in the image of the liquid crystalline template of Figure 5.9. Figure 5.11 shows an SEM micrograph of a freshly deposited and washed H_I mesoporous electrode deposited from an annealed template under the same conditions as was the sample of Figure 5.10. A domain structure is again evident here with the darker domain areas separated by thinner areas of lighter material representing the domain boundaries. Lighter areas denote areas of lower electronic conductivity and probably correspond to the segments of the electrode on which a passivating oxide has formed. The reason for the apparently increased susceptibility of the domain boundaries to passivation has not been established but could result from the predominance of a different crystal face in the domain boundary areas that is more easily oxidised in air than that nickel in the domain bulk.

5.3.2 Post-Deposition Washing

The conditions of post-deposition washing were also found to be critical in obtaining a high quality mesostructure. That is, the large surface areas of H_I mesoporous nickel were found to be electrochemically accessible only with satisfactory removal of the surfactant template after deposition. Figure 5.12 compares the charge/discharge

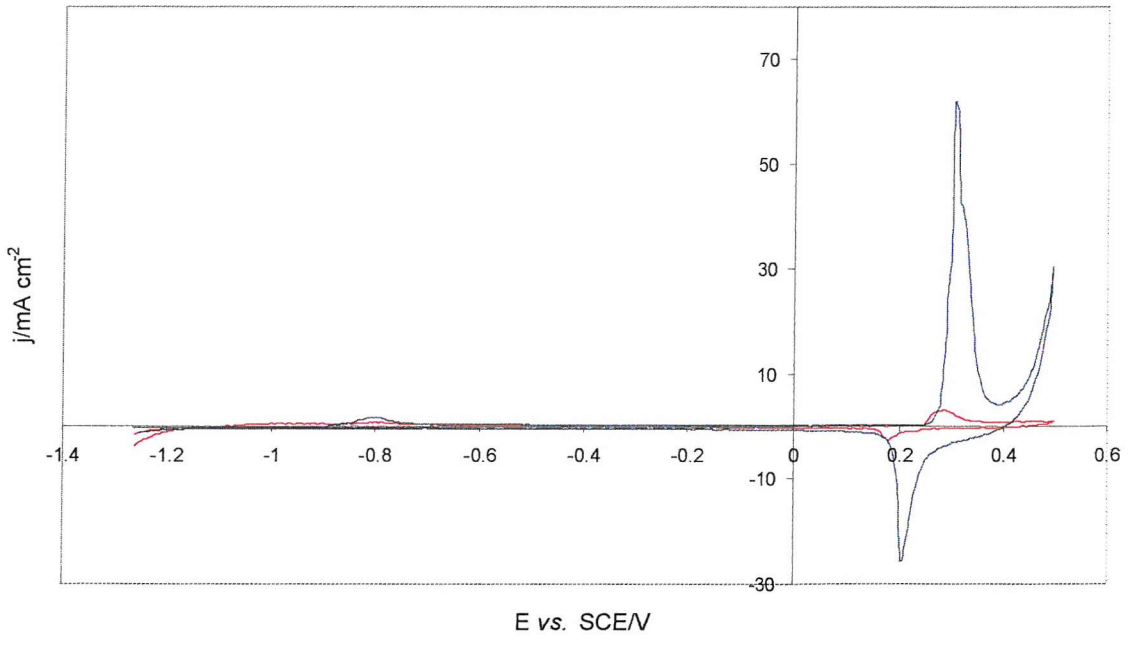

Figure 5.12. The effectiveness of washing treatments using water (red) and isopropanol (blue) are compared here based on charge storage capacity in 3 M KOH at 20 mV s^{-1} for mesoporous nickel deposited from annealed Brij® 56 templates.

behaviour in alkaline solution of two mesoporous nickel electrodes deposited from annealed 65 wt. % Brij® 56/nickel (II) acetate deposition templates for the same period of time washed in water and isopropanol respectively. Mesoporous nickel washed in isopropanol shows a much greater electrochemically accessible surface area than that washed in water. As such, it is concluded that the decreased surface area observed for the water washed H_I mesoporous nickel was due to pore blockage by incomplete surfactant removal.

The greater ability of isopropanol in removing surfactant from the pores of mesoporous nickel results from the higher solubility of the surfactant in the alcohol than in water (this was observed macroscopically during washing). At the molecular level, the isopropanol is expected to mix more readily with the hydrophobic portion of the surfactant (the segment of the surfactant which resides in the pores) than does water and so penetrates the pore network more effectively. In addition, the introduction of the less polar (than water) alcoholic molecule to the pores is thought to weaken the polar interactions between the metal and the hydrophilic ether oxygen groups of the surfactant that might otherwise serve to anchor the surfactant to the pore walls.

5.3.3 Deposition Efficiency

The efficiency of electroreduction reactions for the deposition of non-templated and mesoporous nickel from both 65 wt. % Brij® 56 and 50 wt. % Pluronic® P123 H_I templates at –0.9 V *vs.* SCE and 25 °C was studied as a function of time.

5.3.3.1 Anodic Stripping Voltammetry

Anodic stripping voltammetry (ASV) was used to calculate the efficiency of nickel electrodeposition reactions in both liquid crystalline and aqueous solution media. Figure 5.13 shows a forward cyclovoltammetric sweep in which electrodeposited nickel metal is oxidised to $Ni^{2+}_{(aq)}$ ions. Dissolution of nickel on the substrate surface is seen to be completed by ~0.1 V *vs.* SCE as indicated by the sharp decrease in oxidative current, after which no reaction with the bare gold substrate surface or otherwise is seen until the onset of water oxidation above 0.8 V. The lack of activity of the gold electrode surface is demonstrated by the inclusion in Figure 5.13 of the

cyclic voltammetry of a gold electrode in 0.1 M $HCl_{(aq)}$ solution, indicated in red. With the exception of solvent electrolysis no oxidative or reductive currents are observed. Calculation of the stripping charge and comparison with the charge passed during deposition reactions revealed the efficiency of the nickel electrodeposition reaction from the 0.2 M nickel(II) acetate based aqueous solution to be 90 %. In

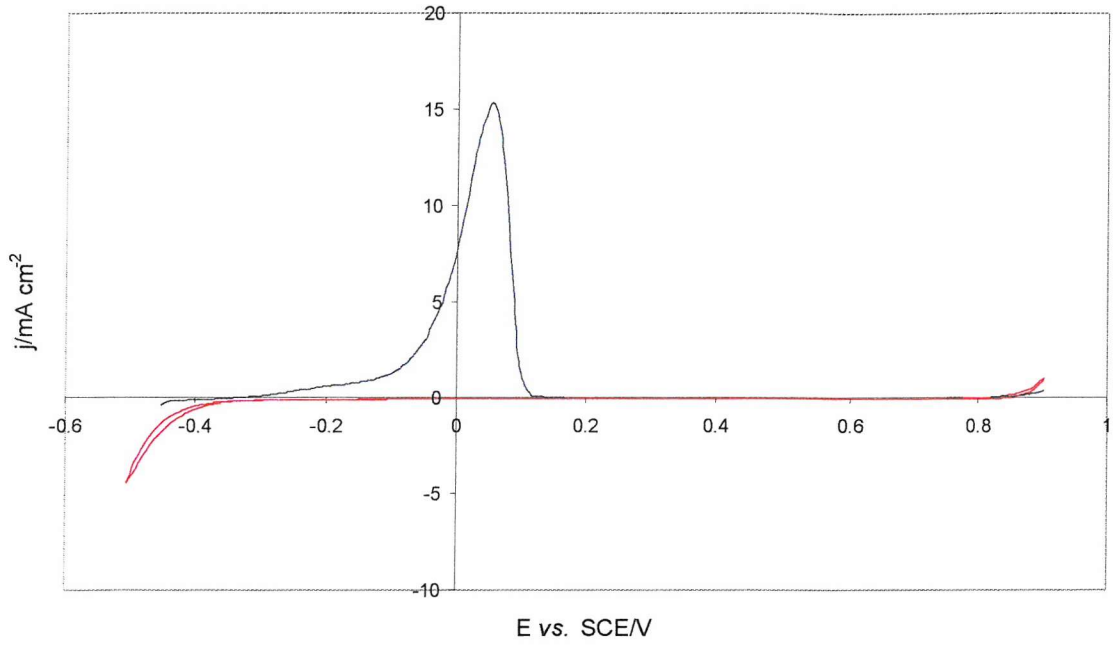

Figure 5.13 shows the oxidation of nickel metal (blue) during a forward voltammetric sweep at 2 mV s^{-1} in 0.1 M $HCl_{(aq)}$. The voltammetry of a gold disc electrode (red) in the same solution at 2 mV s^{-1} shows no activity.

contrast, the efficiency of the electroreduction of $Ni^{2+}_{(aq)}$ in the H_I phase of a 65 % wt. Brij® 56/0.2 M nickel acetate based template was found to be 46% for a 15 h. deposition. In both cases the additional reductive current is thought to be due to hydrogen evolution by solvent reduction as described by the following mechanism:

$$H_2O + e^- \rightarrow \frac{1}{2} H_2 + OH^- \qquad (1)$$

As discussed in Chapter 1, the cathodic electrodeposition of nickel metal from $Ni^{2+}_{(aq)}$ salts proceeds via the following mechanism.

$$Ni^{2+} + H_2O \leftrightarrow NiOH^+ + H^+ \quad (2)$$

$$NiOH^+ + e^- \rightarrow NiOH_{ads} \quad (3)$$

$$NiOH_{ads} + H^+ + e^- \leftrightarrow Ni + H_2O \quad (4)$$

Despite the fact that the electrodeposition of nickel from both the aqueous solution and the liquid crystalline template is carried out at – 0.9 V *vs.* SCE, the efficiency data indicates that the hydrogen evolution reaction (HER) makes a significantly larger relative contribution to the reductive current in the electrodeposition from the liquid crystal than from the aqueous solution. This enhancement of the HER may be a result of the pH difference between the two media; the values being 6.75 and 7.15 for the aqueous solution and liquid crystal respectively. Examination of the HER mechanism reveals however, that the rate of hydrogen evolution is inversely proportional to the pH. As such, the rate of hydrogen evolution would be expected to be greater in the aqueous solution. Consequently, it is more reasonable to suggest that the decreased deposition efficiency observed in the liquid crystal template is not due to an increase in the rate of hydrogen evolution (relative to the rate of nickel electrodeposition) but that the decreased efficiency is derived from a relative decrease in the rate of nickel deposition. Section 2.3.2.2 established that nickel deposition in liquid crystalline media was a diffusion limited process, unlike in the case of deposition from a surfactant-free aqueous solution. Since it is very unlikely that hydrogen evolution is also diffusion limited in the liquid crystal template (as would be the case if water were required to diffuse through a surfactant layer at the electrode surface) it appears that the decreased efficiency observed in this system is due to a decreased rate of nickel electrodeposition relative to hydrogen evolution. This statement is supported in the following Section that describes variation in the deposition efficiency with time.

5.3.3.2 Variation in Deposition Efficiency with Time

The process of ASV described above was used to calculate the efficiency of mesoporous nickel electrodeposition reactions in the H_I phases of Brij® 56 and Pluronic® P123 based templates as a function of time. Figure 5.14 compares the variation of deposition efficiency with time for both surfactant templates. The efficiency of deposition in the P123 template does not show significant variation from 80 % over a 48 h. period. This result agrees well with results presented in Section

2.3.2.2 that demonstrated the electrodeposition of mesoporous nickel from a P123 based template to be a kinetically controlled process. Here, the reaction efficiency would be expected to be constant since the deposition and hydrogen evolution currents are constant current, kinetically controlled processes. In contrast, Figure 5.14 shows the efficiency of deposition from a Brij® 56 based template to decrease from 54

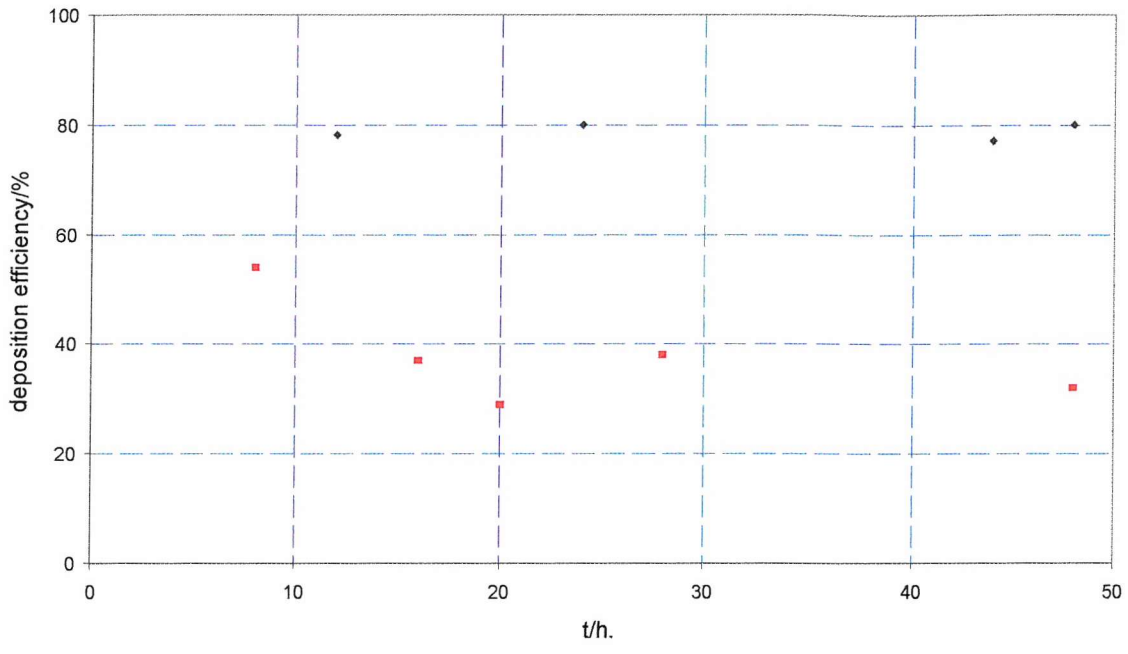

Figure 5.14 compares the efficiency of nickel deposition from H_I Pluronic® P123 (blue) and Brij® 56 (red) deposition templates as a function of time on 1 mm gold disc electrodes.

% after 8 h. to 32 % after 48 h. Unlike the case of deposition in the P123 template, and as was previously shown in Chapter 2, deposition from the Brij® 56 based template is a diffusion limited process. Consequently, while the hydrogen evolution current is expected to remain constant during a deposition experiment, the current of nickel reduction decreases in magnitude with time. The net effect is a decrease in the deposition efficiency with time.

It must also be noted that since deposition efficiency in the Brij® 56 based template depends on a diffusion limited process and therefore the diffusion coefficient, the deposition efficiency may vary with electrode size and geometry. This phenomenon was not investigated.

5.3.4 Variation in Electrode Capacity with Electrode Thickness and Geometric Area

In order to examine the feasibility of fabricating thicker mesoporous nickel electrodes with high area-specific charge capacities, the relationship between mesoporous nickel electrode thickness and charge storage capacity was investigated. Figure 5.15 shows

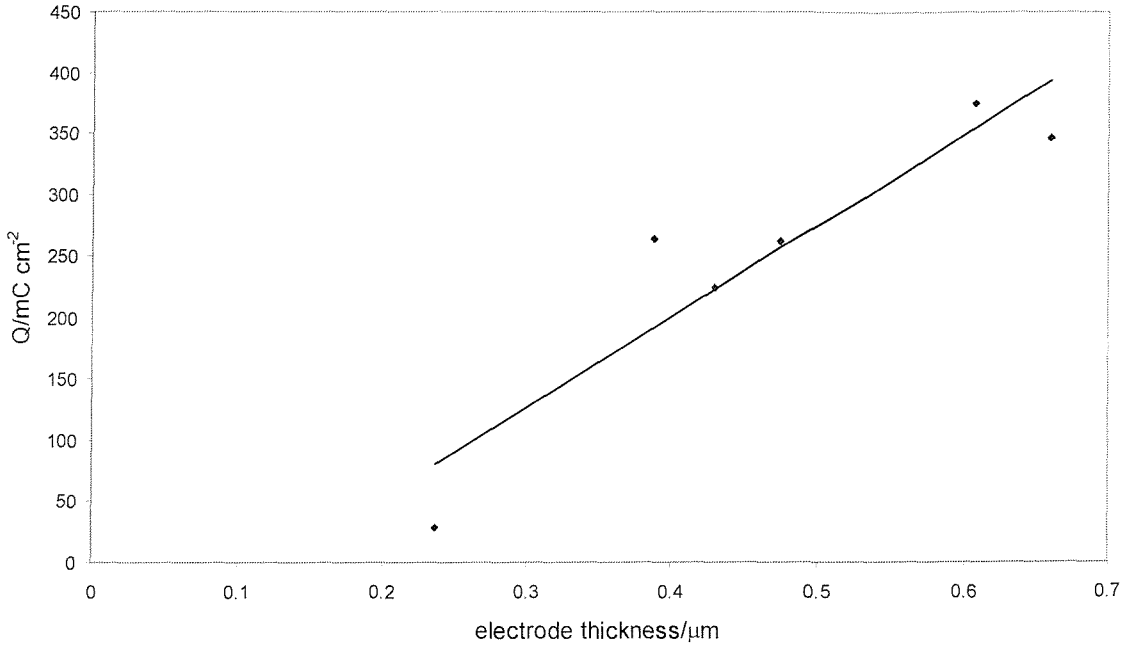

Figure 5.15 shows the increase in reversible charge storage capacity (calculated from the second sweep) with electrode thickness for H_I Brij® 56 templated mesoporous nickel electrodes at 25 °C.

the variation with deposit thickness of the reversible charge capacity of mesoporous nickel as determined by cyclic voltammetry in 6 M KOH. There is a significant amount of scatter in the data, however there is an approximate proportionality between the two parameters. The charge storage capacity increases to a value of almost 400 mC cm^{-2} with an electrode thickness of 0.65 μm. Although this is relatively thin when compared to conventional supercapacitor and battery electrodes, it proves that the mesopores responsible for the high surface area of the material are continuous throughout this length.

The charge storage capacity of mesoporous nickel electrodes in alkaline solution was also investigated as a function of geometric electrode area. This was done both in

order to demonstrate the industrial applicability of the template deposition process and to examine the effect of electrode microstructure on charge storage capacity.

As illustrated in Figure 5.10, mesoporous nickel electrodes possess a domain-like microstructure that is derived from the structure of the template. It was thought that if the H_I pores of the mesostructure were lying parallel with the substrate surface then these pores would not be electrochemically accessible due to truncation by a domain boundary, unless they were situated at the edge of the electrode. As a result, charge storage capacity per unit of geometric electrode area would decrease with increasing electrode area as the ratio of edge located domains to inner electrode domains decreased. Figure 5.16 shows that this is not the case. Here, the reversible charge storage capacity as determined by cyclic voltammetry in 6 M KOH normalised against the deposition charge shows no significant variation with the geometric electrode area. The slight increase in the normalised capacity with electrode area as indicated by the line plot cannot be attributed to any effect because of the relatively

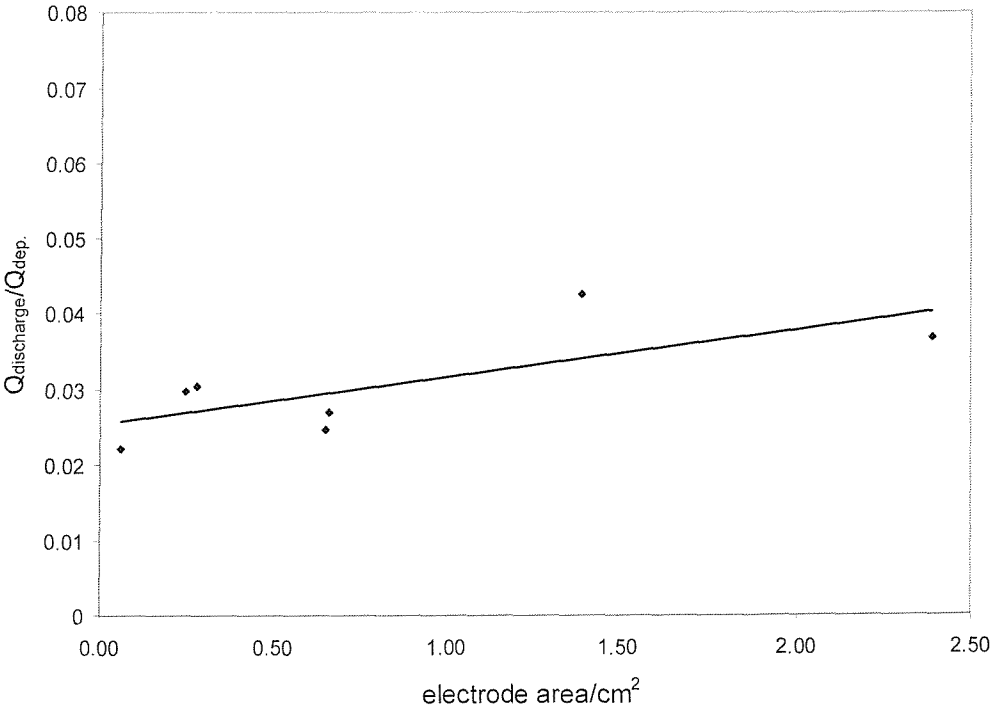

Figure 5.16. Reversible charge storage capacity in 6 M KOH at 25 °C changes only slightly for Brij® 56 templated H_I mesoporous nickel with change in the geometric electrode area.

large degree of scatter in the data. Nevertheless, Figure 5.16 demonstrates that the fabrication of mesoporous nickel electrodes of industrially relevant sizes is possible

and is not detrimental to the intrinsic capacity of the electrodes demonstrated in Chapter 2.

5.4 Conclusions and Further Work

The work described in this Chapter has built on the work of Chapter 2 in which the synthesis and characterisation of mesoporous nickel was discussed. Here, methods of producing mesoporous films of high mesostructural quality were discussed. Thermal annealing of the deposition template prior to deposition and washing the resulting deposited mesostructure in an appropriate solvent were shown to be crucial in obtaining high charge capacity electrodes. It was shown that mesoporous nickel electrodes may be deposited with greater thickness and with larger areas than was demonstrated in Chapter 2 without sacrificing intrinsic activity. In doing so, the feasibility of producing mesoporous nickel for industrial application to power source technologies such as those described in Chapters 3 and 4 was proven. Chapter 5 also saw the establishment of the notion that the efficiency of the nickel electrodeposition reaction in the H_I phase of Brij® 56 is variable with time as a result of the diffusion limitation imposed on the rate of deposition.

Deposition of mesoporous nickel onto less expensive substrates is an important factor in making mesoporous nickel electrodes commercially competitive. The mesoporous materials described here were deposited exclusively onto relatively expensive gold surfaces. Consequently, efforts are required in order to effect the deposition onto less expensive substrates. The rate of deposition must also be increased. Current deposition rates are too slow, requiring deposition times of 48 h. to produce the thickest films described in this Chapter. Since the deposition process has been shown to be diffusion limited, the obvious means of increasing the rate of deposition are increasing electrolyte concentration, increasing deposition temperature and decreasing surfactant concentration.

5.5 References

[1] G. C. Allan, J. R. Aston, F. Grieser and T. W. Healy, J. Colloid Interface Sci., 1989, 128, 258.

[2] H. N. Partick and G. G. Warr, Coll. Surf. A, 2000, 162, 149.

[3] Mitchell, D. J.; Tiddy, G. J. T.; Waring, L.; Bostock, T.; McDonald, M. P. *J. Chem. Soc., Faraday Trans. I* **1983**, 79, 975.

[4] Chen, C.; Postlethwaite, T. A.; Hutchison, J. E.; Samulski, E. T.; Murray, R. W., *J. Phys. Chem.*, **1995**, 99, 8804-8811.

Appendices

Appendix 1: Pore Volume Calculation and Theoretical Surface Area

A1-1. Theoretical Pore Volume

The pore volume was calculated on the basis of a two-dimensional representation of an ideal H_I structure. The unit cell of this structure is illustrated in Figure A1.1.

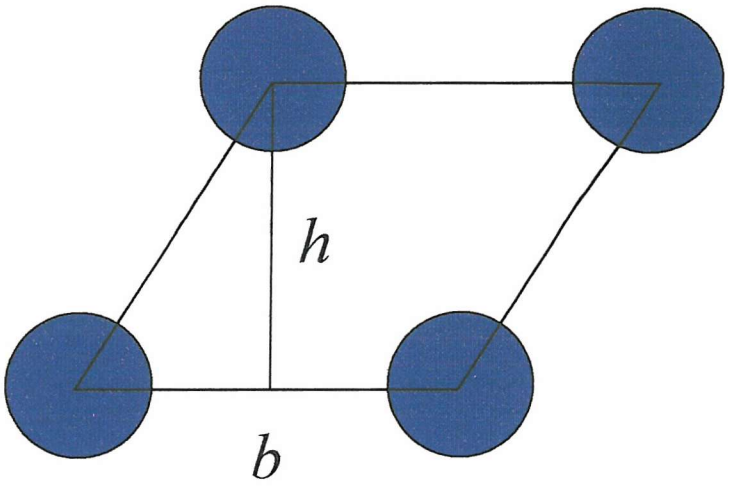

Figure A1.1 shows the most basic unit of the hexagonal geometry.

The area of the unit cell in Figure A1.1 is $b.h$ where b is the centre to centre pore distance and $h=(\sin 60).b$.

Therefore, the area of the unit cell is $(\sin 60).b^2$.

The area occupied by porosity in the unit cell is equal to one pore which has an area of πr^2 where r is the pore radius.

As such, the percentage of the total volume occupied by the pores is,

$$\frac{\pi r^2}{\sin 60.b^2}$$

Since b is equal to $2r+w$ where w is the wall thickness the percentage pore volume is found using Equation 1,

$$\frac{\pi r^2}{\sin 60.(2r+w)^2}.100 \qquad (1)$$

A1-2. Theoretical Surface Area

In the unit cell of Figure A1.1 a single pore in the ideal H_I structure occupies an area equal to $sin\ 60.(2r+w)^2$ where r and w have units of nm.

In 1 cm^2 there are $\frac{10^{14}}{\sin 60.(2r+w)^2}$ pores present.

The circumference of a single pore is equal to $2\pi r$, so the total pore circumference in 1 cm^2 is $2\pi r.\ \frac{10^{14}}{\sin 60.(2r+w)^2}$ (with units of nm).

Therefore, the total area of the pores in 1 cm^3 is $\frac{10^3}{\sin 60.(2r+w)^2}$, with units of m^2 cm^{-3}.

This value is converted to a value with units of $m^2\ g^{-1}$ by using the density of nickel corrected for the pore volume as determined in A1-1.

Appendix 2: Liquid Crystalline Phase Space Group Data

Phase	Space group	Selection rules n = 1, 2, 3, 4	*hkl* list	spacing ratios
Lamellar (L_α)		*h*00: $h = n$	*100* *200* *300*	1 2 3
Hexagonal (H_I)	P6mm	*hk*0: $h + k = n$	*100* *110* *200* *210*	1 √3 2 √7
Cubic (V_I)	Pm3n (223)	*h, k, l* permutable *hhl*: $l = 2n$ *h*00: $h = 2n$	*110* *200* *210* *211* *220* *310* *222*	√2 2 √5 √6 √8 √10 √12
	Pn3m (224)	*h, k, l* permutable *hhl*: $l = 2n$ *h*00: $h = 2n$	*110* *111* *200* *211* *220* *221* *310* *311* *222*	√2 √3 2 √6 √8 3 √10 √11 √12
	Fm3m (225)	*h, k, l* permutable *hkl*: $h+k, h+l, l+k = 2n$ 0*kl*: $k+l = 2n$ *hhl*: $h+l = 2n$ *h*00: $h = 2n$	*110* *200* *220* *311* *222*	√2 2 √8 √11 √12
	Fd3m (227)	*h, k, l* permutable *hkl*: $h+k = 2n$ *and* $h+l, l+k = 2n$ 0*kl*: $k+l = 4n$ and $k, l = 2n$ *hhl*: $h+l = 2n$ *h*00: $h = 4n$	*111* *220* *311* *222*	√3 √8 √11 √12
	Im3m (229)	*h, k, l* permutable *hkl*: $h+k+l = 2n$ 0*kl*: $k+l = 2n$ *hhl*: $l = 2n$ *h*00: $h = 2n$	*110* *200* *211* *220* *310* *222*	√2 2 √6 √8 √10 √12
	Ia3d (230)	*h, k, l* permutable *hkl*: $h+k+l = 2n$ 0*kl*: $k, l = 2n$ *hhl*: $2h+l = 4n$ *h*00: $h = 4n$	*110* *200* *211* *220* *310* *222*	√2 2 √6 √8 √10 √12

Table 1. Selection rules for the space groups associated with lyotropic liquid crystal phases and the relative spacings of the first Bragg reflections. Note that only a

selection of the cubic space groups are given for the more commonly found phases in lyotropic systems. Information obtained from the international tables of crystallography.